

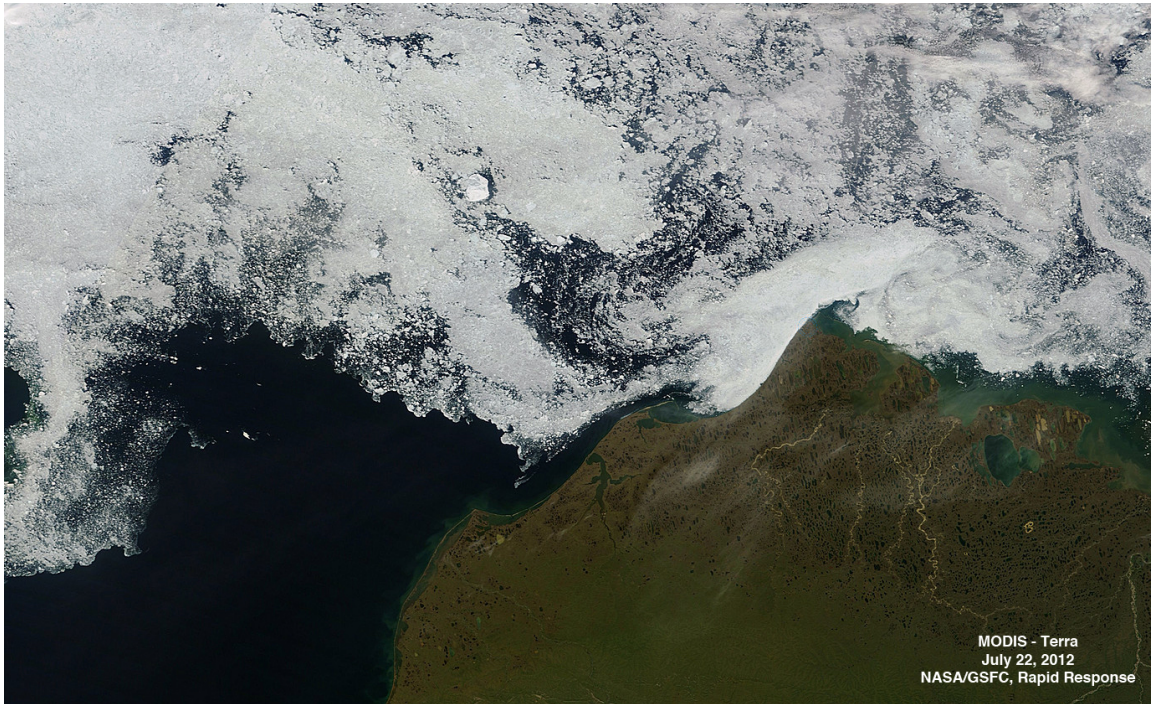
OCS Study BOEM 2012-079

**Application of High Frequency Radar to Potential Hydrocarbon Development
Areas in the Northeast Chukchi Sea**

Final Report
April 2013

Thomas J. Weingartner, Peter Winsor
Rachel A. Potter, Hank Statscewich, Elizabeth L. Dobbins

University of Alaska
School of Fisheries and Ocean Sciences



This project was funded by a partnership among:

U.S. Department of the Interior, Bureau of Ocean Energy Management
Alaska Outer Continental Shelf Region
Contract No: M09AC15207

ConocoPhillips, Inc.
Shell Exploration & Production Company
State of Alaska Coastal Impact Assistance Program
Alaska Ocean Observing System

OCS Study BOEM 2012-079

**Application of High Frequency Radar to Potential Hydrocarbon Development
Areas in the Northeast Chukchi Sea**

Final Report

Thomas J. Weingartner, Peter Winsor
Rachel A. Potter, Hank Statscewich, Elizabeth L. Dobbins

University of Alaska
School of Fisheries and Ocean Sciences
Institute of Marine Science
Fairbanks, AK 99775-7220

This project was funded by a partnership among:

U.S. Department of the Interior, Bureau of Ocean Energy Management
Alaska Outer Continental Shelf Region
Anchorage AK 99503
Contract No: M09AC15207
as part of the BOEM Alaska Environmental Studies Program.

ConocoPhillips, Inc.
P.O. Box 100360
Anchorage, AK 99510-0360

Shell Exploration & Production Company
3601 C Street, Suite 1334
Anchorage, AK 99503

Coastal Impact Assistance Program
Alaska Department of Natural Resources
Juneau, AK 99811

Alaska Ocean Observing System
1007 W. Third Ave., Suite 100
Anchorage, AK 99501

April 2013

The opinions, findings, conclusions, or recommendations expressed in this report or product are those of the authors and do not necessarily reflect the views of the U.S. Department of the Interior, nor does mention of trade names or commercial products constitute endorsement or recommendation for use by the Federal Government.

TABLE OF CONTENTS

LIST OF TABLES	iii
LIST OF FIGURES.....	iv
ABSTRACT.....	xiii
1. Introduction	1
2. Objectives	3
3. Methods	4
3.1 Moorings.....	4
3.2 High-Frequency Radar (HFR)	6
3.3 Gliders.....	9
4. Results	12
4.1 Waves.....	12
4.2 Winds.....	15
4.3 Sub-Surface Currents and Hydrography.....	17
4.3.1 <i>Velocity Structure</i>	17
4.3.2 <i>Barrow Canyon Transport</i>	45
4.3.3 <i>Moored Temperatures and Salinities</i>	52
4.4 Surface Currents.....	58
4.4.1 <i>Comparison of Surface and Near-Surface Currents</i>	60
4.4.2 <i>Monthly Velocity Fields: Means and Variances</i>	64
4.4.3 <i>Mean Surface Currents as a Function of Wind Direction</i>	81
4.4.4 <i>Mean Surface Currents as a Function of ACC Direction</i>	87
4.4.5 <i>Statistical Aspects of the Circulations</i>	92
4.4.6 <i>Wind-Current Relationships</i>	96
4.5 Hydrography from Gliders.....	98
4.5.1 <i>Glider 159 Deployment: August 4 – 21, 2010</i>	98
4.5.2 <i>Glider 159 Deployment: September 18 – October 10, 2010</i>	102
4.5.3 <i>Glider 167 Deployment: September 18 – September 30, 2010</i>	114
4.5.4 <i>Glider 191 Deployment: August 1 –14, 2011</i>	124
4.5.5 <i>Glider 191 Deployment: September 1 –12, 2011</i>	136

4.5.6 <i>Glider 191 Deployment: September 12 –16, 2011</i>	146
4.5.7 <i>Interannual Hydrographic Variability</i>	146
5. Discussion and Summary	149
6. Future Directions	156
7. Acknowledgments	157
8. Publications and Presentations	158
9. References	159

LIST OF TABLES

Table 1. Mooring positions and depths.	6
Table 2. Operational periods for each HFR installation site in 2009, 2010, and 2011.	7
Table 3. Annual statistics for each glider. Only days with active data acquisition are included. ...	9
Table 4. Summary of wind statistics from the NARR gridpoint at 71.25°N, 161.25°W. Listed are mean zonal (\bar{U}) and meridional (\bar{V}) wind velocities and their standard deviations (s_u , s_v), mean vector wind speed (W), mean wind direction (Θ), mean wind components along major (\bar{U}_r) and minor axes (\bar{V}_r) of the variance ellipses and standard deviations along each axis (s_{ur} , s_{vr}), percentage of the total variance explained by the major axis wind component, orientation of the major axis (Θ_M), and steadiness (S).	16
Table 5. Monthly and record-length statistics for the vertically averaged velocities at BC1. Number of hourly records in each month (N), mean zonal (\bar{U}) and meridional (\bar{V}) velocities and their standard deviations (s_u , s_v), percent variance explained by the principal axis, and orientation of the principal axis (θ).....	25
Table 6. Monthly and record-length statistics for the vertically averaged velocities at BC2.	25
Table 7. Monthly and record-length statistics for the vertically averaged velocities at BC3.	26
Table 8. Monthly and record-length statistics for the vertically averaged velocities at BC4.	26
Table 9. Monthly and record-length statistics for the vertically averaged velocities at BC5.	27
Table 10. Monthly and record-length statistics for the vertically averaged velocities at BC6.	27
Table 11. Wind-transport regression results.	47

LIST OF FIGURES

Figure 1. Mean depth-integrated streamlines (white) in the Chukchi Sea, after <i>Spall</i> [2007]. The bathymetry is colored. Geographical names are included in the figure.	2
Figure 2. Map showing HFR coverage area (golden crosshatch) and mooring locations (blue squares) overlaid on bathymetric contours (m). Barrow, Wainwright, Point Lay, Hanna Shoal, Barrow Canyon, Icy Cape (IC), and Point Franklin (PF) are identified, as are industry study areas Klondike (K), Burger (B), and Statoil (S).	5
Figure 3. Example mooring package for moorings BC2 – BC6.	5
Figure 4. HFR antenna setup in Barrow (top), Wainwright (middle), and Point Lay (bottom).	8
Figure 5. Cross spectra collected by the HFR system in Wainwright. The top figure shows Bragg peaks when ionospheric interference is absent, and the bottom figure depicts Bragg peaks when the HFR signal is reflected by the ionosphere.	9
Figure 6. Two Webb Slocum gliders being deployed in the northeast Chukchi Sea off the Wainwright-based vessel Tukpuk in 2010.	10
Figure 7. Waterfall plot of vertical temperature profiles from glider #159 showing an example of down-casts (blue) and up-casts (red). The thermal lag issue is visible in the thermocline around 25 m depth as differences in the temperature traces.	11
Figure 8. Time series of the significant wave height (H_S), period of H_S (T_p), direction from which H_S waves are propagating (Θ), and the east (U_w) and north (V_w) components of the winds. Wave data are from the August 18 – November 7, 2010 time period.	13
Figure 9. Time series of the significant wave height (H_S), period of H_S (T_p), direction from which H_S waves are propagating (Θ), and the east (U_w) and north (V_w) components of the winds. Wave data are from the May 18 – August 24, 2011 time period.	14
Figure 10. Time series of zonal and meridional wind components from Wainwright (blue) and the NARR grid point closest to BC6 for August – September 2010 (top) and October – November 2010 (bottom).	18
Figure 11. Time series of zonal and meridional wind components from Wainwright (blue) and the NARR grid point closest to BC6 for January 2011 (top) and February – March 2011 (bottom).	19
Figure 12. Time series of zonal and meridional wind components from Wainwright (blue) and the NARR grid point closest to BC6 for April – May 2011 (top) and June – July 2011 (bottom).	20
Figure 13. Linear regression results for NARR vs. Barrow winds. Panels on the left (right) are for the zonal (meridional) wind components. The results are for 2-month long periods beginning August – October 2010 (top) through January – February 2011 (bottom).	21
Figure 14. Linear regression results for NARR vs. Barrow winds. Panels on the left (right) are for the zonal (meridional) wind components. The results are for 2-month long periods beginning February – April 2011 (top) through June – August 2011 (bottom).	22

Figure 15. Linear regression results for NARR vs. Wainwright winds. Panels on the left (right) are for the zonal (meridional) wind components. The results are for 2-month long periods beginning August – October 2010 (top) through January – February 2011 (bottom).	23
Figure 16. Linear regression results for NARR vs. Wainwright winds. Panels on the left (right) are for the zonal (meridional) wind components. The results are for 2-month long periods beginning February – April 2011 (top) through June – August 2011 (bottom).	24
Figure 17. Depth averaged mean velocity vectors and variance ellipses for mooring array. Bathymetry is shaded.	28
Figure 18. Along-shore (top) and cross-shore (bottom) record-length mean velocity component sections. Contours are in cm s^{-1} . Dotted vertical lines show the locations of the moorings. Mean winds were $\sim 2.4 \text{ m s}^{-1}$ towards 255°T	29
Figure 19. Time series of the downcanyon (blue) and upcanyon (red) currents at 20.5 m depth for mooring BC2.	29
Figure 20. Vertical sections of the along-shore (top) and cross-shore (bottom) velocities for the downcanyon composite. Dotted vertical lines show the locations of the moorings, with BC6 on the left and BC1 on the right.	30
Figure 21. Vertical sections of the along-shore (top) and cross-shore (bottom) velocities for the upcanyon composite. Dotted vertical lines show the locations of the moorings, with BC6 on the left and BC1 on the right.	31
Figure 22. Vertical sections of the along-shore (upper panel top) and cross-shore (upper panel bottom) velocities for August 18 – 31, 2010. Mean winds (lower panel) over the mooring array were 2.8 m s^{-1} towards 262°T	32
Figure 23. Vertical sections of the along-shore (upper panel top) and cross-shore (upper panel bottom) velocities for September 2010. Mean winds (lower panel) over the mooring array were 2.0 m s^{-1} towards 275°T	33
Figure 24. Vertical sections of the along-shore (upper panel top) and cross-shore (upper panel bottom) velocities for October 2010. Mean winds (lower panel) over the mooring array were 8.2 m s^{-1} towards 252°T	34
Figure 25. Vertical sections of the along-shore (upper panel top) and cross-shore (upper panel bottom) velocities for November 2010. Mean winds (lower panel) over the mooring array were 1.3 m s^{-1} towards 225°T	35
Figure 26. Vertical sections of the along-shore (upper panel top) and cross-shore (upper panel bottom) velocities for December 2010. Mean winds (lower panel) over the mooring array were 1.6 m s^{-1} towards 218°T	36
Figure 27. Vertical sections of the along-shore (upper panel top) and cross-shore (upper panel bottom) velocities for January 2011. Mean winds (lower panel) over the mooring array were 1.3 m s^{-1} towards 266°T	37
Figure 28. Vertical sections of the along-shore (upper panel top) and cross-shore (upper panel bottom) velocities for February 2011. Mean winds (lower panel) over the mooring array were 1.7 m s^{-1} towards 33°T	38

Figure 29. Vertical sections of the along-shore (upper panel top) and cross-shore (upper panel bottom) velocities for March 2011. Mean winds (lower panel) over the mooring array were 1.3 m s^{-1} towards 315°T	39
Figure 30. Vertical sections of the along-shore (upper panel top) and cross-shore (upper panel bottom) velocities for April 2011. Mean winds (lower panel) over the mooring array were 1.6 m s^{-1} towards 248°T	40
Figure 31. Vertical sections of the along-shore (upper panel top) and cross-shore (upper panel bottom) velocities for May 2011. Mean winds (lower panel) over the mooring array were 1.9 m s^{-1} towards 261°T	41
Figure 32. Vertical sections of the along-shore (upper panel top) and cross-shore (upper panel bottom) velocities for June 2011. Mean winds (lower panel) over the mooring array were 5.0 m s^{-1} towards 247°T	42
Figure 33. Vertical sections of the along-shore (upper panel top) and cross-shore (upper panel bottom) velocities for July 2011. Mean winds (lower panel) over the mooring array were 3.8 m s^{-1} towards 245°T	43
Figure 34. Vertical sections of the along-shore (upper panel top) and cross-shore (upper panel bottom) velocities for August 1 – 26, 2011. Mean winds (lower panel) over the mooring array were 2.9 m s^{-1} towards 262°T	44
Figure 35. The cross-sectional areas (defined by green lines) used for each mooring (black dotted lines) to compute the along-canyon transport. The nearshore mooring, BC1, is on the left-hand side and mooring BC6 is on the right-hand side of the figure.	46
Figure 36. Mean daily winds projected along 20°T (top; blue) and mean daily transport (bottom; black). Positive (negative) values of transport are toward 56°T (236°T). The dashed, vertical line denotes the October 2, 2010, upcanyon event discussed in the text.	46
Figure 37. Wind-transport coherence-squared spectrum.	47
Figure 38. Demeaned records of sea-level from Red Dog (black) and from the pressure gauge at mooring BC1 (blue) for the period of Sept. 28 – Oct. 5, 2010.	49
Figure 39. Sea level autospectra (top) at BC1 (black), Red Dog (blue), and Prudhoe Bay (red), and coherence (middle) and phase (bottom) spectra between Red Dog and BC1 (black) and Red Dog and Prudhoe Bay (blue).	49
Figure 40. Time series of $\partial u / f \partial y$, the Rossby number computed from moorings BC1 – BC2 (blue) and BC2 – BC3 (red) at 26 m depth.	50
Figure 41. Mean monthly transports from Bering Strait climatology (red) and the 2010-2011 mooring record in Barrow Canyon (black).	51
Figure 42. Scatterplot of Barrow Canyon transport versus vertically averaged currents at mooring BC2.	51

Figure 43. T/S diagrams constructed from each mooring. Ellipses in BC1 encompass T/S properties of summer water (red) and winter-formed dense waters (green). Ellipses in BC2 encompass waters drawn from the Atlantic Layer along the Chukchi-Beaufort continental slope (blue) and Bering Sea Water (yellow). The dashed blue line in each plot indicates the freezing point curve.	53
Figure 44. Time series of temperature (blue) and salinity (green) at moorings BC1 (top) and BC2 (bottom).	54
Figure 45. Time series of temperature (blue) and salinity (green) at moorings BC3 (top) and BC4 (bottom).	55
Figure 46. Time series of temperature (blue) and salinity (green) at moorings BC5 (top) and BC6 (bottom).	56
Figure 47. Mean daily salinity (top), temperature (middle), and along-shore currents (bottom) from mooring BC2.	57
Figure 48. Timeline of HFR system runtime for each year and each field site. Red numbers represent the percentage of time each system was operational within each field season.	58
Figure 49. Map of HFR coverage (golden crosshatch) with gaps in spatial coverage defined.	59
Figure 50. HFR percent coverage for 2010. Similar results were found for 2009 and 2011.	60
Figure 51. Average number of HFR data returns per hour of day for Barrow (top), Wainwright (middle), and Point Lay (bottom).	61
Figure 52. Time series of u and v -components for the HFR (blue) and ADCP (black) at BC2 (upper two panels) and BC6 (lower two panels). ADCP data were measured at 8 m.	62
Figure 53. Scatterplots of u and v -components for the HFR and ADCP at BC2 (upper two panels) and BC6 (lower two panels).	63
Figure 54. Time series of Stokes' drift based on H_S for the period of August 18 – November 1, 2010 (upper panel) and difference in the Stokes' drift between the surface and 1.5 m depth (bottom).	63
Figure 55. Comparison of H_S measured at BC1 (blue) and the Wavewatch model (green) from September 1 – November 2, 2010.	64
Figure 56. Mean surface currents (top) and principal axes (bottom) for July 2010. Mean wind and principal axes values are plotted within the land mask at 160°W for this and all subsequent figures.	65
Figure 57. Mean surface currents (top) and principal axes (bottom) for July 2011.	66
Figure 58. Mean surface currents (top) and principal axes (bottom) for August 2010.	68
Figure 59. Mean surface currents (top) and principal axes (bottom) for August 2011.	69
Figure 60. Mean surface currents (top) and principal axes (bottom) for September 2009.	70
Figure 61. Mean surface currents (top) and principal axes (bottom) for September 2010.	71
Figure 62. Mean surface currents (top) and principal axes (bottom) for September 2011.	72
Figure 63. Mean surface currents (top) and principal axes (bottom) for October 2009.	73

Figure 64. Mean surface currents (top) and principal axes (bottom) for October 2010.	75
Figure 65. Mean surface currents (top) and principal axes (bottom) for October 2011.	76
Figure 66. Mean surface currents (top) and principal axes (bottom) for November 2009.	77
Figure 67. Mean surface currents (top) and principal axes (bottom) for November 2010.	78
Figure 68. Mean surface currents (top) and principal axes (bottom) for November 2011.	79
Figure 69. Examples of surface current mesoscale variability over the northeast Chukchi Sea. .	80
Figure 70. Wind rose for HFR operational dates in 2009 (top), 2010 (middle), and 2011 (bottom). The directions are those toward which the wind is blowing.	82
Figure 71. Mean surface currents in 2009 (top), 2010 (middle), and 2011 (bottom) for periods when winds blew towards 0 - 90°T.	83
Figure 72. Mean surface currents in 2009 (top), 2010 (middle), and 2011 (bottom) for periods when winds blew towards 90 - 180°T.	84
Figure 73. Mean surface currents in 2009 (top), 2010 (middle), and 2011 (bottom) for periods when winds blew towards 180 - 220°T.	85
Figure 74. Mean surface currents in 2009 (top), 2010 (middle), and 2011 (bottom) for periods when winds blew towards 220 - 260°T at <6 m/s.	86
Figure 75. Mean surface currents in 2009 (top), 2010 (middle), and 2011 (bottom) for periods when winds blew towards 220 - 260°T at >6 m/s.	88
Figure 76. Mean surface currents in 2009 (top), 2010 (middle), and 2011 (bottom) for periods when winds blew towards 260 - 280°T.	89
Figure 77. Mean surface currents in 2009 (top), 2010 (middle), and 2011 (bottom) for periods when winds blew towards 280 - 360°T.	90
Figure 78. Mean surface currents in 2009 (top), 2010 (middle), and 2011 (bottom) when the ACC was flowing to the northeast.	91
Figure 79. Mean surface currents in 2009 (top), 2010 (middle), and 2011 (bottom) when the ACC was flowing to the southwest.	93
Figure 80. Location of the HFR transect (red line) used for surface current correlations across the ACC, which are shown in Figure 81.	94
Figure 81. Cross-correlation coefficients (R) as a function of distance along the transect shown in Figure 80. All correlations were computed with respect to the values at ~15 km from shore, where R=1.	94
Figure 82. Contour maps for 2011 of r^2 , the magnitude squared of the complex correlation coefficient. The black asterisk represents the origin of the correlation, and the color bar to the right of each plot denotes the value of r^2	95
Figure 83. The first eigenmode of the major axis velocity component from 2011.	96

Figure 84. Wind-current complex correlation results for each year. The left-hand panels map r^2 , and the right-hand panels map phase, θ . Color bars to the right of each map denote the values of the respective mapped variables. The asterisk is the location of the NARR wind grid point used in the analysis.97

Figure 85. Map showing the 2010 and 2011 glider survey tracks in the northeast Chukchi Sea. Also shown are the three main lease patches (Burger (B), Klondike (K), and Statoil (S); black boxes). The darker-shaded glider tracks are discussed in this report.98

Figure 86. Section plots of temperature (top panel), salinity (middle panel), and density (sigma- t ; bottom panel) from glider 159, August 4-10, 2010 (see Figure 85 for section location). ...100

Figure 87. Section plots of temperature (top panel), salinity (middle panel), and density (sigma- t ; bottom panel) from glider 159, August 12-21, 2010 (see Figure 85 for section location). .101

Figure 88. Mean surface currents on September 18 (top) and 19 (bottom), 2010. The glider track is red (denoting the track on the indicated day) and tan (denoting the entire glider track). 103

Figure 89. Mean surface currents on September 20 (top) and 21 (bottom), 2010. The glider track is red (denoting the track on the indicated day) and tan (denoting the entire glider track). 104

Figure 90. Mean surface currents on September 22 (top) and 23 (bottom), 2010. The glider track is red (denoting the track on the indicated day) and tan (denoting the entire glider track). 105

Figure 91. Mean surface currents on September 24 (top) and 25 (bottom), 2010. The glider track is red (denoting the track on the indicated day) and tan (denoting the entire glider track). 106

Figure 92. Mean surface currents on September 26 (top) and 27 (bottom), 2010. The glider track is red (denoting the track on the indicated day) and tan (denoting the entire glider track). 107

Figure 93. Mean surface currents on September 28 (top) and 29 (bottom), 2010. The glider track is red (denoting the track on the indicated day) and tan (denoting the entire glider track). 108

Figure 94. Mean surface currents on September 30 (top) and October 1 (bottom), 2010. The glider track is red (denoting the track on the indicated day) and tan (denoting the entire glider track).109

Figure 95. Mean surface currents on October 2 (top) and 3 (bottom), 2010. The glider track is red (denoting the track on the indicated day) and tan (denoting the entire glider track).110

Figure 96. Mean surface currents on October 4 (top) and 5 (bottom), 2010. The glider track is red (denoting the track on the indicated day) and tan (denoting the entire glider track).111

Figure 97. Mean surface currents on October 6 (top) and 7 (bottom), 2010. The glider track is red (denoting the track on the indicated day) and tan (denoting the entire glider track).112

Figure 98. Mean surface currents on October 8 (top) and 9 (bottom), 2010. The glider track is red (denoting the track on the indicated day) and tan (denoting the entire glider track).113

Figure 99. Mean surface currents on October 10, 2010. The glider track is red (denoting the track on the indicated day) and tan (denoting the entire glider track).114

Figure 100. Section plots of temperature (top), salinity (middle), and density (sigma- t ; bottom) from glider 159 September 19-30, 2010.115

Figure 101. Section plots of temperature (top), salinity (middle), and density (σ_t ; bottom) from glider 159 October 1-10, 2010.	116
Figure 102. Mean surface currents on September 17 (top) and 18 (bottom), 2010. The glider track is red (denoting the track on the indicated day) and tan (denoting the entire glider track).	117
Figure 103. Mean surface currents on September 19 (top) and 20 (bottom), 2010. The glider track is red (denoting the track on the indicated day) and tan (denoting the entire glider track).	118
Figure 104. Mean surface currents on September 20 (top) and 21 (bottom), 2010. The glider track is red (denoting the track on the indicated day) and tan (denoting the entire glider track).	119
Figure 105. Mean surface currents on September 22 (top) and 23 (bottom), 2010. The glider track is red (denoting the track on the indicated day) and tan (denoting the entire glider track).	120
Figure 106. Mean surface currents on September 24 (top) and 25 (bottom), 2010. The glider track is red (denoting the track on the indicated day) and tan (denoting the entire glider track).	121
Figure 107. Mean surface currents on September 26 (top) and 27 (bottom), 2010. The glider track is red (denoting the track on the indicated day) and tan (denoting the entire glider track).	122
Figure 108. Mean surface currents on September 28 (top) and 29 (bottom), 2010. The glider track is red (denoting the track on the indicated day) and tan (denoting the entire glider track).	123
Figure 109. Section plots of temperature (top), salinity (middle), and density (σ_t ; bottom) from glider 159 September 18-24, 2010.	125
Figure 110. Section plots of temperature (top), salinity (middle), and density (σ_t ; bottom) from glider 159 September 24-30, 2010.	126
Figure 111. Mean surface currents on July 31 (top) and August 2 (bottom), 2011. The glider track is red (denoting the track on the indicated day) and tan (denoting the entire glider track).	127
Figure 112. Mean surface currents on August 3 (top) and August 4 (bottom), 2011. The glider track is red (denoting the track on the indicated day) and tan (denoting the entire glider track).	128
Figure 113. Mean surface currents on August 5 (top) and August 6 (bottom), 2011. The glider track is red (denoting the track on the indicated day) and tan (denoting the entire glider track).	129
Figure 114. Mean surface currents on August 7 (top) and August 8 (bottom), 2011. The glider track is red (denoting the track on the indicated day) and tan (denoting the entire glider track).	130

Figure 115. Mean surface currents on August 9 (top) and 10 (bottom), 2011. The glider track is red (denoting the track on the indicated day) and tan (denoting the entire glider track).	131
Figure 116. Mean surface currents on August 11 (top) and 12 (bottom), 2011. The glider track is red (denoting the track on the indicated day) and tan (denoting the entire glider track).	132
Figure 117. Mean surface currents on August 13 (top) and 14 (bottom), 2011. The glider track is red (denoting the track on the indicated day) and tan (denoting the entire glider track).	133
Figure 118. Section plots of temperature (top), salinity (middle), and density (sigma-t; bottom) from glider 191 August 1-6, 2011. Glider headings are given in uppermost panel.	134
Figure 119. Section plots of temperature (top), salinity (middle), and density (sigma-t; bottom) from glider 191 August 7-14, 2011. Glider headings are given in uppermost panel.	135
Figure 120. Mean surface currents on August 31 (top) and September 1 (bottom), 2011. The glider track is red (denoting the track on the indicated day) and tan (denoting the entire glider track).	137
Figure 121. Mean surface currents on September 2 (top) and 3 (bottom), 2011. The glider track is red (denoting the track on the indicated day) and tan (denoting the entire glider track).	138
Figure 122. Mean surface currents on September 4 (top) and 5 (bottom), 2011. The glider track is red (denoting the track on the indicated day) and tan (denoting the entire glider track).	139
Figure 123. Mean surface currents on September 6 (top) and 7 (bottom), 2011. The glider track is red (denoting the track on the indicated day) and tan (denoting the entire glider track).	140
Figure 124. Mean surface currents on September 8 (top) and 9 (bottom), 2011. The glider track is red (denoting the track on the indicated day) and tan (denoting the entire glider track).	141
Figure 125. Mean surface currents on September 10 (top) and 11 (bottom), 2011. The glider track is red (denoting the track on the indicated day) and tan (denoting the entire glider track).	142
Figure 126. Mean surface currents on September 12 (top), 2011. The glider track is red (denoting the track on the indicated day) and tan (denoting the entire glider track).	143
Figure 127. Section plots of temperature (top), salinity (middle), and density (sigma-t; bottom) from glider 191 September 1-7, 2011.	144
Figure 128. Section plots of temperature (top), salinity (middle), and density (sigma-t; bottom) from glider 191 September 7-12, 2011.	145
Figure 129. Mean surface currents on September 11 (top) and 12 (bottom), 2011. The glider track is red (denoting the track on the indicated day) and tan (denoting the entire glider track).	147
Figure 130. Mean surface currents on September 13 (top) and 14 (bottom), 2011. The glider track is red (denoting the track on the indicated day) and tan (denoting the entire glider track).	148
Figure 131. Mean surface currents on September 15, 2011. The glider track is red (denoting the track on the indicated day) and tan (denoting the entire glider track).	149

Figure 132. Section plots of temperature (top), salinity (middle), and density (sigma-t; bottom) from glider 191 September 12-16, 2011.150

Figure 133. Temperature-Salinity plot of CTD data collected in the northeast corner of the Burger lease patch in 2010 and 2011. Left panel shows CTD data from August 9-11, 2010, and right panel data are from August 17-20, 2011.151

Figure 134. Temperature-Salinity plot of CTD data collected in the southeast corner of the Klondike lease patch in 2010 and 2011. Left panel shows CTD data from September 23-36, 2010, and right panel data are from September 13-15, 2011.151

Abstract

We describe the results of a multi-year investigation of the circulation and hydrography of the northeast Chukchi Sea involving shore-based, high frequency radars (HFR), moorings, and gliders (also known as autonomous underwater vehicles). HFR operations occurred during three open water seasons: September through November, 2009; July through November, 2010; and July through November 2011. Glider operations were based out of Wainwright and occurred in August and September of 2010 and 2011. The moorings were deployed year-round at the head of Barrow Canyon between August 2010 and August 2011. The results herein provide an unprecedented view of the circulation and dynamics of the northeast Chukchi shelf.

The current meter and HFR data show that the Alaskan Coastal Current is a narrow (~40 km) swift flow, centered over the axis of the Canyon. The record-length transport is northeastward (downcanyon) at 0.3 Sv, ~40% of the long-term mean transport through Bering Strait. Transport variations are moderately correlated with the local along-shore winds, with the correlation stronger in winter than in summer. The correlation is weaker than expected and may be due to remote wind-forcing over the southern Chukchi/northern Bering Seas, differential along-shore surface stress dependent upon the ice distribution function and ice mobility, non-linear processes (as suggested by the cross- and along-shore Rossby numbers that are occasionally >0.1), and/or forcing over the Chukchi/Beaufort shelfbreak. The flow in the canyon can upwell slope waters onto the shelf. Mooring and HFR data suggest that upwelling events exceeding ~5 days may transport slope waters over a broad area of the northeast Chukchi shelf. Temperature and salinity characteristics of the water masses flowing into the canyon indicate that Bering Sea summer waters are confined to the central and eastern side of the canyon, whereas flow along the western side of the canyon frequently consists of winter waters that may originate along the east side of Hanna Shoal.

HFR data suggests that the shelf circulation includes an eastward flow between 70.5°N and 71.5°N that transports waters toward Barrow Canyon. These flow characteristics hold under all wind conditions, including westward winds as long as westward wind speeds are $<6 \text{ m s}^{-1}$. When westward winds are $>6 \text{ m s}^{-1}$ the surface circulation over much of the northeast Chukchi shelf is westward, while within ~40 km of the coast, the flow is southwestward. About 15% of the time the onshore flow diverges with one branch flowing downcanyon and the other turning southwest toward Point Lay. This flow divergence occurs when the winds are moderate, suggesting that the along-shore pressure gradient south of Wainwright is weaker than the along-shore pressure gradient within the canyon. Offshore of Point Lay, the circulation patterns suggest frequent exchanges between near and offshore waters, which may involve anticyclonic eddies. North of 71.5°N, and between Hanna Shoal and Barrow Canyon, the surface circulation is comparatively weak and more variable in direction. Although there are occasional suggestions that it includes a clockwise flow around Hanna Shoal, this feature is not consistently evident.

The glider data suggest that there is a west/east trending front at 71° - 71.5°N in summer through at least early fall. The front separates weakly stratified or well-mixed Bering Sea summer waters to the south from a strongly stratified, 2-layered system to the north. The stratified waters include a fresh, cool, ~20 m deep surface layer and a near-freezing, saline bottom layer of ~20 m. Our results suggest that south of this front the HFR data is probably a good proxy for the flow throughout the water column. North of the front, the HFR surface currents may only reflect the

upper 20 m of the circulation field. Nevertheless, the horizontal density gradients across these fronts are weak over most of the shelf, except in Barrow Canyon, so that the geostrophic shear over most of the shelf is feeble.

Our results have important implications regarding the prediction of ice formation, given the highly advective nature of the Chukchi Sea shelf. Through summer and fall the mean circulation provides an oceanic heat flux convergence that may exceed in magnitude the loss of heat to the atmosphere and so delay ice formation. On the other hand reversals in the shelf circulation may bring very cold ($\sim 0^{\circ}\text{C}$) water southward onto the shelf from east of Hanna Shoal. Should these reversals be prolonged and occur in early fall, they may accelerate the formation of ice due to air-sea heat exchanges.

1. Introduction

The Chukchi and Beaufort seas are the northernmost shelves bordering Alaska. Although properly a part of the western Arctic Ocean, the Chukchi shelf is atmospherically and oceanographically linked to the Pacific Ocean. These connections influence the wind and wave regimes, ice distribution, and the water masses and circulation characteristics of both seas. The atmospheric connection is primarily via the Aleutian Low, whose time-varying position, strength, and interactions with polar air masses affects regional meteorological conditions. The oceanographic link is via mean northward flow through Bering Strait, which is sustained by a large-scale pressure gradient between the Pacific and Atlantic Oceans [*Coachman et al.*, 1975; *Aagaard et al.*, 2006].

The northward transport of mass, heat, nutrients, carbon, and organisms through the Strait bequeath this region with biophysical characteristics unique among arctic shelves. For example, the spring retreat of ice occurs earlier and fall ice formation is delayed in the Chukchi Sea in comparison to most other arctic shelves because of the northward heat flux through the Strait. *Woodgate et al.* [2006] and *Shimada et al.* [2006] contend that this heat flux may be an important source of interannual variability in the ice cover over the western Beaufort Sea. Similarly, the enormous biological productivity of the region [*Walsh et al.*, 1989; *Grebmeier and McRoy*, 1989; *Springer and McRoy*, 1993], including its ability to support large and diverse marine mammal populations, is attributed to the carbon and nutrient loads carried through Bering Strait.

The shallow (~50 m) Chukchi shelf extends ~800 km northward from Bering Strait to the shelfbreak along the 200 m isobath. Present understanding of the shelf circulation is based upon the distribution of hydrographic properties collected in summer and fall, numerical circulation results, and a few long-term ocean current measurements (of which many were obtained from sub-surface measurements made within 10 m of the bottom). Figure 1 [from *Spall*, 2007] illustrates the mean circulation over the shelf. The model results largely agree with the inferences drawn from the observations. Although the mean flow is nominally northward over much of the shelf, the bulk of the transport proceeds along three principal pathways with each pathway associated with a distinct bathymetric feature; Herald Canyon, the Central Channel, and Barrow Canyon. The troughs are separated from one another by shoals: Herald Shoal separates Herald Canyon from the Central Channel, and Hanna Shoal lies between Barrow Canyon and the Central Channel.

As indicated in Figure 1, the western branch enters Herald Canyon [*Coachman et al.*, 1975; *Walsh et al.*, 1989; *Hansell et al.*, 1993; *Pickart et al.*, 2010]. Although some of it appears to spread eastward across the central shelf, a significant portion of the water in the western branch diverts to the east upon exiting Herald Canyon to form an eastward-flowing shelfbreak jet along the edge of the Chukchi Sea [e.g. *Mathis et al.*, 2007; *Pickart et al.*, 2010]. The flow passing through the Central Channel is steered eastward around Hanna Shoal [*Johnson* 1989; *Münchow and Carmack*, 1997; *Gong and Pickart*, 2011]. Thus, a large portion of the water flushing the central and western Chukchi Sea moves eastward north of Hanna Shoal. According to models [*Winsor and Chapman*, 2004; *Spall*, 2007], the shelf portion of this flow turns southward along the east side of Hanna Shoal and eventually enters the head of Barrow Canyon (although there are no observations in this area for model verification). Upon exiting Barrow Canyon – in the absence of winds – the water turns to the right and forms a shelfbreak jet along the edge of the

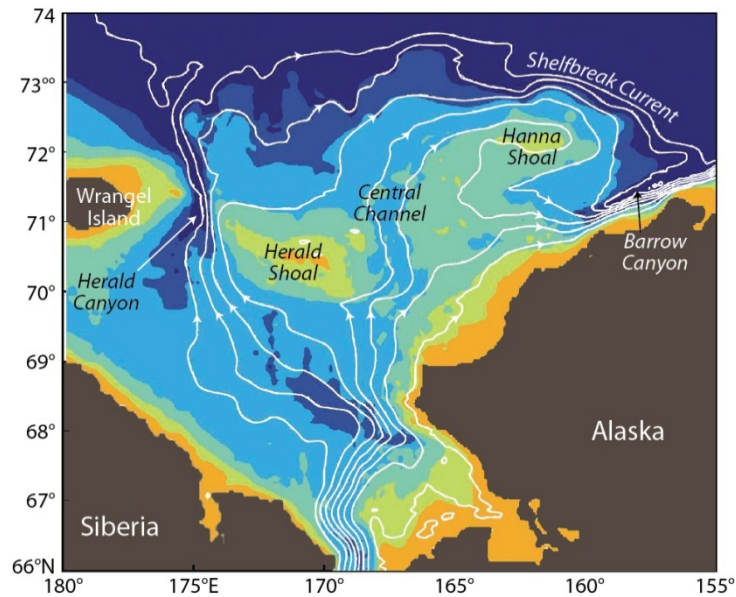


Figure 1. Mean depth-integrated streamlines (white) in the Chukchi Sea, after Spall [2007]. Bathymetry is color-shaded, and major bathymetric features are labeled.

Beaufort Sea [Nikolopoulos *et al.*, 2009; von Appen and Pickart, 2012]. However, strong westward winds may divert some of the flow to the west of Barrow canyon. Overall then, much of the water that enters the Pacific sector of the Arctic Ocean ultimately ends up exiting the Chukchi shelf via Herald or Barrow Canyon to form an eastward-flowing shelfbreak jet along the Chukchi and Beaufort Seas.

Before reaching the western edge of Hanna Shoal, the Central Channel branch [Paquette and Bourke, 1974; Weingartner *et al.*, 2005; Weingartner *et al.*, 2013] splits, with some water continuing eastward toward the Alaskan coast over the central shelf. More recently, hydrographic-based inferences [Weingartner *et al.*, 2013] suggest that Bering Sea summer waters spread eastward from the Central Channel along its entire length. As these waters flow eastward they encounter dense (cold, salty) bottom waters south of Hanna Shoal (formed the previous winter over the northern Bering and Chukchi seas). Model results (Figure 1) suggest that the source of this dense water is most likely from the east side of Hanna Shoal.

The third branch flows northeastward along the Alaskan coast towards Barrow Canyon at the junction of the Chukchi and Beaufort shelves [Mountain *et al.* 1976; Paquette and Bourke, 1981]. In summer, this flow includes the northward extension of the Alaskan Coastal Current (ACC) that originates south of Bering Strait [Aagaard *et al.*, 1985; Aagaard, 1988; Münchow *et al.* 2000]. At the head of Barrow Canyon, the ACC is joined by waters flowing eastward from the central shelf, and as suggested by the model streamlines, with water flowing southward from the east side of Hanna Shoal. The merged flow then continues downcanyon as a narrow, but strong, coastal jet [Aagaard and Roach, 1990; Pickart *et al.*, 2005]. Hence in summer and fall, the canyon outflow contains a horizontally- and vertically-structured complex of water masses [Pickart *et al.*, 2005; Shroyer and Plueddemann, 2012] that includes warm, dilute Alaskan

Coastal Water (carried by the ACC); cold, dilute waters due to melting shelf ice; dense winter waters; relatively warm and salty Bering Sea Water, and mixtures of each.

Mean current speeds within Herald and Barrow canyons are swift ($\sim 25 \text{ cm s}^{-1}$), more moderate in the Central Channel ($\sim 10 \text{ cm s}^{-1}$), and generally $\leq 5 \text{ cm s}^{-1}$ elsewhere. Long-term transport estimates are approximate at best, with suggestions that the transport through the Central Channel is $\sim 0.2 \text{ Sv}$ [Weingartner *et al.*, 2005] and in Herald Canyon is $\sim 0.3 \text{ Sv}$ [Woodgate *et al.*, 2005]. Transport estimates based on the 2010-2011 Barrow Canyon mooring array (and presented below), suggest a mean annual transport of $\sim 0.3 \text{ Sv}$.

The flow field described above is influenced by the winds; however, on average these blow from the east-northeast, so the mean flow tends to oppose the mean winds. Nevertheless, flow variations tend to be coherent with wind variations on similar time scales. Many of the historical current measurements were obtained from current meters installed $\sim 10 \text{ m}$ above the seabed in depths $\geq 40 \text{ m}$. Thus there has been concern that these measurements may not reflect the near-surface currents. In fact, dynamical reasoning suggests there may be a wind-forced shear layer across which the currents change directions. The thickness of this layer presumably varies geographically, as well as with seasonal changes in stratification, ice cover, and wind velocity.

This last point is crucial in considering the ultimate development of oil spill trajectory models for the Chukchi shelf. Models that incorporate only wind-forcing to compute surface drift could produce serious discrepancies on the Chukchi shelf, where the surface currents arise in response to forcing by both the winds and the large-scale (and opposing) pressure field.

2. Objectives

In anticipation of potential offshore hydrocarbon development activities in the northeast Chukchi Sea, the overall goals of this program were to improve our understanding of the circulation and to provide an extensive data set that can be used to test and evaluate circulation models. Toward this end we focused on a number of specific issues that define the project objectives:

1. Determine whether the surface (upper 1 m) circulation reflects the sub-surface circulation as captured by historical current meter measurements. If not, determine if these differences are related to topographic gradients, seasonally-varying winds, stratification, and/or fronts.
2. Determine if there is a return (southwestward) flow between the western flank of Barrow Canyon and Hanna Shoal as predicted by circulation models. If so, determine the strength and persistence of these flows.
3. Determine if coastal polynyas generate a vigorous cross-shelf flux of dense water.

Additional project objectives were to:

4. Obtain a better understanding of the wave climate of the northeast Chukchi Sea;

5. Develop an infrastructure in Chukchi Sea coastal communities for supporting shore-based, high frequency surface current mapping radars. (This goal is also cost-effective since it will minimize costs associated with routine maintenance of the proposed radars);
6. Provide several useful oceanographic data sets for guiding the development and evaluation of oil spill trajectory models.

With respect to the final objective, we note that Chukchi Sea trajectory models need to impose a regional pressure field in order to correctly resolve the wind-forced circulation. This can be done by applying appropriate time-varying boundary conditions in Bering Strait for the southern Chukchi Sea. Detailed moored measurements are presently being made in Bering Strait under joint support by NSF and NOAA. The results will improve prior estimates of the mean and wind-driven mass, heat, and salt transports, and therefore the boundary conditions for future models. As noted earlier, however, the transport estimates along the three pathways are approximate at best. An important verification metric for model evaluation would be reasonably accurate estimates of the time-varying transport along one of the pathways. Our field program achieved this objective at the entrance to Barrow Canyon. The data from this project has been submitted to BOEM and available to be utilized by modelers.

3. Methods

Field measurements involved a combination of various sensor systems, each of which is described in the following sub-sections. The sensors included moored oceanographic instruments that measure the sub-surface circulation, shore-based, high-frequency radars (HFR) capable of mapping the surface circulation in real-time, and gliders (also known as autonomous underwater vehicles, AUVs) that collected 3-dimensional hydrographic data over the northeast Chukchi shelf. Figure 2 is a bathymetric map of the study area, which includes place names, and the locations of the Statoil (Statoil), Burger (Shell), and Klondike (ConocoPhillips) areas of exploration interest. The figure also includes the nominal HFR radar masks and the locations of the current meter moorings deployed as part of this project. For clarity, we have not included the trajectories of the various glider missions conducted during the program. These are shown in separate figures later. However, most of the glider operations occurred within the radar mask.

3.1 Moorings

An array of 6 current-meter moorings (labeled BC1 – BC6), each spaced about 13 km apart, was deployed across the entrance to Barrow Canyon (Figure 2). Moorings BC2 – BC6 were all of similar construction and included a 300 or 600 kHz Teledyne Acoustic Doppler Current Profiler (ADCP) and a temperature/conductivity/pressure (T/C/P) recorder (Seabird MicroCat or SeaCat) housed in a 36” diameter float and connected, through an acoustic release, to an anchor (Figure 3). The moorings were constructed to be as close to the bottom as possible in order to avoid damage from drifting ice keels and to profile as much of the water column as possible. The ADCP transducers and T/C/P recorders were ~4 m above the bottom (Table 1). A sixth mooring, BC1, was funded by the State of Alaska’s Community Impact Assistance Program (CIAP) and consisted of the same instrumentation. BC1 was deployed nearest to the shore in a water depth of

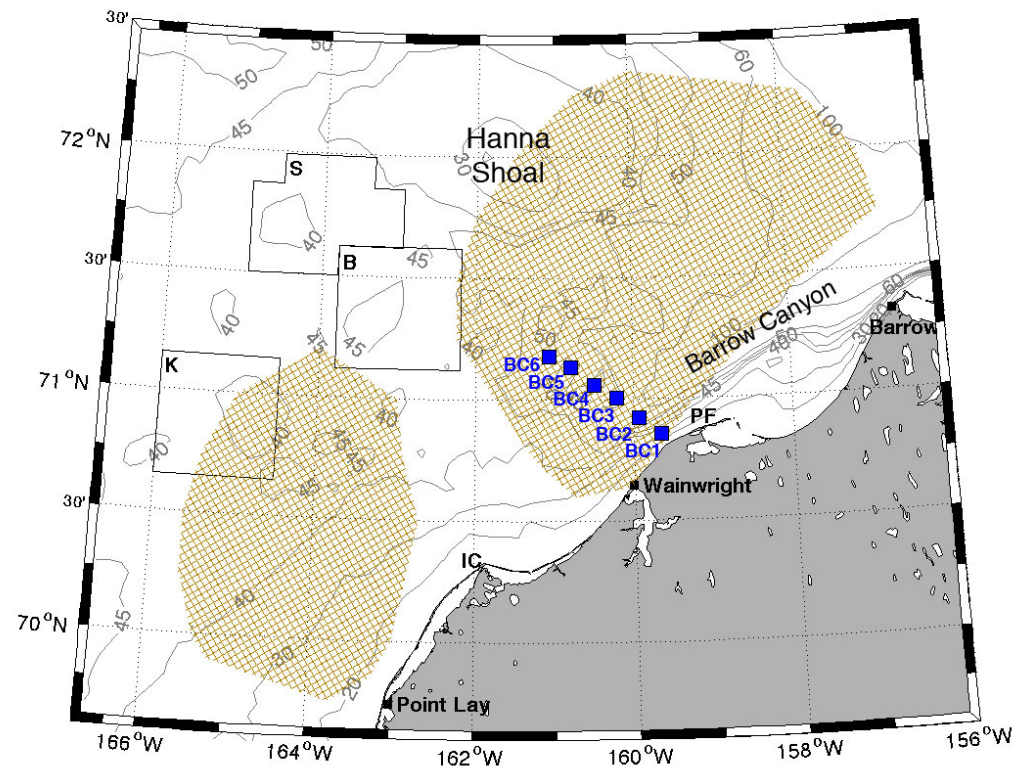


Figure 2. Map showing HFR coverage area (golden crosshatch) and mooring locations (blue squares) overlaid on bathymetric contours (m). Barrow, Wainwright, Point Lay, Hanna Shoal, Barrow Canyon, Icy Cape (IC), and Point Franklin (PF) are identified, as are industry study areas Klondike (K), Burger (B), and Statoil (S).

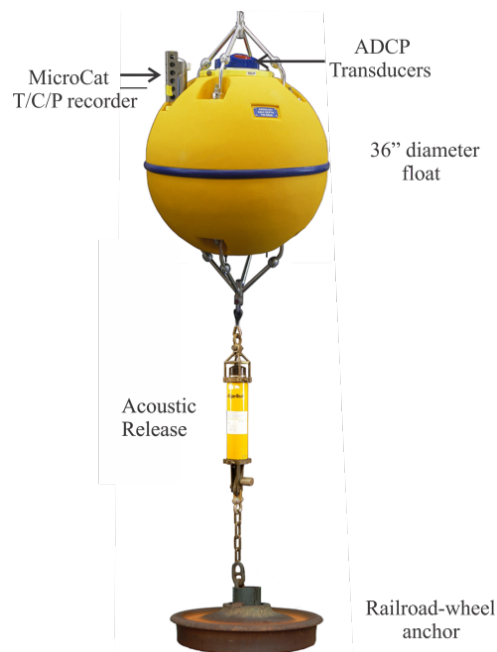


Figure 3. Example mooring package for moorings BC2 – BC6.

30 m. Instruments on BC1 were mounted 1-m above the seabed and in a small frame (SeaSpider) that rests on the seabed. This design was used due to concerns about damage from nearshore ice keels that could exceed 25 m depth.

In addition to hourly velocity sampling, the ADCPs on moorings BC1 and BC6 included the capability to measure the directional wave spectrum once every three hours. Wave-detection sensitivity for these instruments depends upon the depth of deployment. As instrument depth increases, higher frequency waves are less likely to be detected. We obtained reasonably good wave data from mooring BC1, however, after working with Teledyne on reprocessing, the wave record from BC6, deployed at 43 m depth, is of poor quality and was not analyzed. Had we deployed the ADCP at BC6 at shallower depths, we would have obtained better wave data. We understood the wave-measuring constraints on BC6 prior to deployment but determined that obtaining current velocities over most of the water column was more important than the wave data given the project objectives.

Table 1. Mooring positions and depths.

Mooring Name	Latitude (°N)	Longitude (°W)	Water Depth (m)	ADCP Height Above Bottom (m)
BC1	70.8533	-159.6676	30.1	1.0
BC2	70.9214	-159.9396	52.3	3.5
BC3	71.0025	-160.2090	53.3	4.5
BC4	71.0569	-160.4932	49.3	4.0
BC5	71.1340	-160.7881	49.5	3.5
BC6	71.1745	-161.0701	46.6	3.5

3.2 High-Frequency Radar (HFR)

During the open water seasons of 2009, 2010, and 2011, we measured hourly surface currents in the northeast Chukchi Sea using shore-based 5 MHz HFR systems, manufactured by CODAR Ocean Sensors. Field sites were located on native corporation lands in the villages of Barrow, Wainwright, and Point Lay, Alaska (Figure 2). The locations allowed for data collection within 200 km of the coastline over an area of ~30,000 km². Current vectors were calculated at 6 km spatial resolution and represent the upper 1 - 2 m of the water column.

In 2009, HFR systems consisting of a transmit antenna, a receive antenna, and electronics chassis were deployed in mid-September in Barrow and Wainwright (Figure 4). In 2010, the systems in Barrow and Wainwright were installed in mid-July, hence earlier in the open water season than in 2009, and a third site was added in Point Lay in mid-September. (The delay in the 2010 installation at Point Lay was due to the long lead time needed to secure permission for the installation.) In 2011, the Barrow HFR was installed mid-July, Wainwright in mid/late June, and the Point Lay HFR was established in early August. At all sites and in all years, the systems remained operational through mid-November when sea ice cover ended data returns. All equipment was subsequently removed from the field sites and winterized until the following

Table 2. Operational periods for each HFR installation site in 2009, 2010, and 2011.

	Barrow	Wainwright	Point Lay
2009	Sep 10 – Nov 12	Sep 13 – Nov 14	N/A
2010	Jul 13 – Nov 5	Jul 13 – Nov 6	Sep 10 – Nov 6
2011	Jul 14 – Nov 12	Jun 21 – Nov 14	Aug 4 – Nov 21

open water season. The specific dates of the operational periods for each site are given in Table 2.

HFR measures surface currents by processing the Doppler spectrum from transmitted radar waves backscattered by ocean waves [Barrick *et al.*, 1985]. At 30-minute intervals, each HFR collected one-dimensional current vectors up to 200 km in range, measuring the velocity of the current moving toward or away from the field site in a radial pattern. All radial measurements acquired in a three-hour window were then averaged to produce an hourly radial current file.

When a one-dimensional radial current vector from one site intersected the radial from another site, a two-dimensional current was calculated. Since each site is dependent on another to produce two-dimensional current vectors, effective operational dates for two-dimensional currents were September 13 – November 12, 2009; July 21 – November 6, 2010; and July 18 – November 14, 2011. During these periods, the two-dimensional current vectors were displayed on the internet (www.chukchicurrents.com) and updated in real-time.

There were various limitations on HFR data acquisition. The radar signal does not propagate over land; therefore, the coastline geometry, specifically Icy Cape and Point Franklin (Figure 2), limited the coverage area and thus the overlap of the one-dimensional current data between field sites. The geometric dilution of precision (GDOP) between sites is also a factor, and determines if the angles of intersection of the radial components (acquired from each individual site) are sufficient to calculate a two-dimensional current vector [Barrick, 2002]. A significant limitation at our high-latitude locations was nightly reflections of the HFR signal from the ionospheric layer of the atmosphere [Teague, 2001], which increased noise in spectral returns originating more than ~90 km offshore. At such times, the signal to noise ratio was too low to measure current velocities (Figure 5), and data coverage was reduced to a minimal overlap region between field sites.

Sea ice also limits HFR data coverage by attenuating the HFR signal [Gurgel, 1997] and indirectly affects data quality by dampening the wave field necessary for HFR backscatter returns. The latter can also occur under calm wind conditions. Sea ice was a major factor in data processing for a previous BOEM funded project in the Beaufort Sea [Potter and Weingartner, 2009]; however with the lower frequency HFR systems used in this project, the presence of ice proved less challenging during the analysis phase. Additionally, low salinity waters (i.e. <~10 for 5 MHz systems) such as those created by ice melt, rivers, or a large rainstorm reduce signal propagation [Barrick and Long, 2006]. We do not believe that low-salinity was an issue in this program because our installations are far from any major river discharges, rain storms are seldom sufficiently heavy to create a dilute surface layer, and ancillary Conductivity-Temperature-Depth sensor (CTD) data from the general area show no surface salinities <~25.



Figure 4. HFR antenna setup in Barrow (top), Wainwright (middle), and Point Lay (bottom).

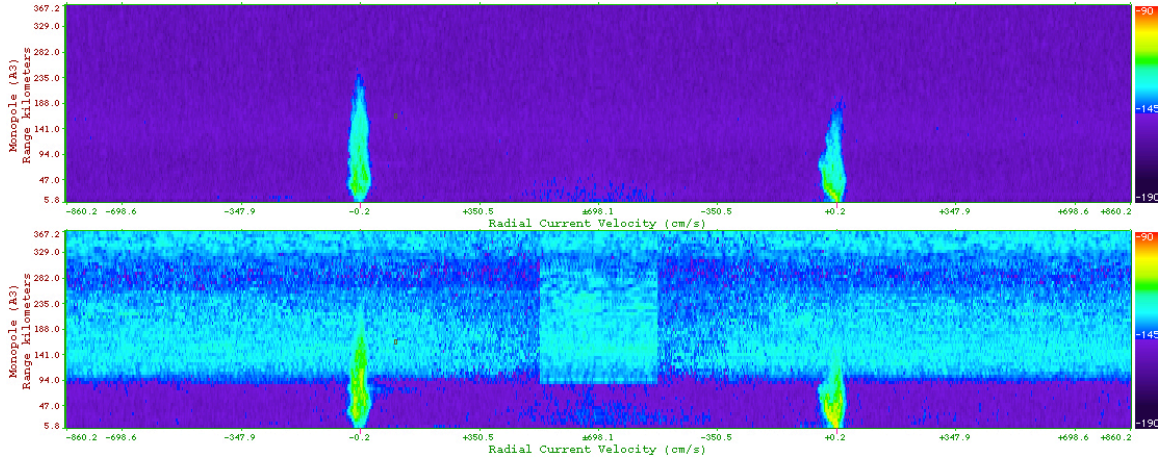


Figure 5. Cross spectra collected by the HFR system in Wainwright. The top figure shows Bragg peaks when ionospheric interference is absent, and the bottom figure depicts Bragg peaks when the HFR signal is reflected by the ionosphere.

Antennas were calibrated using a beam pattern measurement to correct for background noise in the frequency spectrum [Barrick and Lipa, 1986; Kohut, 2003]. Subsequent to acquisition, collected cross spectra are visually inspected to ensure software parameters are optimized for the environmental conditions at each site. Data is further quality controlled by removing one-dimensional velocities collected at each field site greater than 200 cm s^{-1} and velocities greater than three standard deviations from the temporal mean of each grid point. After the two-dimensional currents are calculated, grid points with less than $\sim 50\%$ coverage over time are removed from the dataset.

3.3 Gliders

During the open water seasons of 2010 and 2011, we operated three Teledyne Webb Slocum gliders (#157, 167 and 191) in the northeast Chukchi Sea (Table 3). Gliders are a special class of autonomous vehicle that propel themselves by changing their buoyancy compared to ambient water and generate forward propulsion by gliding on wings attached to the body. This results in a relatively slow forward motion ($\sim 30 - 40 \text{ cm s}^{-1}$) but is extremely energy efficient compared to a propelled AUV. Gliders equipped with alkaline batteries have a typical mission duration of 30 days, whereas Lithium battery powered gliders can operate continuously for >3 months.

Table 3. Annual statistics for each glider. Only days with active data acquisition are included.

Glider ID	Year	Mission Days	Number of casts	Distance traveled (km)
159	2010	48	10434	622
167	2010	25	2703	400
167	2011	8	934	184
191	2011	56	5511	1248



Figure 6. Two Webb Slocum gliders being deployed in the northeast Chukchi Sea off the Wainwright-based vessel Tukpuk in 2010.

We used the 32 ft landing craft “Tukpuk” (owned by Olgoonik Corporation and based in Wainwright) for glider deployments and recoveries. This vessel is capable of quickly (15 – 20 knot speeds) reaching deployment or recovery areas for gliders in fair weather, and the bow can be lowered, thus simplifying field operations (Figure 6).

During a mission, the gliders communicate with UAF’s RUDICS (internet IP-based Iridium) data server every time they surface, where they establish Iridium satellite data transfer protocol and receive new mission information (if available). This two-way communication enables the operator to change the mission flight characteristics, sampling interval, etc., in real time. While surfacing, the gliders also collect multiple GPS fixes and compute their current location compared to the programmed waypoint. This information is used to calculate a new heading based on the surface drift and waypoint-to-actual GPS fix offset. We typically operated the gliders on a 6-hour surfacing schedule, between which the gliders dead reckon and glide from the surface to the bottom and up in a sea-saw pattern. We typically collect data throughout the water column from within ~3 m of the surface and bottom. The gliders use an altimeter for bottom avoidance and have several built in self-rescue mechanisms in the event they get stuck on a sub-surface object.

Each glider was equipped with a glider-specific Seabird CTD. Glider #191 was equipped with a pumped Seabird T/C/P recorder, and glider #167 also had a Wetlabs Eco Puck three-channel optical instrument installed. The CTDs sampled continuously, every 1-3 s throughout their deployment period, which produced a voluminous data set. From the raw data, sub-sampled pressure, temperature, salinity data was sent via Iridium to UAF during surfacing events, thus

providing oceanographic data every 6 hours. Given the gliders typical mean horizontal speed ($\sim 30 - 40 \text{ cm s}^{-1}$) and the mean depth of the Chukchi Sea ($\sim 40 \text{ m}$), the resolution of the hydrographic data was $\sim 1 \text{ m}$ vertical and $\sim 300 \text{ m}$ horizontal. We developed automated processing scripts to archive, map and display the glider data in real time on the internet (<http://www.ims.uaf.edu/artlab/>), where the hydrographic data from different times and transects can be queried and plotted.

Once recovered, the full-resolution raw data (engineering, flight, and science data) was downloaded from the gliders and backed up in multiple locations. CTD data processing followed Seabird's standard CTD protocols for calculating depth, salinity and density, including adjusting for thermal mass and spatial-temporal lag between the conductivity cell and the thermistor. Special attention was given to the un-pumped CTD data as the glider passed through strong stratification gradients. Comparing up and downcasts (upward and downward flights), we identified differences resulting from thermal mass and sampling issues (Figure 7). These mainly affect the very limited vertical area of the strong pycnocline (thermocline/halocline) and display too warm waters or alternatively too cold waters when flying from cold to warm and vice versa. This results in temperature "spikes". Using recent methodology [Garau *et al.*, 2011], we minimized this effect by analyzing spatial-temporal structures of the full-resolution glider data, accounting for variable glider speed and sampling rates. This resulted in CTD data with minimal salinity and temperature spiking in the pycnocline area. Multiple data sets were generated at different processing levels. These included raw to fully processed data, vertically and horizontally binned data, and separate data sets for up- and downcasts.

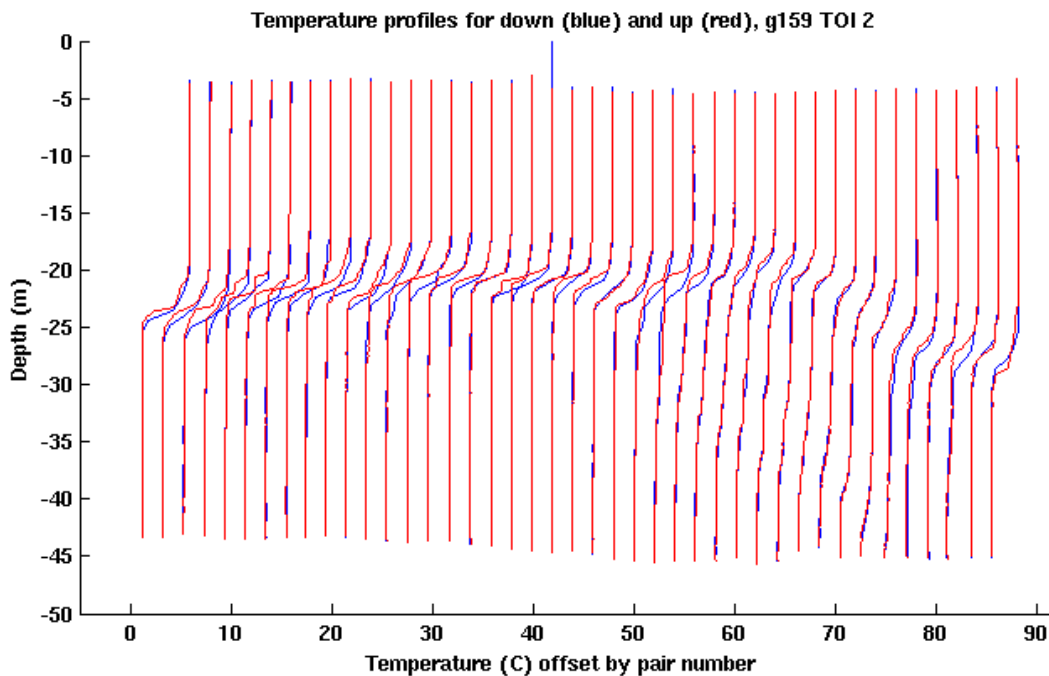


Figure 7. Waterfall plot of vertical temperature profiles from glider #159 showing an example of down-casts (blue) and up-casts (red). The thermal lag issue is visible in the thermocline around 25 m depth as differences in the temperature traces.

Glider missions that occurred nearshore of Wainwright and within the strong coastal jet, typically did not follow their pre-programmed survey routes. Instead the gliders were quickly advected by the strong current, forcing us to recover and redeploy the gliders so that they would not be swept into the Arctic Ocean. Transects offshore of the coastal jet were able to more closely follow their pre-programmed routes. Since one of the main mission goals was to sample high-resolution time-space variable stratification data under the HFR mask, most of the glider missions were deemed a success. The total distance covered during active missions for the two years was ~2,500 km, with ~ 20,000 CTD casts collected.

4. Results

4.1 Waves

Two moorings (BC1 and BC6) measured the directional wave spectrum (Figure 2). A subset of these data from BC1, is shown for the period of August 18 – November 7, 2010 (Figure 8) and May 12 – August 25, 2011 (Figure 9), along with corresponding winds. The plots show the significant wave height, (H_s), defined as:

$$H_s = 4 \left[\int_0^\infty S(f) df \right]^{1/2} = 4\sigma_w$$

where f is the wave frequency, $S(f)$ is the spectral density, and σ_w is the standard deviation of the wave height. (Note that this definition of H_s yields results similar to earlier definitions where H_s is defined as the average of the highest one-third of the waves.) Also plotted on the figure is the period (T_p) of H_s and the direction from which H_s propagates. For the August – November, 2010 portion of the record (Figure 8), H_s was generally less than 2 m, with ranging between 4.0 - 8.4 seconds. The latter value for T_p exceeds the upper bound for the deep water wave approximation at the 30 m depth of BC1. For $4.0 \text{ s} < T_p < 8.4 \text{ s}$ deep water wavelengths range between 25 and 110 m. The HFR, operating at a frequency of 5 MHz, Bragg scatters from wavelengths of ~30 m ($T_p \sim 4.3 \text{ s}$), so the wave environment should generally have been rich enough to support HFR measurements in this area. Waves with periods $> 8.4 \text{ s}$ are intermediate water waves. With the exception of a storm event in late September 2010, the longer period waves (swell) had $H_s < 0.5 \text{ m}$. The majority of all wind waves propagated from the northeast, north, and northwest (from 320° to 30°T). In contrast the swell originated from the south and/or west. The largest waves detected occurred on September 26, had an H_s of ~3.8 m, and propagated onshore from the northwest (between $340^\circ - 350^\circ\text{T}$). These waves occurred about 12 hours after the onset of strong ($\sim 15 \text{ m s}^{-1}$) northwesterly winds. After November 7, wave detection was sporadic as ice began to develop over the region, which either reduced the fetch and/or damped the waves. Detectable waves did occur in January 2011 when a polynya developed along the northwest coast of Alaska, however they were small, $H_s < 1.0 \text{ m}$.

Ice started to retreat along the northwest coast of Alaska in early May 2011, with waves consistently detected by May 12 (Figure 9). In 2011, H_s was $< 1.0 \text{ m}$ through May, and while H_s gradually increased through the end of the record, it rarely exceeded 2 m. We note that even though relatively strong winds ($\sim 10 \text{ m s}^{-1}$) developed in July and August 2011 and the ice edge

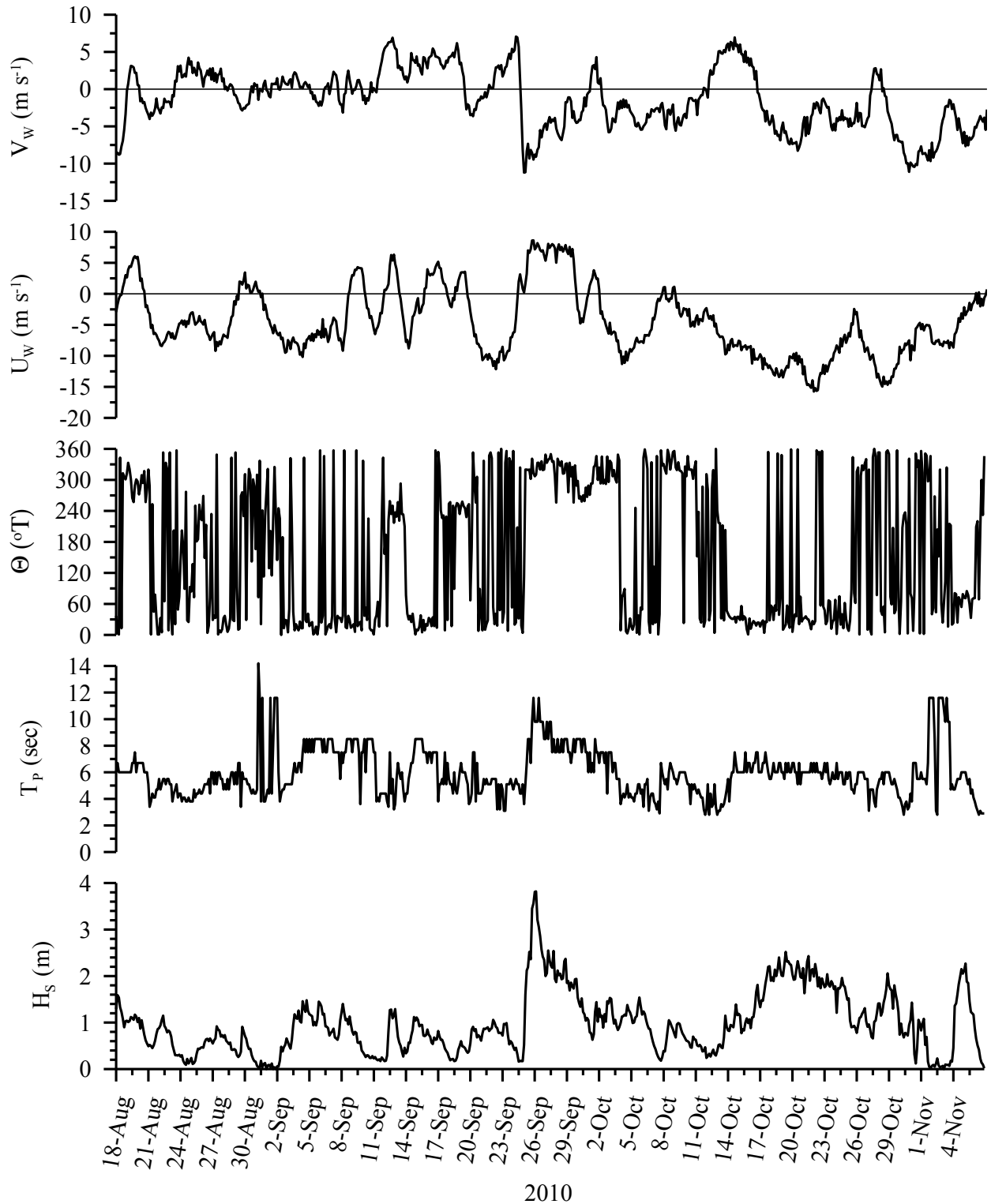


Figure 8. Time series of the significant wave height (H_s), period of H_s (T_p), direction from which H_s waves are propagating (Θ), and the east (U_w) and north (V_w) components of the winds. Wave data are from the August 18 – November 7, 2010 time period.

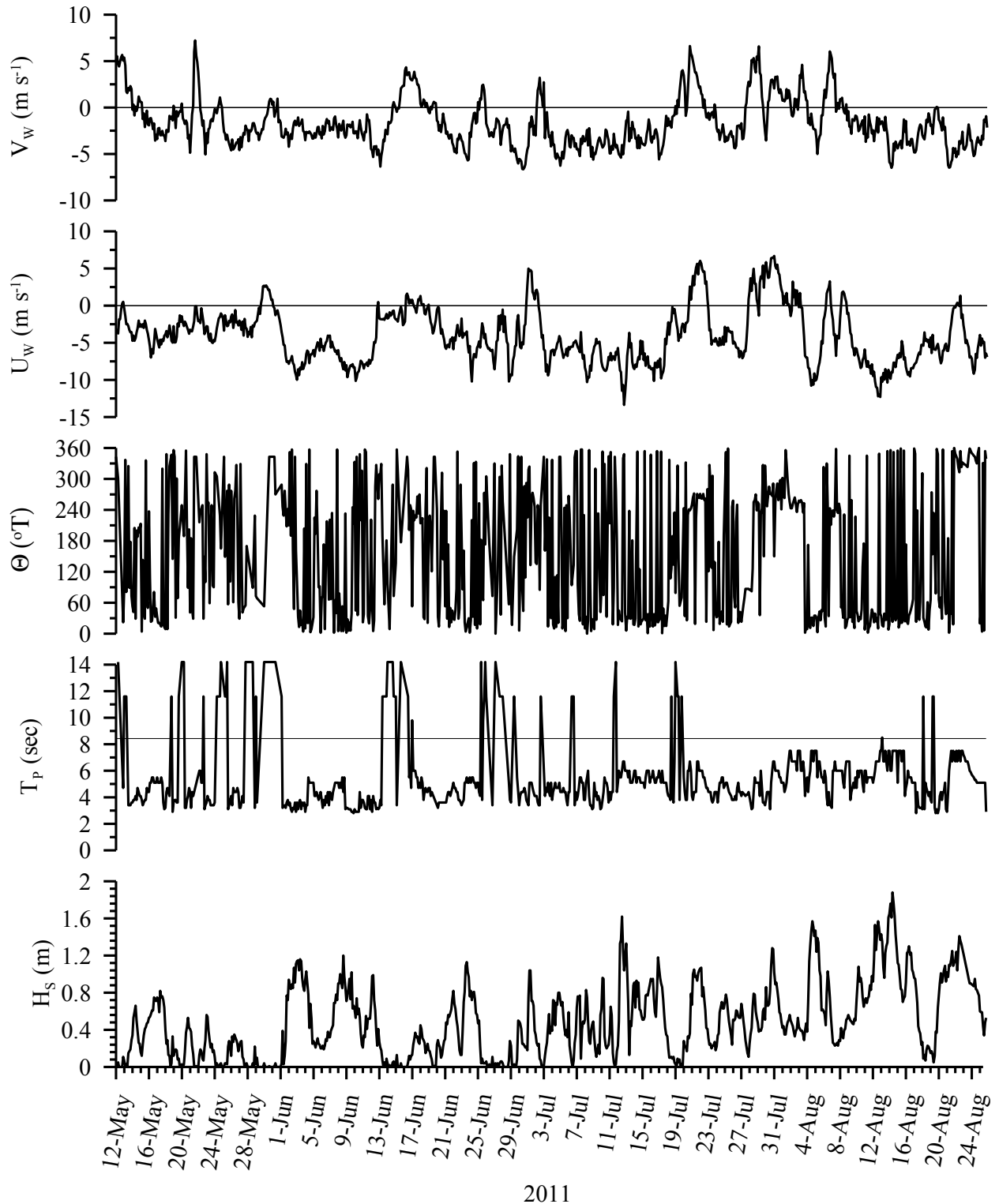


Figure 9. Time series of the significant wave height (H_s), period of H_s (T_p), direction from which H_s waves are propagating (Θ), and the east (U_w) and north (V_w) components of the winds. Wave data are from the May 18 – August 24, 2011 time period.

was ~100 km to the north, the H_s remained small compared to the large waves observed in conjunction with the strong winds from the northwest in late September 2010. The differences in H_s magnitudes between these strong-wind events are probably related to the wind direction. In 2011, the strongest winds were from the east-northeast (e.g., thus blew offshore). This suggests that the waves generated by these winds were fetch-limited. According to the Shore Protection Manual [U. S. Army Corps of Engineers, 1984], H_s should range from 0.7 (fetch = 5 km) and 1.4 m (fetch = 25 km) for wind speeds of $\sim 10 \text{ m s}^{-1}$. This range in H_s is consistent with the measurements in July and August 2010. In contrast, weather maps suggest that the fetch during the September 2010 storm was at least ~ 200 km. Under these conditions the Shore Protection Manual [U. S. Army Corps of Engineers, 1984] predicts H_s of ~ 4 m, in good agreement with the observations. Since the regional winds are generally from the east-northeast, we expect that the nearshore wavefield is largely fetch-limited by land during the open water season.

4.2 Winds

Before discussing the current meter data from the August 2010 – 2011 period, we provide a brief overview of the wind conditions over the northeastern Chukchi Sea shelf for the period of the mooring deployment. The presentation is based on the 3-hourly wind records at the NOAA-North American Regional Re-analysis (NARR) gridpoint located at 71.25°N , 161.25°W , which is near mooring BC6. Table 4 lists wind statistics for the length of the mooring record and for each calendar month. One of the variables computed is steadiness, S , which is the ratio of the vector mean wind speed to the wind speed. S is an index of the persistence of the wind and ranges between 0 (for random winds) and 100% (for winds blowing in the same direction as the mean) and is calculated from:

$$S = 100 \left[\overline{U^2} + \overline{V^2} \right]^{1/2} / \left[\overline{U^2 + V^2} \right]^{1/2}$$

For the period of August 2010 – 2011, the mean winds were to the west-southwest at $\sim 3 \text{ m s}^{-1}$. The mean monthly winds were southwestward to westward for 11 of the 13 months. The two exceptions were February 2011, when the mean monthly winds were weaker (0.8 m s^{-1}), and northeastward (32°T), and March 2011 when they were northwestward (314°T) at 1.2 m s^{-1} . The maximum mean monthly wind speed was 8.2 m s^{-1} and occurred in October 2010. The standard deviations of the wind velocities were larger in summer and early fall than they were in winter, and monthly coefficients of variation are generally much larger for the meridional component of the wind than for the zonal component. The principal axis of variation is, on average, oriented along 67°T , and accounts for $\sim 74\%$ of the wind variance. Hence the winds vary primarily from east-northeast to west-southwest. This orientation holds for 8 of the 13 months, with notable departures occurring in September, November, and December 2010 and February and May, 2011. Wind steadiness is, on average, 50%, suggesting moderate levels of persistence. However, the May – August 2011 period was characterized by $S > \sim 60\%$, and both October 2010 and June 2011 had values of $S = 88\%$.

We have also compared the winds at the NARR gridpoint with those observed at Barrow and Wainwright. We have done this by plotting time series of each velocity component from NARR

Table 4. Summary of wind statistics from the NARR gridpoint at 71.25°N, 161.25°W. Listed are mean zonal (\bar{U}) and meridional (\bar{V}) wind velocities and their standard deviations (s_u, s_v), mean vector wind speed (W), mean wind direction (Θ), mean wind components along major (\bar{U}_r) and minor axes (\bar{V}_r) of the variance ellipses and standard deviations along each axis (s_{ur}, s_{vr}), percentage of the total variance explained by the major axis wind component, orientation of the major axis (Θ_M), and steadiness (S).

Time	\bar{U} (m s ⁻¹)	s_u (m s ⁻¹)	\bar{V} (m s ⁻¹)	s_v (m s ⁻¹)	W (m s ⁻¹)	MAG (m s ⁻¹)	Θ (°)
8/10-8/11	-2.5	4.4	-0.6	3.1	2.6	5.1	256
8/10	-2.9	5.4	0.2	3.8	2.9	6.5	274
9/10	-1.9	5.8	0.2	3.8	1.9	6.7	275
10/10	-7.8	4.3	-2.5	3.9	8.2	9.3	252
11/10	-0.9	3.3	-0.9	3.8	1.3	4.5	223
12/10	-1.0	2.9	-1.3	2.5	1.6	3.9	219
1/11	-1.3	3.1	-0.1	2.1	1.3	3.5	265
2/11	0.9	3.6	1.4	3.0	1.7	4.5	32
3/11	-0.9	2.4	0.9	1.7	1.2	3.0	314
4/11	-1.5	3.3	-0.6	2.1	1.6	3.9	250
5/11	-1.9	2.0	-0.3	2.4	1.9	3.3	260
6/11	-4.7	3.0	-2.0	2.2	5.1	5.8	247
7/11	-3.5	4.7	-1.6	3.0	3.8	6.4	246
8/11	-4.6	3.7	-1.4	2.5	4.9	5.9	253

Time	\bar{U}_r (m s ⁻¹)	s_{ur} (m s ⁻¹)	\bar{V}_r (m s ⁻¹)	s_{vr} (m s ⁻¹)	Var. (%)	Θ_M (°)	S (%)
8/10-8/11	-2.5	4.6	0.4	2.7	74	67	50
8/10	-2.4	6.0	1.6	2.7	84	60	45
9/10	-1.9	5.9	-0.4	3.5	74	106	29
10/10	-8.1	4.5	1.3	3.7	59	63	88
11/10	-1.3	4.5	0.1	2.3	79	38	28
12/10	-1.0	2.9	-1.3	2.5	58	93	42
1/11	-1.3	3.1	0.2	2.0	71	74	36
2/11	0.8	3.6	1.5	3.0	60	92	38
3/11	-0.7	2.5	1.0	1.6	69	76	42
4/11	-1.6	3.6	0.1	1.6	83	65	42
5/11	-1.3	2.6	1.4	1.7	69	32	57
6/11	-5.1	3.2	0.4	1.9	74	62	88
7/11	-3.8	5.2	0.2	2.0	87	62	60
8/11	-4.8	4.0	0.8	1.9	82	63	82

with that from the corresponding observational point and regressing the NARR wind components against the observed wind components. While done for both Barrow and Wainwright, for purposes of brevity we only show the time series comparisons between Wainwright and NARR winds (Figures 10 – 12). The linear regressions results are shown for both sites (Figures 13 – 16). The plots and regressions were done over two-month long periods between August 2010 and August 2011.

The overall impression from the time series comparisons are that the winds at both sites are in good agreement with one another on time scales of a day or longer. In general, the wind magnitudes at Wainwright are slightly greater than at NARR BC6. The more quantitative comparison from the linear regressions (Figures 13 – 16), indicate that both the meridional and zonal velocity components are significantly correlated between Barrow (or Wainwright) and NARR BC6. For example, the r^2 values for the Wainwright and NARR BC6 zonal wind components range between 0.62 (July – August, 2011) to 0.83 (August – October, 2010), with a comparable range in the Barrow and NARR BC6 comparison. The correlations are slightly smaller for the meridional components, although all are statistically significant. The root mean square differences between the observed and modeled wind components are $2 - 3 \text{ m s}^{-1}$ and show no seasonal variation. However, the regression slopes vary seasonally with these being ~ 1.0 in the fall and summer, and ~ 0.5 in winter and early spring. Finally we note that the intercepts indicate that NARR BC6 winds are slightly more southward and westward than those at Wainwright. We conclude that the NARR winds are a reliable proxy for the actual winds. We use the model winds in this report because these winds have no data gaps and our analyses incorporate larger-scale wind fields for which the NARR product is the only source.

4.3 Sub-Surface Currents and Hydrography

We begin with a summary of monthly and mean (record-length) statistics for the August 2010 – August 2011 period (Tables 5 – 10) and in subsequent figures. We show the record-length mean of the vertically-averaged velocity vectors and variance ellipses at each site in Figure 17. For moorings BC1 – BC3, mean vectors are toward the northeast at $10 - 20 \text{ cm s}^{-1}$, with BC2 having the maximum value. Farther offshore (BC4 – BC6), mean vectors are southeastward, or onshore, at $\sim 10 \text{ cm s}^{-1}$. This suggests the mean flow between BC3 and BC4 makes a 90° turn to the northeast within a turning radius of $\sim 13 \text{ km}$. Hence the along-shore flow entering the head of Barrow Canyon is confined to within 40 km of the coast. The variance ellipses also change in magnitude and direction across the array. Major axes are largest nearshore (and a maximum at BC2) and decrease offshore. The ellipse orientation also changes moving offshore from the coast. It is strongly along-shore polarized at BC1 – BC3 and onshore polarized at BC5 and BC6. In all cases, however, the major axes of the ellipses are oriented in nearly the same direction as the mean velocity vector.

4.3.1 Velocity Structure

We next show mean velocity sections where we have rotated the velocity vectors into along- (56°T) and cross-shore (326°T) directions. This coordinate system thus approximates the mean

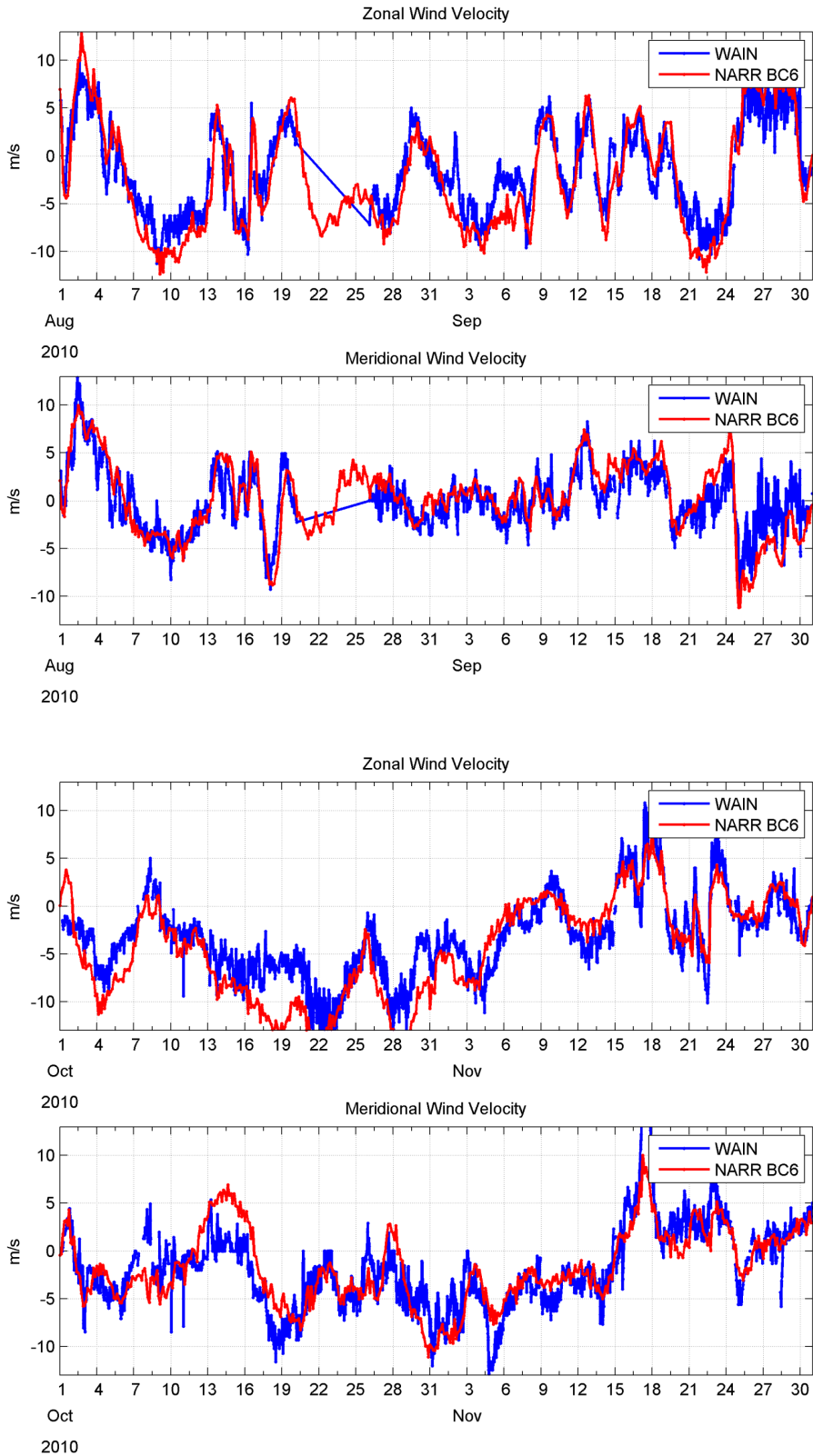


Figure 10. Time series of zonal and meridional wind components from Wainwright (blue) and the NARR grid point closest to BC6 for August – September 2010 (top) and October – November 2010 (bottom).

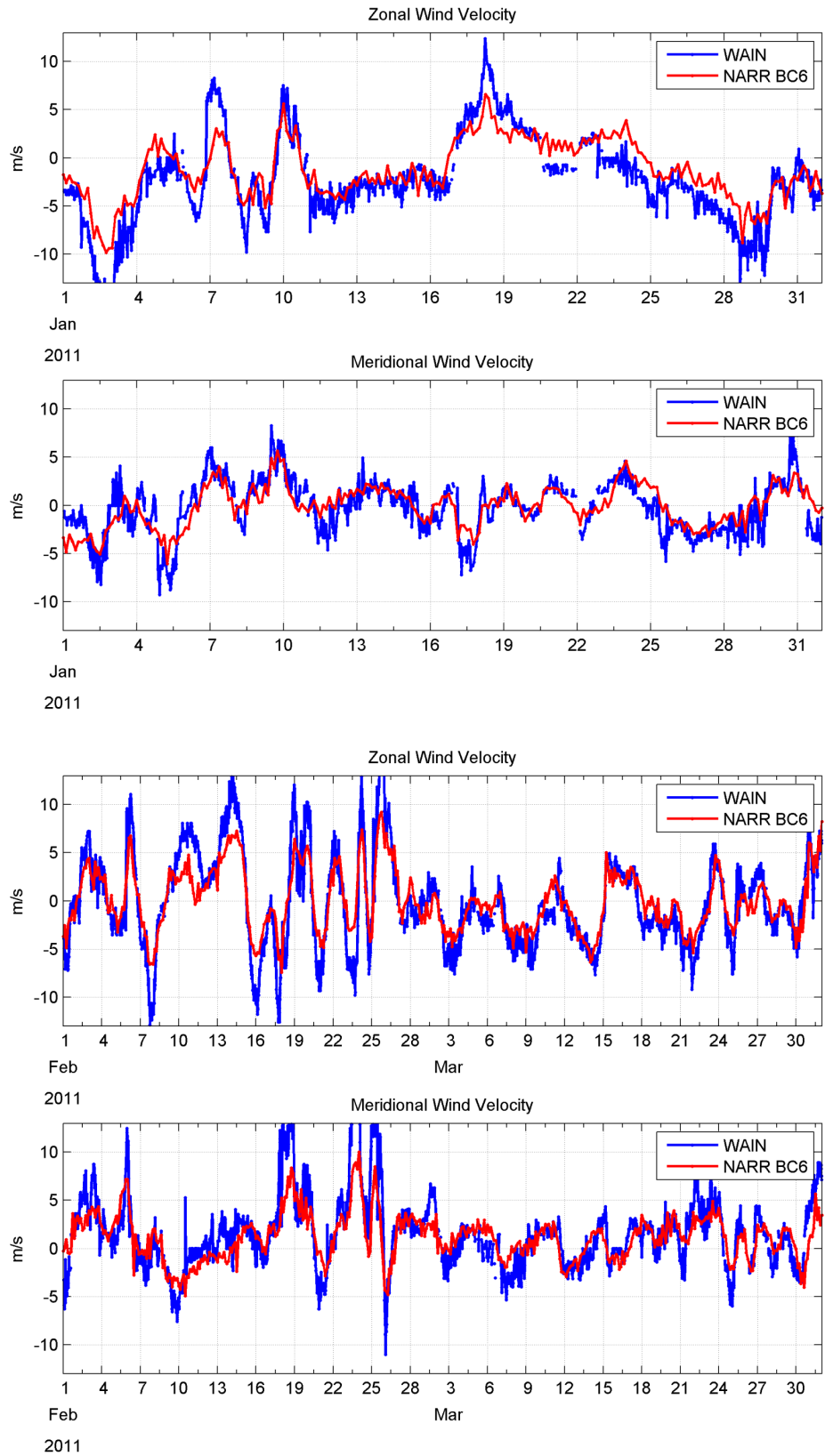


Figure 11. Time series of zonal and meridional wind components from Wainwright (blue) and the NARR grid point closest to BC6 for January 2011 (top) and February – March 2011 (bottom).

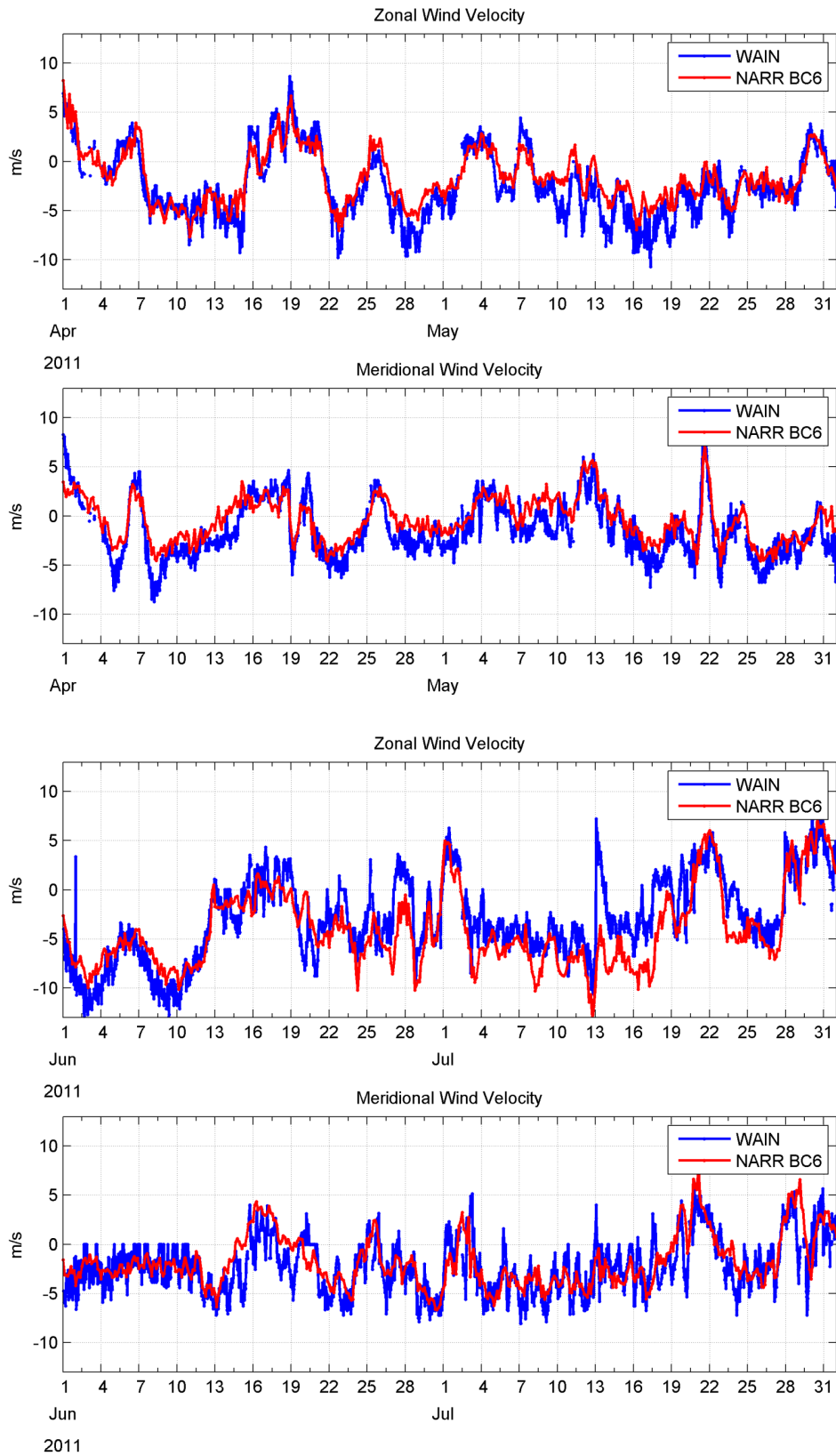


Figure 12. Time series of zonal and meridional wind components from Wainwright (blue) and the NARR grid point closest to BC6 for April – May 2011 (top) and June – July 2011 (bottom).

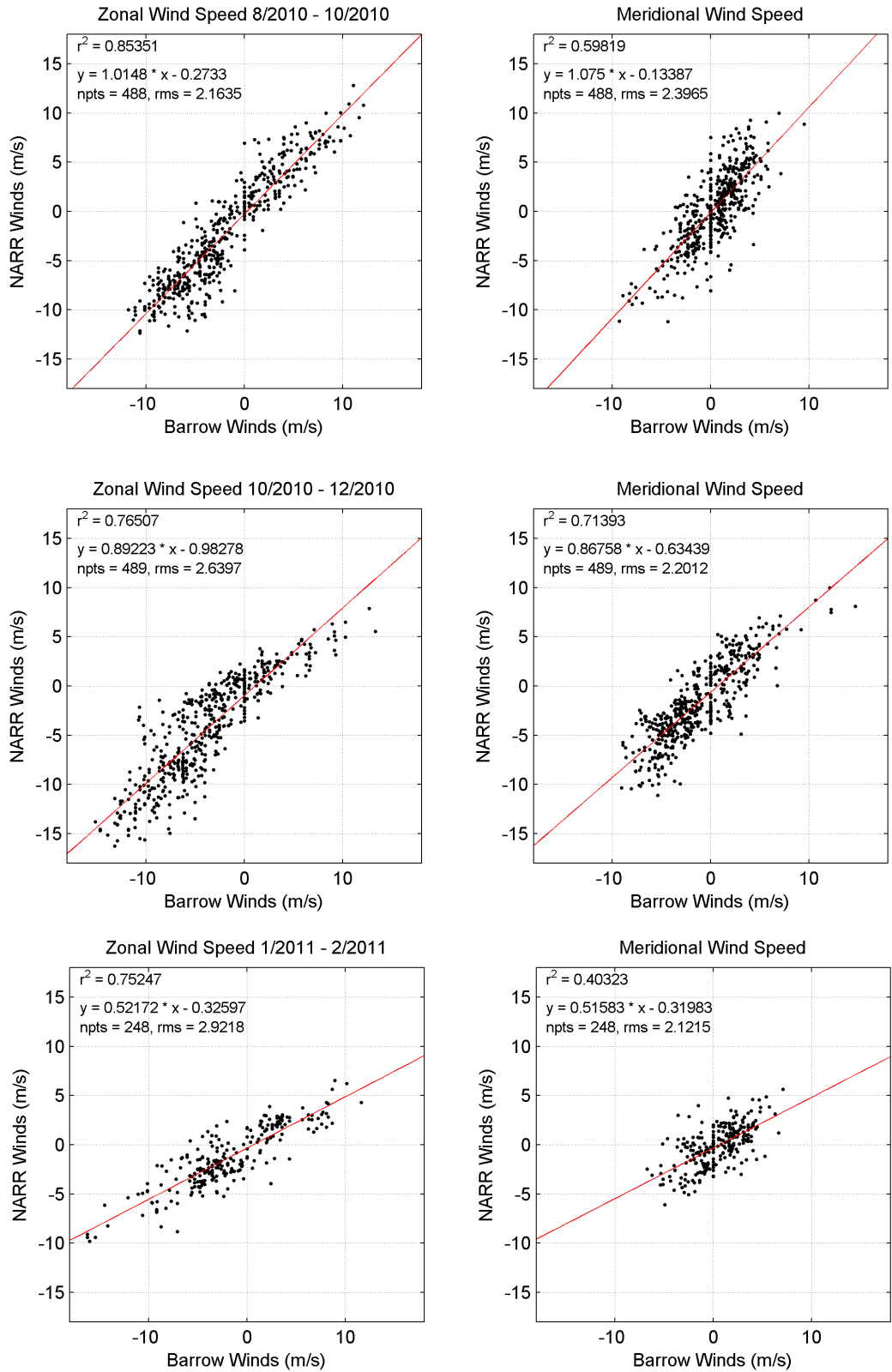


Figure 13. Linear regression results NARR vs. Barrow winds. Panels on the left (right) are for the zonal (meridional) wind components. The results are for 2-month long periods beginning August – October 2010 (top) through January – February 2011 (bottom).

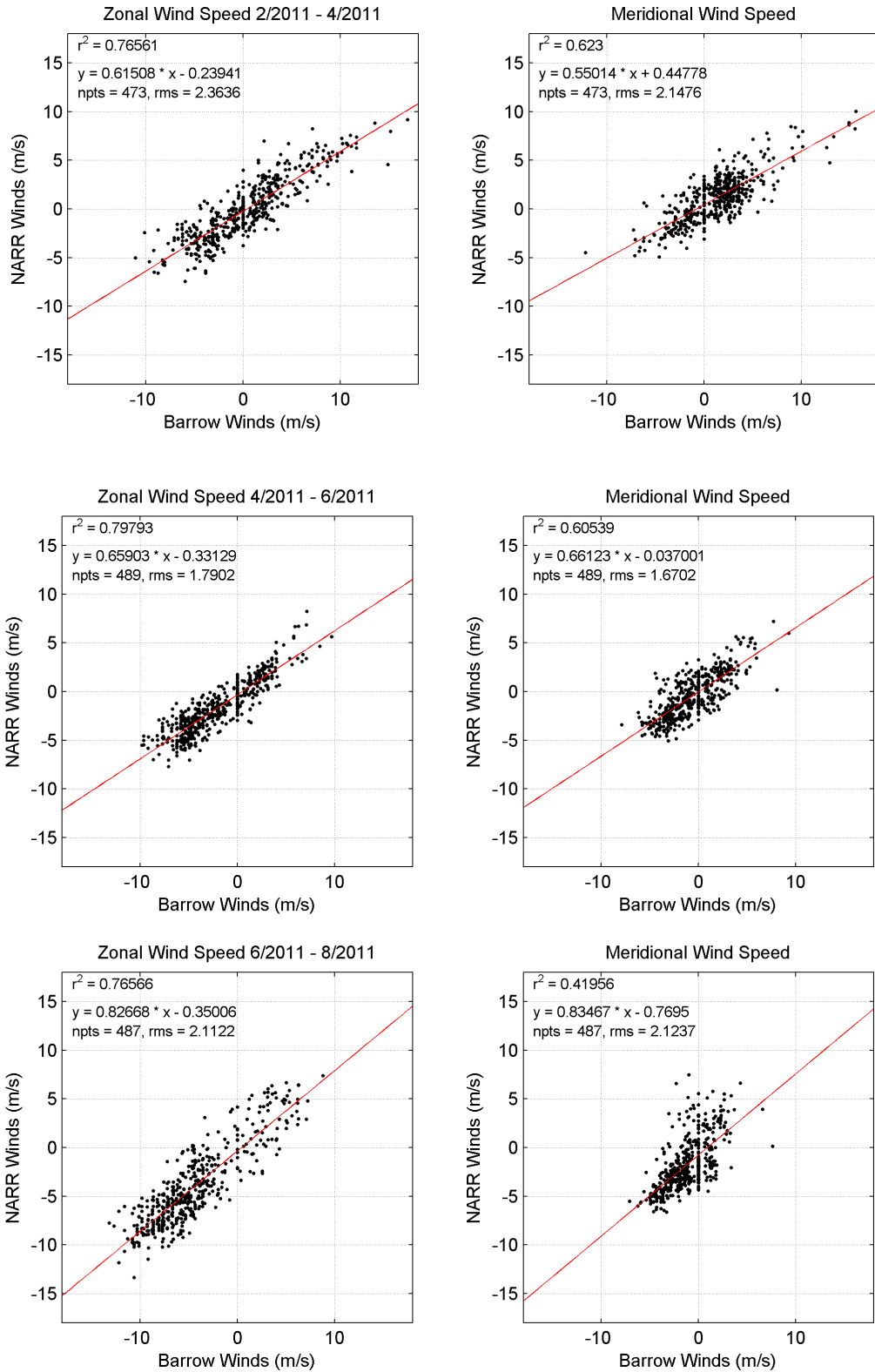


Figure 14. Linear regression results NARR vs. Barrow winds. Panels on the left (right) are for the zonal (meridional) wind components. The results are for 2-month long periods beginning February – April 2011 (top) through June – August 2011 (bottom).

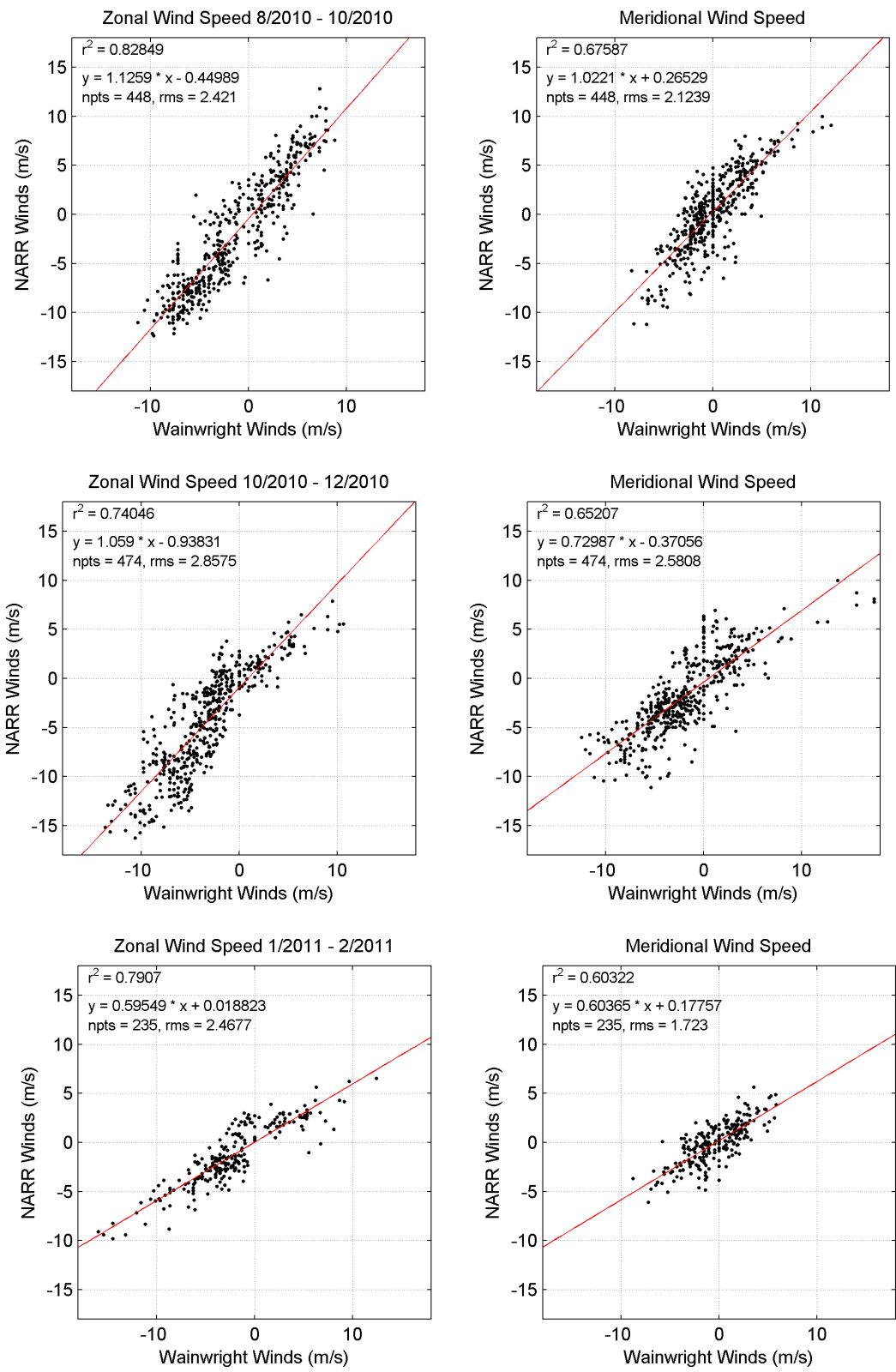


Figure 15. Linear regression results NARR vs. Wainwright winds. Panels on the left (right) are for the zonal (meridional) wind components. The results are for 2-month long periods beginning August – October 2010 (top) through January – February 2011 (bottom).

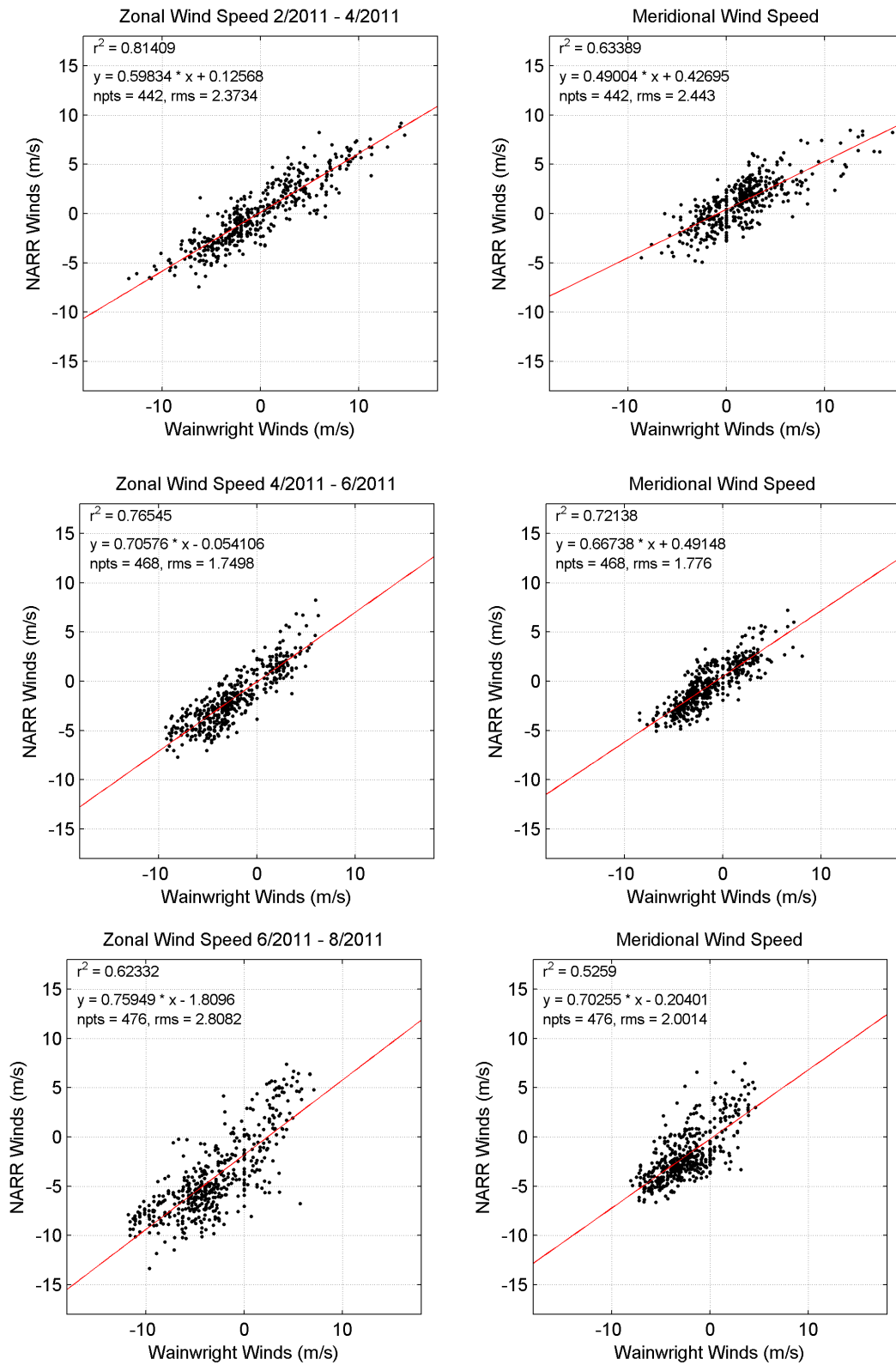


Figure 16. Linear regression results NARR vs. Wainwright winds. Panels on the left (right) are for the zonal (meridional) wind components. The results are for 2-month long periods beginning February – April 2011 (top) through June – August 2011 (bottom).

Table 5. Monthly and record-length statistics for the vertically averaged velocities at BC1. Number of hourly records in each month (N), mean zonal (\bar{U}) and meridional (\bar{V}) velocities and their standard deviations (s_u, s_v), percent variance explained by the principal axis, and orientation of the principal axis (θ).

Mooring	Month	N	\bar{U} (cm s ⁻¹)	s_u (cm s ⁻¹)	\bar{V} (cm s ⁻¹)	s_v (cm s ⁻¹)	% Variance	θ
BC1	Aug	336	32.5	9.9	23.9	8.8	99.4	48
BC1	Sep	720	29.3	22.0	20.5	18.2	99.7	50
BC1	Oct	744	-30.5	27.3	-20.5	17.4	99.3	58
BC1	Nov	720	10.6	45.0	8.0	32.7	99.8	54
BC1	Dec	744	-3.4	34.7	-4.1	26.9	99.9	52
BC1	Jan	744	13.4	32.2	9.2	23.2	99.7	54
BC1	Feb	672	22.8	17.5	14.6	12.0	99.4	56
BC1	Mar	744	15.5	8.4	9.6	5.3	98.0	58
BC1	Apr	720	-10.6	25.8	-6.8	16.6	99.9	57
BC1	May	744	24.9	12.5	16.1	8.5	99.7	56
BC1	Jun	720	8.2	26.3	5.2	17.3	99.9	56
BC1	Jul	744	31.4	12.4	22.3	11.7	99.4	47
BC1	Aug	605	16.0	24.0	11.5	18.7	99.5	52
BC1	ALL	8957	11.27	31.0	7.6	22.2	99.6	54

Table 6. Monthly and record-length statistics for the vertically averaged velocities at BC2.

Mooring	Month	N	\bar{U} (cm s ⁻¹)	s_u (cm s ⁻¹)	\bar{V} (cm s ⁻¹)	s_v (cm s ⁻¹)	% Variance	θ
BC2	Aug	358	42.0	9.7	24.6	7.6	96.6	52
BC2	Sep	720	37.8	17.5	20.1	12.4	98.7	55
BC2	Oct	744	-37.7	32.9	-13.0	12.0	96.1	73
BC2	Nov	720	12.9	55.6	7.3	26.6	98.7	65
BC2	Dec	744	-6.2	45.8	-3.8	18.9	99.4	68
BC2	Jan	744	16.8	39.7	6.2	17.9	98.5	66
BC2	Feb	672	33.1	20.0	14.1	11.0	98.8	62
BC2	Mar	744	23.0	10.4	7.1	4.8	98.9	66
BC2	Apr	720	-13.5	35.4	-8.0	13.2	98.1	71
BC2	May	744	34.9	14.0	8.2	5.0	95.4	74
BC2	Jun	720	11.5	33.4	2.9	10.0	99.5	74
BC2	Jul	744	41.7	11.8	12.0	6.7	98.8	61
BC2	Aug	475	29.8	21.0	9.0	9.4	97.6	67
BC2	ALL	8849	15.9	38.8	5.74	16.7	98.1	68

Table 7. Monthly and record-length statistics for the vertically averaged velocities at BC3.

Mooring	Month	N	\bar{U} (cm s ⁻¹)	s_u (cm s ⁻¹)	\bar{V} (cm s ⁻¹)	s_v (cm s ⁻¹)	% Variance	θ
BC3	Aug	356	32.2	10.5	3.30	4.9	96.1	67
BC3	Sep	720	28.6	17.9	2.55	7.3	97.6	69
BC3	Oct	744	-21.1	27.7	-3.38	8.1	92.2	91
BC3	Nov	720	8.3	45.9	3.35	11.0	97.4	80
BC3	Dec	744	-8.4	38.1	1.96	7.3	97.6	84
BC3	Jan	744	9.2	35.8	3.40	8.6	97.2	80
BC3	Feb	672	26.3	20.4	8.16	9.0	98.4	67
BC3	Mar	744	16.8	8.5	3.54	3.6	97.6	68
BC3	Apr	720	-14.0	28.1	-2.16	6.3	96.0	85
BC3	May	744	19.6	12.2	2.93	3.4	94.0	83
BC3	Jun	720	5.4	23.3	1.48	4.6	97.0	85
BC3	Jul	744	28.6	10.6	3.86	6.2	96.0	61
BC3	Aug	617	19.9	14.9	3.02	6.7	93.1	70
BC3	ALL	8989	10.6	30.6	2.38	7.6	96.5	81

Table 8. Monthly and record-length statistics for the vertically averaged velocities at BC4.

Mooring	Month	N	\bar{U} (cm s ⁻¹)	s_u (cm s ⁻¹)	\bar{V} (cm s ⁻¹)	s_v (cm s ⁻¹)	% Variance	θ
BC4	Aug	355	26.8	9.5	-4.17	3.9	89.1	78
BC4	Sep	720	24.5	14.1	-4.64	4.7	94.1	77
BC4	Oct	744	-10.9	20.9	-3.24	8.3	86.5	92
BC4	Nov	720	10.3	35.5	-3.77	5.4	98.1	86
BC4	Dec	744	-4.0	29.4	-1.17	7.3	94.4	87
BC4	Jan	744	9.4	29.0	-3.32	6.6	95.3	87
BC4	Feb	672	23.8	19.6	1.07	5.0	97.1	79
BC4	Mar	744	15.2	7.3	-1.23	1.8	94.8	86
BC4	Apr	720	-6.6	22.5	-2.17	3.2	98.1	88
BC4	May	744	16.5	9.6	-3.31	3.0	92.3	97
BC4	Jun	720	6.8	17.4	-3.21	5.2	91.9	92
BC4	Jul	744	24.6	8.5	-6.55	3.6	88.7	77
BC4	Aug	619	16.6	11.6	-4.51	4.1	89.0	89
BC4	ALL	8990	11.0	23.7	-3.06	5.5	95.0	88

Table 9. Monthly and record-length statistics for the vertically averaged velocities at BC5.

Mooring	Month	N	\bar{U} (cm s ⁻¹)	s_u (cm s ⁻¹)	\bar{V} (cm s ⁻¹)	s_v (cm s ⁻¹)	% Variance	θ
BC5	Aug	354	17.2	7.6	-8.78	3.2	85.1	87
BC5	Sep	720	13.4	11.5	-9.49	3.9	91.2	82
BC5	Oct	744	-8.7	14.7	-1.71	9.4	77.2	110
BC5	Nov	720	6.7	24.4	-7.20	5.9	95.5	96
BC5	Dec	744	-4.1	21.5	-1.27	8.5	87.9	98
BC5	Jan	744	5.2	21.9	-4.92	9.1	86.8	98
BC5	Feb	672	19.2	17.6	-4.38	3.5	96.3	92
BC5	Mar	744	10.4	6.3	-4.94	1.9	94.0	100
BC5	Apr	720	-5.7	15.8	-2.73	4.3	93.7	95
BC5	May	744	8.2	6.5	-7.02	4.3	76.4	112
BC5	Jun	720	1.5	11.2	-4.70	6.1	79.4	102
BC5	Jul	744	13.4	7.6	-11.66	2.8	88.0	91
BC5	Aug	620	7.9	8.0	-7.46	4.8	76.6	104
BC5	ALL	8990	5.9	17.1	-5.73	6.6	89.2	99

Table 10. Monthly and record-length statistics for the vertically -averaged velocities at BC6.

Mooring	Month	N	\bar{U} (cm s ⁻¹)	s_u (cm s ⁻¹)	\bar{V} (cm s ⁻¹)	s_v (cm s ⁻¹)	% Variance	θ
BC6	Aug	336	18.4	6.3	-5.78	3.0	82.5	82
BC6	Sep	720	15.3	10.5	-7.16	3.7	90.6	82
BC6	Oct	744	-5.1	13.2	0.77	9.8	76.1	118
BC6	Nov	720	9.8	21.5	-3.73	5.8	94.2	96
BC6	Dec	744	-1.1	18.6	-0.02	8.8	83.0	98
BC6	Jan	744	7.5	19.9	-2.62	9.0	84.4	98
BC6	Feb	672	19.4	17.4	-1.66	4.0	96.0	84
BC6	Mar	744	10.6	6.1	-3.36	1.7	93.1	94
BC6	Apr	720	-3.6	14.6	-1.13	3.9	93.7	93
BC6	May	744	9.1	6.8	-5.70	3.0	85.2	99
BC6	Jun	720	4.9	10.4	-2.65	6.0	77.8	103
BC6	Jul	744	15.7	7.4	-8.78	2.5	90.0	88
BC6	Aug	621	9.8	7.9	-5.34	4.1	81.2	100
BC6	ALL	8973	8.0	15.6	-3.52	6.4	87.3	98

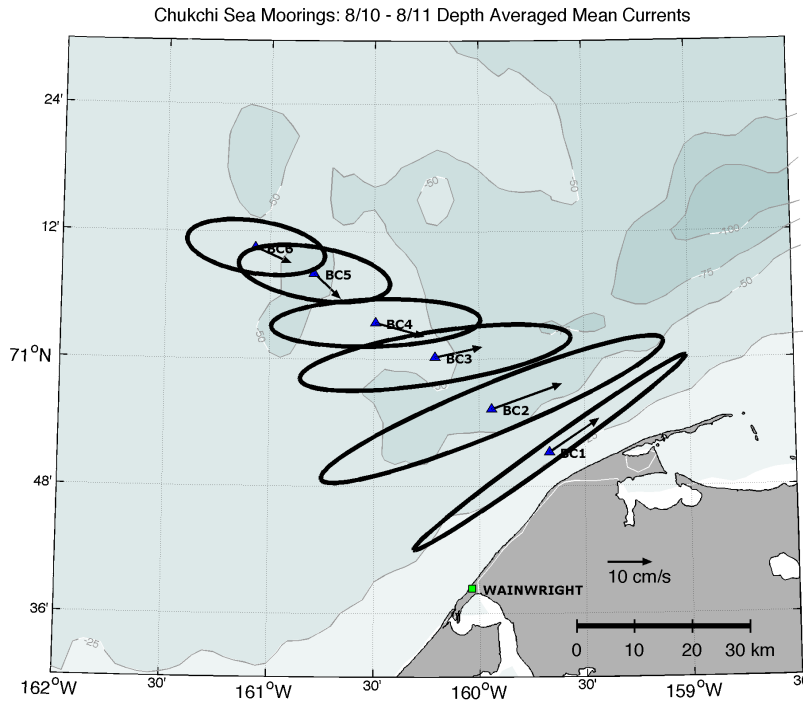


Figure 17. Depth averaged mean velocity vectors and variance ellipses for mooring array. Bathymetry is shaded.

orientation of the coastline (along-shore) between Wainwright and Barrow. For this rotation, positive along-shore velocities, denoted by U_r , are toward 56°T (negative U_r toward 236°T), and positive offshore velocities, denoted by V_r , are toward 326°T (negative V_r toward 146°T). Our classification also means that $U_r > 0$ ($U_r < 0$) implies downcanyon (upcanyon) flow or transport. Record-length means for the along-shore and cross-shore velocity components are shown in Figure 18. These indicate that the flow is down canyon on average and has a velocity maximum of $\sim 16 \text{ cm s}^{-1}$ at BC2 at $\sim 30 \text{ m}$ depth. The cross-shore flow is a maximum onshore below 20 m depth and at the three moorings farthest offshore. There are two regions of maximum onshore convergence. One is centered between BC3 and BC4 (between km 30 and 40), where the contours in Figure 18 imply that the mean flow makes a nearly 90° turn into the canyon. The other occurs between BC1 and BC2 (km 10 and 20) and reflects the impeding influence of the coast on cross-shore flow.

Composite vertical sections of each velocity component were constructed for cases in which the flow was downcanyon and upcanyon. Downcanyon composites were formed from all cases in which the along-shore velocity component at 20 m depth at BC2 was positive (blue points in Figure 19) and vice-versa for the upcanyon composite (red points in Figure 19). In general, the flow is downcanyon, with downcanyon currents at this location typically between 20 and 50 cm s^{-1} . However, downcanyon currents exceed 50 cm s^{-1} on many occasions, and the maximum observed speed was $\sim 100 \text{ cm s}^{-1}$. Although upcanyon currents were less frequent, they were generally swifter than downcanyon flows and had maximum speeds exceeding 100 cm s^{-1} . Note

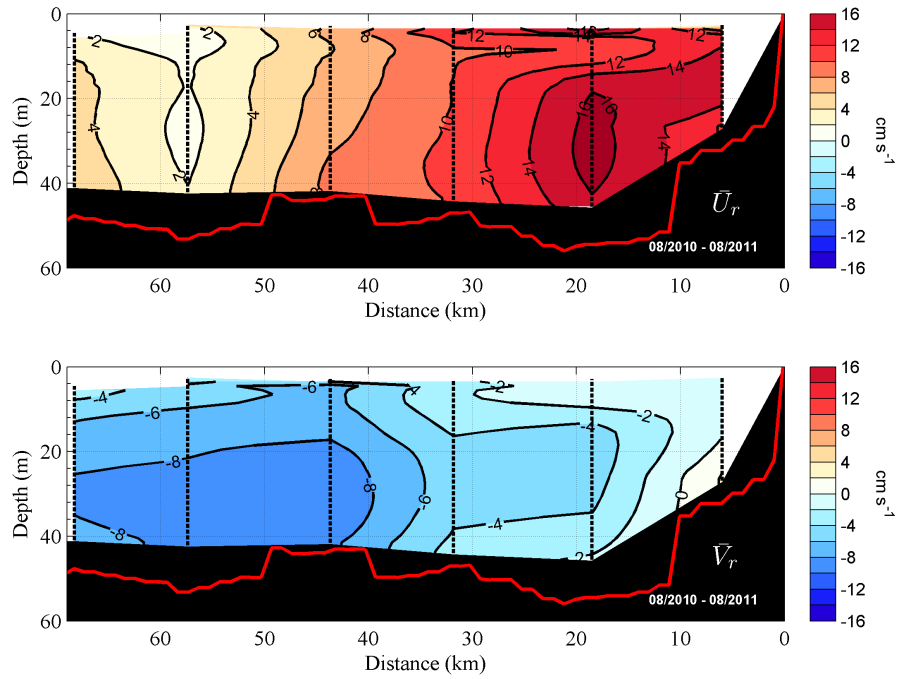


Figure 18. Along-shore (top) and cross-shore (bottom) record-length mean velocity component sections. Contours are in cm s^{-1} . Dotted vertical lines show the locations of the moorings. Mean winds were $\sim 2.4 \text{ m s}^{-1}$ towards 255°T .

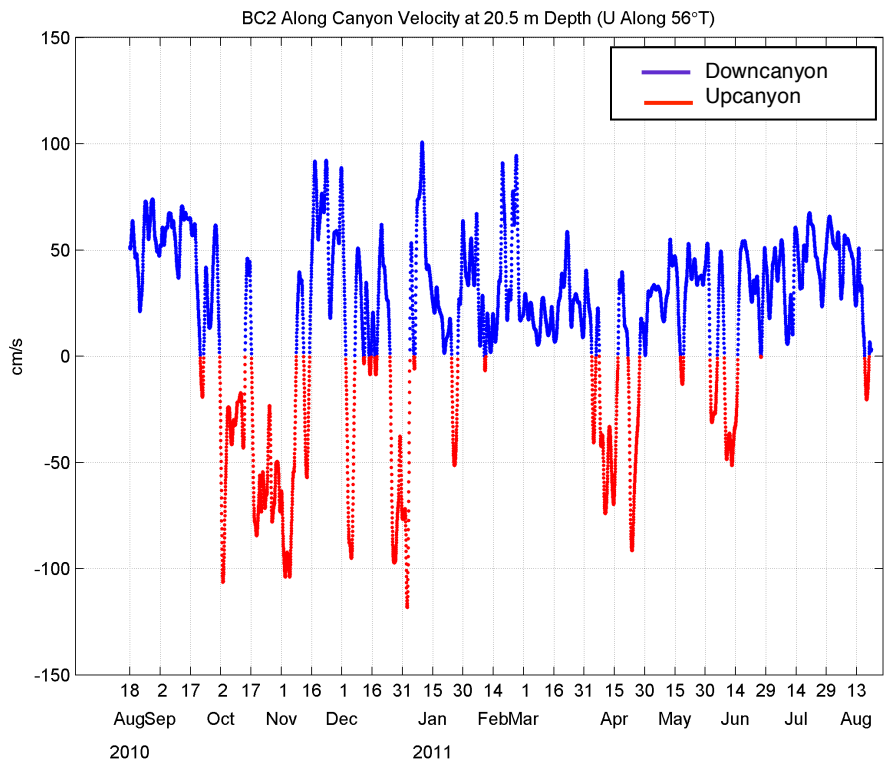


Figure 19. Time series of the upcanyon (red) and downcanyon (blue) currents at 20.5 m depth for mooring BC2.

also that current variations are greatest in winter, when maxima in both the up- and downcanyon currents occurred. In contrast to winter, the flow is steadier and directed downcanyon in September 2010 and from May – August 2011.

Composite downcanyon and upcanyon velocity sections are shown in Figures 20 and 21, respectively. Both cases are similar insofar as the flow includes a jet, centered at BC2, with maximum along-shore current speeds in the upper 20 m of the water column. For the downcanyon composite (Figure 20), the jet is slightly asymmetrical; the horizontal shear is somewhat larger on the offshore side of the jet axis than on the inshore side. There is little vertical shear in the along- and cross-shore velocity components across the whole section. The Rossby number ($Ro = \partial u / f \partial y$, where u is the along-shore current, y is the cross-shore coordinate, and f is the Coriolis parameter) is the ratio of the mean relative vorticity (given by the cross-shore shear in the along-canyon flow) to the Coriolis parameter. The maximum in Ro is ~ 0.01 and occurs between BC2 and BC3, indicating that the dynamics of the mean downcanyon flow are linear. The cross-shore velocity distribution indicates that the flow is everywhere onshore and convergent across most of the section, with the maximum convergence between BC1 and BC2. For the downcanyon case, the mean velocity sections suggest that most of the onshore flow turns downcanyon within ~ 20 km of the coast, as might be expected given the coastal barrier to cross-shore flow.

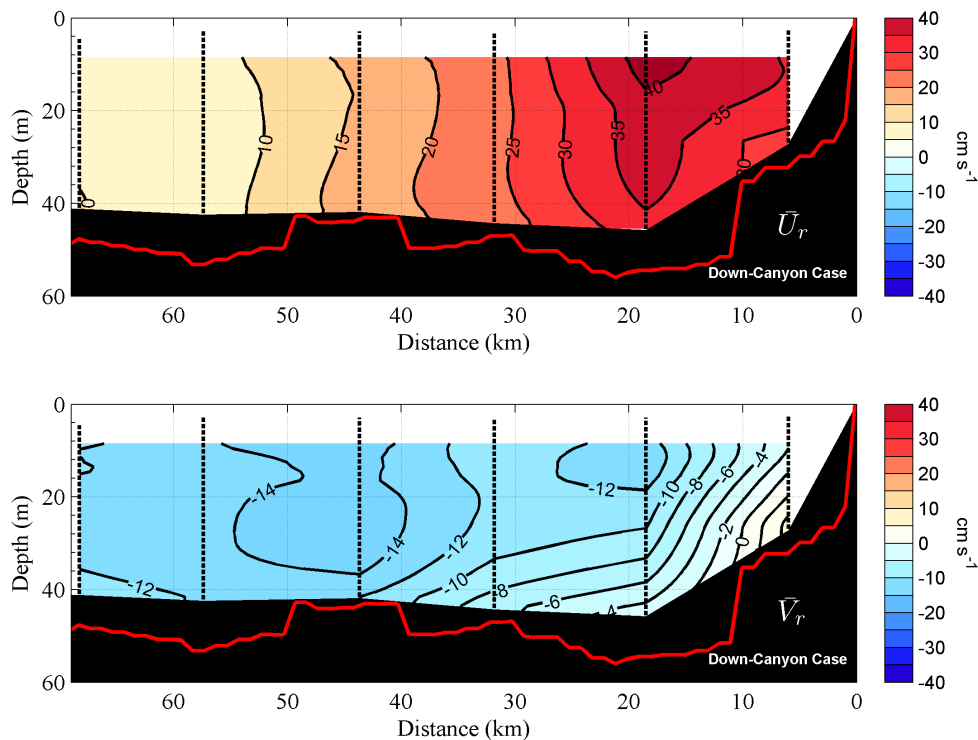


Figure 20. Vertical sections of the along-shore (top) and cross-shore (bottom) velocities for the downcanyon composite. Dotted vertical lines show the locations of the moorings, with BC6 on the left and BC1 on the right.

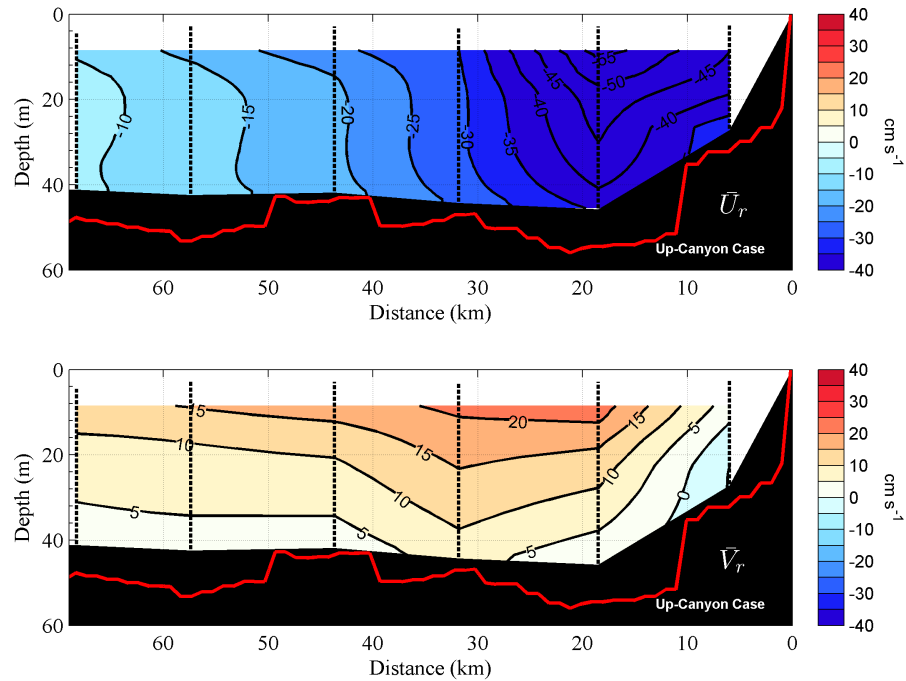


Figure 21. Vertical sections of the along-shore (top) and cross-shore (bottom) velocities for the upcanyon composite. Dotted vertical lines show the locations of the moorings, with BC6 on the left and BC1 on the right.

For the upcanyon composite (Figure 21), the jet is also slightly asymmetrical, with maximum shear on the offshore side of the jet maximum. Mean speeds in this case are larger than those for the mean downcanyon composite. Although the vertical shear is weak seaward of approximately 25 km, the shear can be substantial ($\sim 5 \times 10^{-3} \text{ s}^{-1}$) within the jet. The $Ro \sim 0.01$, small on average. The cross-shore velocity distribution indicates an offshore, vertically-sheared flow everywhere, with maximum divergence between BC1 and BC2 and weaker convergence on the offshore side of BC2.

We have also examined the mean monthly velocity sections and the shelf-scale wind fields (Figures 22 – 34) for August 2010 to August 2011. Based on our “upcanyon/downcanyon” criterion, August and September of 2010, and January, February, March, May, June, July, and August of 2011 are downcanyon months. For each of these months, there were very few upcanyon events, except in June 2011 when upcanyon flows occurred about half of the time. Overall the velocity structure in each of these downcanyon months was similar to the downcanyon mean. Thus, the current maximum is centered at BC2, with the horizontal shear about the maximum jet being slightly larger on the offshore side of the jet compared to its inshore side. The vertical shear is weak in both the along- and cross-shore velocity components, and the cross-shore flow is onshore and convergent across most of the sections, with the maximum convergence between BC1 and BC2. Although January and June 2011 had downcanyon flow on average, the maximum along-shore current speeds are less than half that observed, based on the mean downcanyon flow field. In both of these months, the maximum

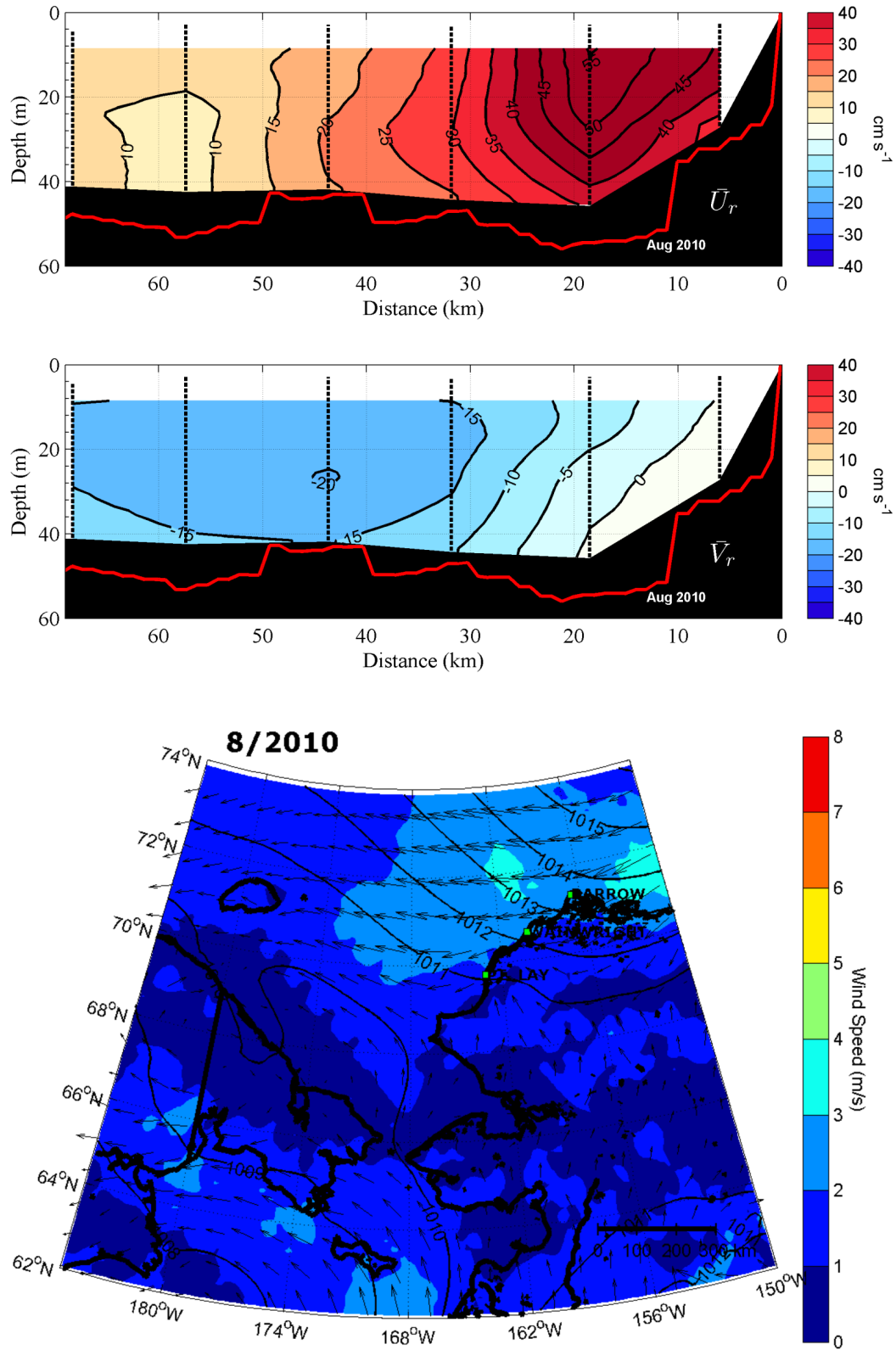


Figure 22. Vertical sections of the along-shore (upper panel top) and cross-shore (upper panel bottom) velocities for August 18 – 31, 2010. Mean winds (lower panel) over the mooring array were 2.8 m s^{-1} towards 262°T .

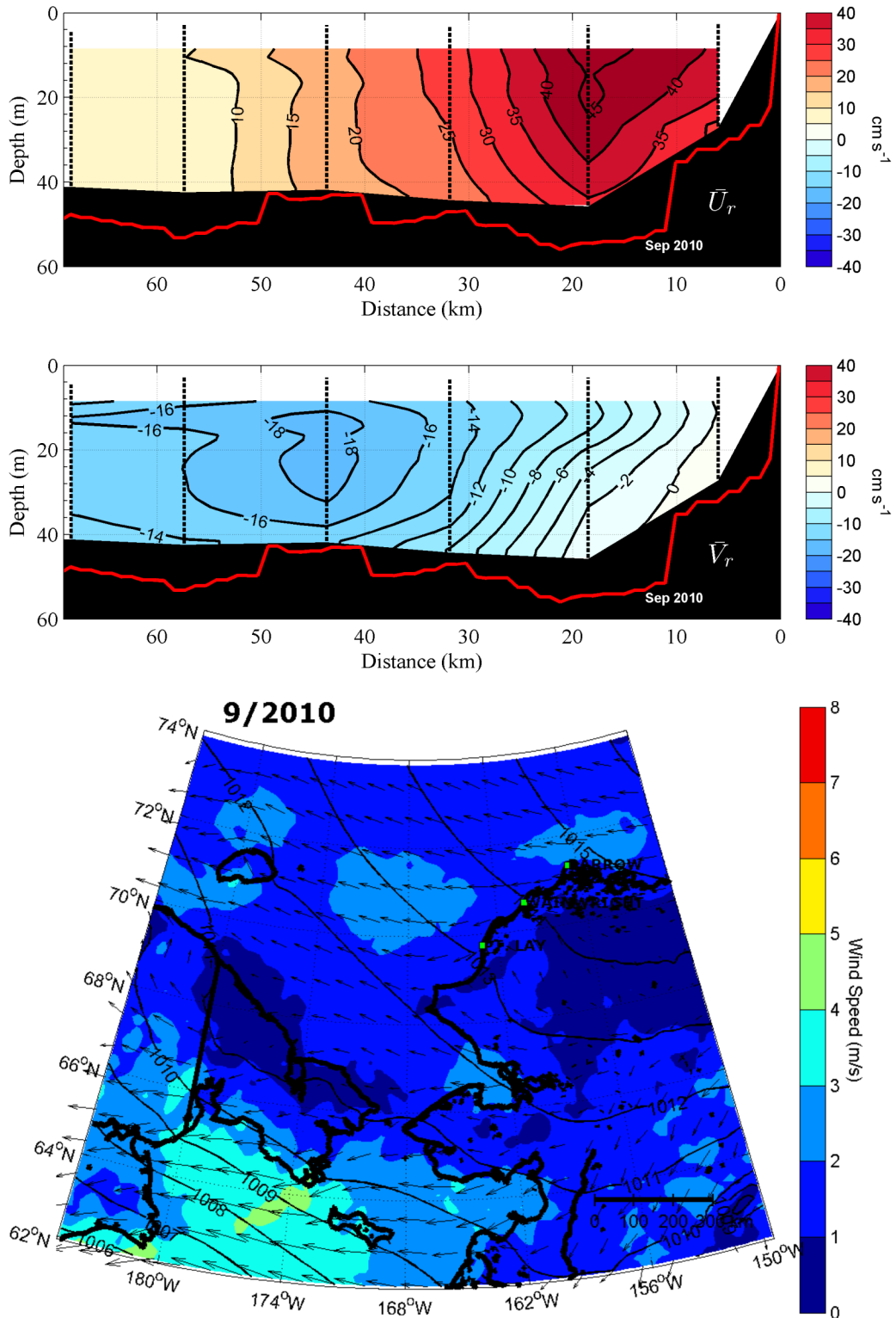


Figure 23. Vertical sections of the along-shore (upper panel top) and cross-shore (upper panel bottom) velocities for September 2010. Mean winds (lower panel) over the mooring array were 2.0 m s^{-1} towards 275°T .

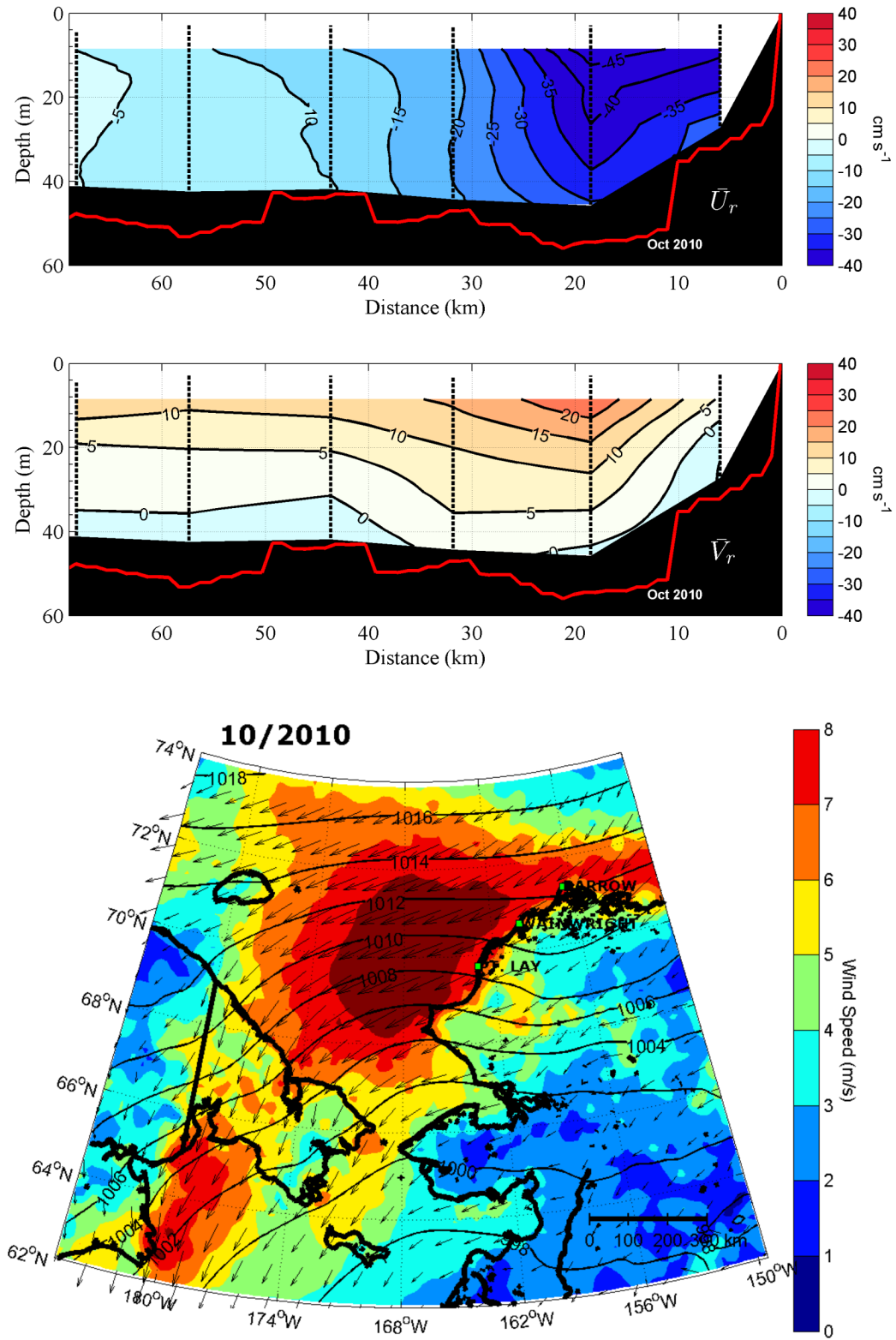


Figure 24. Vertical sections of the along-shore (upper panel top) and cross-shore (upper panel bottom) velocities for October 2010. Mean winds (lower panel) over the mooring array were 8.2 m s^{-1} towards 252°T .

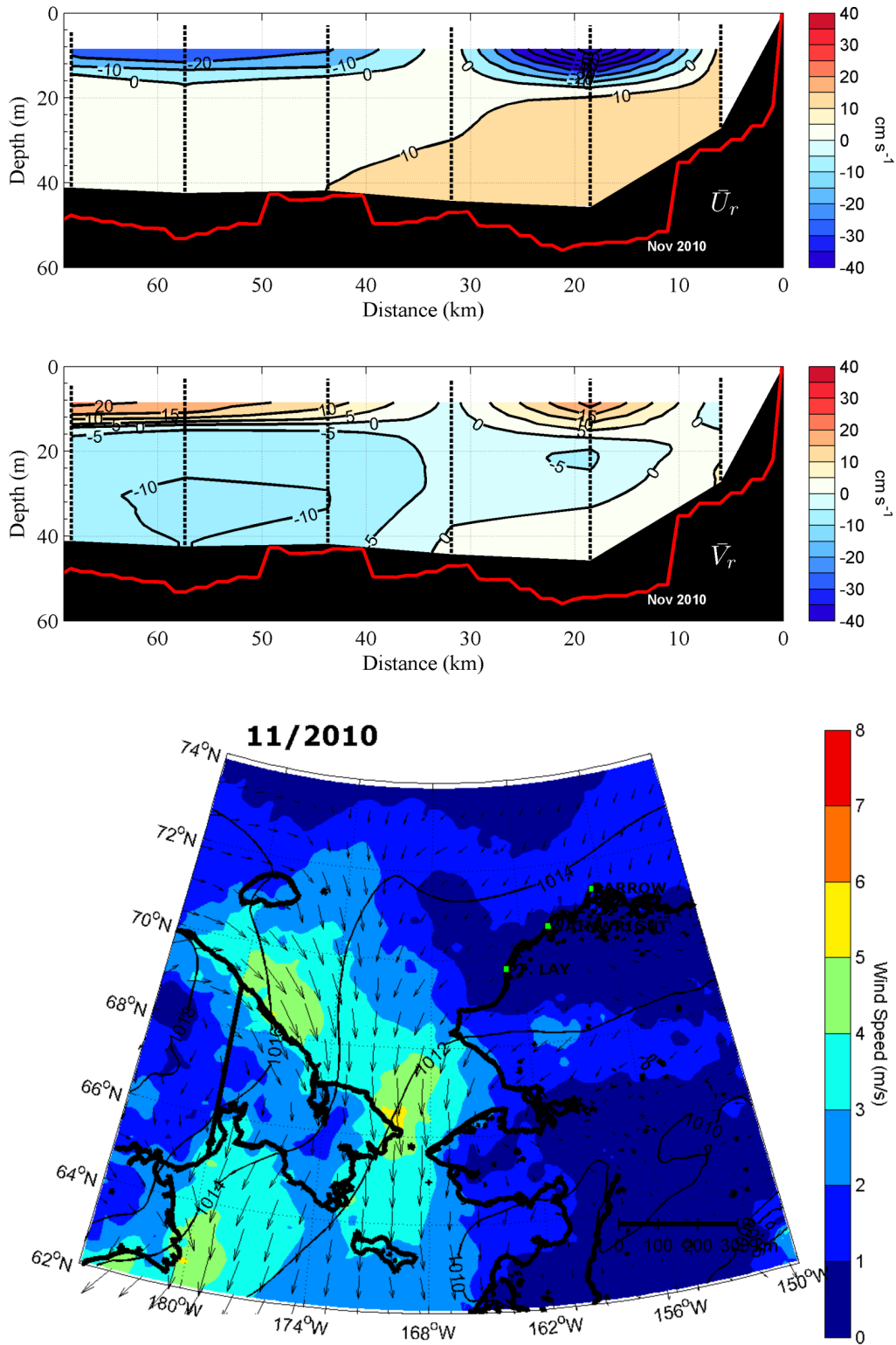


Figure 25. Vertical sections of the along-shore (upper panel top) and cross-shore (upper panel bottom) velocities for November 2010. Mean winds (lower panel) over the mooring array were 1.3 m s^{-1} towards 225°T .

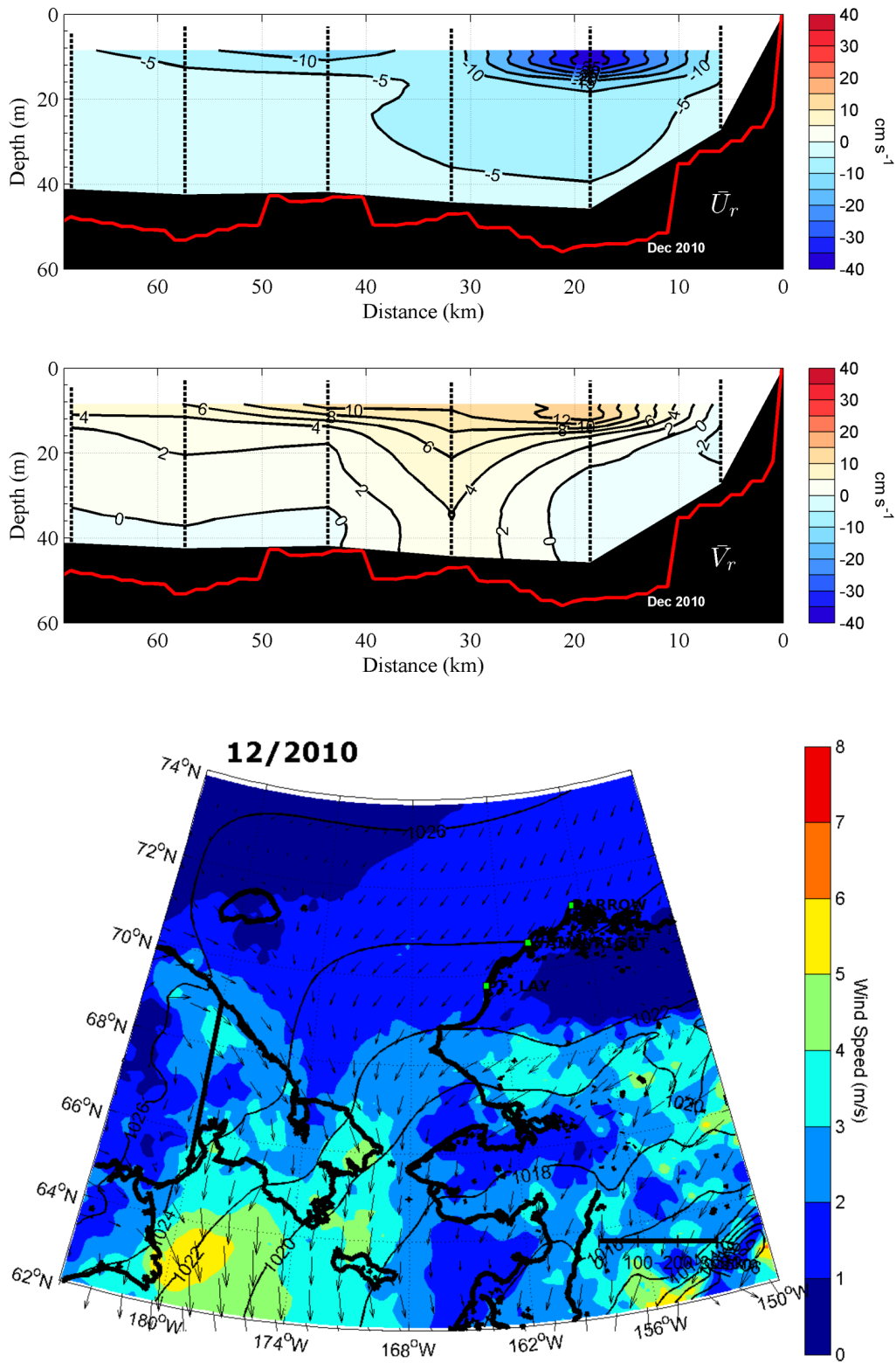


Figure 26. Vertical sections of the along-shore (upper panel top) and cross-shore (upper panel bottom) velocities for December 2010. Mean winds (lower panel) over the mooring array were 1.6 m s^{-1} towards 218°T .

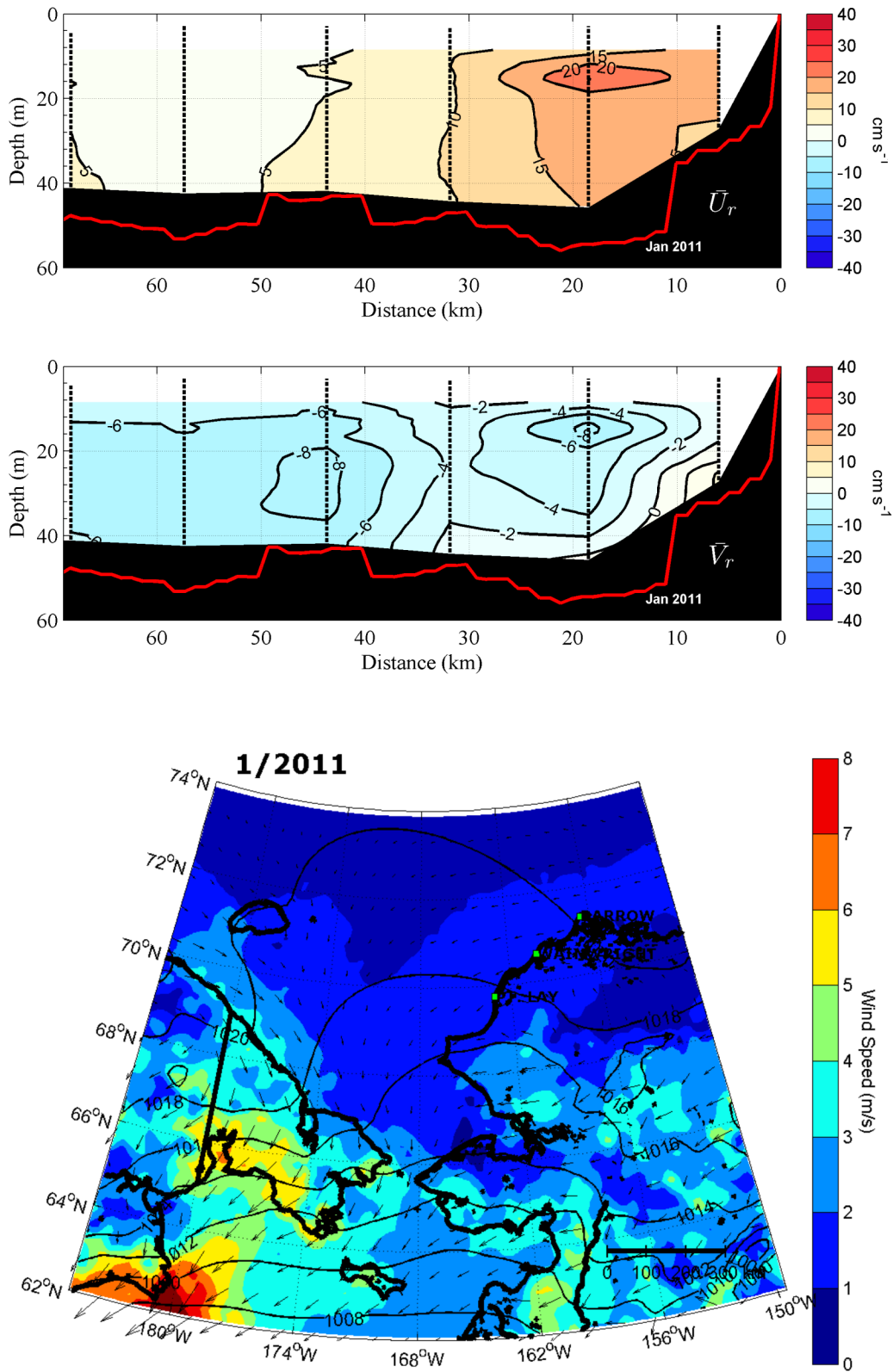


Figure 27. Vertical sections of the along-shore (upper panel top) and cross-shore (upper panel bottom) velocities for January 2011. Mean winds (lower panel) over the mooring array were 1.3 m s^{-1} towards 266°T .

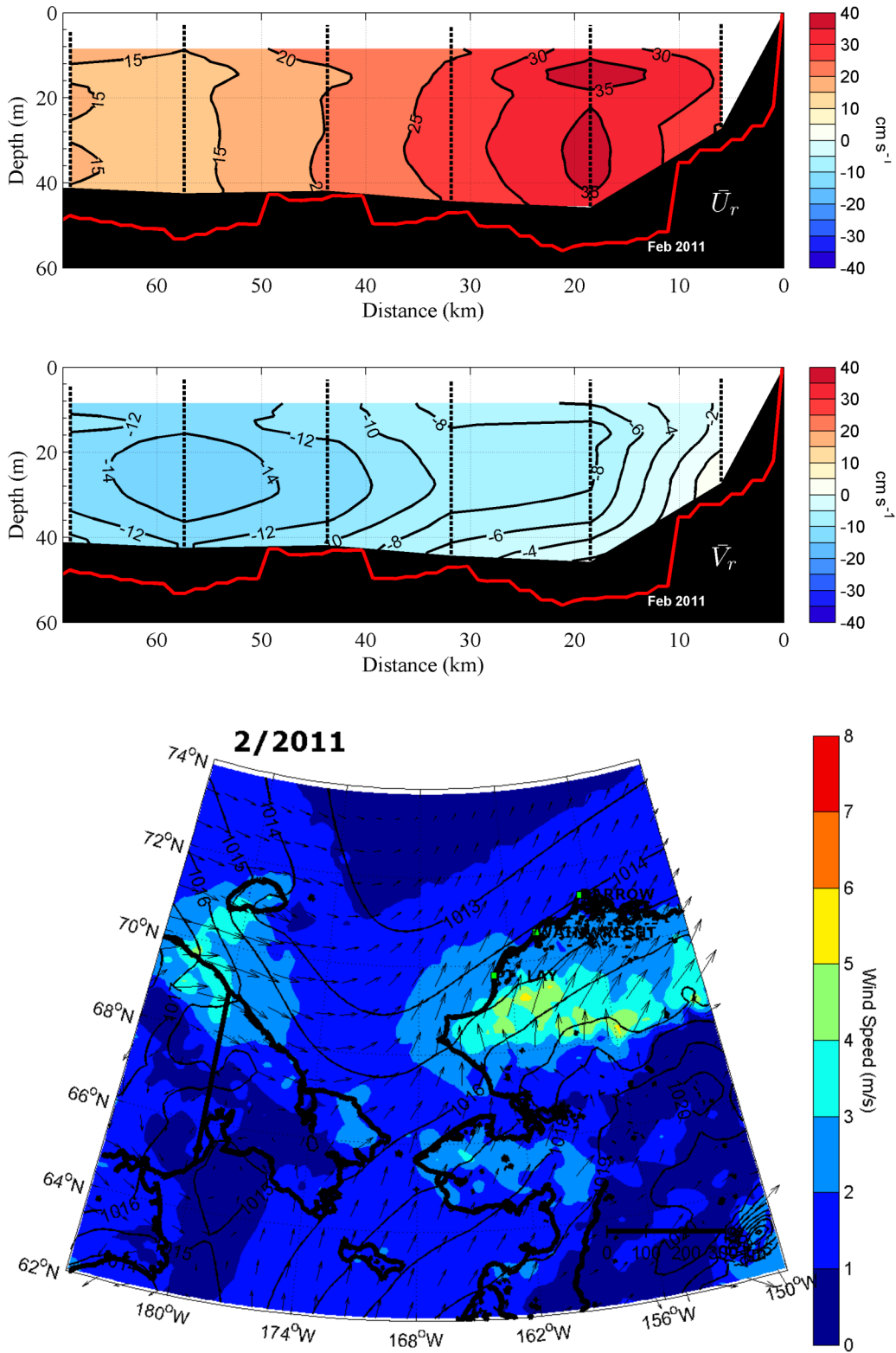


Figure 28. Vertical sections of the along-shore (upper panel top) and cross-shore (upper panel bottom) velocities for February 2011. Mean winds (lower panel) over the mooring array were 1.7 m s^{-1} towards 33°T .

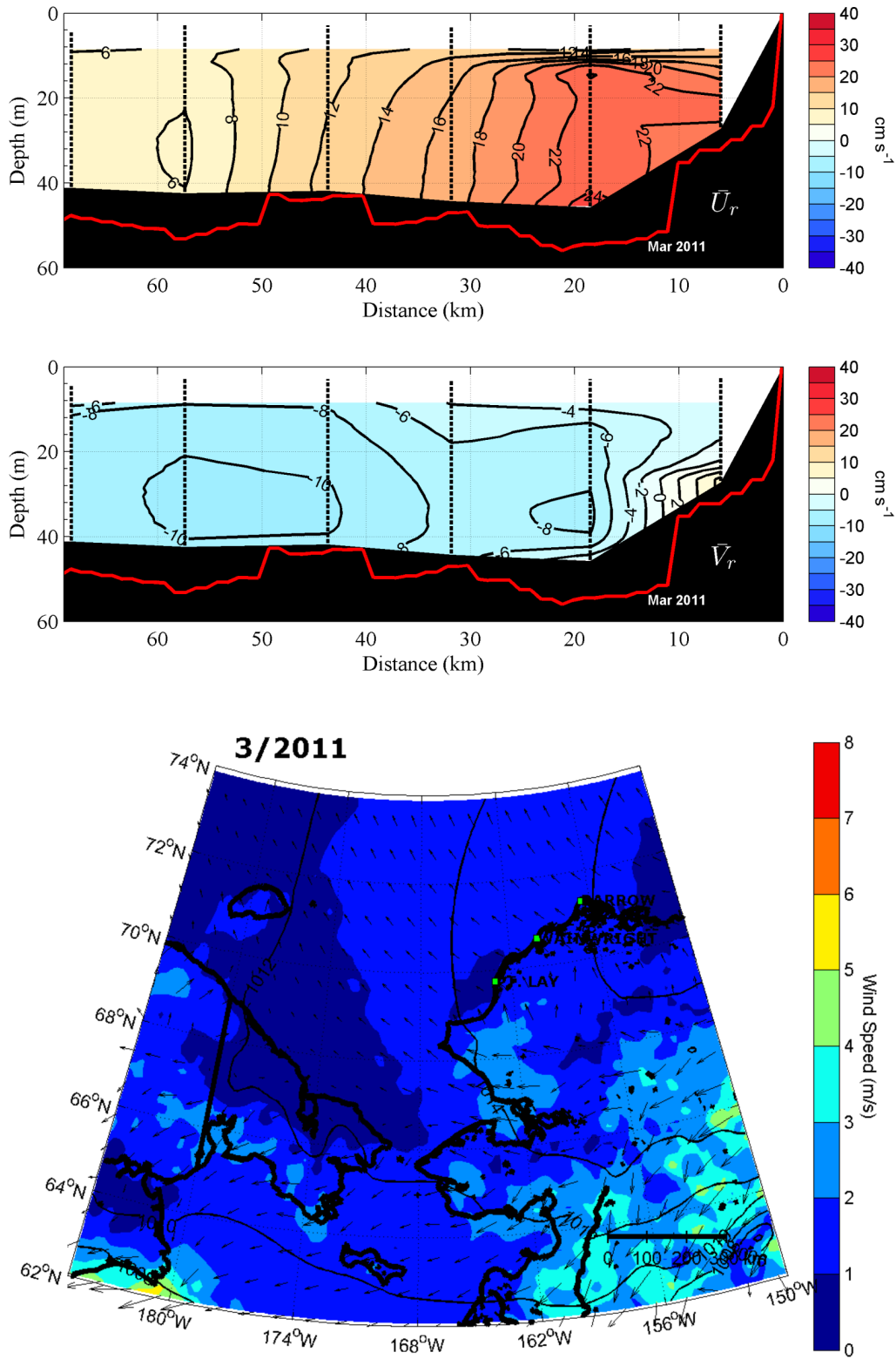


Figure 29. Vertical sections of the along-shore (upper panel top) and cross-shore (upper panel bottom) velocities for March 2011. Mean winds (lower panel) over the mooring array 1.3 m s^{-1} towards 315°T .

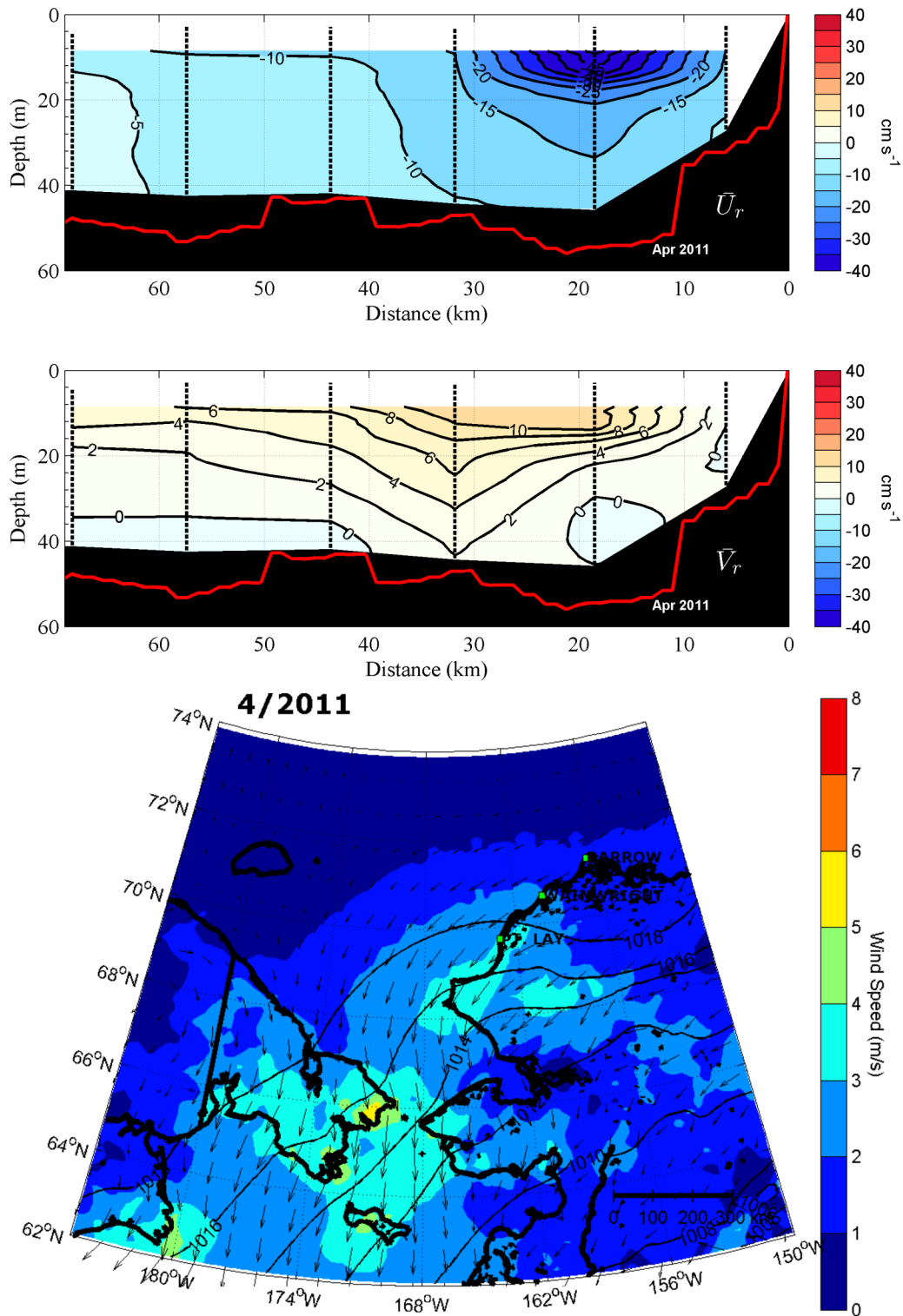


Figure 30. Vertical sections of the along-shore (upper panel top) and cross-shore (upper panel bottom) velocities for April 2011. Mean winds (lower panel) over the mooring array were 1.6 m s^{-1} towards 248°T .

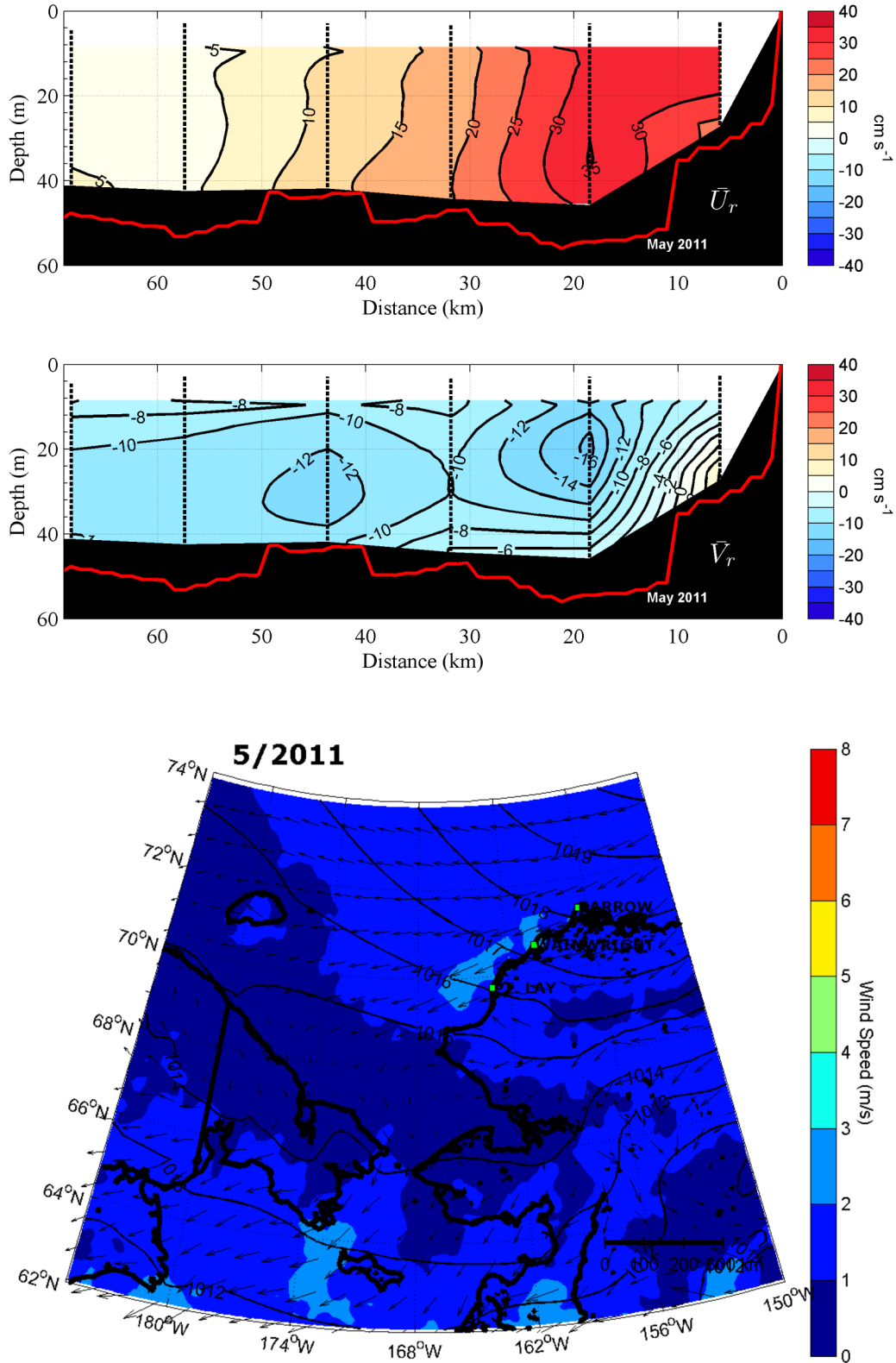


Figure 31. Vertical sections of the along-shore (upper panel top) and cross-shore (upper panel bottom) velocities for May 2011. Mean winds (lower panel) over the mooring array were 1.9 m s^{-1} towards 261°T .

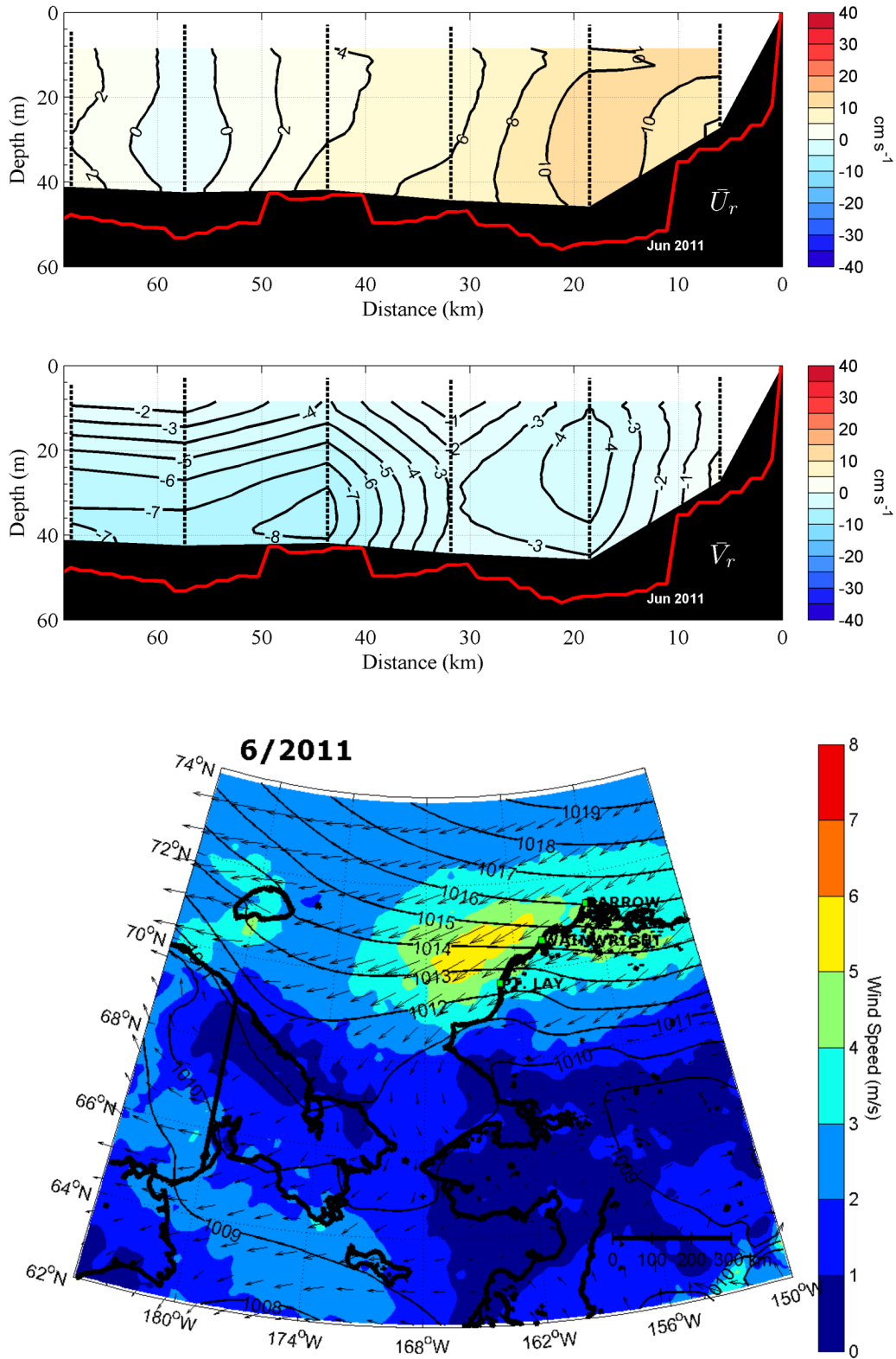


Figure 32. Vertical sections of the along-shore (upper panel top) and cross-shore (upper panel bottom) velocities for June 2011. Mean winds (lower panel) over the mooring array were 5.0 m s^{-1} towards 247°T .

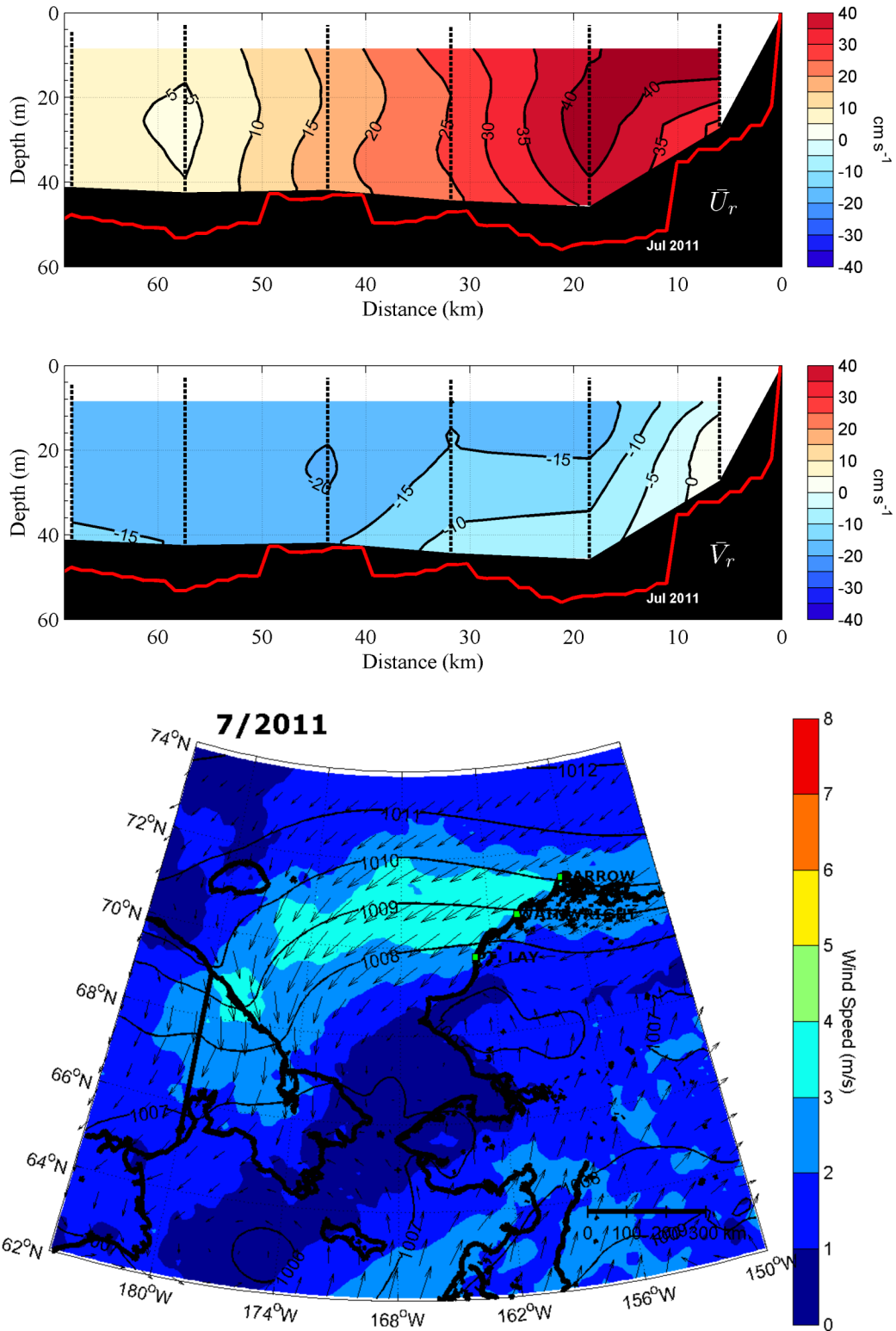


Figure 33. Vertical sections of the along-shore (upper panel top) and cross-shore (upper panel bottom) velocities for July 2011. Mean winds (lower panel) over the mooring array were 3.8 m s^{-1} towards 245°T .

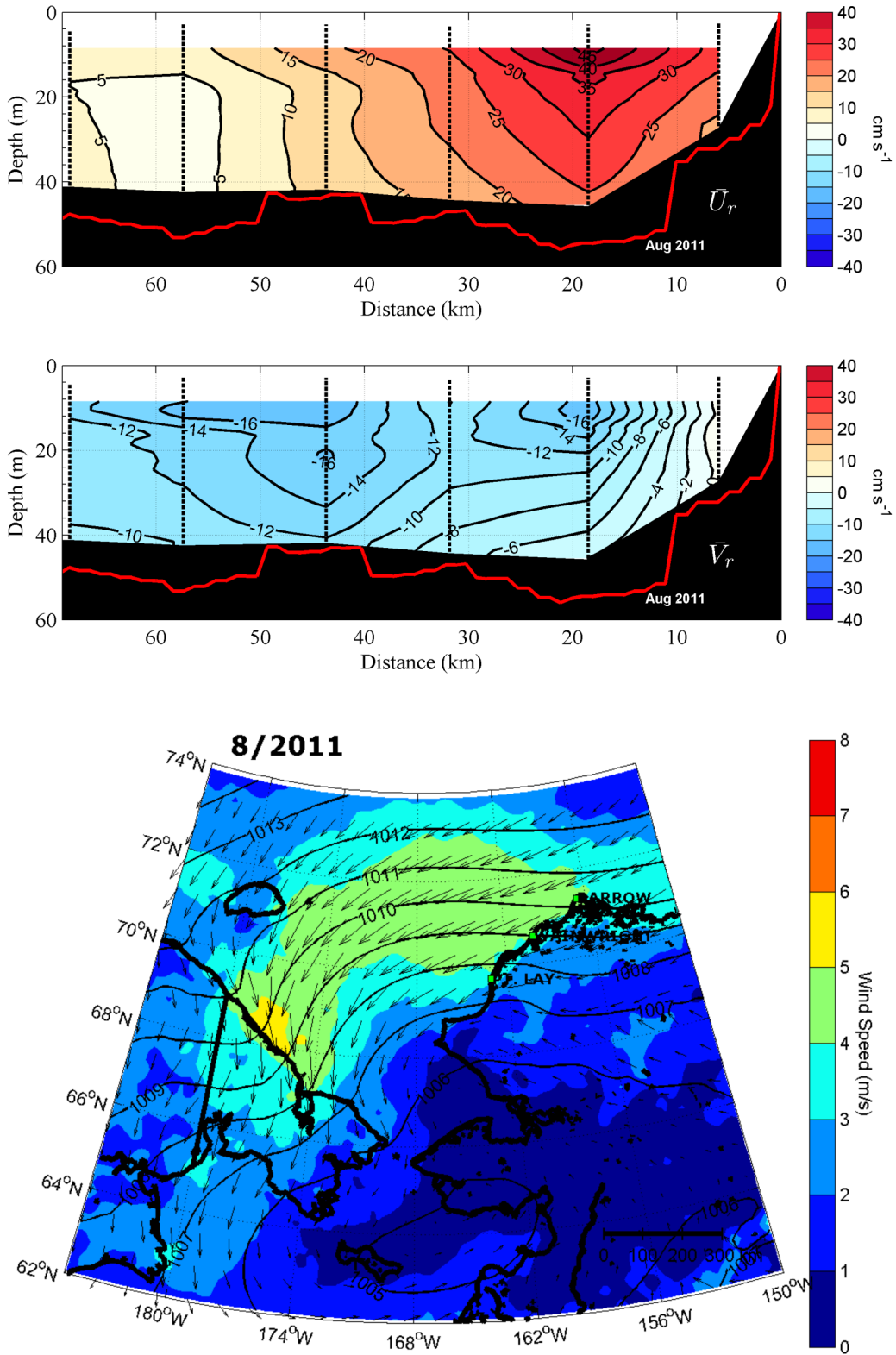


Figure 34. Vertical sections of the along-shore (upper panel top) and cross-shore (upper panel bottom) velocities for August 1 – 26, 2011. Mean winds (lower panel) over the mooring array were 2.9 m s^{-1} towards 262°T .

along-shore current was still centered at BC2, but the region of maximum cross-shore convergence occurs offshore of the jet, rather than inshore.

The upcanyon months in which the velocity structure was similar to the upcanyon mean are October and December of 2010 and April 2011. Note again that the jet is centered at BC2 in each case, and that it is more highly sheared in the vertical than in the downcanyon cases. In December 2010 and April 2011, the jet is very symmetrical, whereas in October 2010, the jet is slightly asymmetrical with maximum horizontal shear on its offshore side. In each of these cases, the region of maximum cross-shore divergence is between BC1 and BC2, whereas there is weak convergence on the offshore side of the jet center.

November 2010 is unique among months insofar as its velocity structure consists of a mix between the down- and upcanyon cases. Above ~ 20 m depth the structure is similar to the upcanyon case. At these depths a symmetrical jet is centered at BC2 and includes a large vertical shear; the along-canyon velocity varies from ~ -60 cm s⁻¹ (i.e., upcanyon) at ~ 10 m depth to $\sim +10$ cm s⁻¹ (downcanyon) at 20 m. Offshore of the jet, the surface flow consists of a narrow band of weak downcanyon flow at BC3, while seaward of this mooring the flow is upcanyon and increases to a maximum of ~ 20 cm s⁻¹ by BC6. The cross-shore flow above 20 m is offshore and strongly sheared in the vertical, divergent between BC1 and BC2, convergent between BC2 and BC3, and divergent beyond BC3. Below 20 m, the flow is downcanyon, and there is no jet structure because the horizontal (and vertical) shears are weak. Moreover, the downcanyon flow is sluggish with speeds being < 10 cm s⁻¹. Below 15 m the cross-shore flow is onshore everywhere, has little vertical shear, and is weakly convergent.

A remarkable feature that emerges from our classification scheme is that the velocity sections appear to have little relation to the local winds. The sole exception is October 2010, when strong and persistent northeasterly winds blew over the mooring array, which led to upcanyon flow. However, winds over the northeast Chukchi Sea in December 2010 and April 2011 (both upcanyon months) were weaker than those in June, July, and August 2011 when the downcanyon flow structure held. It appears, at least on a monthly average, that upcanyon flow was associated with stronger northerly winds over the southern Chukchi Sea and Bering Strait than over the northeastern Chukchi shelf. In contrast, in all downcanyon months the winds over Bering Strait were weak, regardless of the magnitude of the winds over the northeast shelf.

4.3.2. Barrow Canyon Transport

Transports entering Barrow Canyon were calculated by projecting the velocity components along 56°T (the along- and cross-shore coordinate system) and then multiplying the vertically-averaged velocity by the area representative of each mooring, as indicated in Figure 35.

Mean daily transports and winds are shown in Figure 36. The wind time series are from Barrow and projected along 20°T , chosen because this wind component yielded the best correlation with the transport. The record-length mean transport is ~ 0.3 Sv, and the 95% confidence limits on the mean are ± 0.15 Sv. Transport variability is large; the standard deviation is ~ 0.6 Sv, and transports range between ± 1.6 Sv. Compared to other months, transport variability is greater from October through April. Note that transports can vary rapidly over the course of a few days.

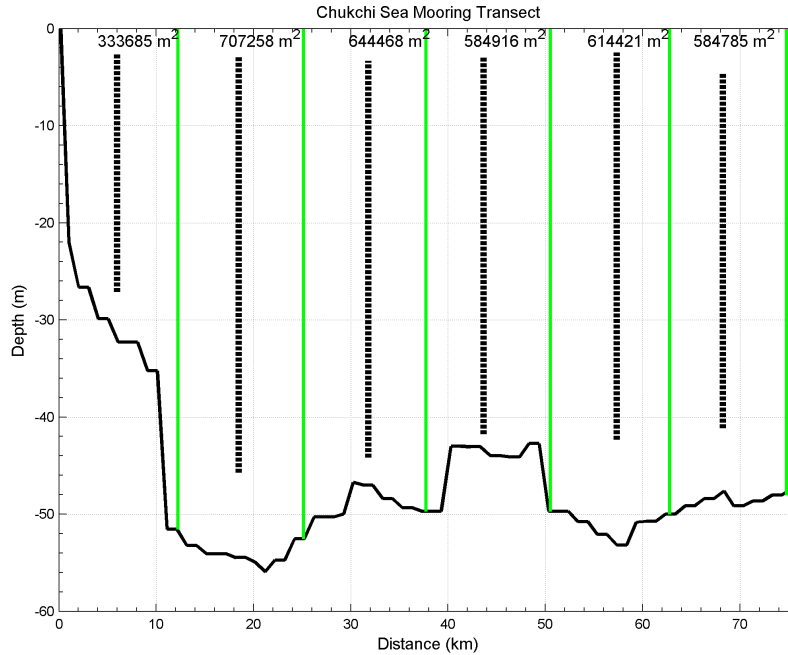


Figure 35. The cross-sectional areas (defined by green lines) used for each mooring (black dotted lines) to compute the along-canyon transport. The nearshore mooring, BC1, is on the left-hand side and mooring BC6 is on the right-hand side of the figure.

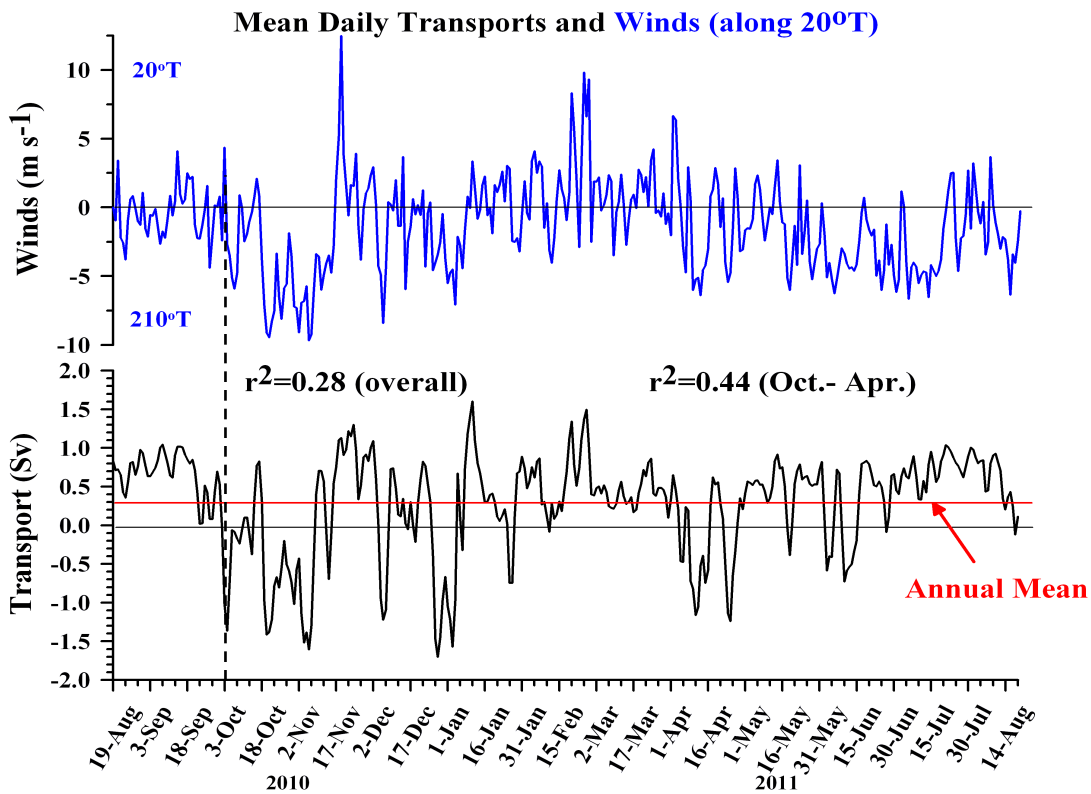


Figure 36. Mean daily winds projected along 20°T (top; blue) and mean daily transport (bottom; black). Positive (negative) values of transport are toward 56°T (236°T). The dashed, vertical line denotes the October 2, 2010, upcanyon event discussed in the text.

Indeed, the record-length minimum occurred on December 27, 2010, while the maximum transport occurred on January 6, 2011.

Overall transport variations are significantly correlated with the Barrow winds, projected onto an axis oriented along 20°T. (This projection yielded the best correlation, although a number of other projections were tried.) The correlation ($r^2 \sim 0.28$) explains only 28% of the variance over the entire year and so not especially strong. However, the correlation is much stronger for the October - April period ($r^2 \sim 0.44$) than for the entire year. We have also examined the wind-current relationship using the NARR winds, and the results were similar insofar as the strongest correlations are between winds projected along 20°T with the along-canyon transport lagging the winds by 9 hours. We explored seasonal variations in the wind-current relationship by dividing the time series into three different periods:

- a) ice-free: August – October 2010,
- b) strong winds and ice-covered: October 2010 – April 2011,
- c) weak winds and ice-retreating, May – August 2011.

The results, listed in Table 11, indicate that the wind-current relationship varies through time. In all cases, the mean wind projected along 20°T is <0 indicating that the transport opposes the winds. Furthermore, the y -intercept is always >0 , implying a net downcanyon transport in the absence of wind-forcing.

The coherence-squared spectrum (Figure 37) indicates that the wind-transport relationship varies with the frequency of the wind-forcing. For example $\sim 70\%$ of the transport variability is coherent with the winds at periods between 12 and 20 days. However, the coherence-squared decreases at longer periods and is variable, although generally <0.4 for periods <10 days.

Table 11. Wind-transport regression results.

Time Period	y -intercept (Sv)	Slope Sv/(m s ⁻¹) ⁻¹	r^2
8/18/10 – 8/20/11	0.5	0.13	0.32
8/18/10 – 10/31/10	0.6	0.14	0.45
11/1/10 – 4/32/11	0.3	0.22	0.49
5/1/11 – 8/20/11	0.7	0.07	0.24

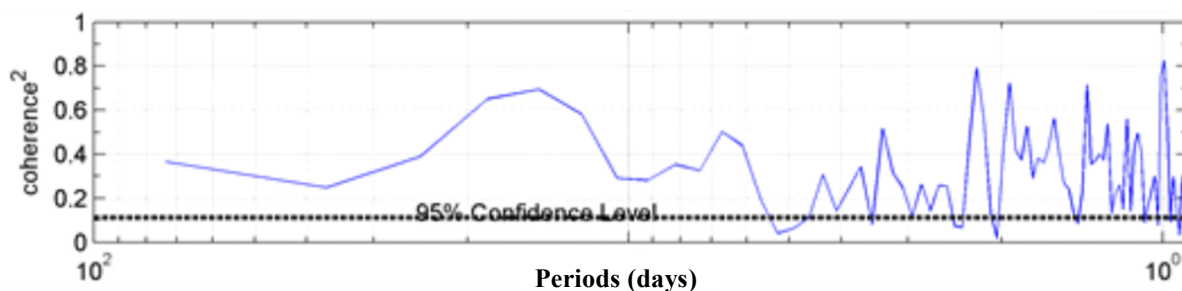


Figure 37. Wind-transport coherence-squared spectrum.

There are several plausible reasons why the wind-current transport relationship varies seasonally. One reason is that differences in the regional ice thickness distribution (concentration and thickness) and ice mobility will lead to differences in stress at the ice-ocean interface. This would result in the ocean responding differently to the same wind-forcing because of variations in ice cover characteristics. Another reason, discussed later with respect to the HFR data, may be related to variable upstream forcing over the northeast Chukchi shelf near the head of the canyon. A third reason was suggested in discussing the mean monthly velocity sections, where we indicated that the wind field over the northern Bering/southern Chukchi seas may affect the structure of the canyon transport.

In fact, a connection between transport variations and the southern Chukchi Sea/Bering Strait may also occur on shorter time scales. For example, note the upwelling event indicated by the dashed line in early October, 2010 (Figure 36). Upwelling began on October 2, before the winds over the northern Chukchi Sea began blowing from the northeast. However, strong northerly winds (not shown) developed over Bering Strait and the Gulf of Anadyr on September 30 and intensified through the early hours of October 3. These winds would have slowed the northward flow through Bering Strait or possibly even reversed it. The along-shore sea-level (pressure gradient) over the Chukchi shelf would have also diminished or reversed and induced upcanyon flow.

Such a scenario is suggested by the time series of demeaned sea level from the Red Dog dock (NOAA National Ocean Service) and the pressure gauge at BC1 (Figure 38). The sea level at Red Dog begins falling rapidly in the early hours of September 30th and reaches a minimum late on October 2nd. Thereafter, sea level at Red Dog begins to increase. The pressure record at BC1 (expressed as an equivalent in sea level change) begins to drop precipitately on September 30th and reaches its minimum about 5 hours after the Red Dog minimum. BC1 is ~500 km (measured along the coast) downstream (in the sense of Kelvin-wave propagation) from Red Dog. The time lag in the arrival of the minimum in sea level yields a phase speed $\sim 28 \text{ m s}^{-1}$. This speed is comparable to that of a long-wavelength ($>$ the Rossby radius of deformation = 140 km), topographic Rossby-wave, propagating northward along the coast from the southern Chukchi Sea. For such a wave the theoretical bottom slope is $\sim 4 \times 10^{-4}$, which is consistent with the bottom slope over much of the northeast Chukchi shelf.

We have also computed the coherency spectrum for sea level between Red Dog and BC1 and Red Dog and Prudhoe Bay (NOAA National Ocean Service; Figure 39). These show the signals are coherent over a broad frequency band, with sea-level being either in-phase at the longest periods or with sea level at Red Dog leading that at the other locations. These preliminary results suggest that remote forcing may be an important aspect of the circulation dynamics in the northeast Chukchi Sea, although additional analyses will be required to determine this conclusively.

Another reason why the wind-current correlation is variable through time may be related to non-linear processes associated with the flow field. Although the Ro is small on average, time series of $\partial u / f \partial y$ (Figure 40) indicate that the magnitude of this term within the ACC often varies between 0.1 and 0.2 and occasionally approaches 0.3. The time series of $\partial u / f \partial y$ were computed

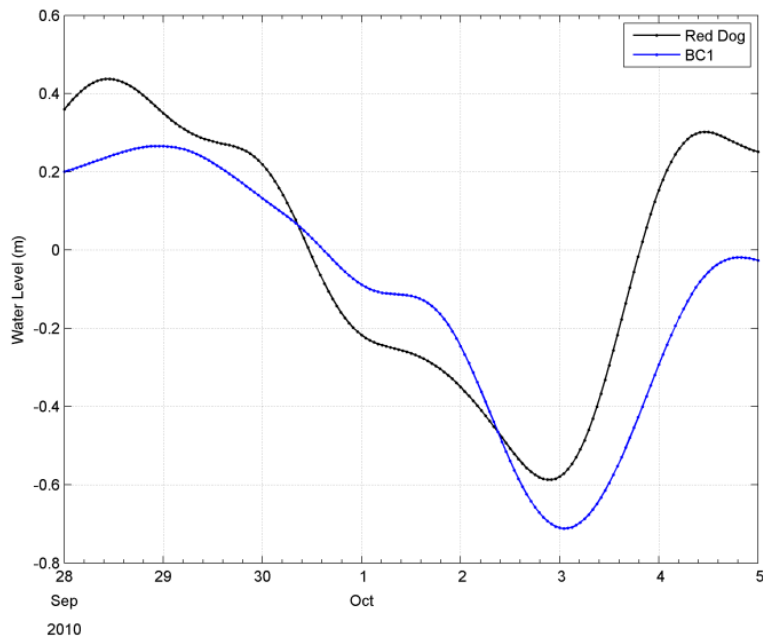


Figure 38. Demeaned records of sea-level from Red Dog (black) and from the pressure gauge at mooring BC1 (blue) for the period of Sept. 28 – Oct. 5, 2010.

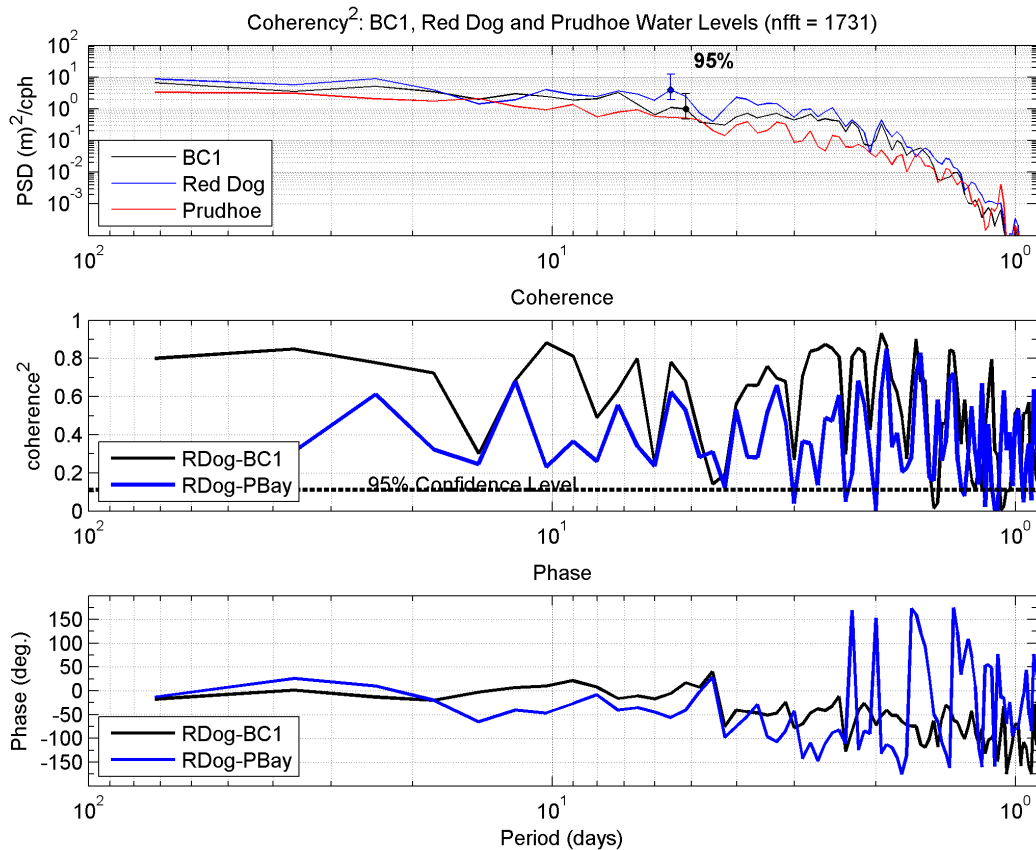


Figure 39. Sea level autospectra (top) at BC1 (black), Red Dog (blue), and Prudhoe Bay (red), and coherence (middle) and phase (bottom) spectra between Red Dog and BC1 (black) and Red Dog and Prudhoe Bay (blue).

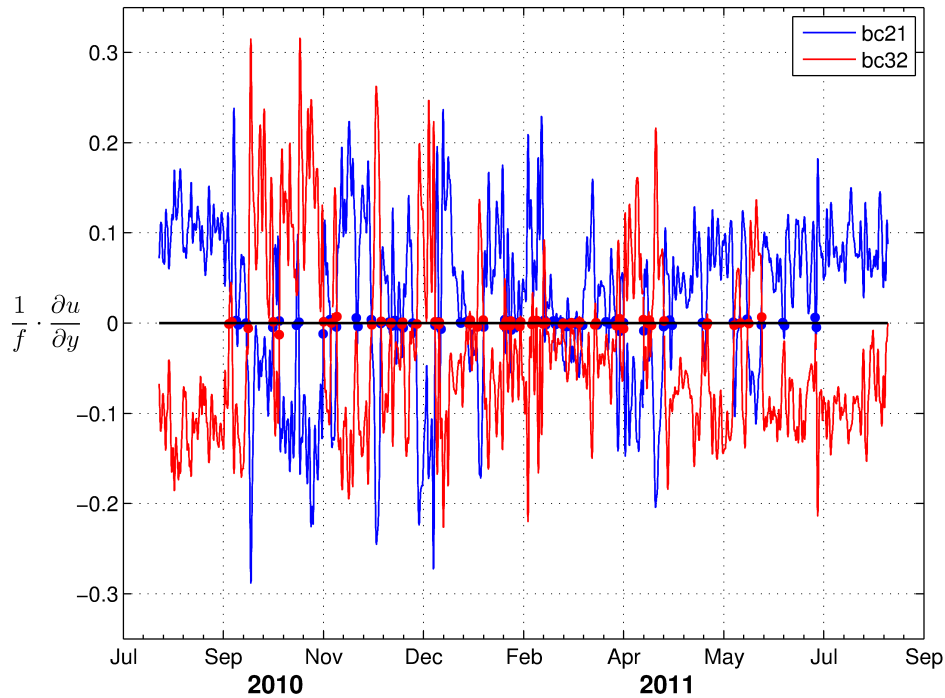


Figure 40. Time series of $\frac{\partial u}{f \partial y}$, the Rossby number computed from moorings BC1 – BC2 (blue) and BC2 – BC3 (red) at 26 m depth.

at 26 m depth between moorings BC1 and BC2 and BC2 and BC3. The magnitude of Ro is largest in fall and winter, however even in summer its value is often ~ 0.1 .

In Figure 41, we compare the mean monthly Barrow Canyon transport for the 2010-2011 record with the mean monthly Bering Strait transport climatology of *Woodgate et al.* [2005]. The climatological record (based on ~ 15 years of data) from the Strait indicates mean northward transport in all months with an annual average of ~ 0.8 Sv. The Strait transport undergoes a distinct annual cycle with maximal transport in June (1.3 Sv) and minimal transport in January (0.4 Sv). Although, as noted by *Woodgate et al.* [2005], there is large interannual variability in the monthly transports through Bering Strait. The Barrow Canyon record shows no distinct annual cycle, although this may reflect the small sample size (1 year) presently available. As additional data becomes available in the future, we may be able to discern a distinct annual cycle in the transport through Barrow Canyon. In this regard, moorings BC1 – BC6 were redeployed in their same locations in August 2011 and were recovered in the summer of 2012. That record will afford comparison with the 2010 - 2011 data set and upon completion of analysis will be submitted as a supplement to this report.

The vertically averaged along-shore transport measured at BC2 is statistically significant with the total transport across the BC1 – BC6 section (Figure 42). Although this relationship will be reassessed using the 2011 – 2012 mooring data, the strong linear relationship between BC2 and transport across the array should allow efficient monitoring of the transport at the head of the canyon using only one mooring. We intend to continue sampling at mooring BC2 for the next

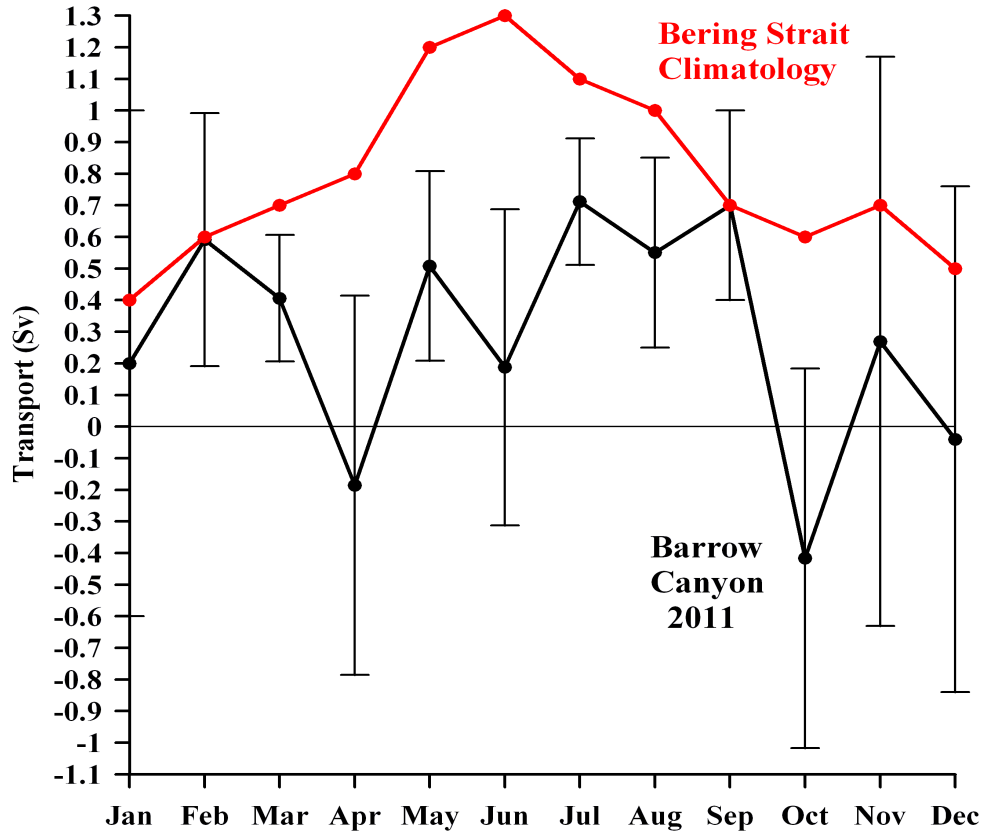


Figure 41. Mean monthly transports from Bering Strait climatology (red) and the 2010-2011 mooring record in Barrow Canyon (black).

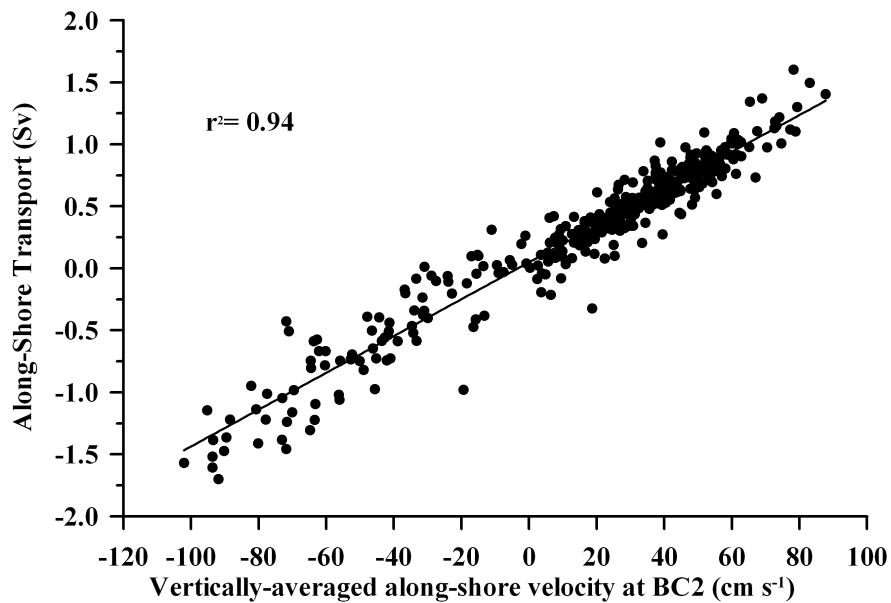


Figure 42. Scatterplot of Barrow Canyon transport versus vertically averaged currents at mooring BC2.

several years in order to establish a transport climatology in Barrow Canyon and to develop a better understanding of the circulation connections between the flow at the head of Barrow Canyon and the circulation elsewhere on the shelf and slope. These other regions will be measured from moorings being deployed in the near future by industry, the NSF, and BOEM.

4.3.3. Moored Temperatures and Salinities

We begin the discussion of water properties observed at the moorings with the aid of temperature/salinity (T/S) diagrams (scatterplots) constructed for each mooring (Figure 43). The T/S scatterplots illustrate four major water masses. The first consists of points distributed along a limb that protrudes toward warm, low-salinity (red ellipse) waters. These are summer waters that have flowed northward from Bering Strait within the Alaskan Coastal Current. The second water mass has high-salinities (>34) and temperatures between -1°C and 0°C (blue ellipse). These waters originated from within the Atlantic Layer at about 200 m depth along the Chukchi-Beaufort continental slope and were transported onto the shelf during upcanyon events. The third prominent water mass consists of points that fall along the freezing point curve (green ellipse). These waters are formed on the Chukchi and/or Bering Sea shelves in winter as a result of cooling and freezing. They encompass a broad salinity range ($\sim 31.8 - 34.8$, with both extrema occurring at BC1). The highest salinities reflect brine expulsion from sea-ice formation in coastal polynyas in winter 2011. Satellite images from the winter of 2011 suggest that narrow ($\sim 10 - 30$ km wide) polynyas formed intermittently along the coast between Cape Lisburne and Barrow. The fourth water mass (yellow ellipse) has temperatures between $0^{\circ}\text{C} - 2^{\circ}\text{C}$ and salinities between 32.5 to 33. This is probably Bering Sea Water, which is colder and saltier than Alaskan Coastal Water. The Bering Sea Water mass probably originated from the Central Channel, then flowed eastward across the Chukchi shelf before entering Barrow Canyon. Note that these waters were observed only at moorings BC2 – BC5. Finally, the scatterplots indicate that the range in T/S properties systematically decreases from inshore (BC1) to offshore (BC6). In fact, moorings BC5 and BC6 show very little signature of the summer waters found at the other moorings.

Temperature and salinity time series (Figures 44 – 46) illustrate the major seasonal changes in these variables. Temperatures were a maximum at all moorings in September (with the largest maximum of $\sim 9^{\circ}\text{C}$ at BC1) and decreased to the freezing point by mid-November. They remain at this level through most of the winter, with the prominent exception of the abrupt increase from -1.8°C to $\sim 0^{\circ}\text{C}$ from late December through early January, when slope waters upwelled into the canyon. Temperatures increased in mid-May and were $\sim 1^{\circ}\text{C}$ by early July. They then decreased in early August, then abruptly increased, and finally decreased again to the end of the record. Salinities exhibited a more complicated seasonal evolution, although in general, increased from fall through winter and then decreased through summer. Sprinkled throughout the October through April portion of the record are large (1 – 1.5) salinity variations, over time-scales of a few days to a few weeks. For example, there are several events in October and November as well as in the late December through early January period when moderately warm, but salty slope waters washed across the array. Each of these events was coherent across the array. There are other salinity excursions that are limited to only a portion of the array however. For example, in late February temperatures remained at the freezing point while salinities began to increase across the array. By March, the salinities decreased at all moorings except BC1. Here salinities

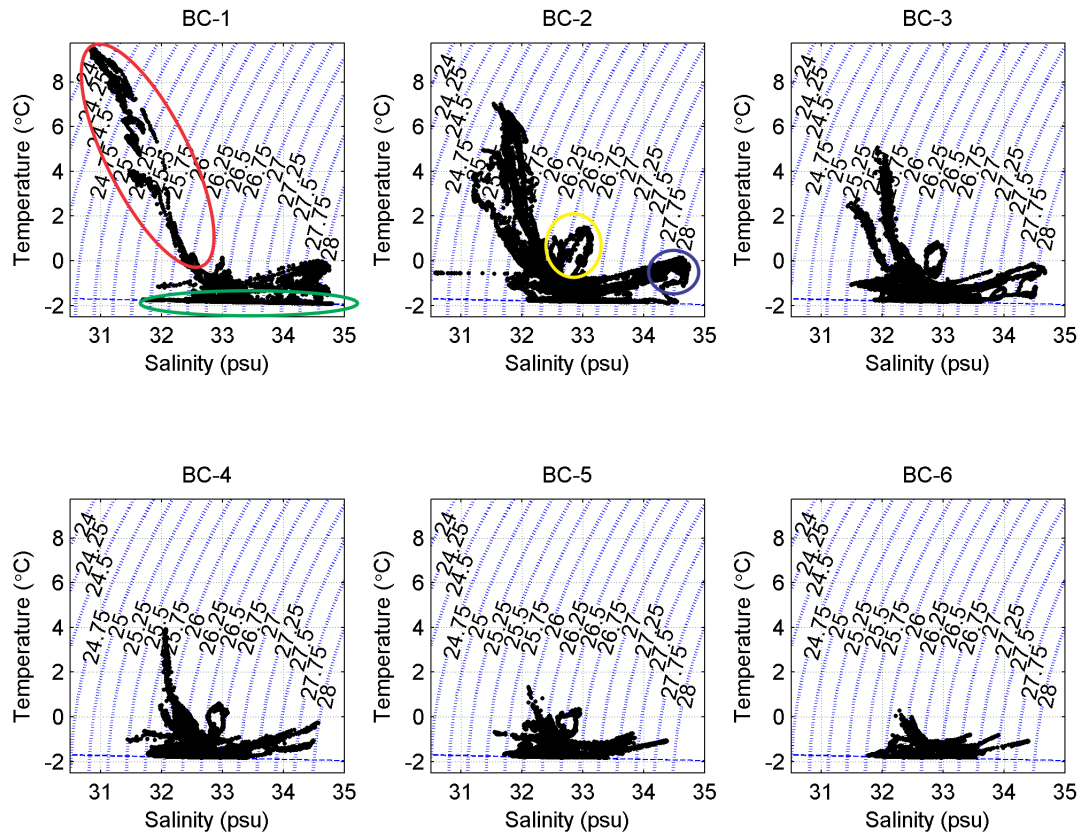


Figure 43. T/S diagrams constructed from each mooring. Ellipses in BC1 encompass T/S properties of summer water (red) and winter-formed dense waters (green). Ellipses in BC2 encompass waters drawn from the Atlantic Layer along the Chukchi-Beaufort continental slope (blue) and Bering Sea Water (yellow). The dashed blue line in each plot indicates the freezing point curve.

remained at about 33.5 and then increased to >34 by early April before diminishing. Salinities also increased again at BC2 for a 2-week period in March before decreasing. These high-salinity waters (all at the freezing point) were probably brine product formed in polynyas. The cold, high-salinity water masses were mainly confined to BC1 and BC2 indicating that there was little cross-shore flux of dense water at this location. Hence, the brines were trapped close to the coast as they were transported toward the canyon.

A more detailed examination of the temporal variations in temperature and salinity in relation to up- and downcanyon flow is provided in Figure 47. In August – September 2010, the flow was persistently downcanyon and transported warm, fresh waters. Beginning in October temperatures decreased to the near-freezing point. From this point until mid-January, the flow was more variable and included episodes of up- and downcanyon flow. The upcanyon events were occasionally accompanied by high-salinity intrusions (denoted by yellow bars), signifying slope waters that were upwelled to the head of the canyon. From mid-January through early April, the flow was downcanyon and carried cold, salty winter waters into the canyon. Although salinity varied throughout this portion of the record, temperatures were at the freezing point. Several pulses of high-salinity water (late February and late March) suggest brine-enhanced waters

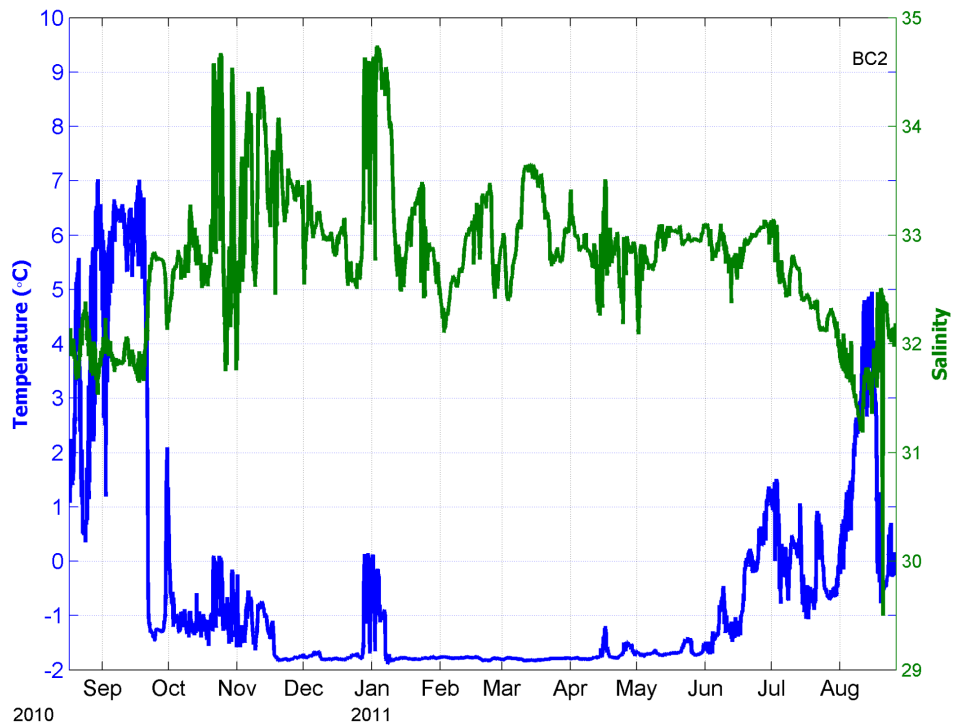


Figure 44. Time series of temperature (blue) and salinity (green) at moorings BC1 (top) and BC2 (bottom).

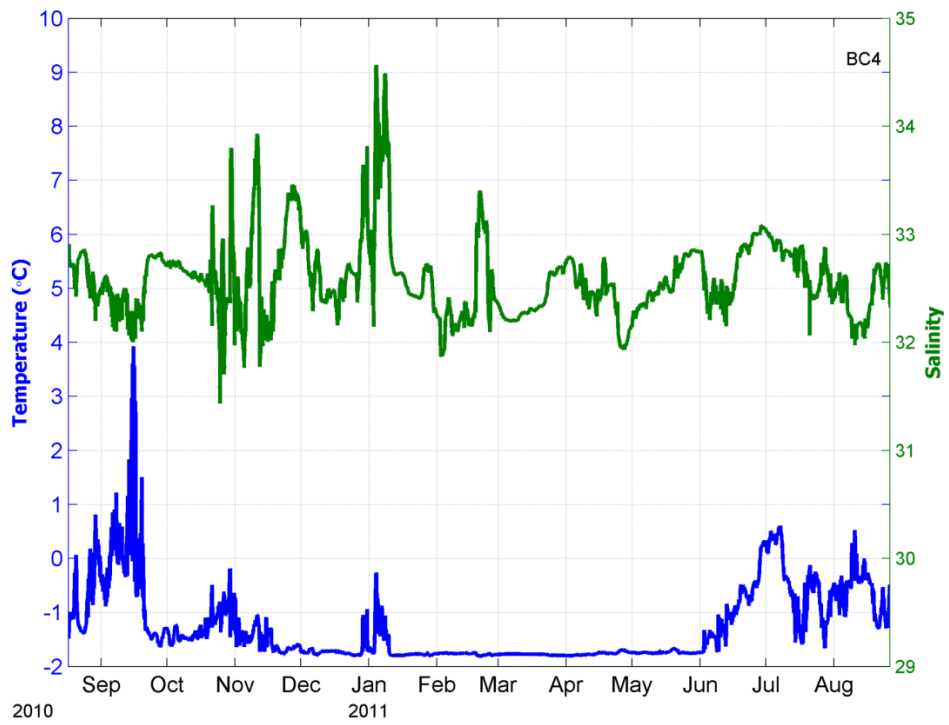
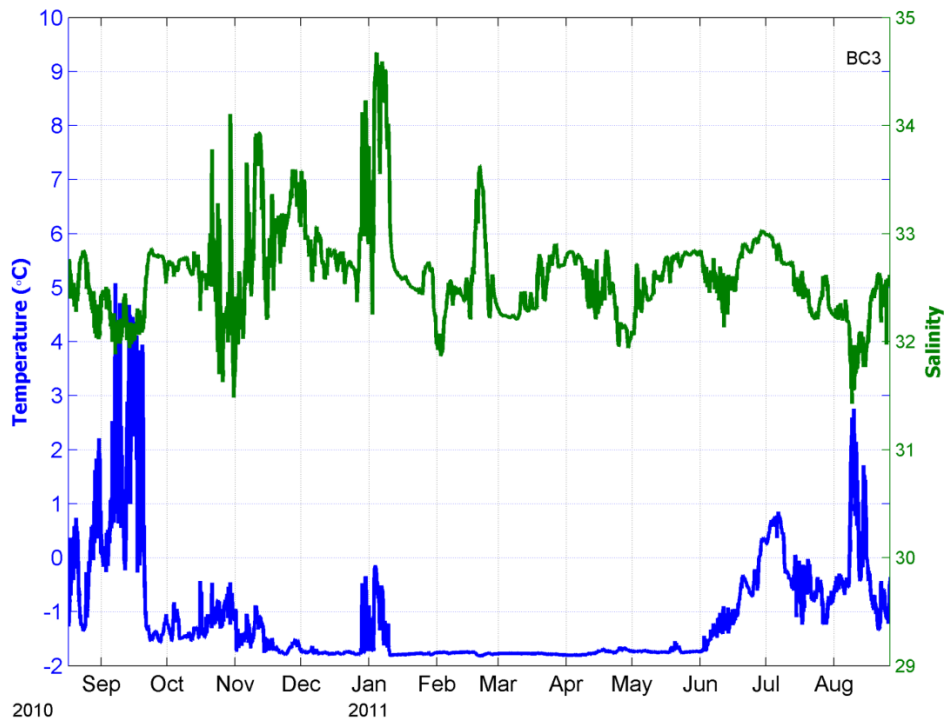


Figure 45. Time series of temperature (blue) and salinity (green) at moorings BC3 (top) and BC4 (bottom).

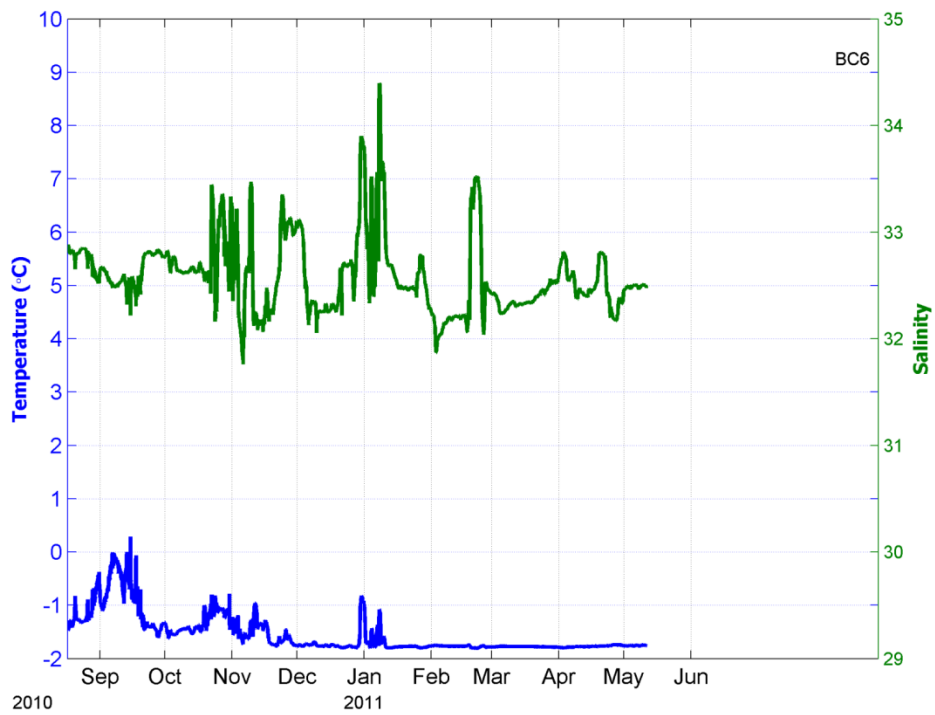
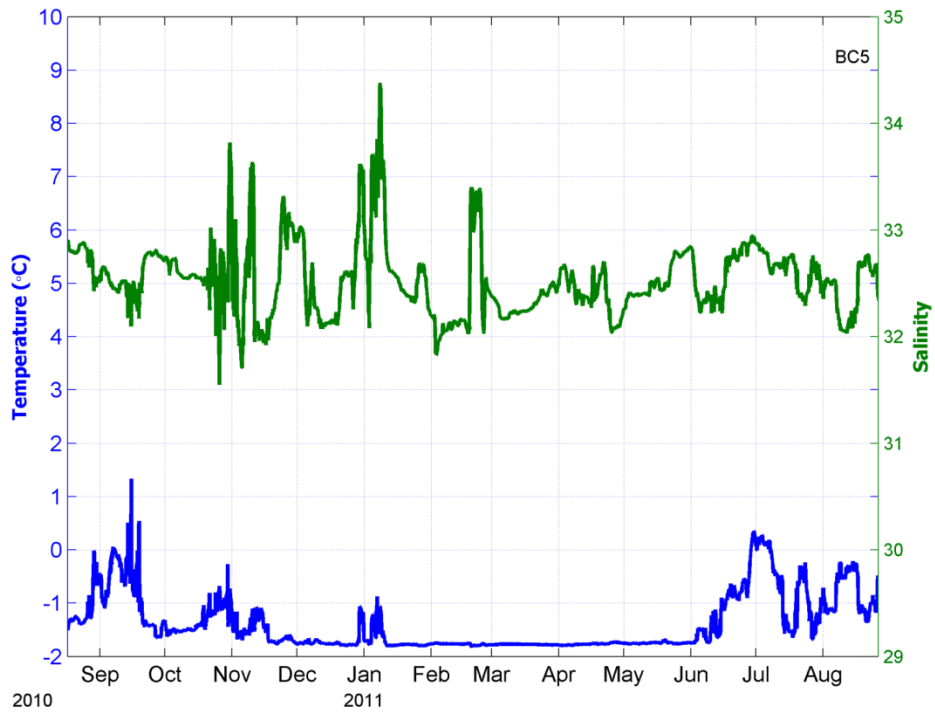


Figure 46. Time series of temperature (blue) and salinity (green) at moorings BC5 (top) and BC6 (bottom).

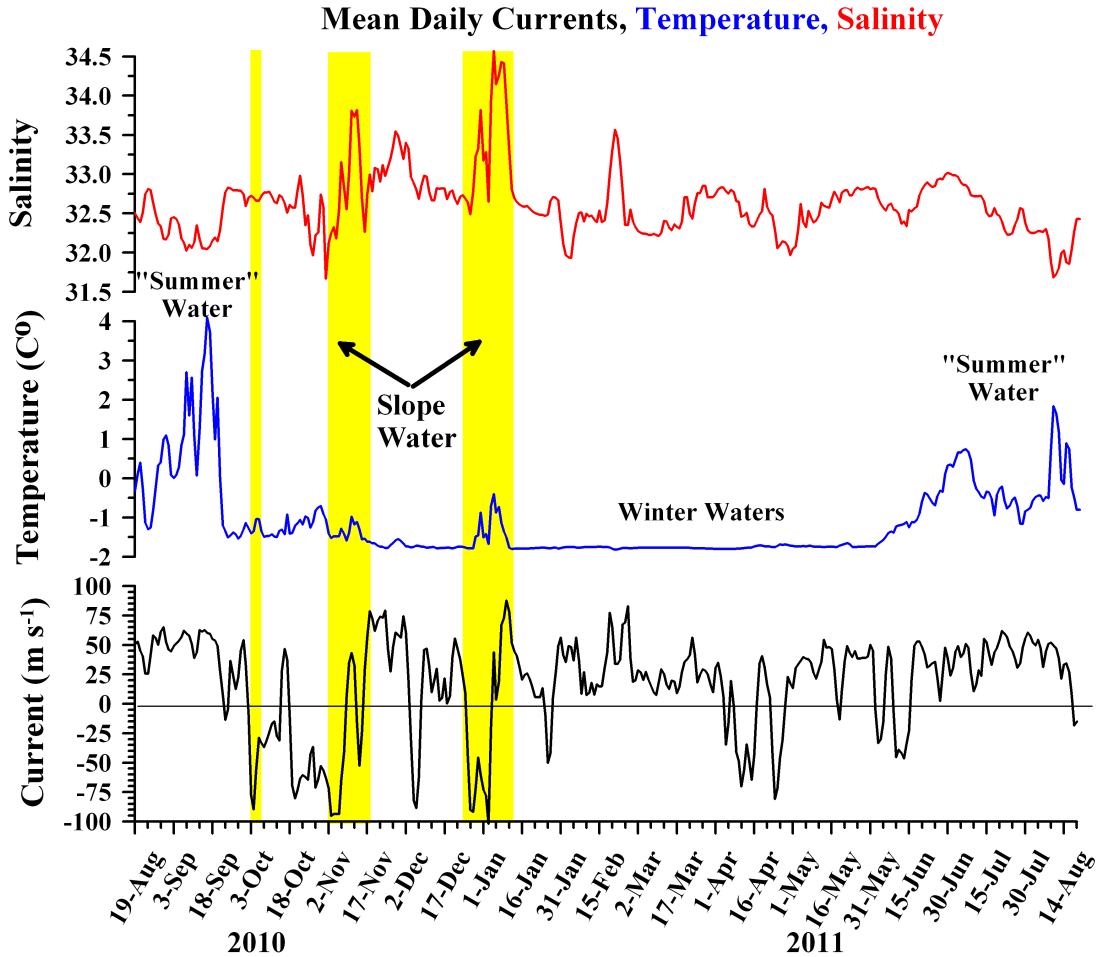


Figure 47. Mean daily salinity (top), temperature (middle), and along-shore currents (bottom) from mooring BC2.

formed in polynyas. Although the flow was upcanyon in April, there was no accompanying signature of slope water. By the end of April, downcanyon flow resumed and remained rather steady through the end of the record. This flow carried winter waters into the canyon until late May, when newly-arrived Bering Sea summer waters were transported into the canyon. We note that not all upcanyon events involve the same water masses. For example, slope waters were transported upcanyon during the November and December events, but were absent in the October and April episodes. These differences may be due to a variety of factors, including variations in stratification over the slope, spatial variations in surface stress due to geographic differences in ice mobility in winter, and/or preconditioning of the slope density field prior to the onset of canyon upwelling. By the latter, we mean that the pycnocline over the slope may be undergoing vertical fluctuations associated with prior wind events and/or the passage of shelf waves.

We also monitored pressure fluctuations to assess mooring diving. These indicate that the pressure variations were ≤ 2 dbars (~ 2 m), with the standard deviation being < 30 cm, so mooring diving due to swift currents was minimal.

4.4 Surface Currents

We begin this section with an outline of some of the performance issues and characteristics of the HFR portion of the field program. In section 4.4.1, we present a subset of the results by discussing the mean monthly surface velocity fields and mean monthly winds (based on the NARR BC6 grid point) for each full and/or partial month of operation. These provide a general descriptive overview of the spatial distribution of the circulation and its variability. It also provides a glimpse of the interannual variations based on the monthly means. Following this description we examine the mean surface current maps (for each open water season) as a function of the wind direction (section 4.4.2) to provide an indication of how the circulation varies with respect to the winds. In section 4.4.3, we show how the mean surface currents are distributed for the case when the ACC is flowing northeastward (downcanyon) and southwestward (upcanyon). Section 4.4.4, describes statistical aspects of the circulation including spatial correlation fields and wind-current correlations.

The HFR data reported herein are the first ever obtained from the northeast Chukchi Sea. HFR operating times indicate that each radar site was operational for more than 90% of each deployment period (Figure 48). Operational gaps were largely due to shutdowns in the village grid power system. On two occasions power surges blew fuses in the HFR electronics, which required servicing. Nevertheless, the systems worked extremely well given the remote locations in which they operated.

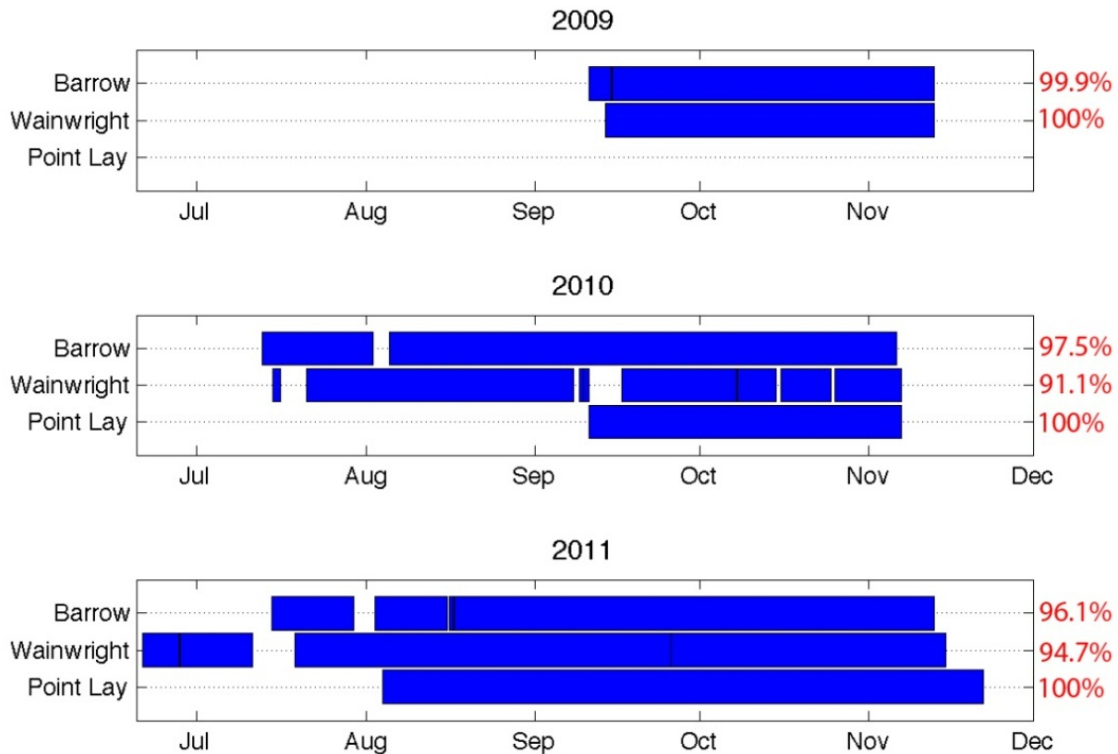


Figure 48. Timeline of HFR system runtime for each year and each field site. Red numbers represent the percentage of time each system was operational within each field season.

The nominal surface area coverage of the HFR systems is shown in Figure 49, in which we note three spatial gaps. Two of these were land shadows due to the presence of Icy Cape and Point Franklin that blocked transmission of the radar wave. These gaps were in the nearshore region between Wainwright and Icy Cape and between Barrow and Point Franklin. A third gap arose because the distance between the installations at Wainwright and Point Lay was too great to provide reliable overlapping coverage in the area noted. Each of the spatial gaps is a consequence of site selection, which was based solely on the necessity to have grid power access rather than chosen to be optimal from a sampling perspective.

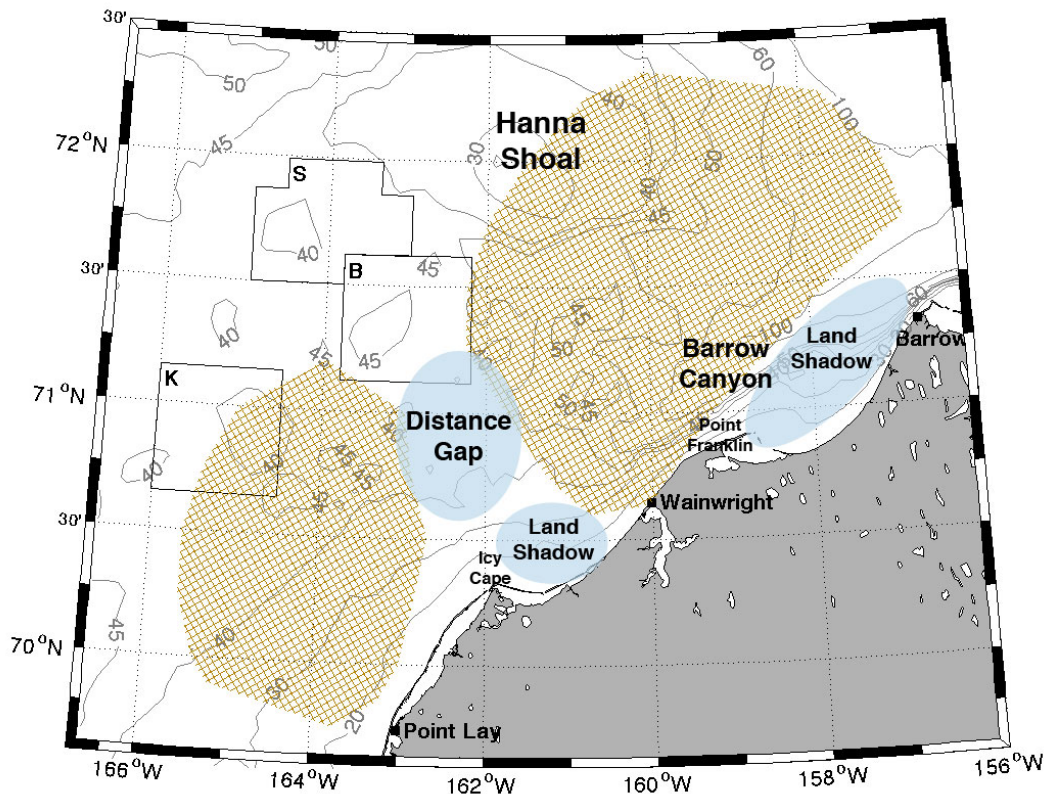


Figure 49. Map of HFR coverage (golden crosshatch) with gaps in spatial coverage defined.

There were also temporal gaps in coverage. Figure 50 maps the temporal coverage obtained in 2010 from all radars. Similar distributions were obtained in 2009 (from the Wainwright and Barrow radars only) and in 2011 (from all radars). Nightly ionospheric interference results in the radar wave being reflected from the ionosphere [Teague, 2001]. This interference reduced coverage for approximately seven hours each day, typically between 07:00 – 13:00 GMT (Figure 51). The interference was greater at the Barrow and Wainwright sites than at Point Lay for reasons not presently understood. Ionospheric interference effectively reduced data returns by ~30% and for this reason we analyzed data only from regions where the temporal coverage exceeded 50% of data returns.

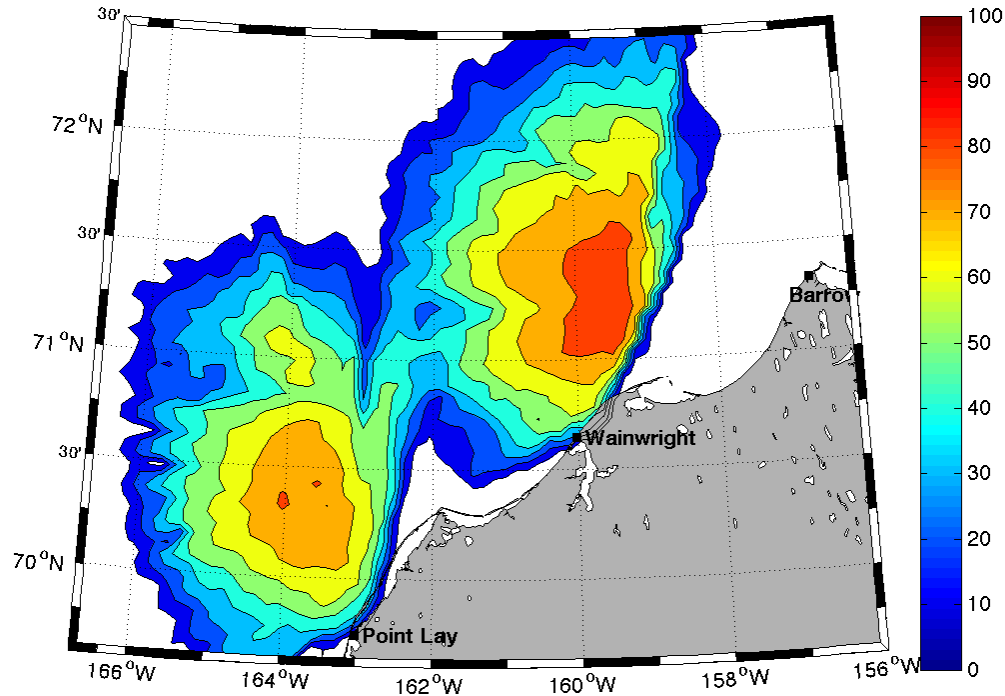


Figure 50. HFR percent coverage through time for 2010. Similar results were found for 2009 and 2011.

4.4.1 Comparison of Surface and Near-Surface Currents

We have compared the HFR data with corresponding data from moorings at a depth of 8 m below the surface. While our comparisons have been done for all moorings, we show two examples that bracket the range from best (BC2) to poorest (BC6) comparisons for the August – early November period in 2010. Time series of the u (east-west) and v (north-south) velocity components from each sensor are shown in Figure 52, and correlation plots are shown in Figure 53. In general, the u -components from both moorings and the HFR and the v -component at BC2 and the HFR agree quite well with one another ($r^2 \sim 0.8$). There is very poor agreement between the v -components at BC6. There may be several reasons for this discrepancy. First, the instruments are measuring over different spatial scales; ~ 9 km averaging for the HFR versus a point location at the moorings. Second, the u -component at BC6 has a much larger dynamic range than the v -component at the same location, e.g., the flow variability here is primarily in the east-west direction so the signal-to-noise ratio in the v -components is much smaller. Third, the HFR senses the Stokes' drift component that can be large on occasion (Figure 54). This velocity signal decays exponentially with depth and is virtually negligible at 8 m. The Stokes' drift was substantial in the latter half of October 2010 when large seas were propagating from the north (that would generate a southward Stokes' drift). At both BC2 and BC6, the largest discrepancies in the v -component occur over this period. Finally, stratification at BC6 is very strong (discussed below) and shallow (~ 12 m) suggesting that there may be large wind shear confined to the upper 10 m of the water column. Moreover, any inertial shear will be confined to depths within and below the pycnocline.

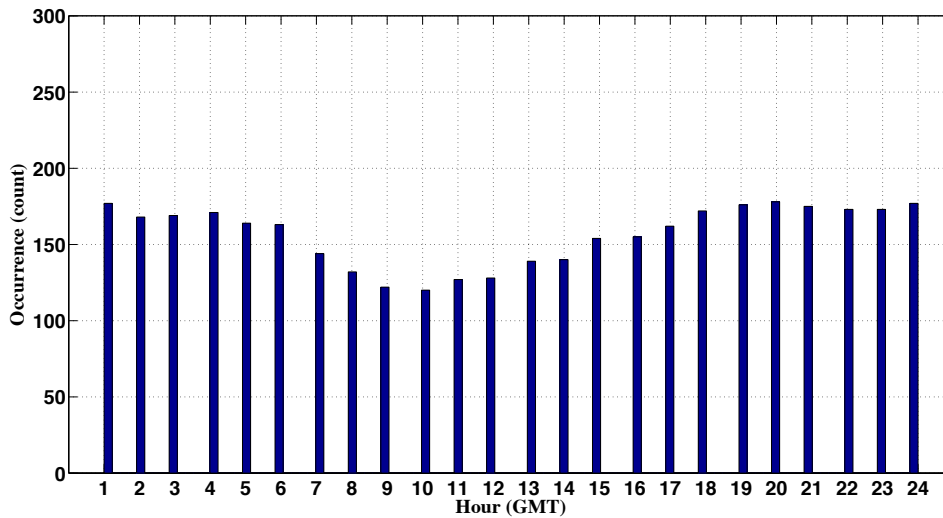
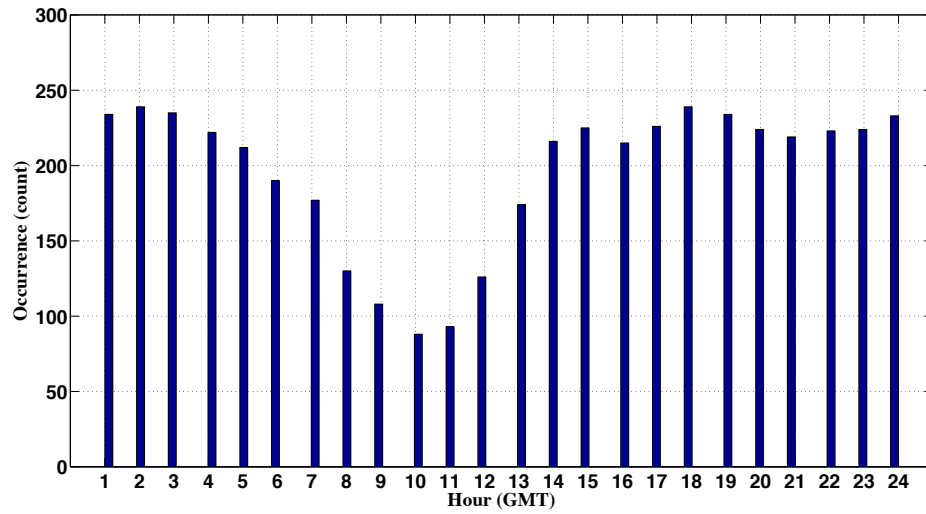
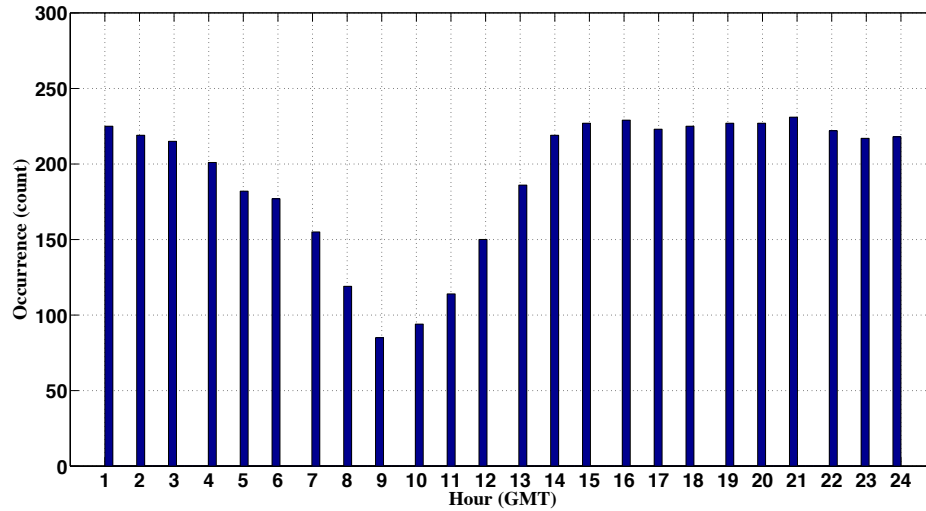


Figure 51. Average number of HFR data returns per hour of day for Barrow (top), Wainwright (middle), and Point Lay (bottom).

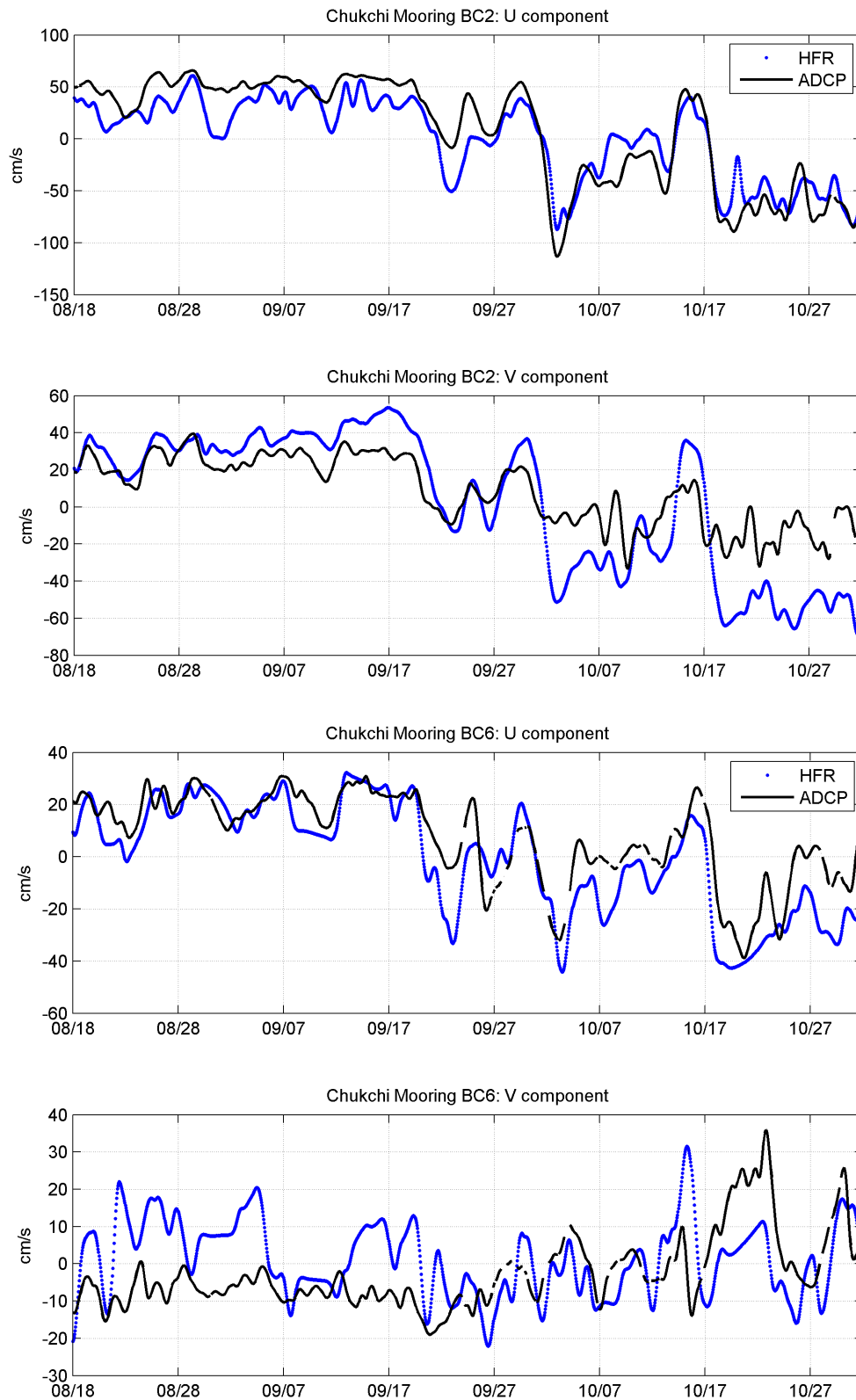


Figure 52. Time series of u and v -components for the HFR (blue) and ADCP (black) at BC2 (upper two panels) and BC6 (lower two panels). ADCP data were measured at 8 m.

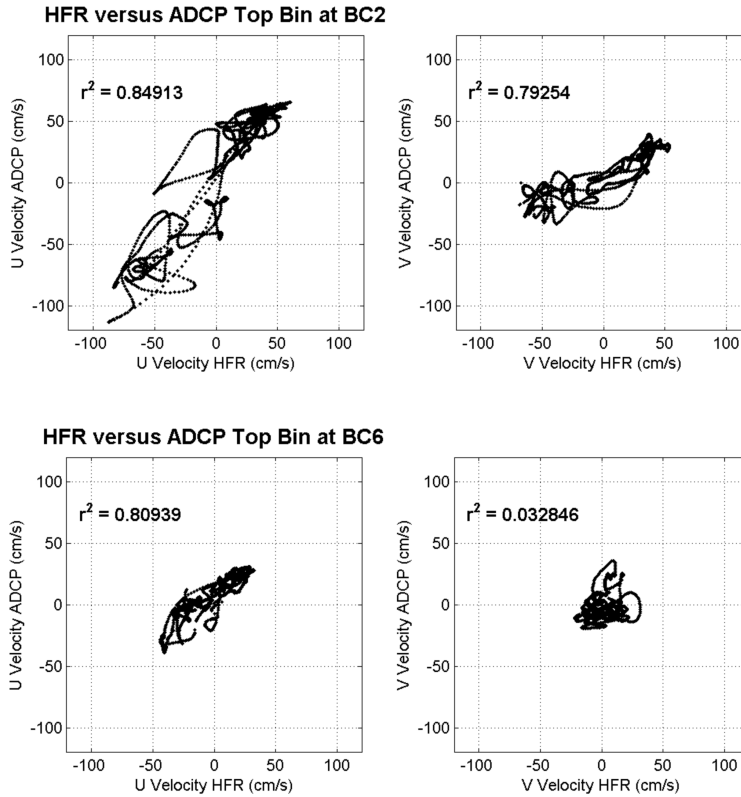


Figure 53. Scatterplots of u and v -components for the HFR and ADCP at BC2 (upper two panels) and BC6 (lower two panels).

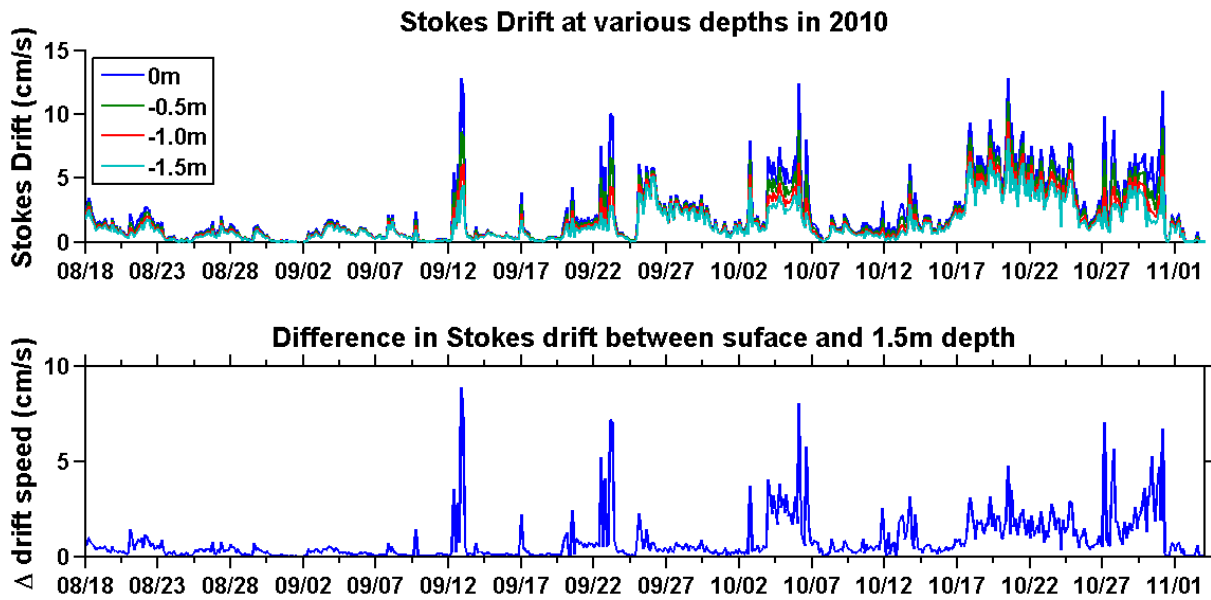


Figure 54. Time series of Stokes' drift based on H_S for the period of August 18 – November 1, 2010 (upper panel) and difference in the Stokes' drift between the surface and 1.5 m depth (bottom).

In principle the Stokes' drift can be removed from the HFR data if sufficient wave information is available. We have begun to explore this by comparing time series of H_s , predicted by the NOAA Wavewatch model, with the wave measurements at BC1 (Figure 55). Over most of the record the comparison is quite good. The largest discrepancies occur over the latter half of October, when the model underestimates the observed H_s by 1 - 2 m. The winds used in the Wavewatch model compare well with the NARR and coastal winds, so we doubt that the difference is due to wind speed. We speculate that the fetch used in the model depends upon the location of the ice edge. If this is overestimated it will result in a shorter fetch and a reduction in model-predicted H_s .

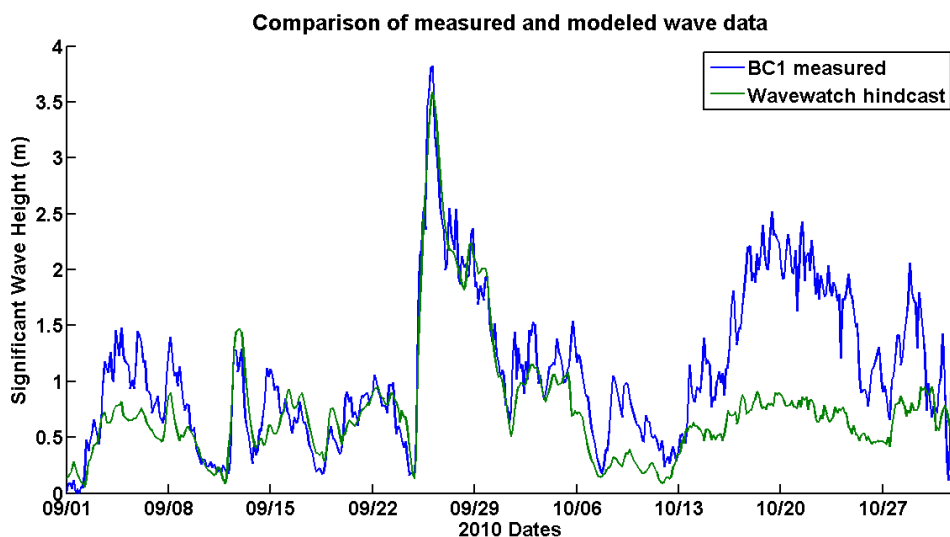


Figure 55. Comparison of H_s measured at BC1 (blue) and the Wavewatch model (green) from September 1 – November 2, 2010.

4.4.2 Monthly Velocity Fields: Means and Variances

We constructed mean monthly maps of the surface velocities and the principal axes of current variance at each grid point where data coverage exceeded 60%. These maps provide the basis for the following discussion. The mean wind vector (in the direction toward which the wind is blowing) and its axes of variance ellipse are also shown on each map. In all cases, the wind statistics (based on NARR) are computed only over the period of HFR operation for the month shown, hence, in some cases (September 2009, July 2010 and 2011, and November of all years), only the relevant portion of that month's wind data contribute to the figure.

In July of both 2010 and 2011 (Figures 56 and 57) the mean winds were northwestward, at $\sim 1.1 \text{ m s}^{-1}$ and 0.7 m s^{-1} , respectively, although the winds varied primarily along-shore, i.e., northeast-southwest. In both years, there was a strong northeastward-flowing surface current concentrated within 35 km of the coast with average velocities of $\sim 50 \text{ cm s}^{-1}$ in 2010 and $\sim 45 \text{ cm s}^{-1}$ in 2011. We will refer to this northeastward flow as the Alaskan Coastal Current (ACC). Farther offshore the currents were weaker at $\sim 10 - 20 \text{ cm s}^{-1}$. South of 71.5° N and offshore of the ACC, the flow tended to be more eastward and convergent upon the western side of Barrow Canyon. This was

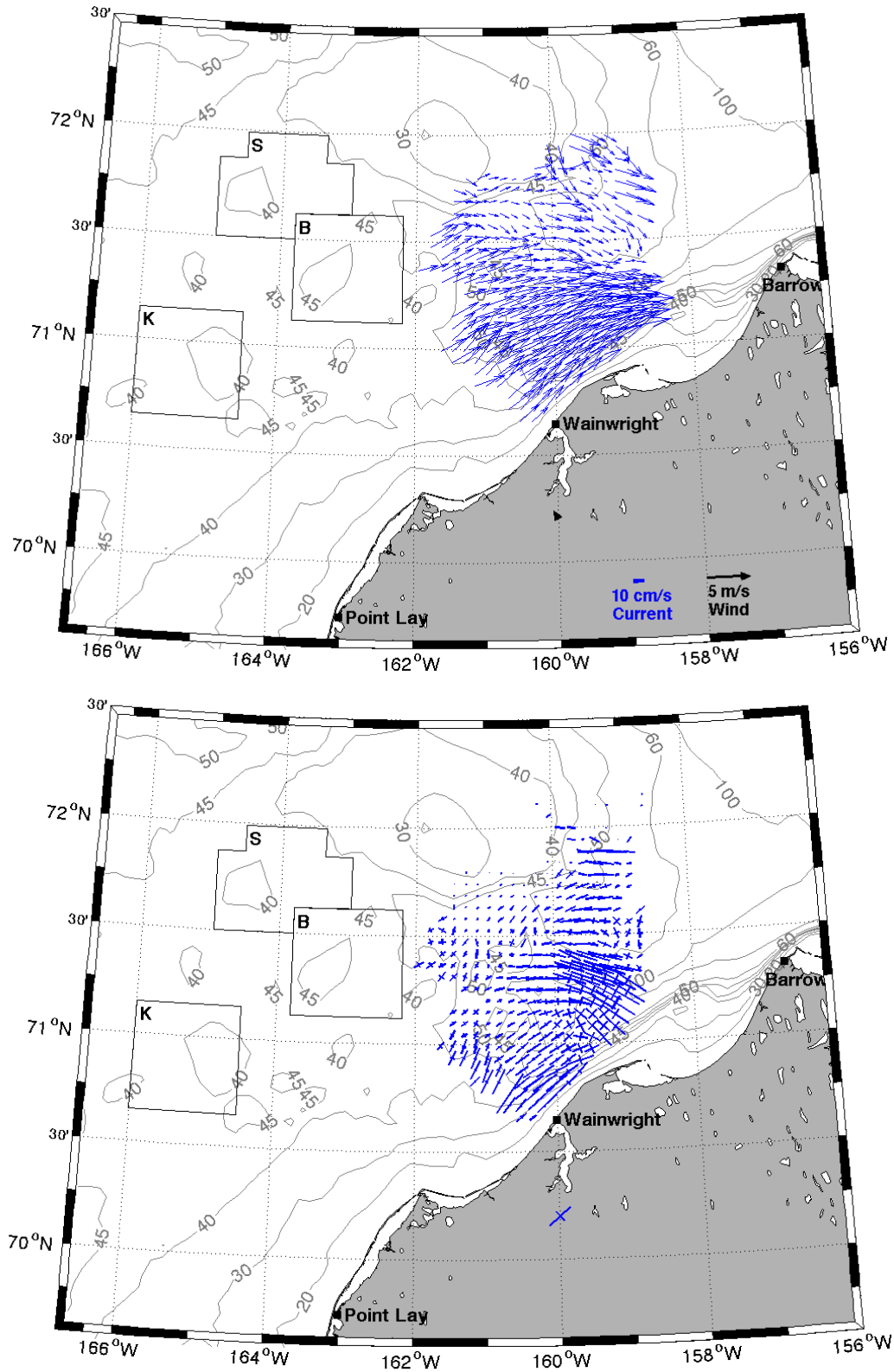


Figure 56. Mean surface currents (top) and principal axes (bottom) for July 2010. Mean wind and principal axes values are plotted within the land mask at 160°W for this and all subsequent figures.

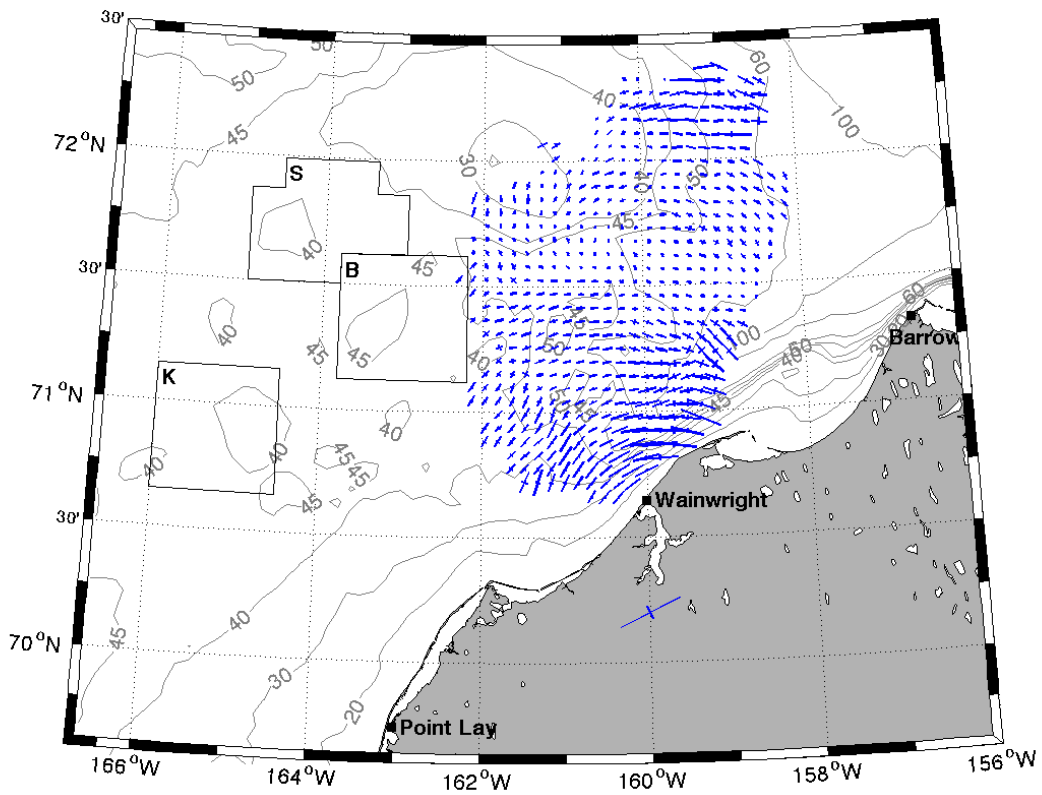
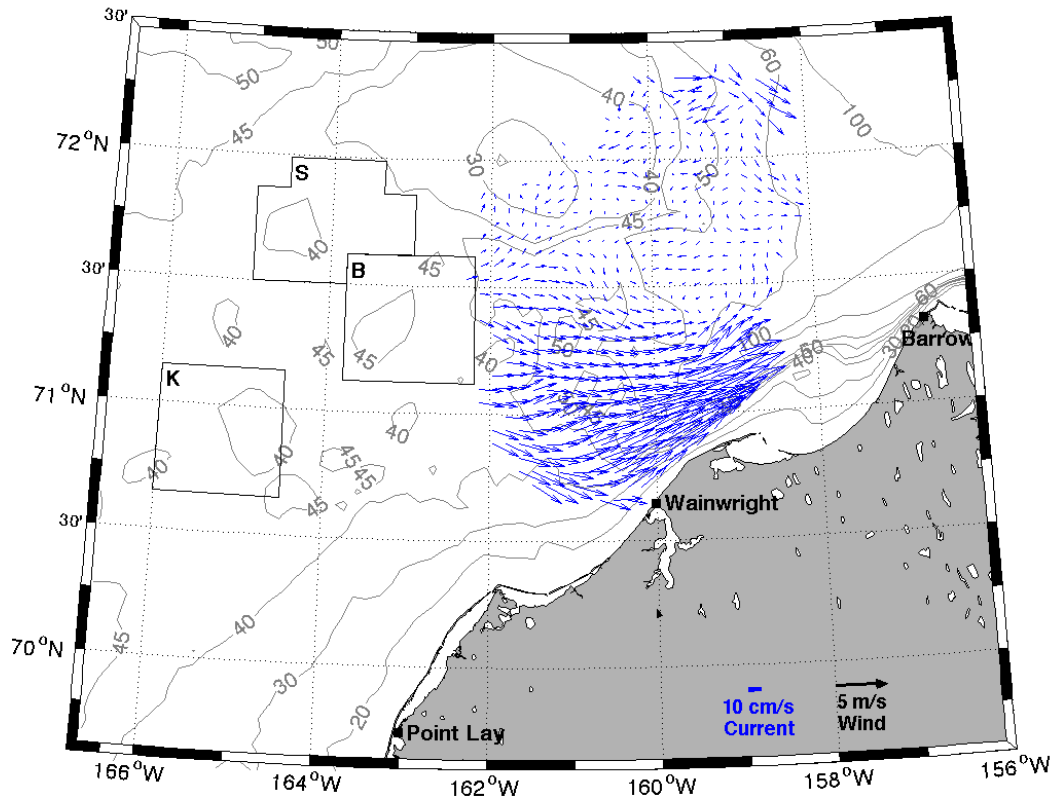


Figure 57. Mean surface currents (top) and principal axes (bottom) for July 2011.

particularly evident in 2010, but much less so in 2011. Within the ACC, the principal axes are aligned northeast-southwest and indicate rectilinear motion since the major axis accounts for more than ~90% of the current variance in each year. Current variability was much smaller offshore and more equitably distributed along the major and minor axes.

In August 2010 (Figure 58) mean winds were 2.9 m s^{-1} and westward. Within the ACC, flow was northeastward at $\sim 30 \text{ cm s}^{-1}$, but offshore of the ACC the flow was weak and variable. South of 71.5° N the offshore flow had an eastward component, whereas north of this latitude, the currents were $<10 \text{ cm s}^{-1}$ and predominantly northward to the west of 160° W and westward to the east 160° W . The distribution of the variance ellipses indicates rectilinear polarization within the ACC and more circularly polarized flow elsewhere. In August 2011 (Figure 59) the mean winds were 4.9 m s^{-1} southwestward. Flow within the ACC was $\sim 20 \text{ cm s}^{-1}$ and less than half this speed elsewhere. In August 2011, the Point Lay HFR site was operational, which permitted coverage to the west and northwest of the site. Here the flow was northward south of 70.5° N , which contrasts with the general sense that the ACC flows northeastward along the Alaskan coast before continuing into Barrow Canyon. Instead the vectors indicate that the flow veered eastward north of 70.5° N (where the 40 m isobaths also turns eastward) and then strengthened upon approaching the coast (although this region also contains the spatial coverage gaps described previously) before turning northeastward at the head of Barrow Canyon. Again there was an apparent transition from an eastward tendency in the flow south of 71.5° N to a northwestward flow north of this latitude. In fact, the vector pattern suggests that some of the flow along the west side of Barrow Canyon veers to the northwest transporting water toward Hanna Shoal. Note again, that the variance ellipses reflect the same disparity in polarization and magnitudes between the ACC and offshore regions.

In September 2009 (Figure 60), the mean winds were 4.2 m s^{-1} southwestward, and mean surface currents were generally to the southwest and fairly uniform over the entire region. The flow was southwestward within the ACC and along the eastern side of Hanna Shoal but veered westward west of 161° W around the south side of Hanna Shoal. Although the mean current speeds were more or less uniform, the current variance within the ACC was much larger than elsewhere. In September 2010 (Figure 61), winds were westward at $\sim 2 \text{ m s}^{-1}$ and varied primarily in the onshore-offshore direction. The velocity field included eastward and onshore flow between about 70.5° and 71° N and northeastward flow within the ACC. Interestingly, this onshore flow appeared partially fed by a southeasterly drift between the Klondike and Burger study areas. Again there was no indication of along-shore flow offshore of Point Lay. Instead, here the flow was feeble and southward along the coast and fed by the eastward flow offshore along $\sim 70.5^\circ \text{ N}$. The variance ellipses are similar to those described previously, e.g., these ellipses are large and along-shore polarized close to the coast and much smaller and less strongly polarized offshore. Note that offshore of Point Lay the ellipses are oriented along-shore, which implies that the flow here fluctuated back and forth along the coast and generally parallel to the isobaths throughout the month. In September 2011 (Figure 62), the winds averaged 4.8 m s^{-1} toward the southwest, with wind variations also principally along this axis in a southwest/northwest direction. Surface currents were southwestward east of Hanna Shoal but westward south of the Shoal. The ACC was also southwestward, but current speeds within the ACC were weak in comparison to other months. Offshore of Wainwright, the vector distribution suggests the flow veered westward (along the isobaths) before turning southwestward along the coast. Hence water moving up the

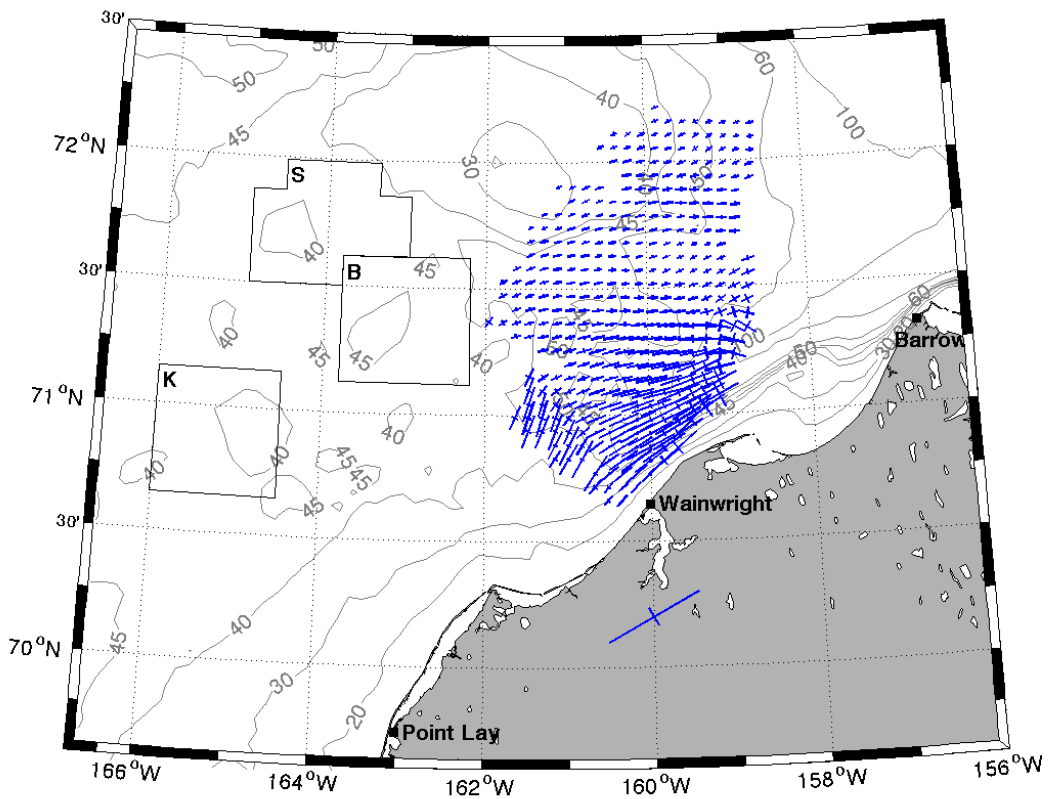
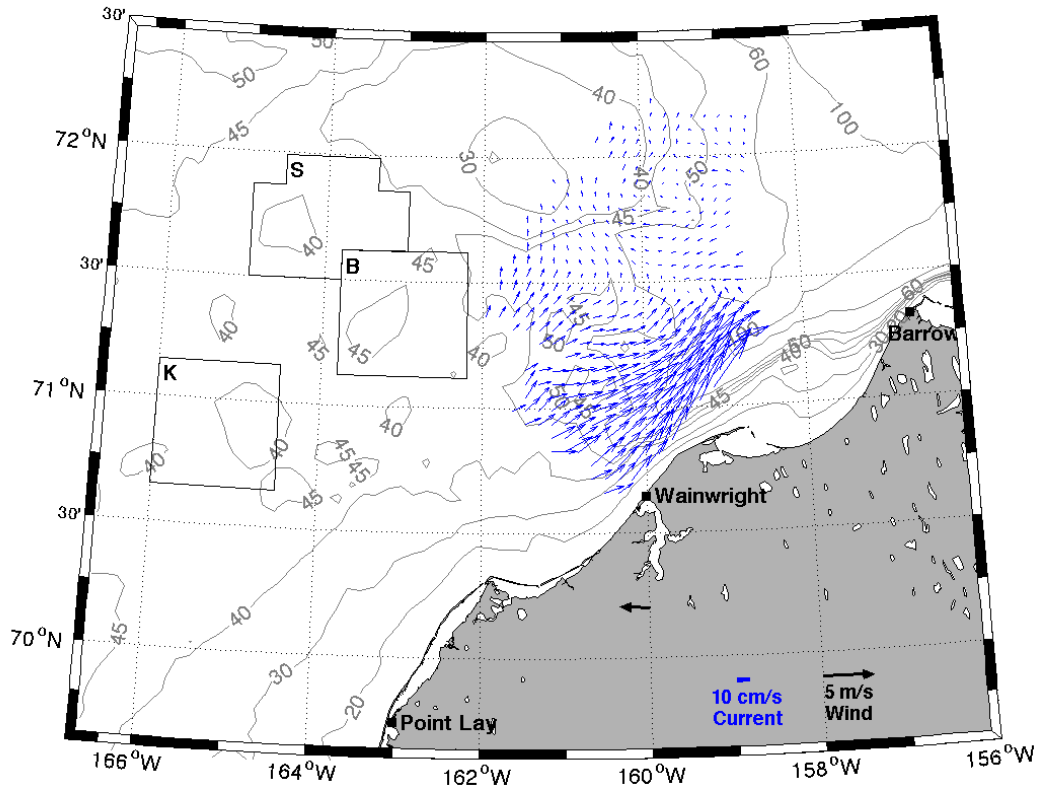


Figure 58. Mean surface currents (top) and principal axes (bottom) for August 2010.

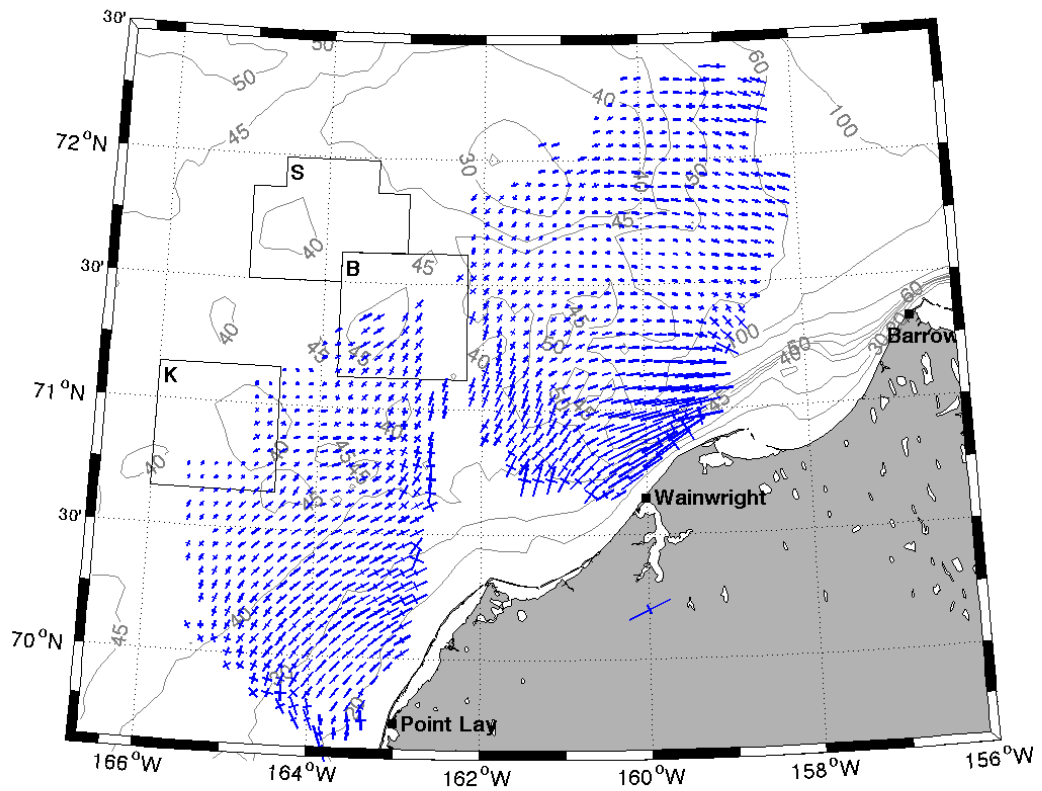
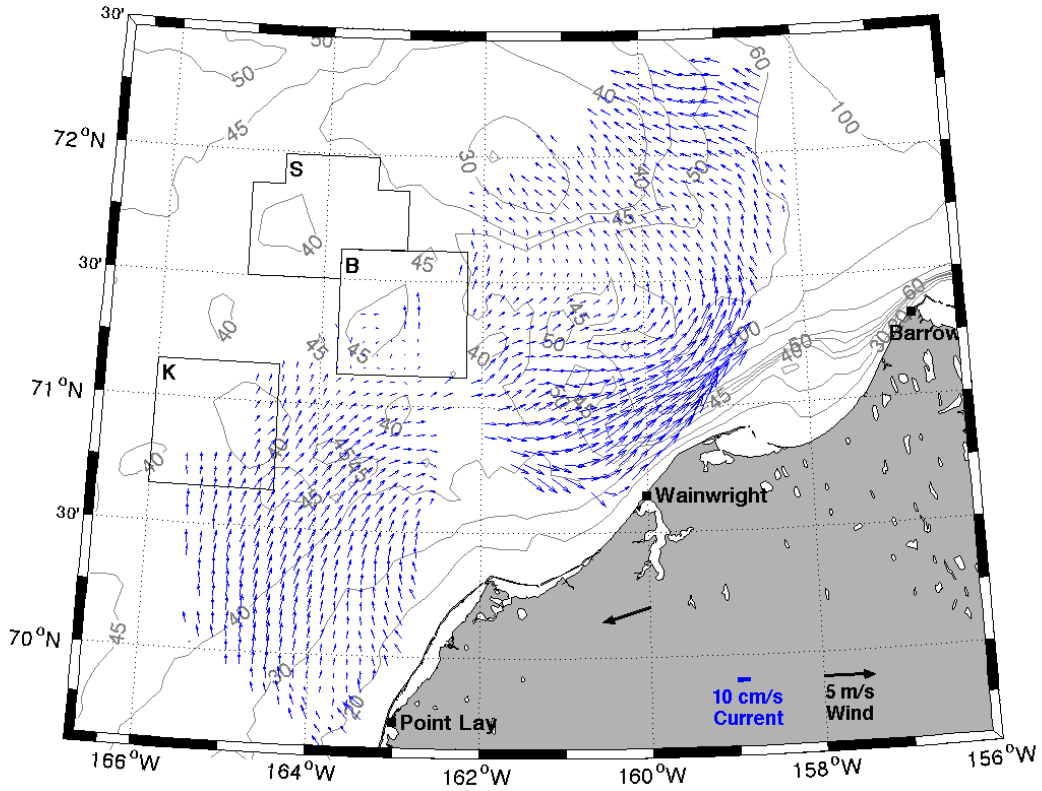


Figure 59. Mean surface currents (top) and principal axes (bottom) for August 2011.

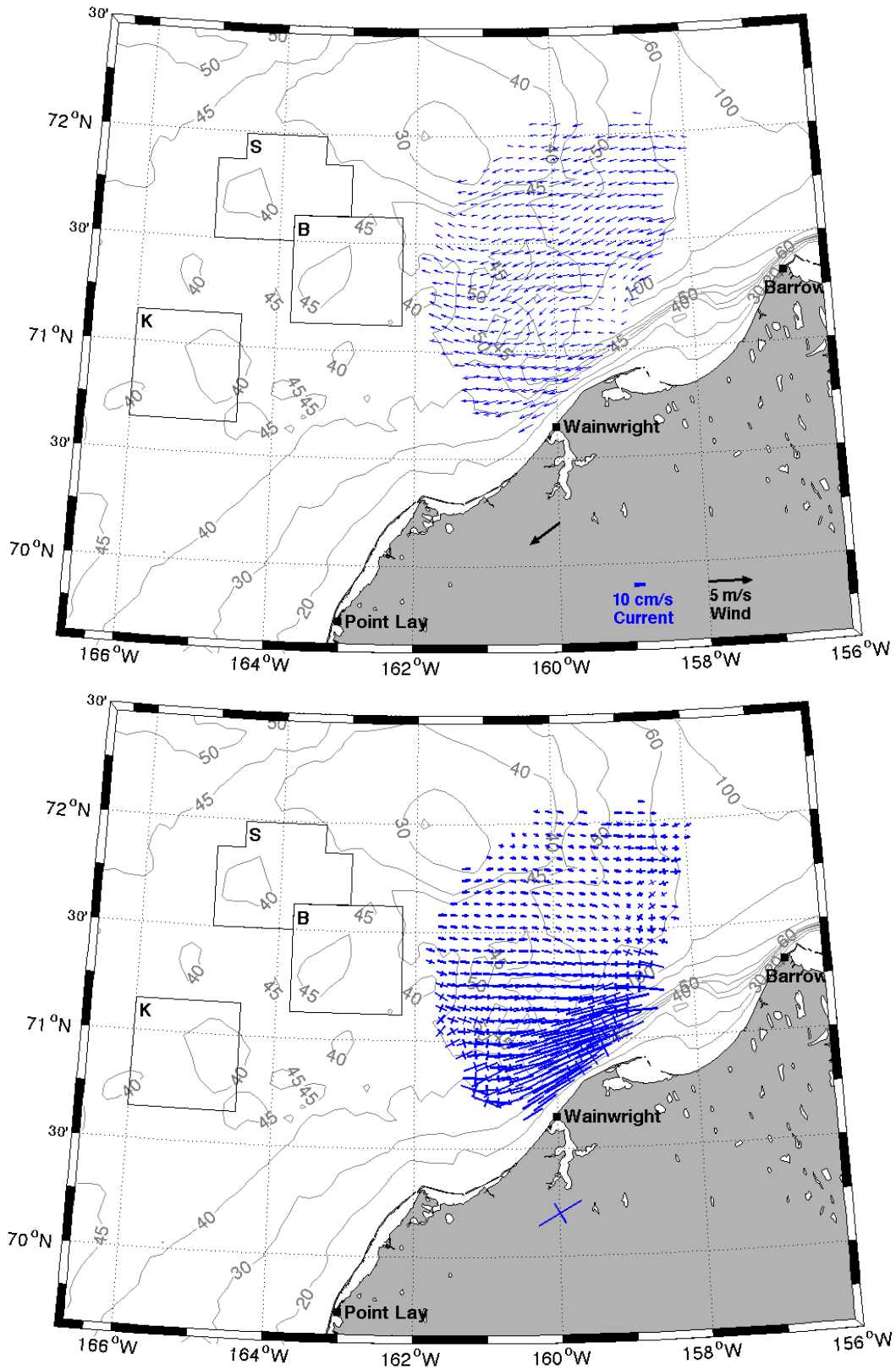


Figure 60. Mean surface currents (top) and principal axes (bottom) for September 2009.

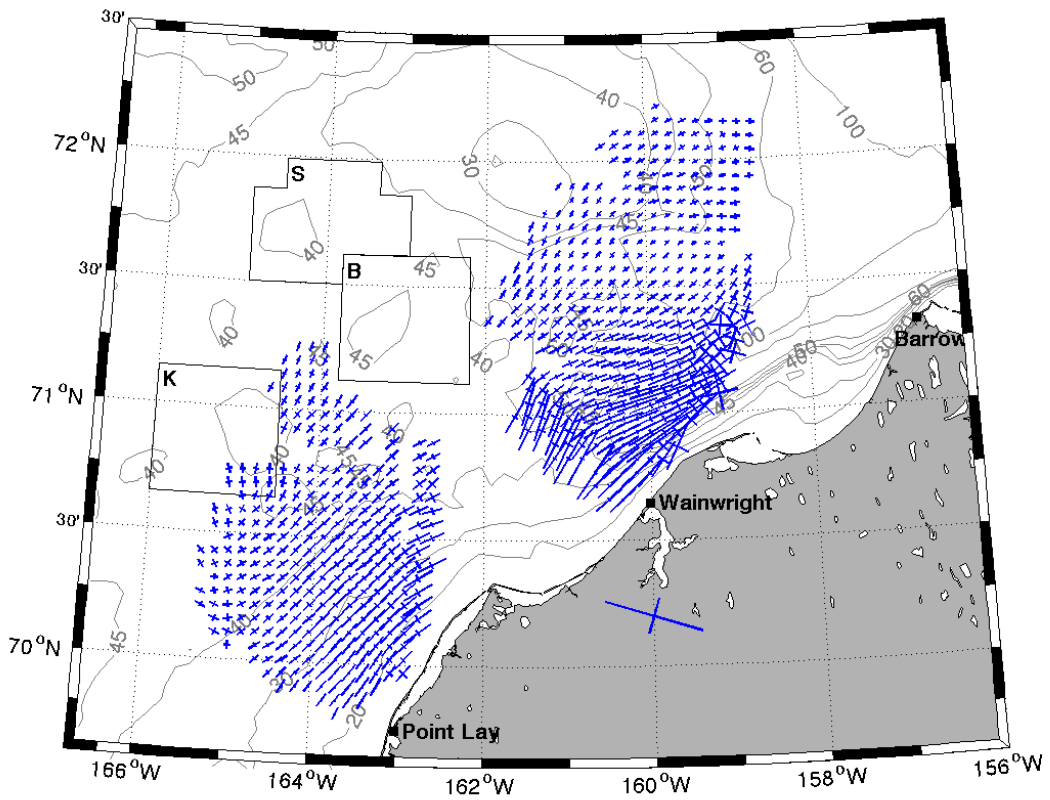
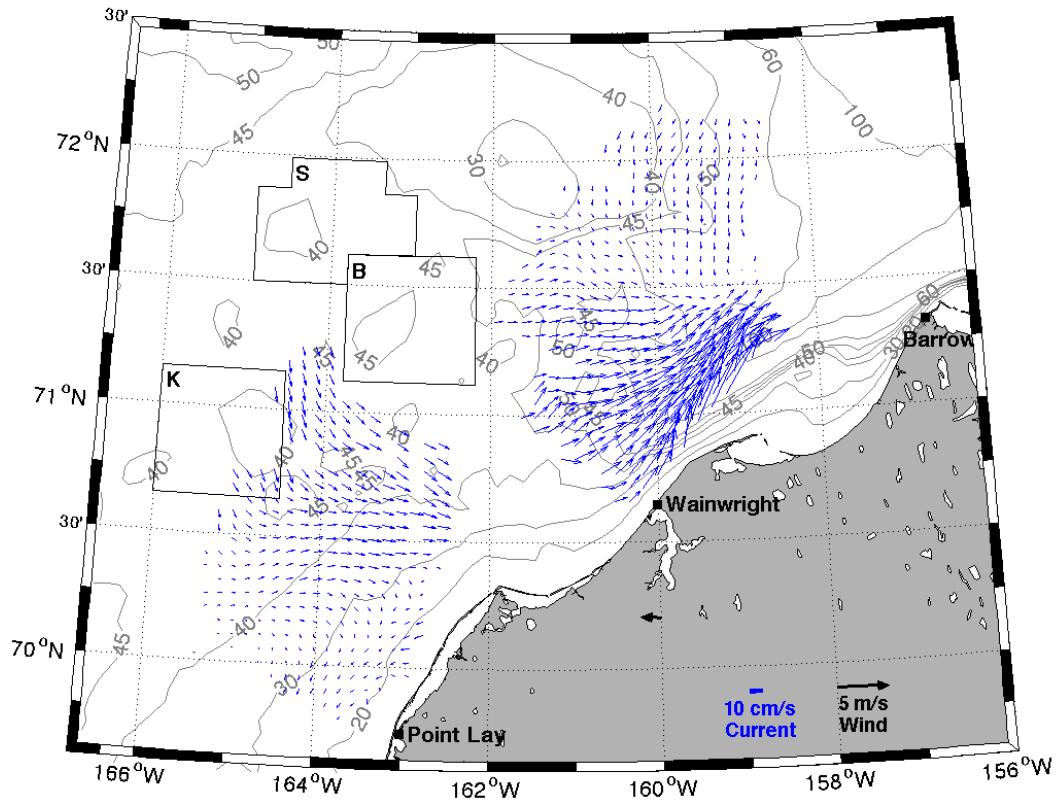


Figure 61. Mean surface currents (top) and principal axes (bottom) for September 2010.

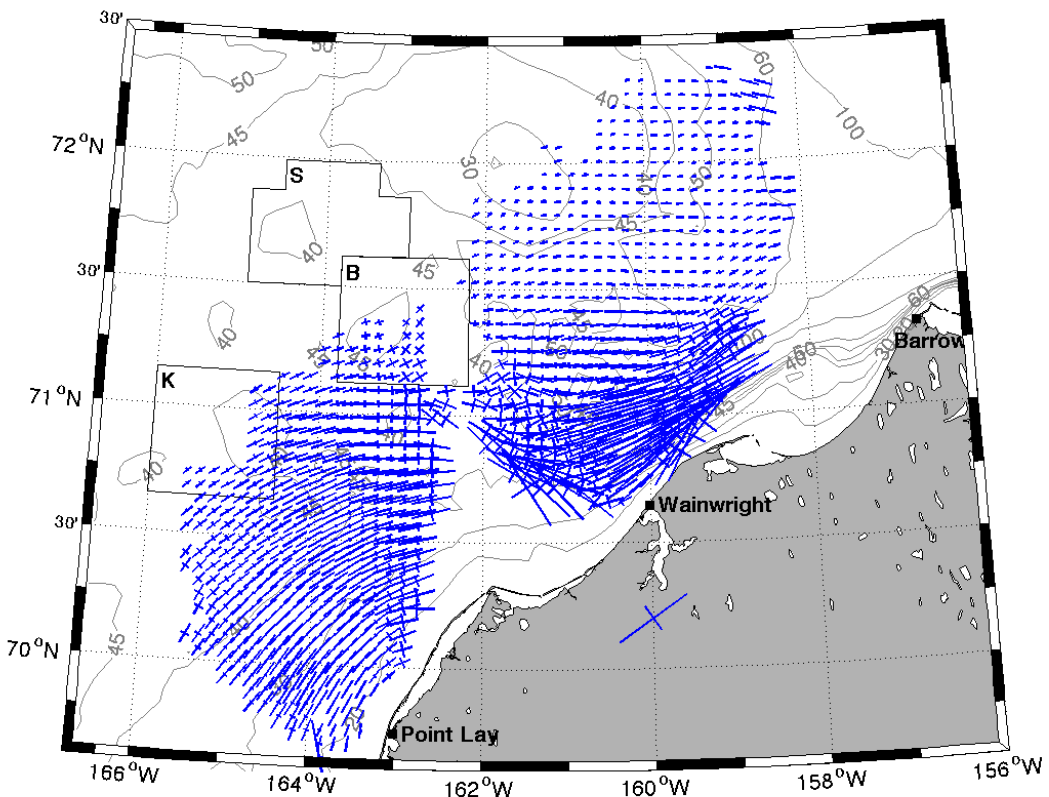
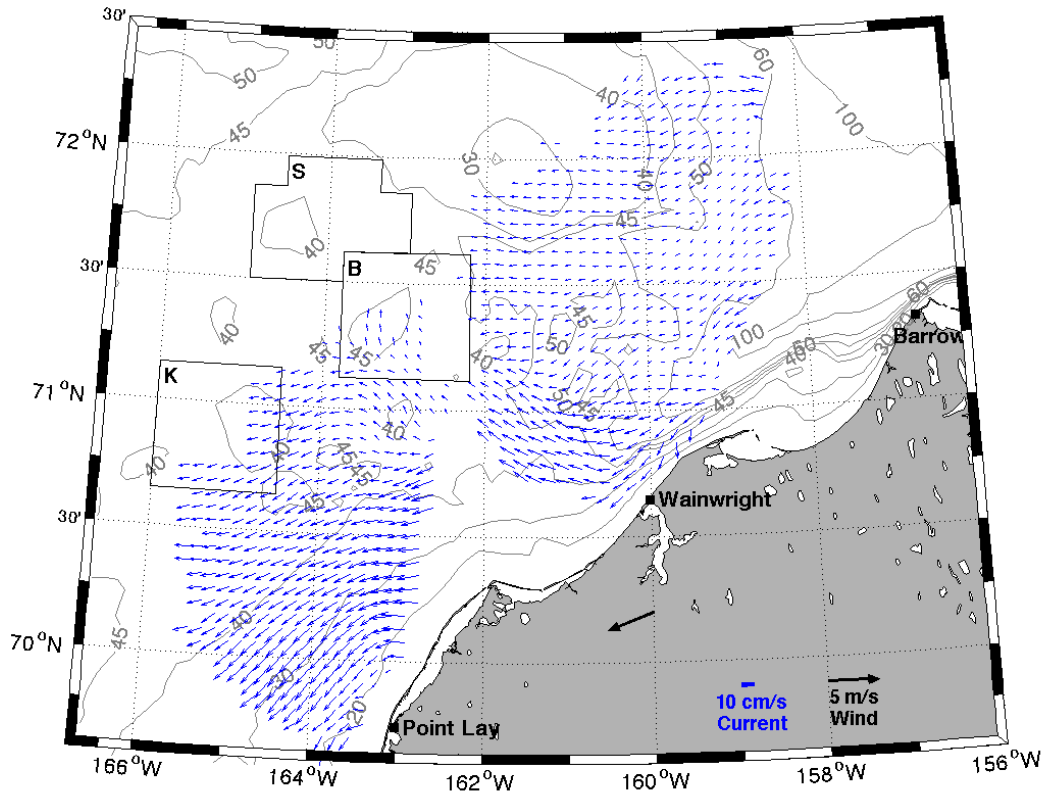


Figure 62. Mean surface currents (top) and principal axes (bottom) for September 2011.

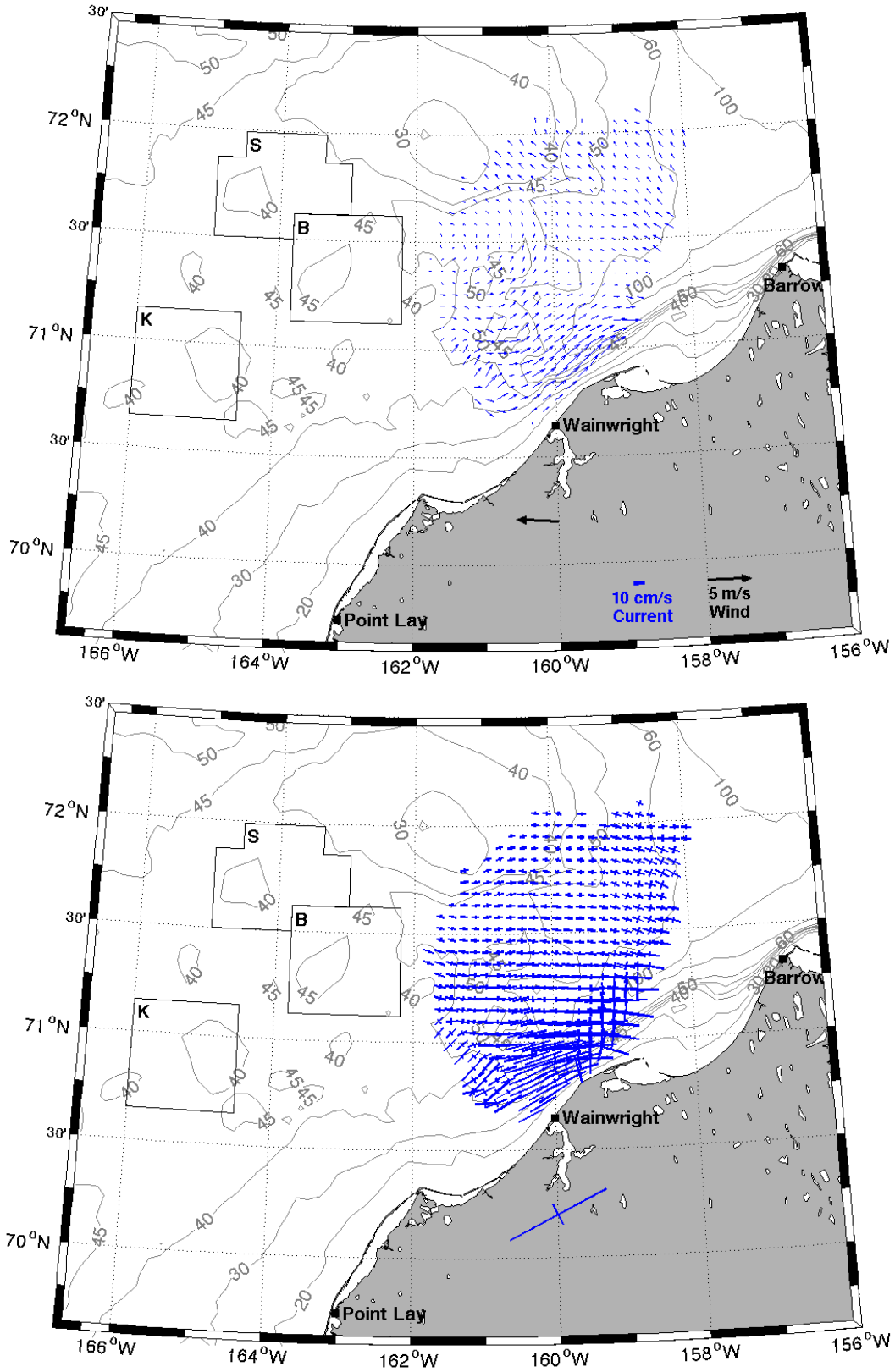


Figure 63. Mean surface currents (top) and principal axes (bottom) for October 2009.

canyon was apparently first carried offshore of Wainwright, possibly as far west as Klondike, and then south of Point Lay.

Mean winds in October 2009 were westward at 4.8 m s^{-1} , although wind variations were primarily northeast-southwest (i.e., along-shore). Flow within the ACC (Figure 63) was to the northeast at $\sim 20 \text{ cm s}^{-1}$, suggesting a reduction in the strength of the ACC relative to other months when northeastward flow prevailed here, and northwestward to the east of Hanna Shoal with speeds $< 10 \text{ cm s}^{-1}$. In October 2010 (Figure 64), the winds were 8.2 m s^{-1} to the southwest and accompanied by strong ($\sim 50 \text{ cm s}^{-1}$) southwestward flow within the ACC. The vector pattern at this time suggests that, offshore of Wainwright, the current diverged, reduced speed (to $\sim 20 \text{ cm s}^{-1}$) and spread water both offshore and to the southwest along the coast. To the east of Hanna Shoal, the surface flow was westward with speeds of $10 - 15 \text{ cm s}^{-1}$. Winds averaged 6.3 m s^{-1} toward the west-southwest in October 2011, and its variance ellipse was similarly oriented (Figure 65). Current speeds were approximately uniform throughout the region. Unlike the other months described, there was no coherent flow field associated with the ACC. Instead the large variability within the ACC implies that this current fluctuated back and forth throughout the month. Moreover, there was a weak, cyclonic eddy centered at 71.25°N and 160°W . The eddy diameter was $\sim 55 \text{ km}$ with azimuthal velocities of $\sim 10 \text{ cm s}^{-1}$. Similarly, the flow offshore of Wainwright and between 70.5° and 71.5°N was also weak and variable in direction. There was however, fairly uniform westward flow east of Hanna Shoal and north of 71.5°N and an apparently organized flow toward the southwest and offshore Point Lay. In October of all three years, the principal axes, which were aligned from northeast to southwest, explain $\sim 90\%$ of the current variance.

Although the HFR record lengths for November of each year vary in length and are less than a half-month, we nonetheless show the statistical results to illustrate the types of regional flow variations. In November 2009 (Figure 66), the mean winds were westward at 9.5 m s^{-1} , with most of the variability aligned along the north-south axis. During this brief period the surface flow was weakly upcanyon near the coast and westward elsewhere. In November 2010, winds over the first week of the month were $\sim 8 \text{ m s}^{-1}$ to the southwest and steady. The current field (Figure 67) included swift southwestward flow within the Canyon and over the shelf south of 71°N . The flow was divergent east of Hanna Shoal and included southwestward flow adjacent to the canyon and generally westward flow elsewhere in this area. In November 2011, the mean winds were $\sim 2.5 \text{ m s}^{-1}$ west-northwestward, although quite variable in the onshore-offshore direction. The circulation field (Figure 68) included eastward (onshore) flow between 70.5° and 71.5°N , which strengthened and veered northeastward nearing Wainwright. East of Hanna Shoal the vectors indicate a southward drift that carried water from the north side of Hanna Shoal southward to $\sim 71.5^\circ\text{N}$, where it then converged with waters moving eastward from along the south side of the Shoal.

Although the mean maps characterize the broad patterns of the circulation field and some of its variability, they necessarily obscure temporal and spatial mesoscale variations embedded with the circulation. Some of this variability is captured in Figure 69, which contains a number of flow fields that illustrate the divergence of the circulation in the region between Icy Cape and Wainwright as well as the cyclonic eddy that forms to the northwest of the head of Barrow

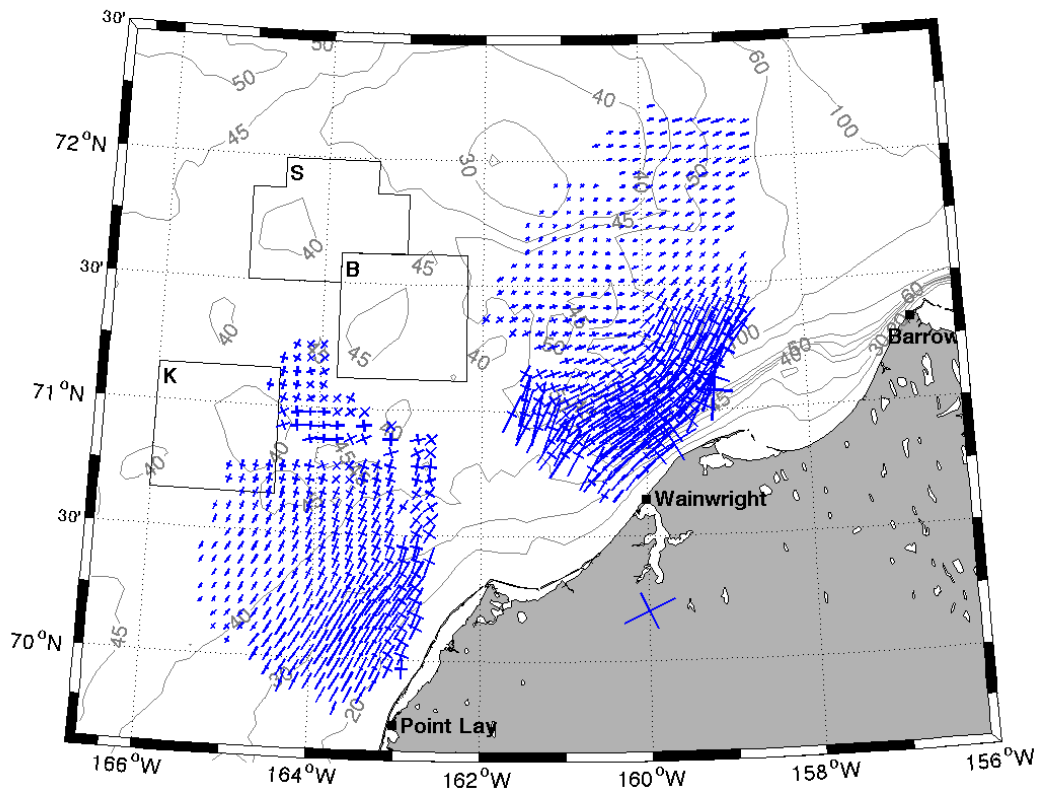
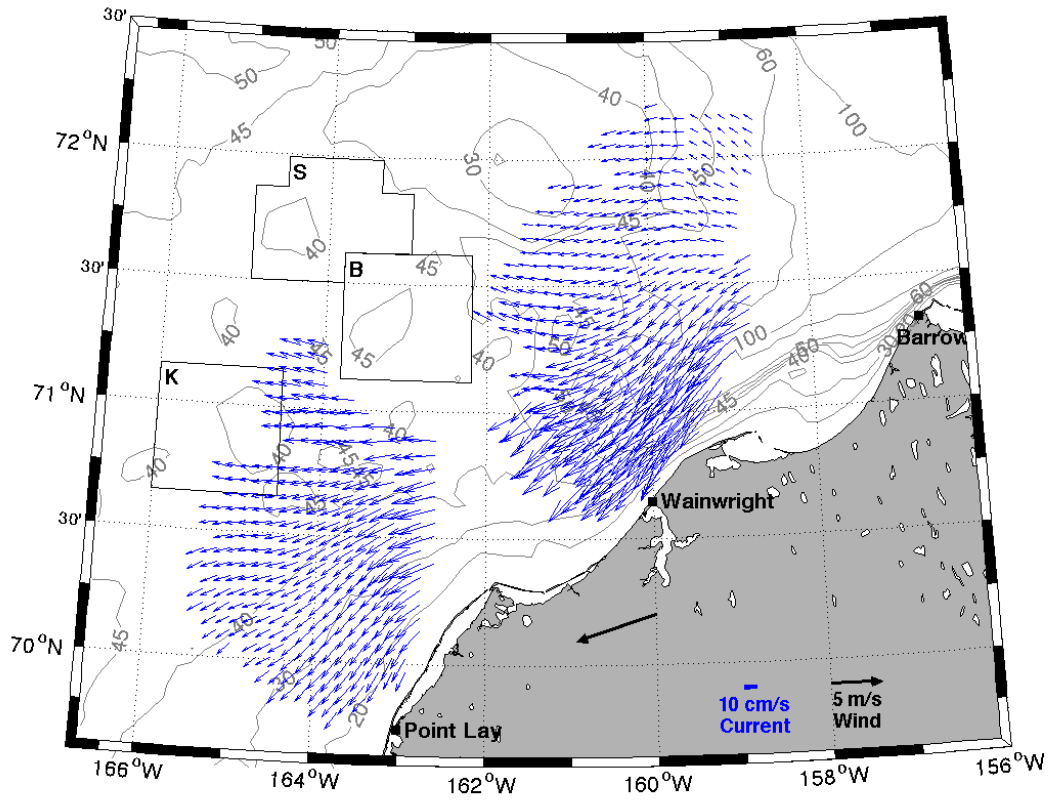


Figure 64. Mean surface currents (top) and principal axes (bottom) for October 2010.

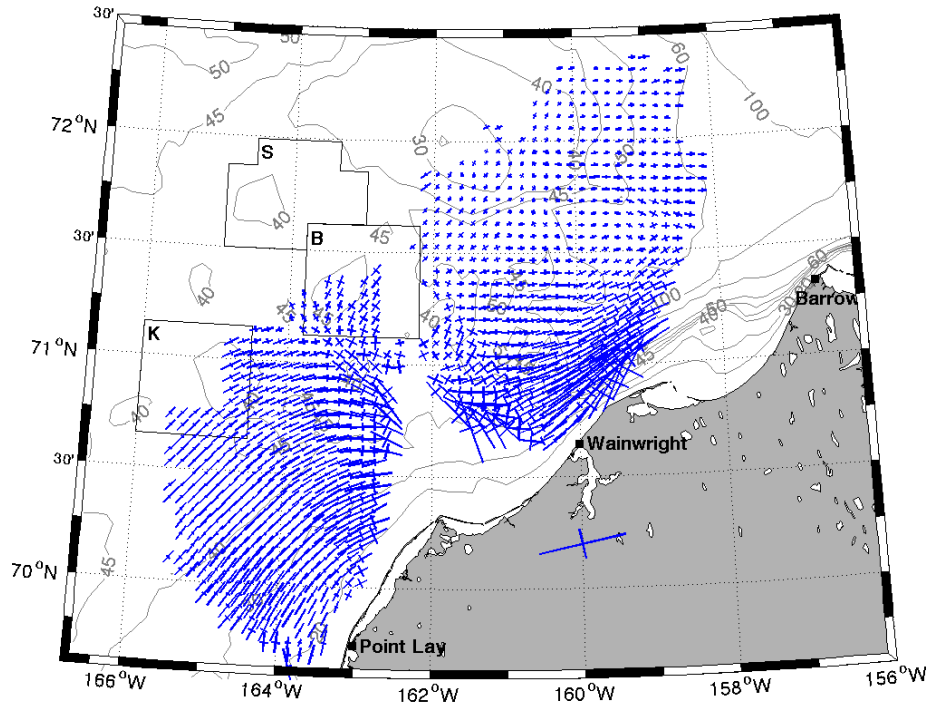
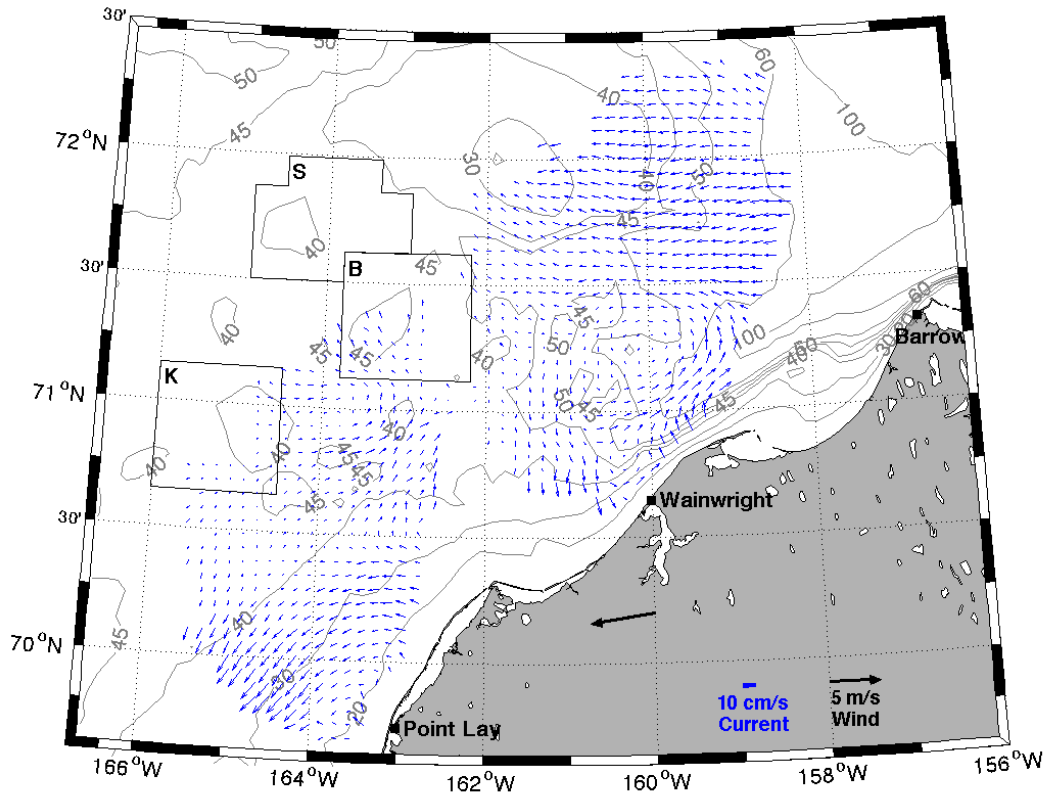


Figure 65. Mean surface currents (top) and principal axes (bottom) for October 2011.

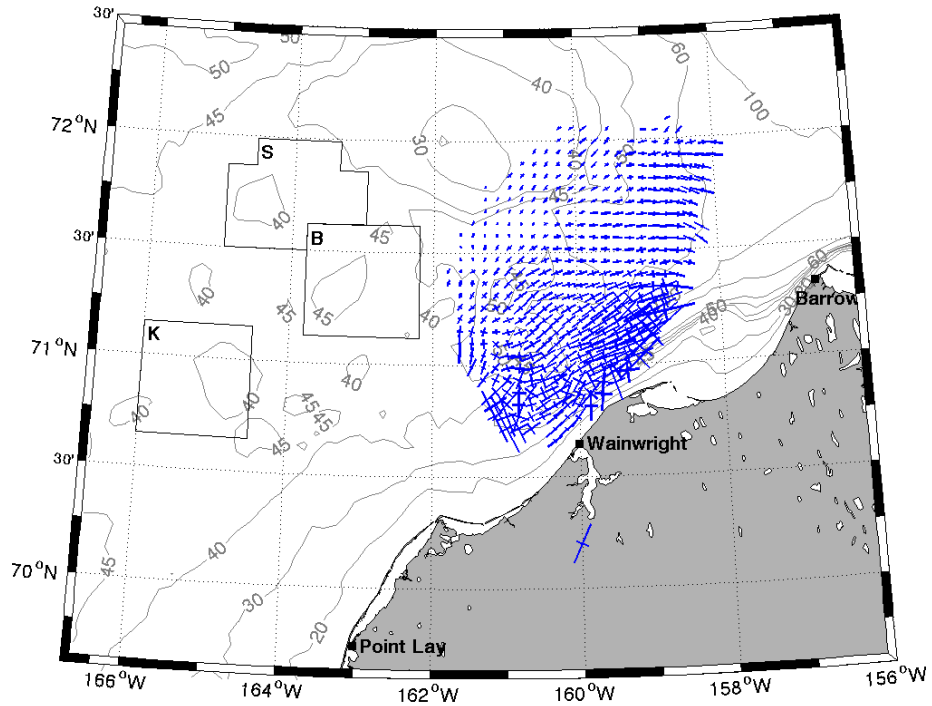
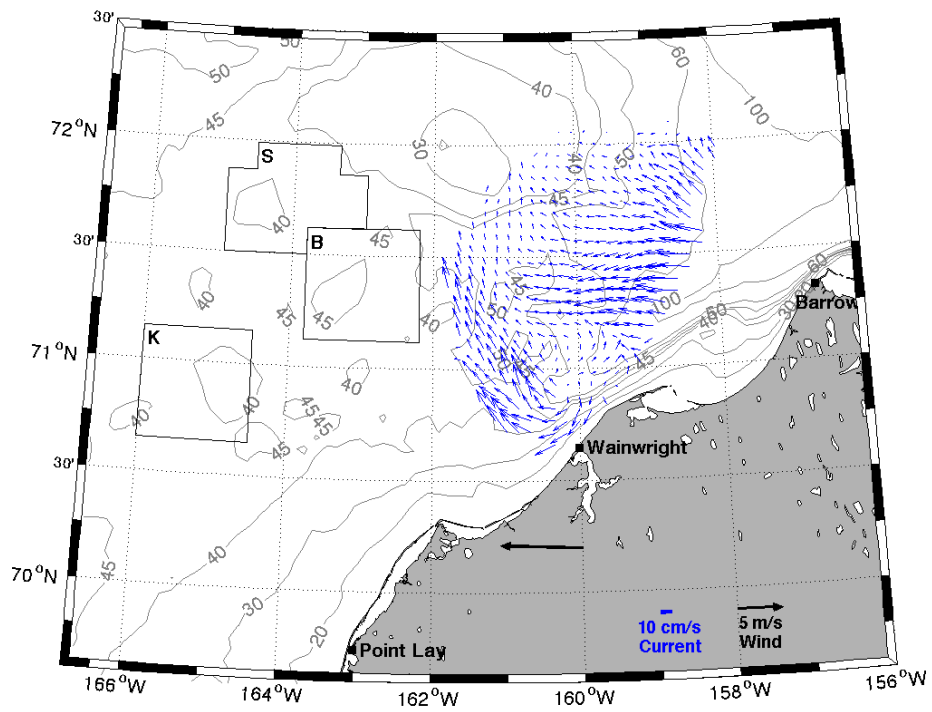


Figure 66. Mean surface currents (top) and principal axes (bottom) for November 2009.

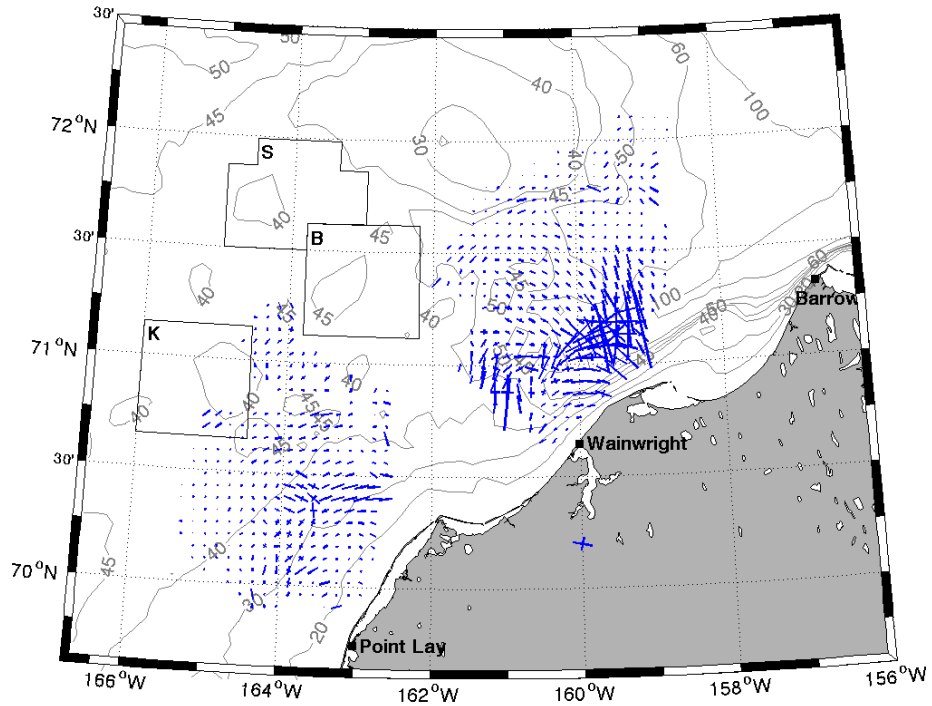
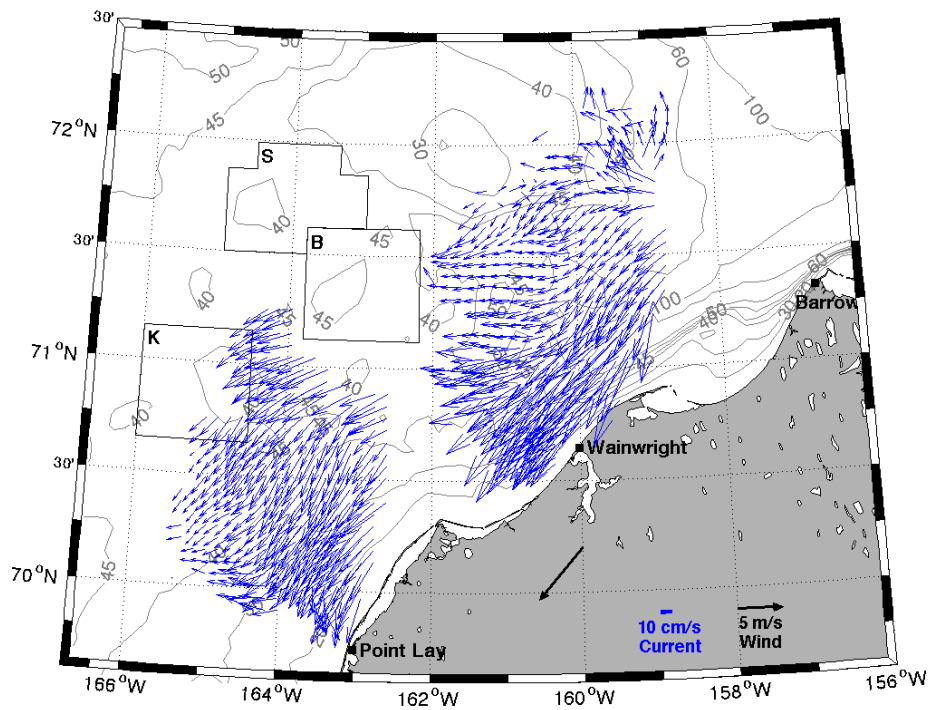


Figure 67. Mean surface currents (top) and principal axes (bottom) for November 2010.

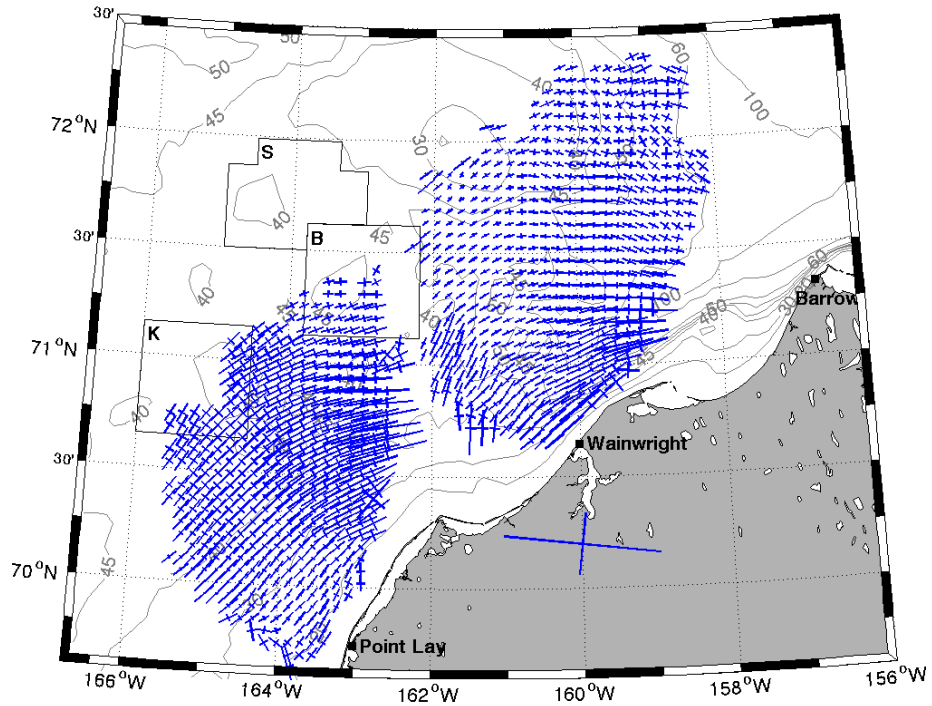
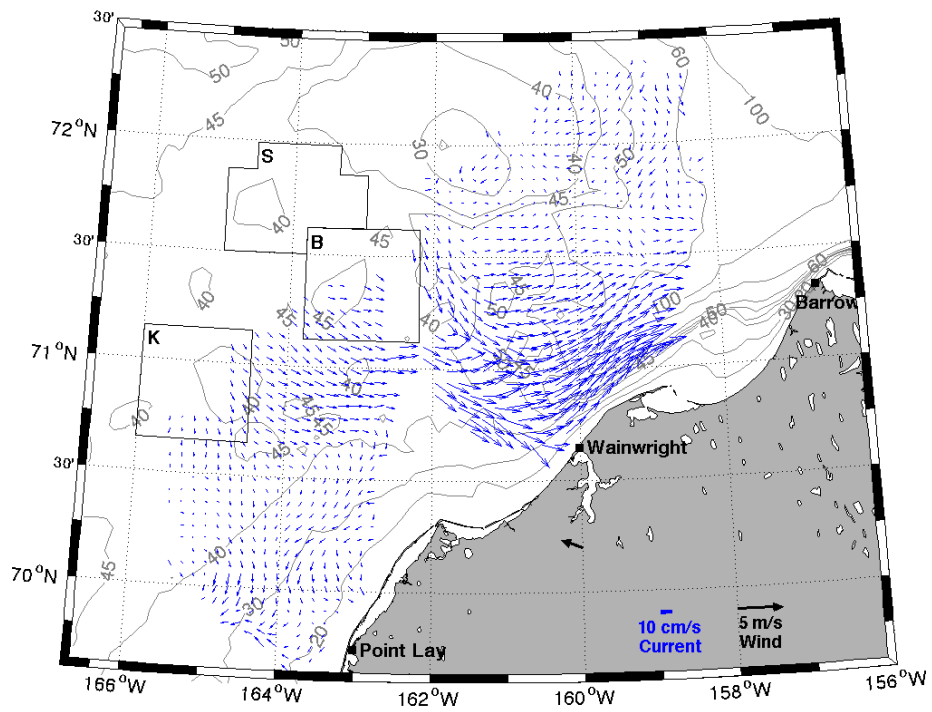


Figure 68. Mean surface currents (top) and principal axes (bottom) for November 2011.

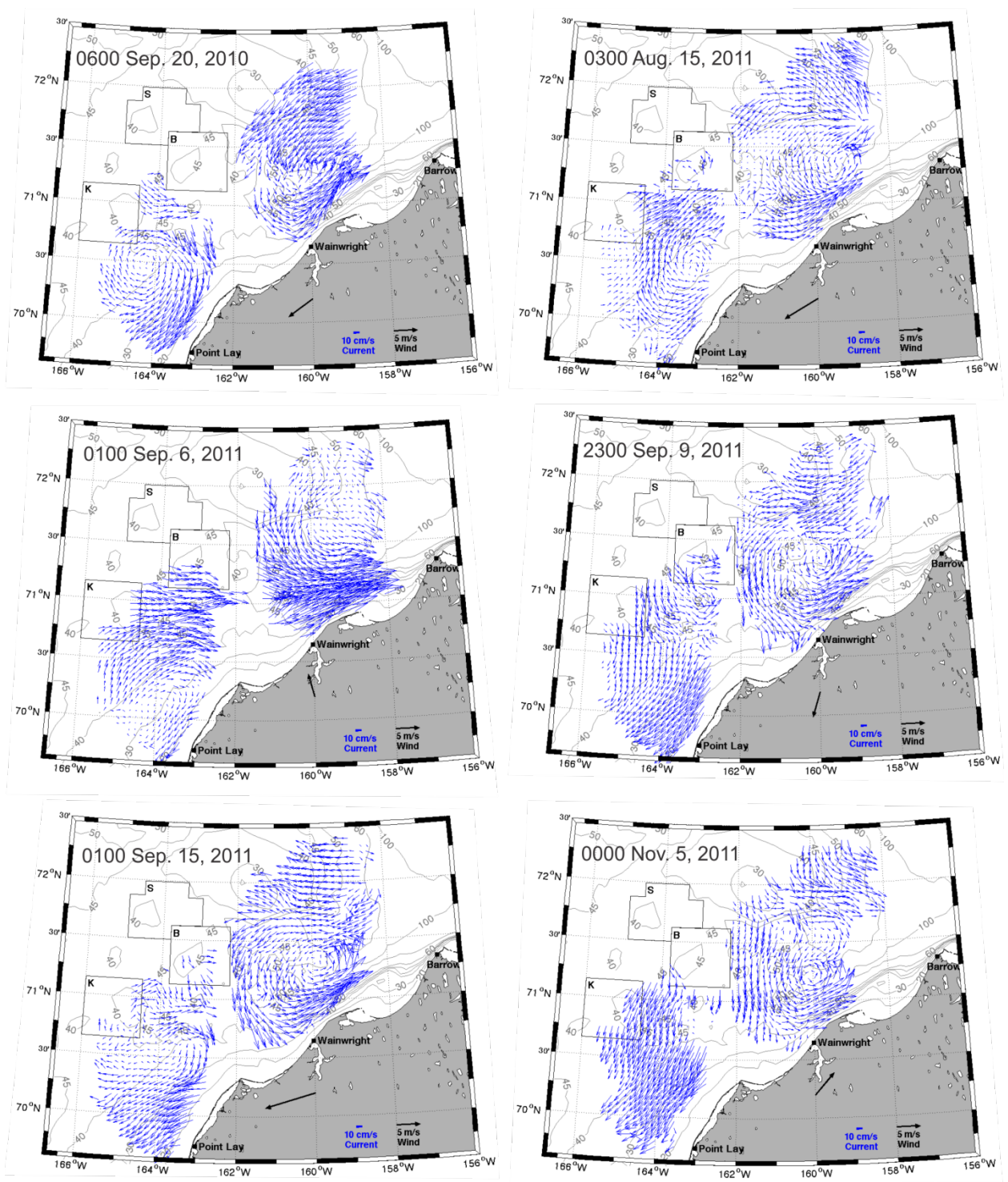


Figure 69. Examples of surface current mesoscale variability over the northeast Chukchi Sea.

Canyon. As evident in the figure, this variability can be vigorous and occur at small spatial scales. Additional examples of flow variability are addressed in Section 4.5

4.4.3. Mean Surface Currents as a Function of Wind Direction

We next examine the structure of the surface circulation as a function of the wind direction. We do so by constructing composite circulation maps for all cases in which the wind is blowing toward a particular sector of the quadrant. Before examining the velocity fields, we present the wind roses constructed for each measurement year and only for those time periods when the HFR were operational (Figure 70). In all years, the majority of the winds blew toward the southwest quadrant. In addition, winds with a westward component were also stronger than those that blew in other directions. Based on the wind roses, we mapped the circulation according to the following sectors: 0-90°T, 90-180°T, 180-220°T, 220-260°T, 260-280°T, and 280-360°T. In addition, we split our analysis of the 220-260°T sector into cases when the winds were $<6 \text{ m s}^{-1}$ and $>6 \text{ m s}^{-1}$.

Currents were similar in all years when winds blew toward the 0 - 90°T quadrant (Figure 71). Under these winds, the circulation included a strong northeastward ACC and northeastward flow along the coast offshore of Point Lay. Farther offshore, the flow is eastward between 71.5°N and the south side of Hanna Shoal and southeastward along the eastern side of the Shoal. North and east of Hanna Shoal the circulation is toward the southeast, with this flow converging with the eastward flow from the central shelf along about 71.5°N.

When winds blew toward the 90 - 180°T sector (Figure 72), the ACC flowed northeastward, although this flow was stronger in 2010 than in the other years for reasons unknown. The flow was southward east of Hanna Shoal and then veered eastward to join the ACC to the northwest of Wainwright. In 2010 and 2011, the flow over the central Chukchi shelf was generally southward, although in 2011, a portion of the shelf flow was eastward between 70.5 and 71.5°N.

For winds blowing toward the 180 – 220°T sector (Figure 73), the ACC was strong and southwest in 2009, but in 2010 it was weaker, more diffuse, although it also flowed southwestward. An organized southwestward flow occurred to the east of Hanna Shoal in both years. In 2010, the flow over the central shelf was generally southward. In 2011, the ACC was not evident when winds blew southward. Instead a ~50 km-wide cyclonic eddy, centered at 71.1°N and 160.5°W formed slightly to the west of the entrance to Barrow Canyon. The eddy is similar to that discussed in relation to October 2011, which developed when the mean winds were southwestward. The currents were westward east of Hanna Shoal and southwestward offshore of Point Lay and over the central shelf.

The next comparison is between circulation patterns for winds blowing toward the 220 – 260°T sector at speeds $<6 \text{ m s}^{-1}$ and $>6 \text{ m s}^{-1}$ (Figures 74 and 75, respectively). A well-developed ACC was present in all years for wind speeds $< 6 \text{ m s}^{-1}$. In 2009, eastward flow developed offshore of the ACC and south of 71.5°N. This flow appeared to veer to the northeast and continue in this direction along the northwestern flank of Barrow Canyon. Along ~72°N, the flow was westward, until it encountered Hanna Shoal, where it then flowed southwestward along the eastern edge of

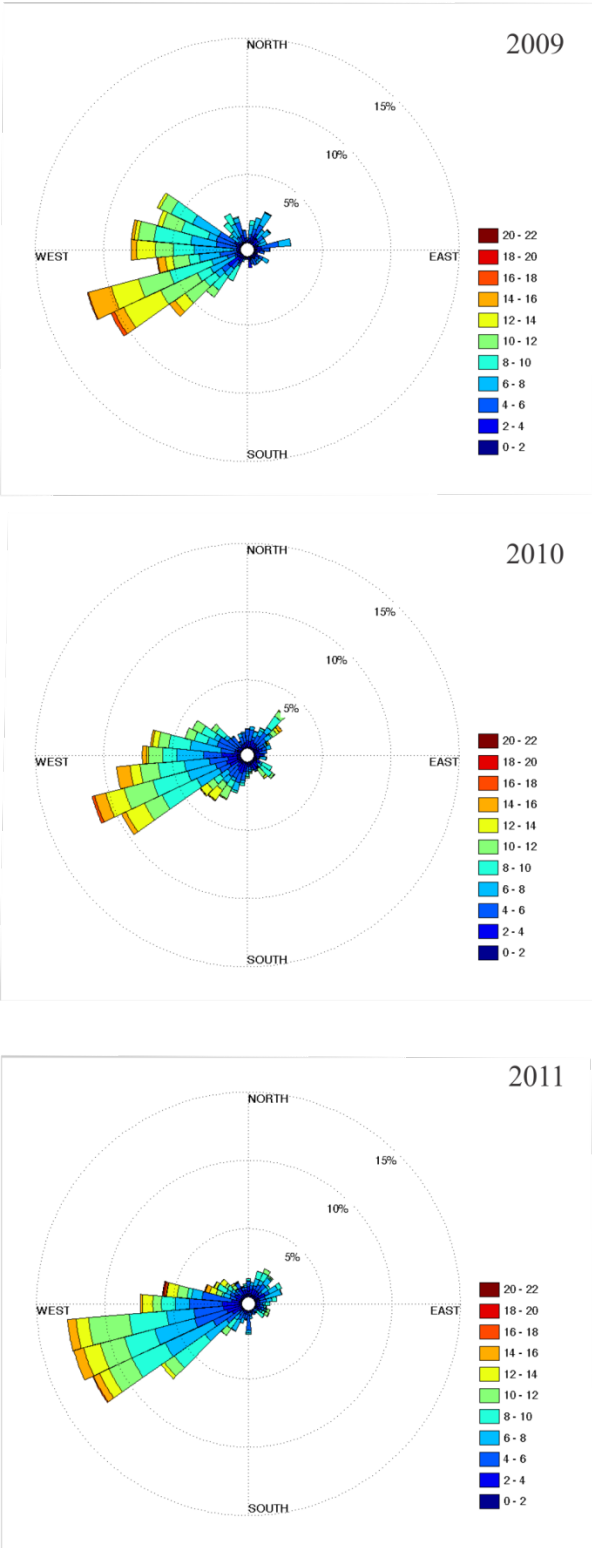


Figure 70. Wind rose for HFR operational dates in 2009 (top), 2010 (middle), and 2011 (bottom). The directions are those toward which the wind is blowing.

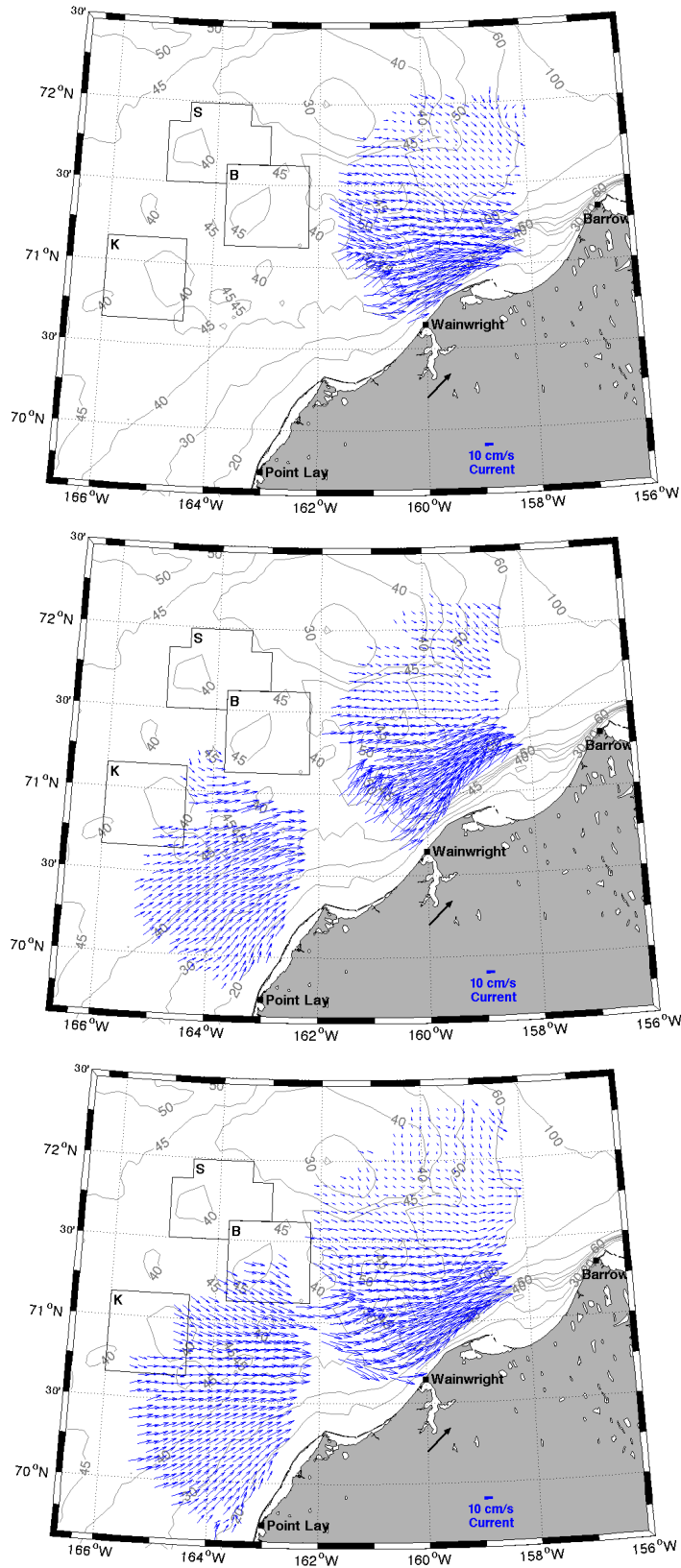


Figure 71. Mean surface currents in 2009 (top), 2010 (middle), and 2011 (bottom) for periods when winds blew towards 0 - 90°T.

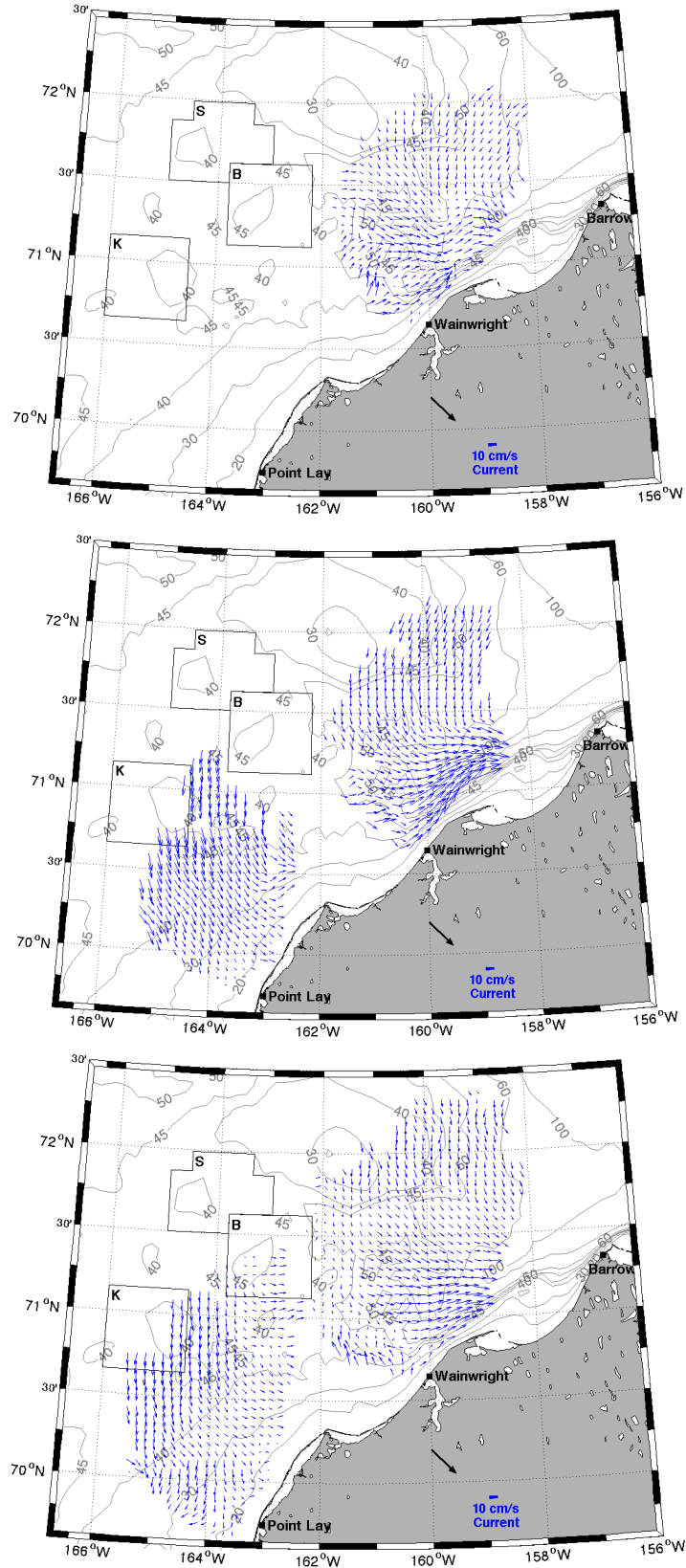


Figure 72. Mean surface currents in 2009 (top), 2010 (middle), and 2011 (bottom) for periods when winds blew towards 90 - 180°T.

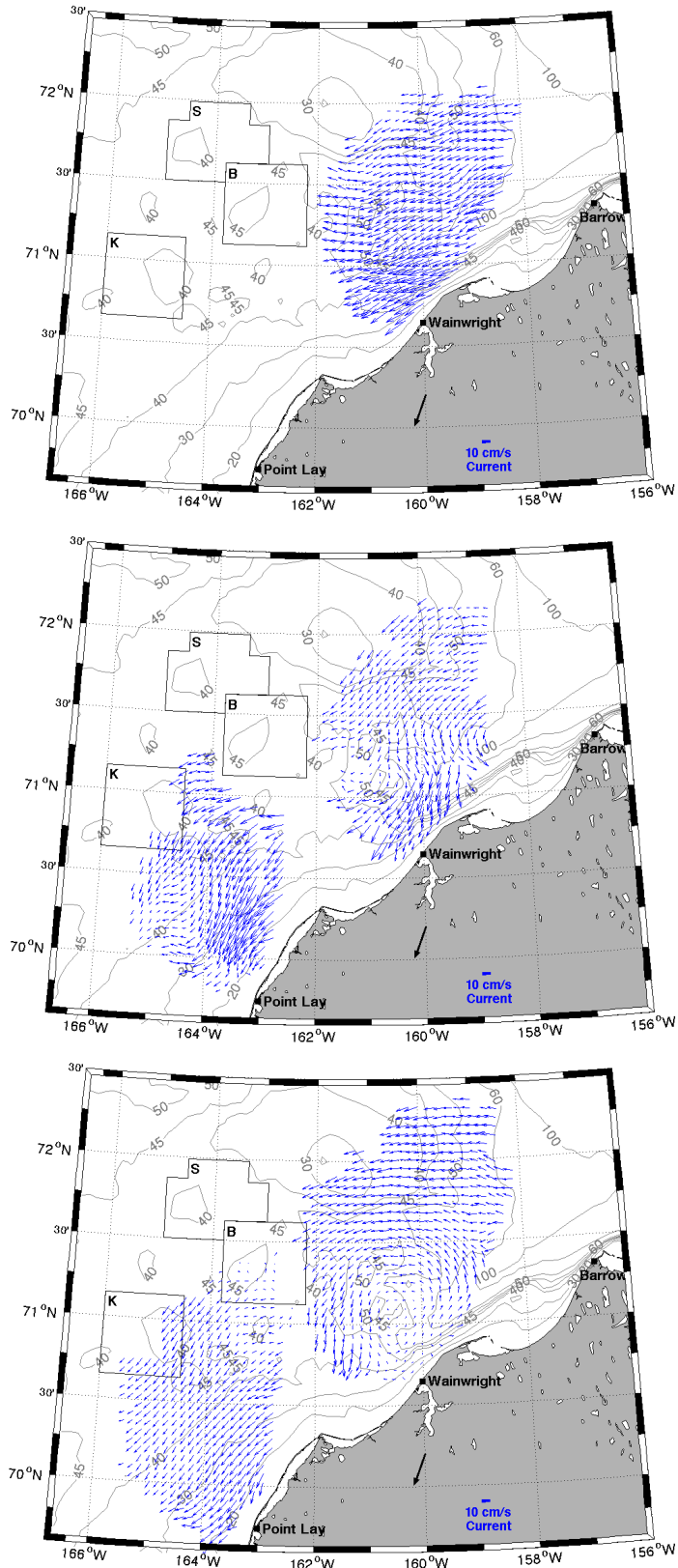


Figure 73. Mean surface currents in 2009 (top), 2010 (middle), and 2011 (bottom) for periods when winds blew towards 180 - 220°T.

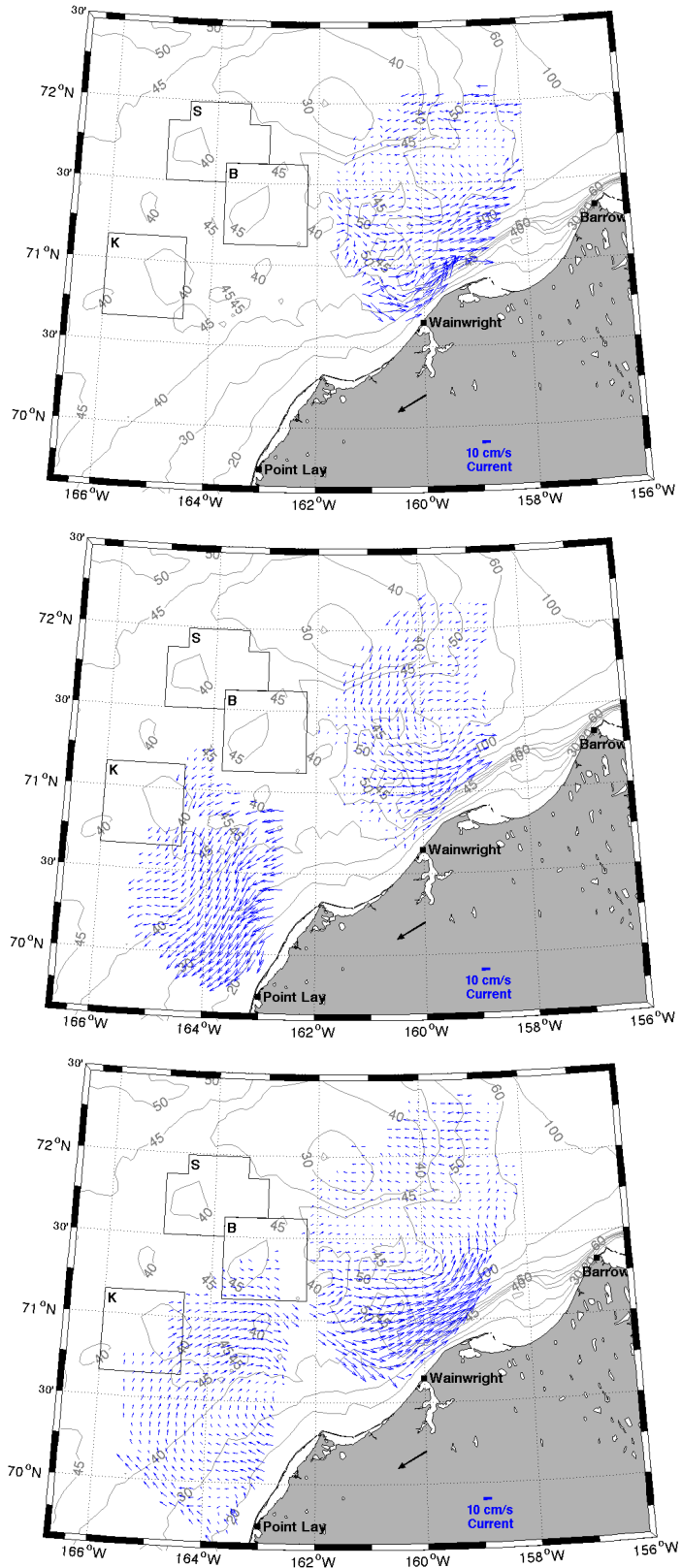


Figure 74. Mean surface currents in 2009 (top), 2010 (middle), and 2011 (bottom) for periods when winds blew towards 220 - 260°T at <6 m/s.

the Shoal. Indeed, the vector pattern suggests a cyclonic circulation pattern centered at $\sim 71.5^\circ\text{N}$ and 159°W in both 2009 and 2010. In 2011, there was also cyclonic turning over the shelf southeast of Hanna Shoal centered at about 71.4°N and 160°W , although a distinct eddy was not apparent. The flow field over the central shelf differs between 2010 and 2011 under these wind conditions. In 2010, the flow was southwestward over the entire region, whereas in 2011, the flow was onshore between 70.5° and 71.5°N . Near the coast, and offshore of Point Lay, the vector pattern suggests a large (~ 110 km) anticyclonic circulation zone that carries nearshore waters offshore and then north between 164 and 166°W . This water was then carried onshore north of 70.5°N and entered Barrow Canyon. Although the spatial gap precludes a definitive conclusion, it seems likely that this onshore flow diverges, with some of the water feeding the ACC and some returning to the southwest offshore of Point Lay. We denote this pattern as the “divergent mode” because the onshore flow apparently bifurcates somewhere between Icy Cape and Wainwright.

A very different circulation pattern emerged for winds blowing toward the same sector but at speeds >6 m s^{-1} (Figure 75). Under these conditions, the ACC reverses and flows southwestward in all years. The flow east of Hanna Shoal is uniformly westward, and the flow offshore of Point Lay and over the central shelf is southwestward.

Winds toward $260 - 280^\circ\text{T}$ (Figure 76) resulted in generally westward flow north of 71.5°N in all years. South of 71.5°N the circulation varied among years. Within the ACC, the flow was southwestward in 2009 and then turned westward seaward of the 40 m isobath. In both 2010 and 2011, the ACC was weak but northeastward. However, the flow over the central shelf and offshore Point Lay was southwestward or westward in 2010. In 2011, the flow over these regions appeared much like the situation for winds blowing toward $220 - 260^\circ\text{T}$ sector at speeds <6 m s^{-1} (Figure 74, bottom panel).

The final condition evaluated was for winds blowing toward the $280 - 360^\circ\text{T}$ sector (Figure 77). For this case, the flow was northward or northeastward everywhere and included a fairly swift ACC. The vectors in 2011 once again suggest that the divergent mode developed in the onshore flow between Wainwright and Icy Cape.

4.4.4. Mean Surface Currents as a Function of ACC Direction

An alternate depiction of the surface circulation is afforded from maps of the mean flow for each year under conditions when the ACC flowed to the northeast or to the southwest. Mean surface currents when the ACC was flowing toward the northeast are shown in Figure 78 and suggest several general features. First, the surface currents have an eastward component over most of the region between $\sim 70.5^\circ$ and 71.5°N . Second, for this scenario the westward component of the winds is <5 m s^{-1} so that the surface flow over much of the central shelf flows upwind. Third, the nearshore, along-shore component of flow between Point Lay and Icy Cape is much weaker than the same component farther offshore. Fourth, the eastward flow converges and then veers northeastward at the head of Barrow Canyon and along the western side of the Canyon. Fifth, the ACC is swifter along the central and eastern side of the canyon than the western side (but note that the HFR coverage is rather limited along the eastern side of the canyon). Sixth, north of

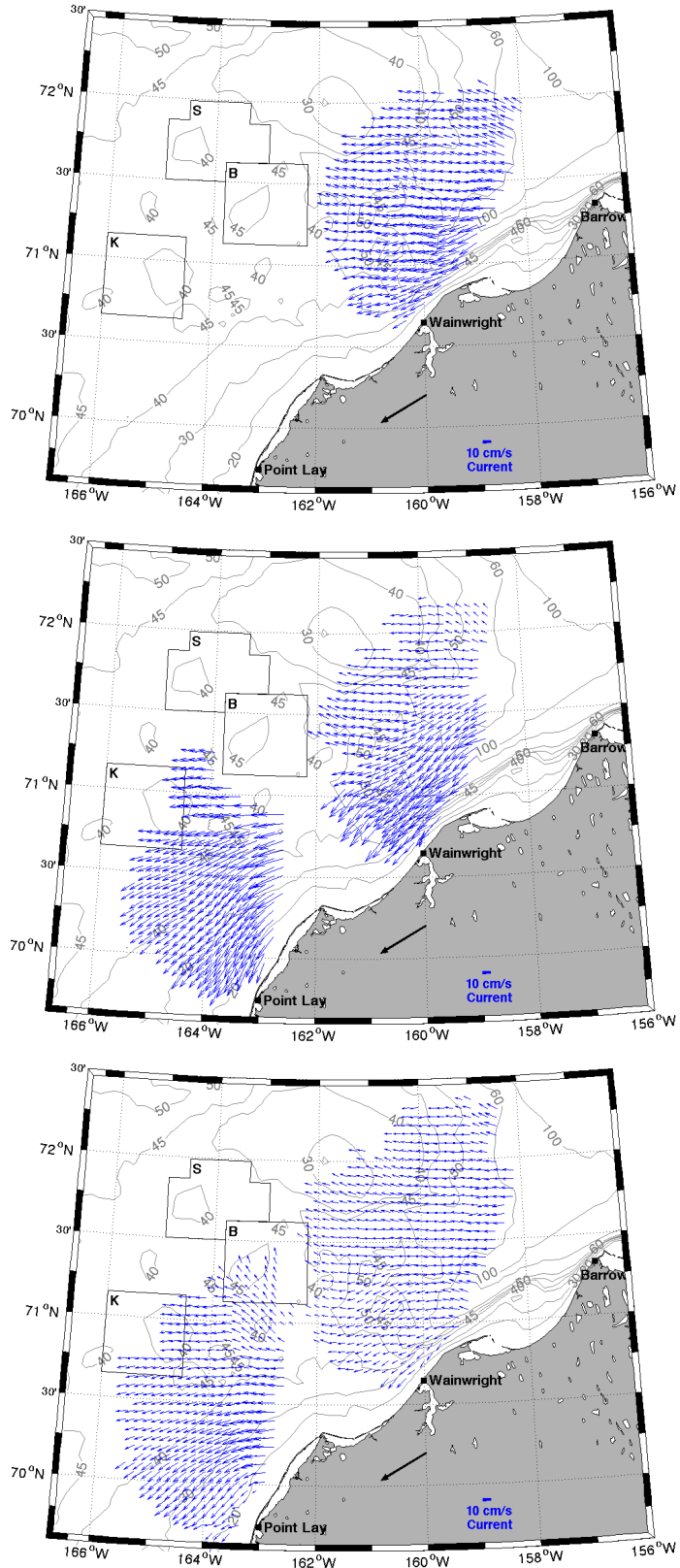


Figure 75. Mean surface currents in 2009 (top), 2010 (middle), and 2011 (bottom) for periods when winds blew towards 220 - 260°T at >6 m/s.

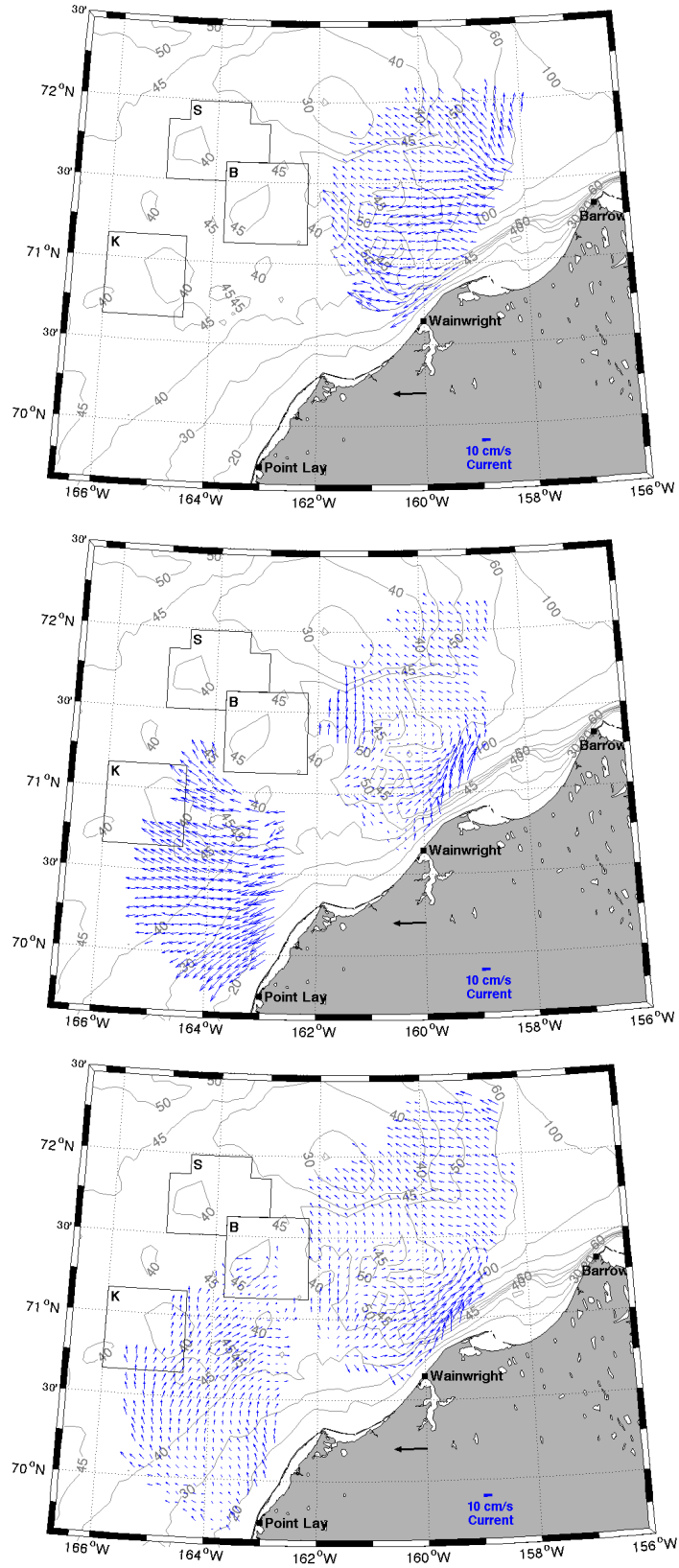


Figure 76. Mean surface currents in 2009 (top), 2010 (middle), and 2011 (bottom) for periods when winds blew towards 260 - 280°T.

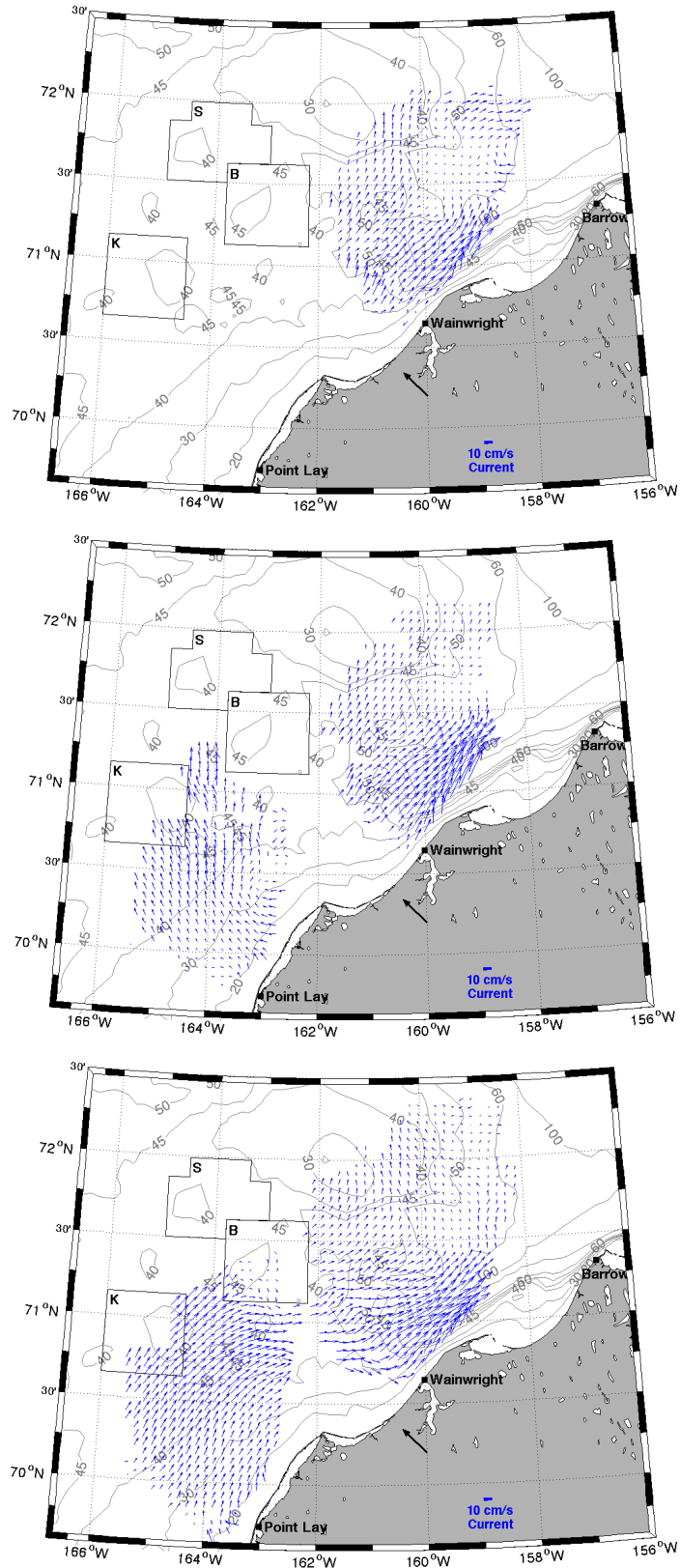


Figure 77. Mean surface currents in 2009 (top), 2010 (middle), and 2011 (bottom) for periods when winds blew towards 280 - 360°T.

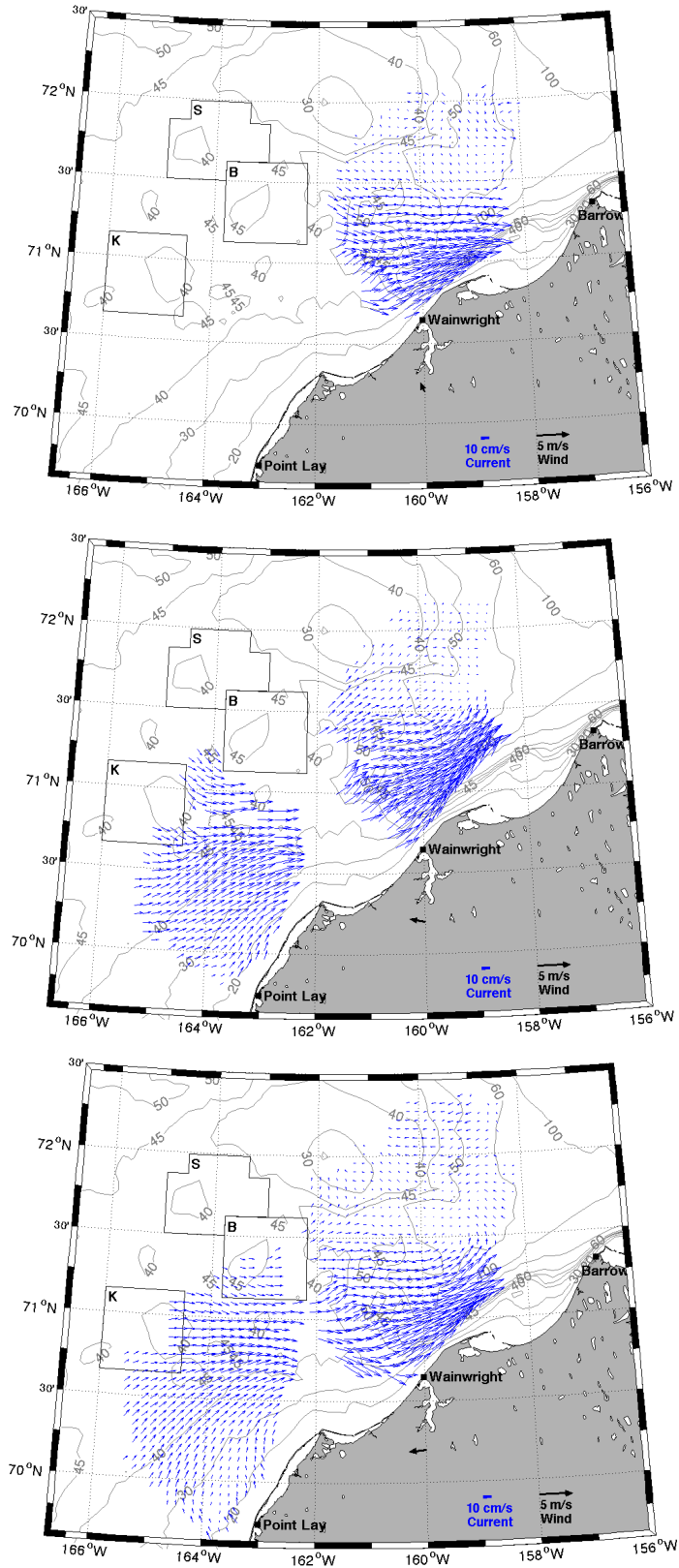


Figure 78. Mean surface currents in 2009 (top), 2010 (middle), and 2011 (bottom) when the ACC was flowing to the northeast.

71.5°N and along the east side of Hanna Shoal, surface currents are substantially weaker than elsewhere within the radar mask and the current vectors in this region show no consistent directional tendency among the years. Finally, the transition in flow from eastward to northeastward at the head of Barrow Canyon implies an along-shore surface divergence $\partial u/\partial x$ of $\sim 3 \times 10^{-5} \text{ s}^{-1}$. This corresponds to an along-shore Rossby number of ~ 0.2 , which suggests that the along-shore advection of along-shore momentum is dynamically important.

When the mean surface currents flow to the southwest within the ACC (Figure 79) the following general features emerge. First, the surface currents have a westward component over the entire area captured by the radars. Second, there is along-shore continuity in the nearshore flow field along the coast, e.g., the flow is southwest offshore of Wainwright and Point Lay. Third, the ACC has an offshore flow component seaward of Wainwright in accordance with the changing orientation of the isobaths in this region. Hence, surface waters flowing up Barrow Canyon can be spread both to the southwest and to the west over a broad region of the shelf. Fourth, as a consequence of the switch in isobath orientation, it appears (at least in 2011) that there is substantial along-shore convergence in the along-shore flow when the ACC is flowing to the southwest. Under this scenario $\partial u/\partial x$ of $\sim 3 \times 10^{-5} \text{ s}^{-1}$ with the Rossby number being ~ 0.2 . Fifth, current speeds for this scenario are much swifter than when the mean flow of the ACC is downcanyon.

4.4.5 Statistical Aspects of the Circulations

In this section we describe the spatial correlation fields among the velocity vectors and between the winds and the velocities. We start by examining the spatial correlation structure across the ACC at the head of Barrow Canyon. For this purpose we compute the correlation coefficient for the along-shore (56°T) and cross-shore (326°T) velocity components along a 100-km long transect, in which the innermost portion of the transect coincides with the mooring array (Figure 80). The results (Figure 81) indicate that the correlation coefficient decays to $1/e$ -of its maximum value (e.g., the e -folding width), which for the along-shore flow is ~ 40 km. This result agrees with the width of the current jet derived from the mooring data. The cross-shore velocity components are significantly correlated across the entire transect.

Additional information on the spatial structure of the current vector fields is deduced from maps of the complex correlation function [Kundu, 1976]. These are presented in Figure 82 as contour maps of r^2 , the square of the magnitude of the complex correlation coefficient. Only the results from 2011 are shown, since the other years had similar patterns. In each map the asterisk shows the reference vector upon which all vectors were correlated. The maps indicate that the flow field is largely correlated over most of the radar mask with two notable exceptions. The first region lies to the north of $\sim 71.5^\circ\text{N}$, i.e., that portion of the shelf between Barrow Canyon and Hanna Shoal. The second area is over the inner shelf (depths < 30 m) from Point Lay north to about 70.5°N . In the previous section we identified both of these regions as appearing distinct based on the mean vector distributions.

We also computed the empirical orthogonal functions (EOFs) using currents aligned along the major axis and the minor axis for each year. In each year, mode 1 for the major axis component

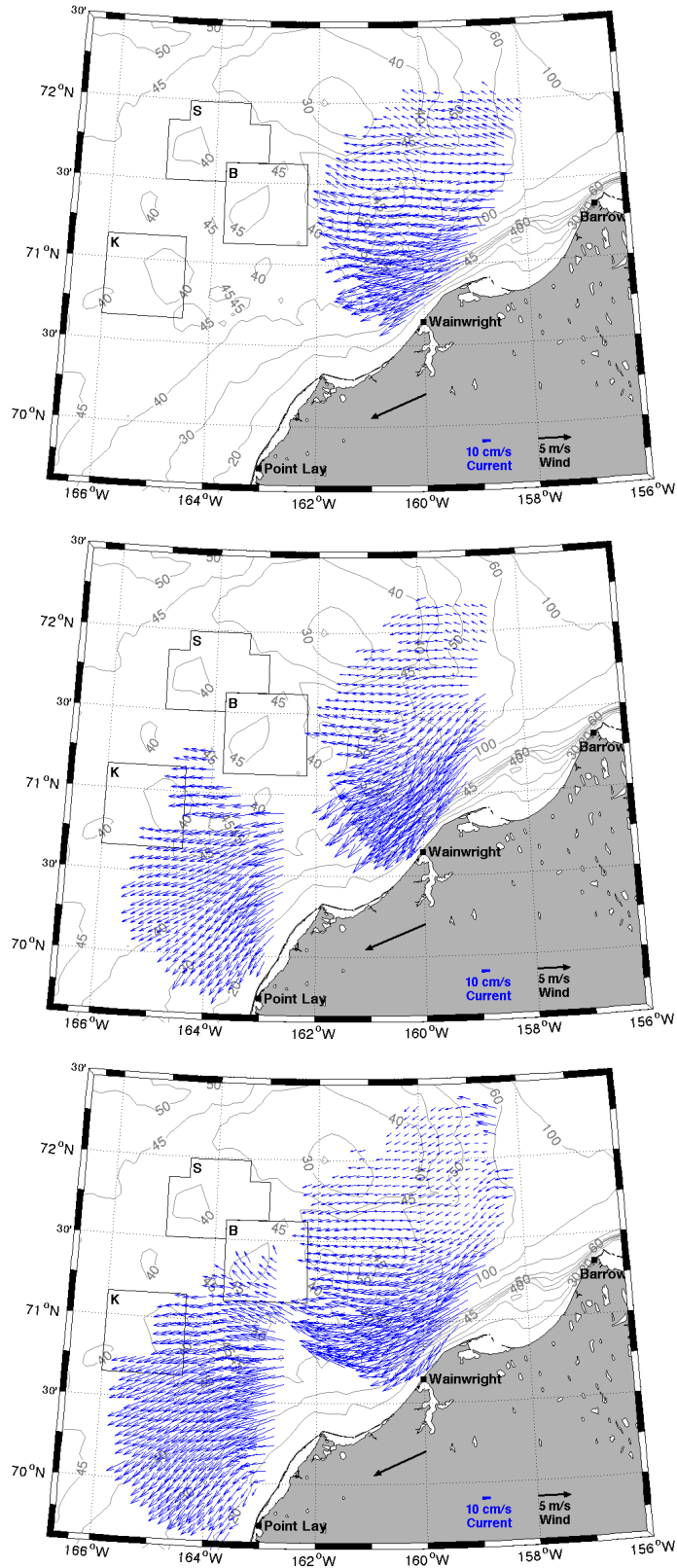


Figure 79. Mean surface currents in 2009 (top), 2010 (middle), and 2011 (bottom) when the ACC was flowing to the southwest.

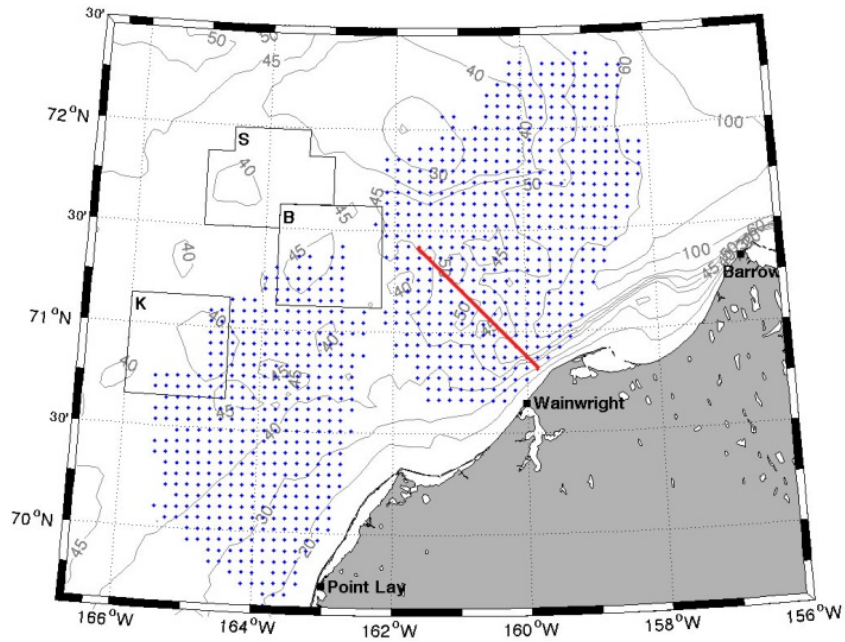


Figure 80. Location of the HFR transect (red line) used for surface current correlations across the ACC, which are shown in Figure 81.

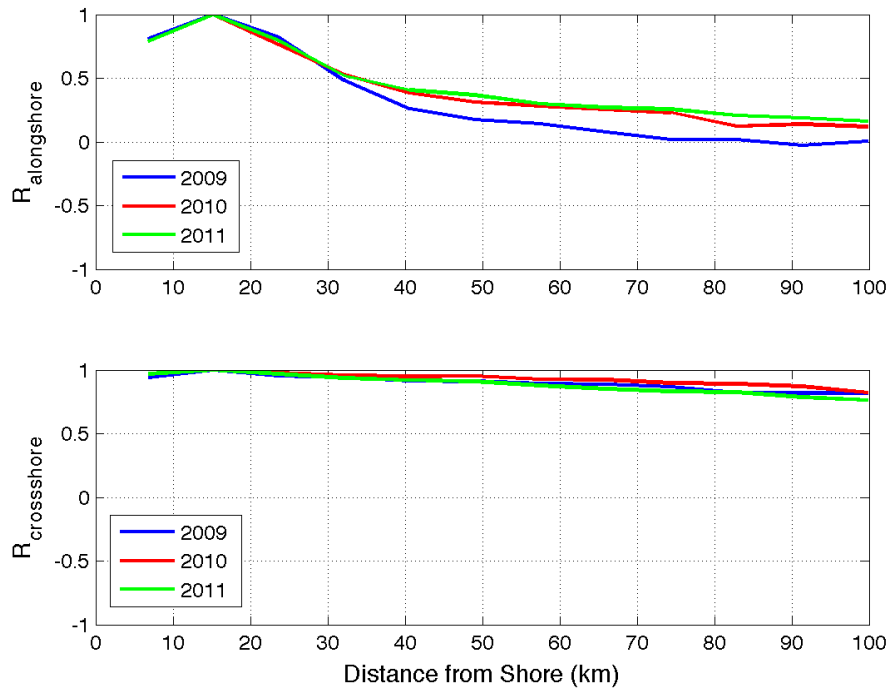


Figure 81. Cross-correlation coefficients (R) as a function of distance along the transect shown in Figure 80. All correlations were computed with respect to the values at ~ 15 km from shore, where $R = 1$.

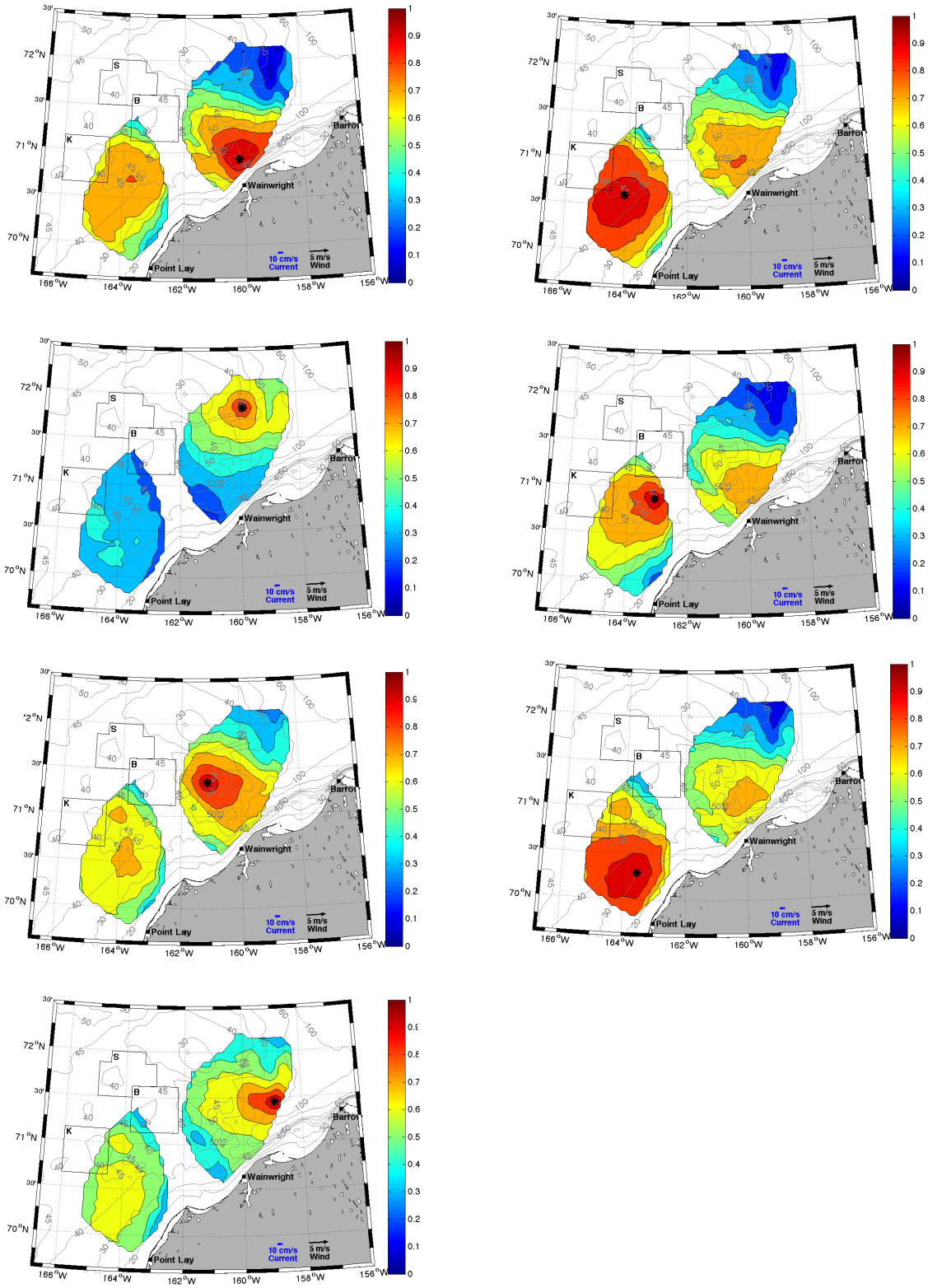


Figure 82. Contour maps for 2011 of r^2 , the magnitude squared of the complex correlation coefficient. The black asterisk represents the origin of the correlation, and the color bar to the right of each plot denotes the value of r^2 .

accounts for more than 75% of this current component's variance. None of the other modes comprise more than 8% of the variance. We show only the 2011 results (Figure 83), since those from 2010 are similar, and the 2009 data set had reduced spatial coverage. The structure of the first mode indicates that the ACC, and a broad region to the west and southwest of the ACC, are coherent and in phase. North of 71.5°N the eigen-weights are small, indicating very little mode 1 influence in this region. Once again the region offshore of Point Lay appears distinct from the rest of the shelf insofar as this region is out-of-phase with the ACC. The EOFs for the minor axis velocity components are not shown, since no mode accounts for more than ~30% of the current variance, and the complicated modal structures do not permit simple interpretations.

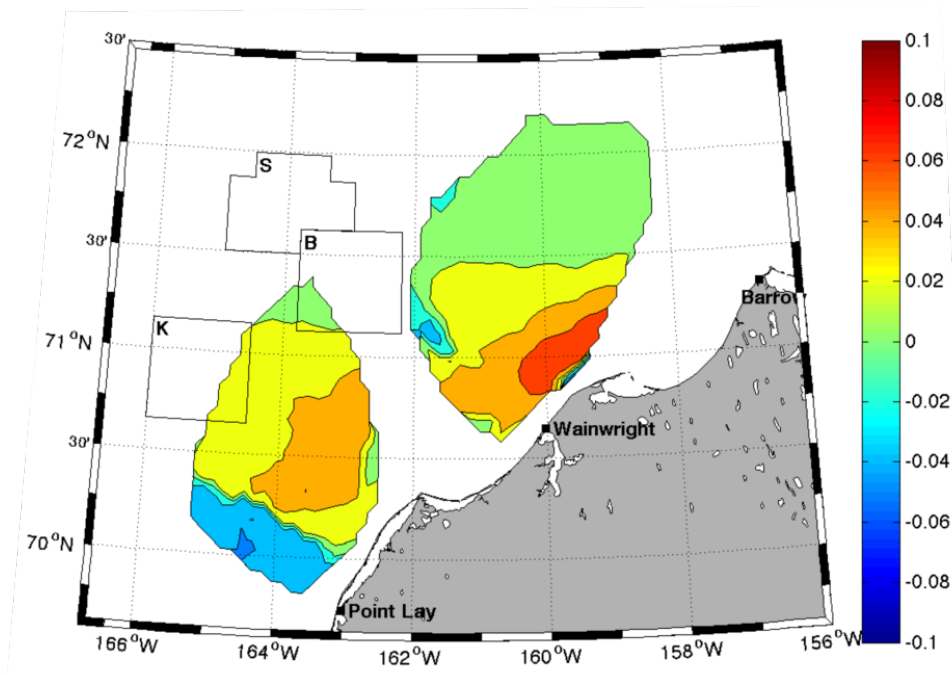


Figure 83. The first eigenmode of the major axis velocity component from 2011.

4.4.6 Wind-Current Relationships

We computed the wind-current complex correlation function for each year and mapped the values of the magnitude squared of the correlation coefficient r^2 and the phase angle (θ , where $\theta > 0$ means the wind vector is rotated counterclockwise from the velocity vector). The values of r^2 are contoured in Figure 84. Overall we find that 40 – 60 % of the current variance is explained by the wind, with wind-current correlations generally stronger in 2009 and 2010 than in 2011. The angles between the wind and current vector change systematically across the region. Over the offshore regions, these angles are between 35° and 60°, as might be expected assuming Ekman dynamics. Inshore and within the ACC the angles vary between -20° and 20°. These differences are not necessarily surprising given that in this region the magnitudes of the correlation are smaller and, as previously suggested, is an area of non-linear dynamics associated with veering, eddies, and retroflexion of the onshore flow.

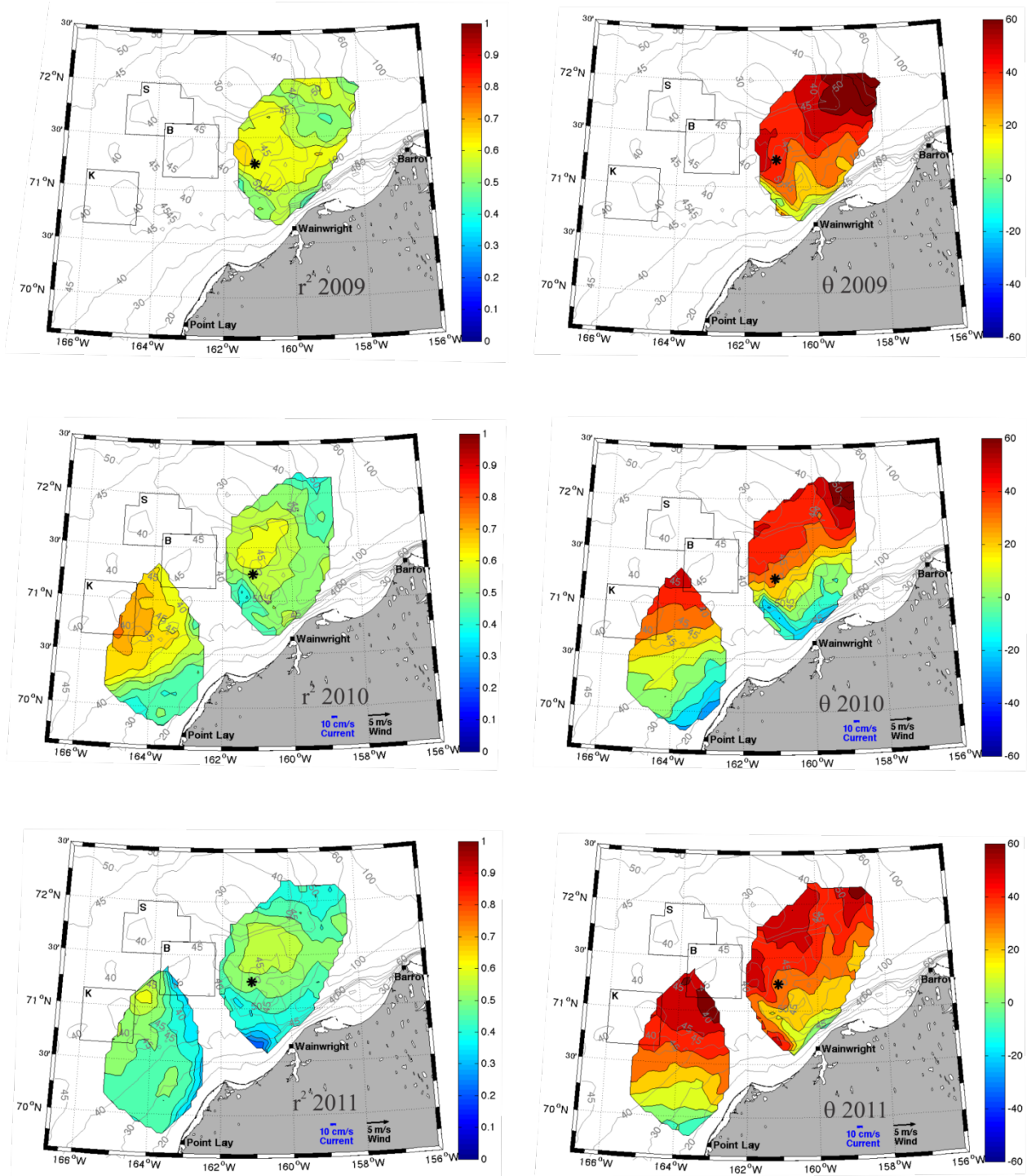


Figure 84. Wind-current complex correlation results for each year. The left-hand panels map r^2 and the right-hand panels map phase, θ . Color bars to the right of each map denote the values of the respective mapped variables. The asterisk is the location of the NARR wind grid point used in the analysis.

4.5. Hydrography from Gliders

The CTD data collected by the gliders is unique with regards to its high horizontal resolution, ~300 m between the top of individual vertical zig-zags. This allows us to examine the mixed layer and its dynamics in detail, in particular its horizontal density structure. During the 2010 and 2011 seasons we operated three gliders over a large area of the northeast Chukchi Sea, extending between 69 to 72°N and 165 to 157°W (Figure 85). A summary of the total distance covered, number of vertical profiles collected, and mission durations is given in Table 3. The hydrography presented here was derived from that collected only during glider downcasts. These data have been averaged into 1 dbar (~1 m) pressure bins.

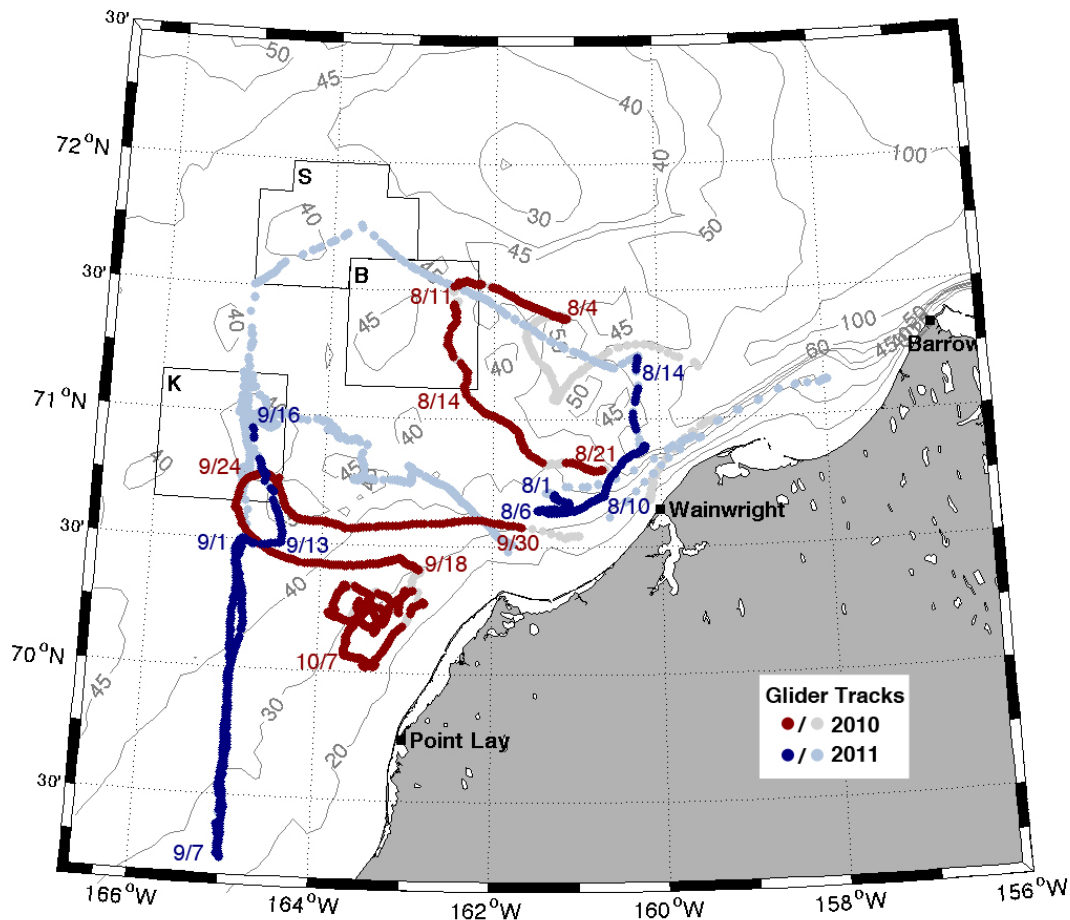


Figure 85. Map showing the 2010 and 2011 glider survey tracks in the northeast Chukchi Sea. Also shown are the three main lease patches (Burger (B), Klondike (K), and Statoil (S); black boxes). The darker-shaded glider tracks are discussed in this report.

4.5.1 Glider 159 Deployment: August 4 – 21, 2010

In 2010, glider 159 was initially deployed offshore of Wainwright but was rapidly advected towards Barrow Canyon. Fearing that it might be swept down the canyon, the glider was

recovered and redeployed to the northeast of the canyon. Beginning August 4, glider 159 moved westward into the northeast corner of Burger and thence southward through Burger before turning eastward toward the coast. It was recovered offshore of Wainwright on August 21. The August 4 - 21 survey is shown by dark red dots in Figure 85. We have broken the data up into two separate transects; the first being the westbound transect between August 4 and 10 (Figure 86) and the other being the southward and onshore transect between August 12 and 21 (Figure 87). Unlike the other glider sections described in this section, there was insufficient HFR coverage over this glider path for mapping the surface currents. Note also that some portions of Figures 86 and 87 lack data because the glider did not come close enough to the surface or bottom along segments of each transect. The hydrographic data from the westward transect show a prominent, spatially uniform “winter-water pool” where waters below ~20 m depth were cold ($\leq -1^\circ\text{C}$) and salty (32 - 33). These dense waters were formed the previous winter during ice formation on the Chukchi and/or Bering shelves. Waters above 20 m were slightly warmer ($\geq 0^\circ\text{C}$) and fresher (≤ 31), with the warmest ($>1.5^\circ\text{C}$) and freshest waters (28.5 - 31) confined to the upper 10 m of the water column. The upper layer waters are ice meltwater products, heated to some extent by solar radiation. Of particular importance is the extremely shallow, thin (~10 m), and strong pycnocline, across which salinity (and density) increases by ~3 (3 kg m^{-3}). This strong stratification is characteristic of the Burger region in August [Weingartner *et al.*, 2013] and likely extends northeastward across the shelf (east of Hanna Shoal).

Subsurface water properties along the first 60 km of the onshore transect (August 11 – 21; Figure 87) were similar to those along the westbound transect in that these consisted of very dense winter waters. However, the upper layer over these first 60 km was warmer (with temperatures between 3 and 5°C) and slightly saltier (30 – 31 versus <30). As the glider moved onshore the dense winter waters along the bottom disappeared (between km 60 and 90 in Figure 87) and the stratification also weakened. Eventually the strongly stratified two-layer structure was replaced by nearly vertically homogenous waters, with water temperatures of 5 - 6°C and salinities < 32 .

Although HFR data were not available during this period, the portion of the shelf occupied by the warmer and more moderately saline water is generally flowing eastward in August [Weingartner *et al.*, 2013; and unpublished data], transporting summer waters from the Bering Sea eastward from the Central Channel across Klondike and the southern portion of Burger. The large differences in water properties between these two sections implies that there is a large front separating eastward moving, well-mixed Bering Sea Water in the south from the strongly stratified, 2-layer system composed of meltwaters and winter waters observed along the westbound transect to the north.

Note that while the subsurface horizontal temperature gradients are large ($\sim 6^\circ\text{C}/40 \text{ km}$), these do not contribute to large horizontal gradients in density, which are $\sim 1 \text{ kg}\cdot\text{m}^{-3}/40 \text{ km}$. Nevertheless, these density gradients support an eastward geostrophic, baroclinic flow, which can be estimated from the thermal wind balance:

$$\partial u / \partial z = -(g/\rho f)(\partial \rho / \partial y) \Rightarrow u \sim -(g/\rho f)(\Delta \rho / \Delta y) \Delta z$$

Here $\partial u / \partial z$ is the vertically sheared, eastward component (u) in geostrophic velocity, where the shear is confined to the bottom 20 m of the water column. For $g = 9.8 \text{ m s}^{-2}$, $\rho = 1025 \text{ kg m}^{-3}$, $f = 1.37 \times 10^{-4} \text{ s}^{-1}$, $\Delta \rho = 1 \text{ kg m}^{-3}$, $\Delta y = 40 \text{ km}$, and $\Delta z = 20 \text{ m}$, u is $\sim 3 \text{ cm s}^{-1}$ which is small compared

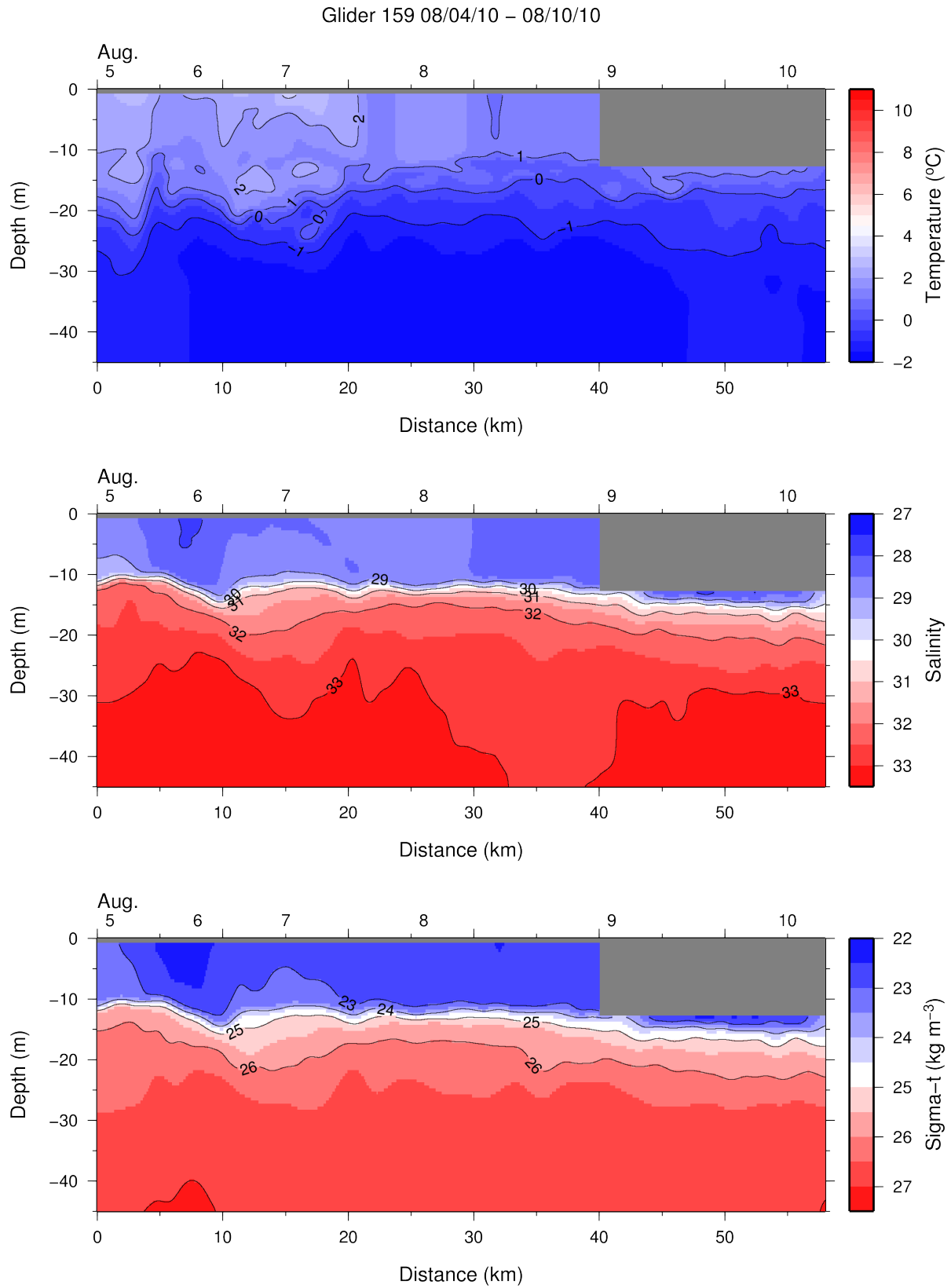


Figure 86. Section plots of temperature (top panel), salinity (middle panel), and density (sigma-t; bottom panel) from glider 159, August 4-10, 2010 (see Figure 85 for section location).

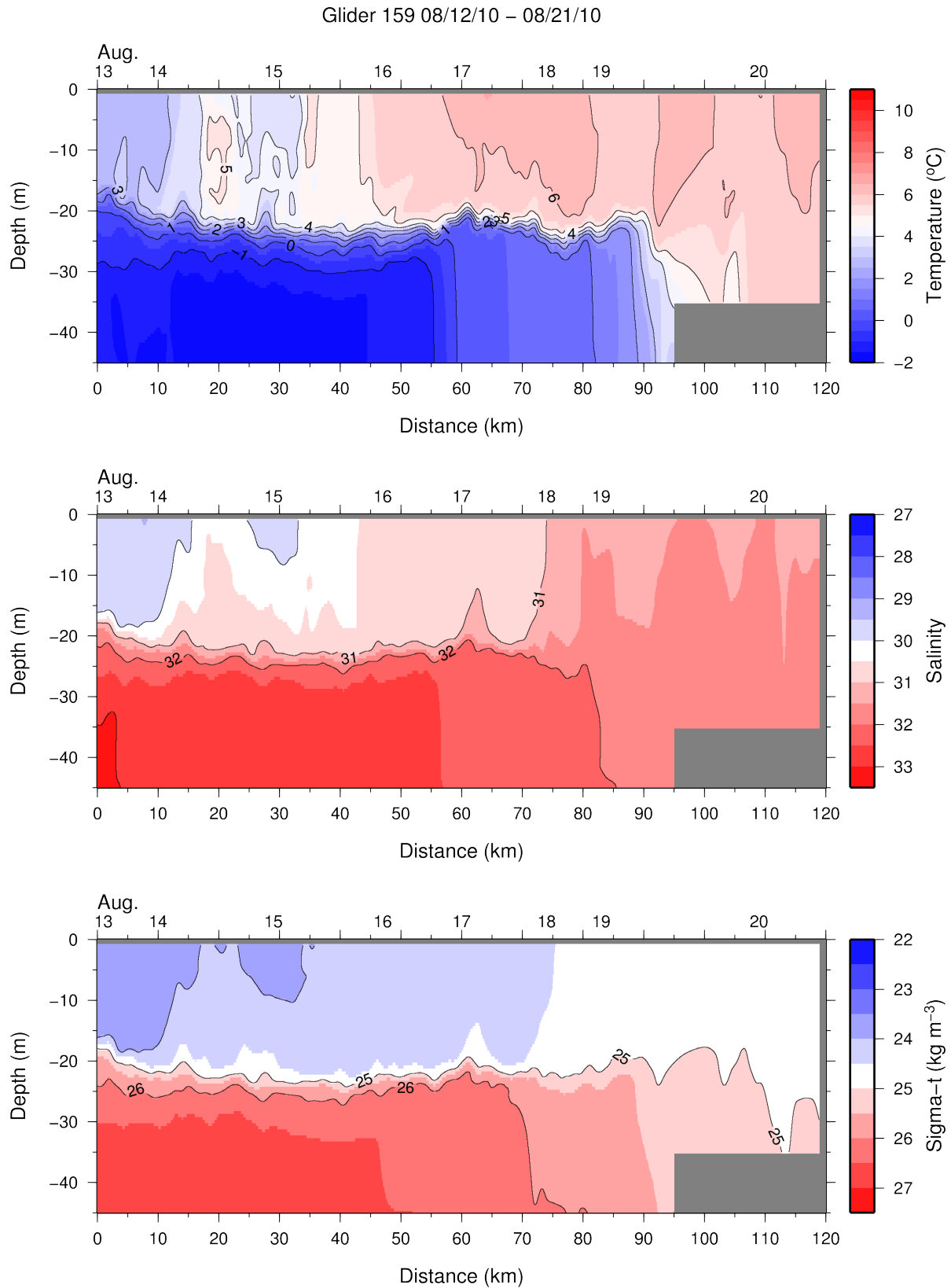


Figure 87. Section plots of temperature (top panel), salinity (middle panel), and density (sigma-t; bottom panel) from glider 159, August 12-21, 2010 (see Figure 85 for section location).

to the surface current speeds of 5 - 15 cm s⁻¹ often detected by HFR in this region. Away from the subsurface front, the geostrophic shears are even weaker. However, the heavy stratification portions of this transect suggest that the influence of the wind on the water column may be confined to the upper 15 m, so that this layer may be moving quite differently than the deeper waters.

4.5.2 Glider 159 Deployment: September 18 – October 10, 2010

Glider 159 sampled for 22 days after being deployed offshore of Point Lay on September 18, 2010 and recovered in the same area on October 10. The glider made minimal excursions (no more than 30 km from its mean position) because the rudder broke and the shallow waters made navigation and horizontal gliding difficult. We thus treat this glider mission to consist effectively of a series of repeated vertical profiles (in water depths of ≤ 30 m) at the same location. Figures 88 - 99 contain the mean daily surface currents and winds and Figures 100 - 101 show the hydrography along the glider track.

Winds on September 18 were light from the south, associated with a strong along-shore flow past Point Lay and into Barrow Canyon. On the 19th, winds were even calmer and to the east, as the divergent mode began to form in the surface currents. Winds from the northeast began on September 20 and intensified on the 21st, so that the nearshore flow fully entered the divergent mode before reversing entirely along the coast. The currents thereafter were generally southwestward except briefly on September 24 when winds calmed and for a 3-day period of northeasterly flow from September 27 – 30 under winds from the northwest. Winds from the northeast were very strong through early October and generated swift, along-shore flows to the southwest. These winds moderated on October 7 – 10, with the coastal flow becoming more weak and variable.

The hydrographic profiles indicate that the water column was well-mixed; the only substantive stratification occurred at ~ 25 m depth during the first 5 days of the survey. Given the weak stratification we surmise that the surface currents are representative of the flow throughout the water column. Temperatures decreased gradually from about 10°C to 6°C between September 19 and 30 and then very rapidly (from 6°C - 0°C) from October 1 to 10. Air-sea heat loss rates (obtained from the NARR modeled heat fluxes) suggest that the mean daily oceanic heat loss to the atmosphere was -112 W m⁻² for the entire period. This flux would have cooled the 30 m deep water column by 1.7°C over 22 days. To balance the observed cooling of $\sim 10^\circ\text{C}$ requires an oceanic heat flux divergence of 535 W m⁻², which is ~ 5 times greater than the oceanic heat lost to the atmosphere. Alongshore advection drew this cold water from Barrow Canyon and/or the northern shelf (as indicated by the current maps). This advection also accounted for the salinity increase of ~ 1 over the same period.

These results have important implications for sea ice formation processes on the Chukchi Sea shelf. *Weingartner et al.* [2013] showed that northward advection of heat from Bering Strait tends to delay cooling (and ice formation) from late summer through fall (at least) in the central Chukchi Sea. In September-October 2010, southwestward advection of cold water rapidly decreased nearshore water temperatures and thus primed this portion of the shelf for ice

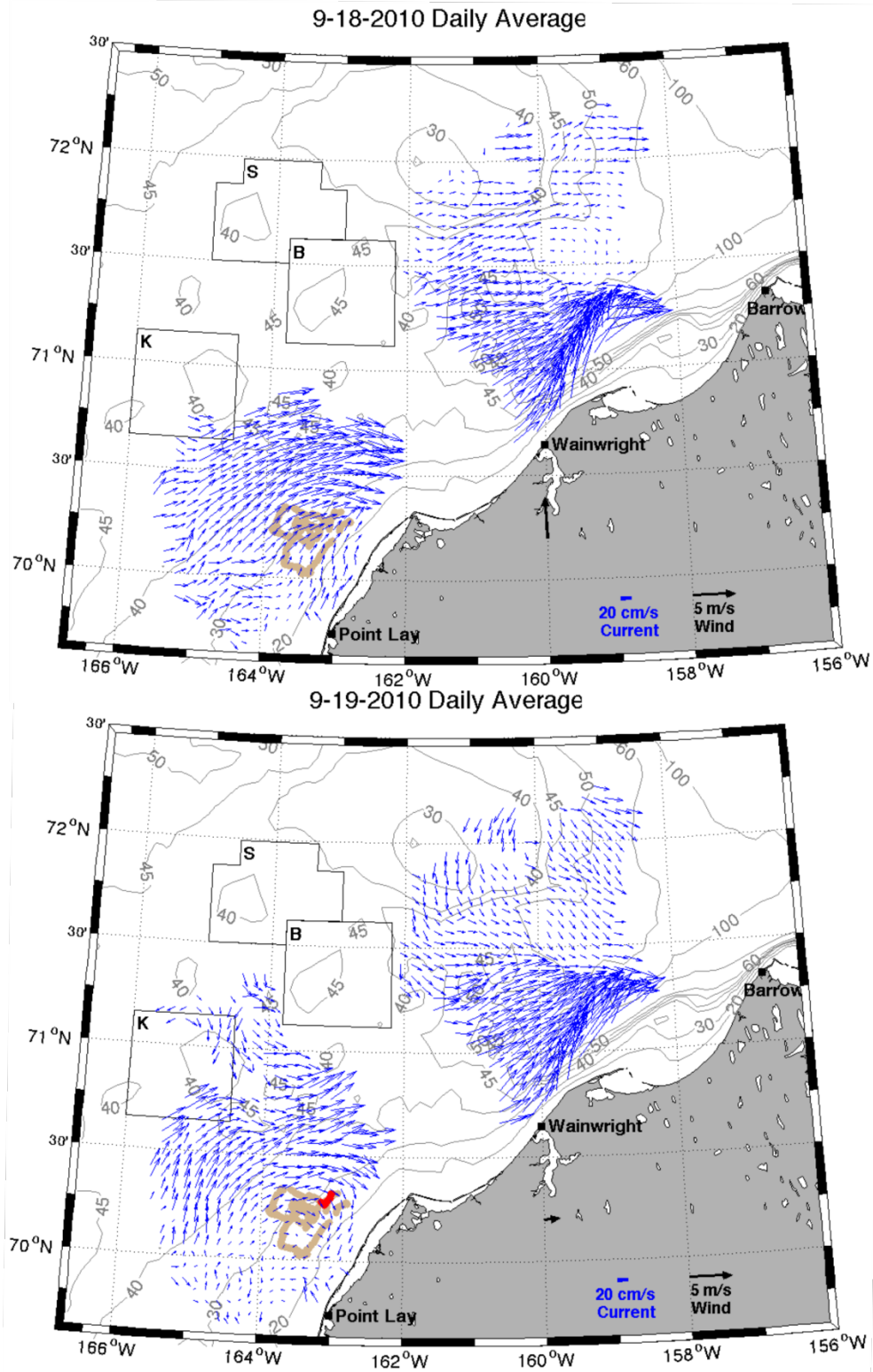


Figure 88. Mean surface currents on September 18 (top) and 19 (bottom), 2010. The glider track is red (denoting the track on the indicated day) and tan (denoting the entire glider track).

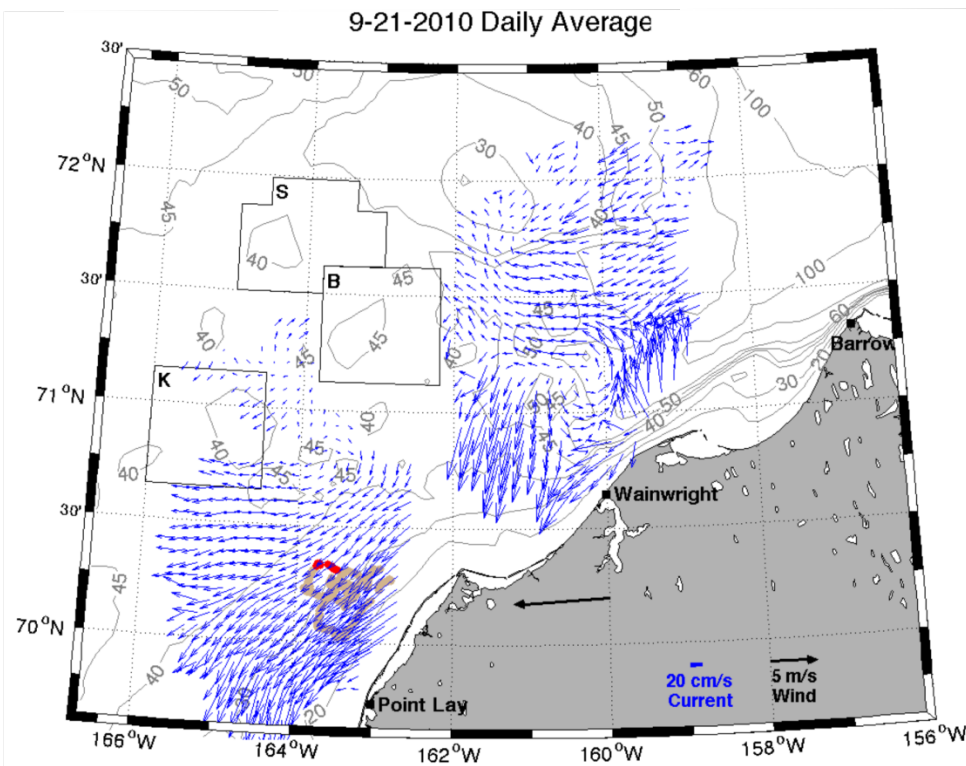
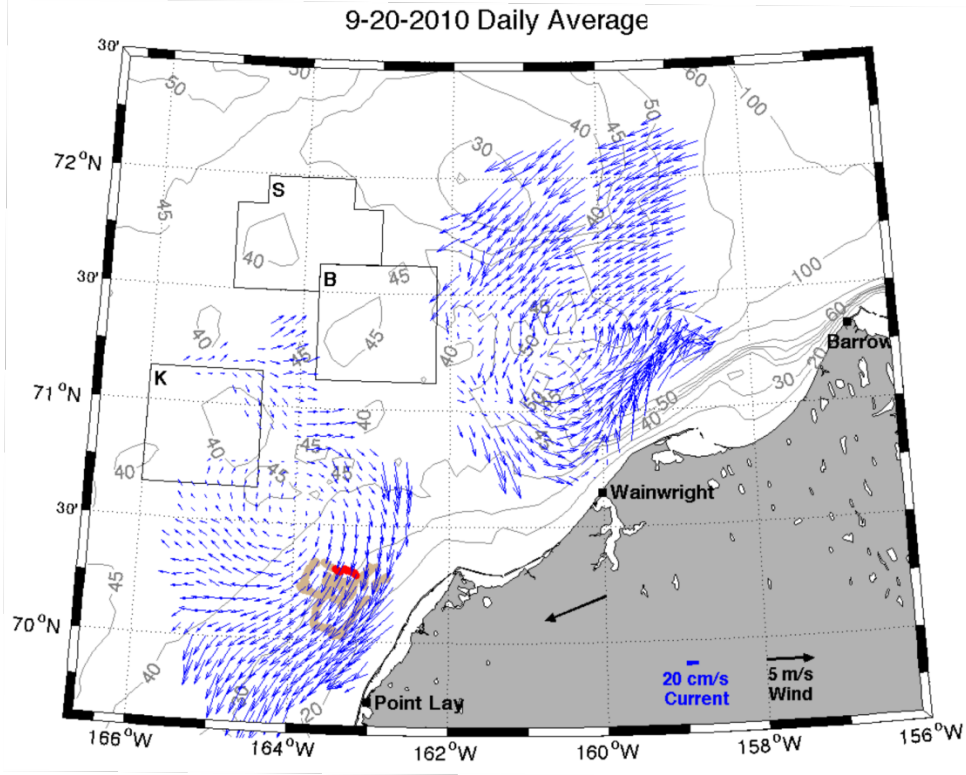


Figure 89. Mean surface currents on September 20 (top) and 21 (bottom), 2010. The glider track is red (denoting the track on the indicated day) and tan (denoting the entire glider track).

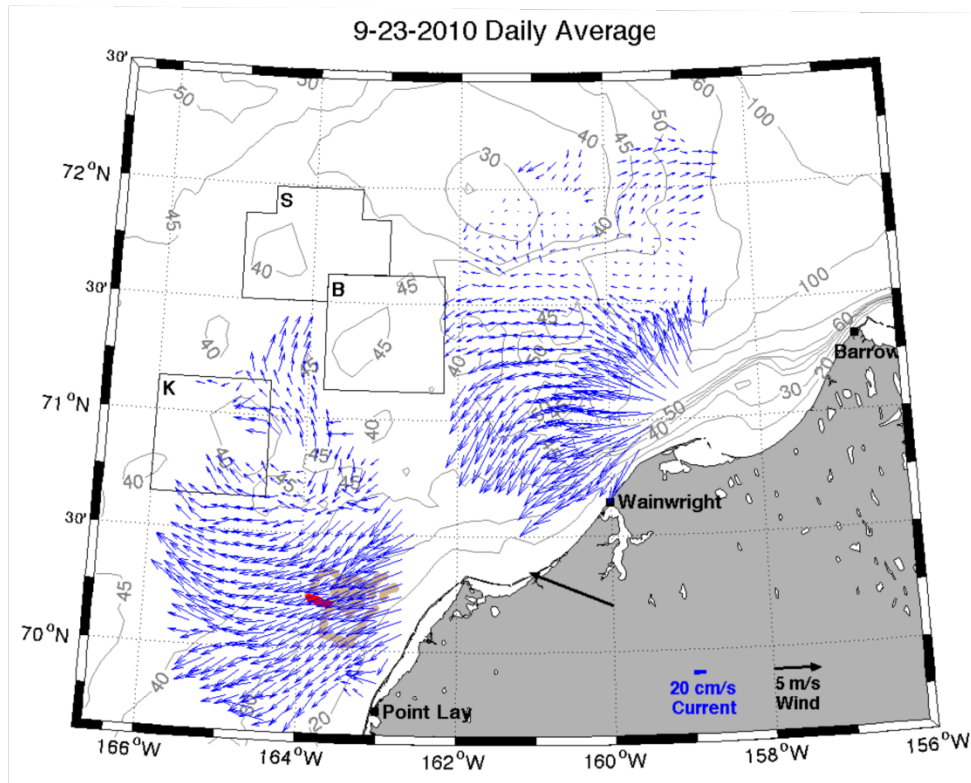
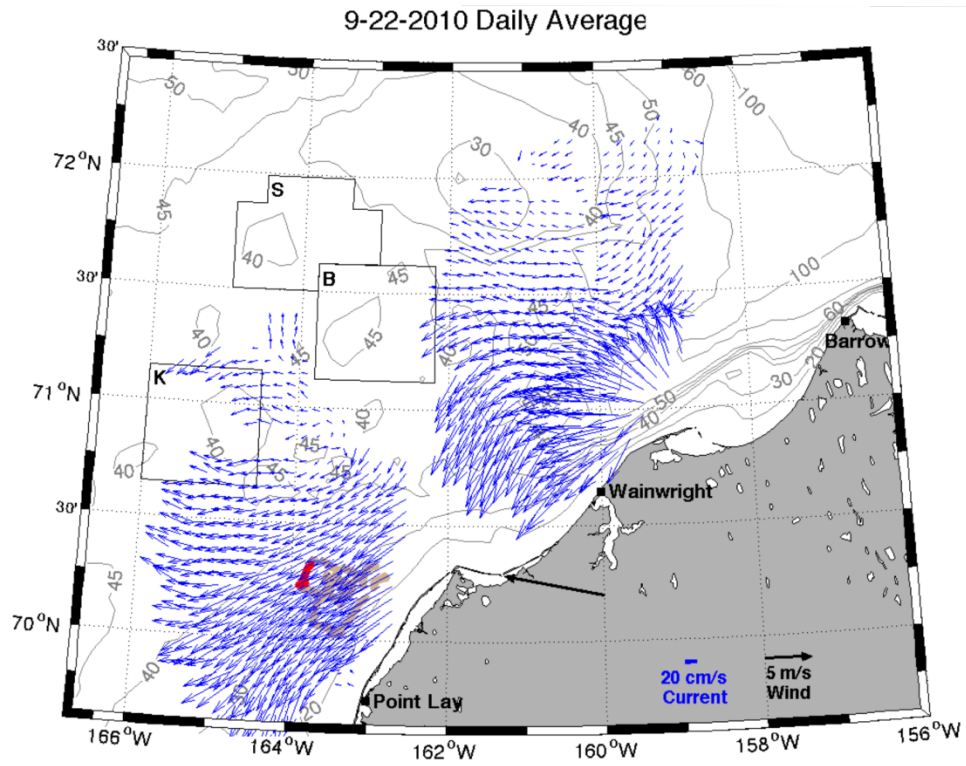


Figure 90. Mean surface currents on September 22 (top) and 23 (bottom), 2010. The glider track is red (denoting the track on the indicated day) and tan (denoting the entire glider track).

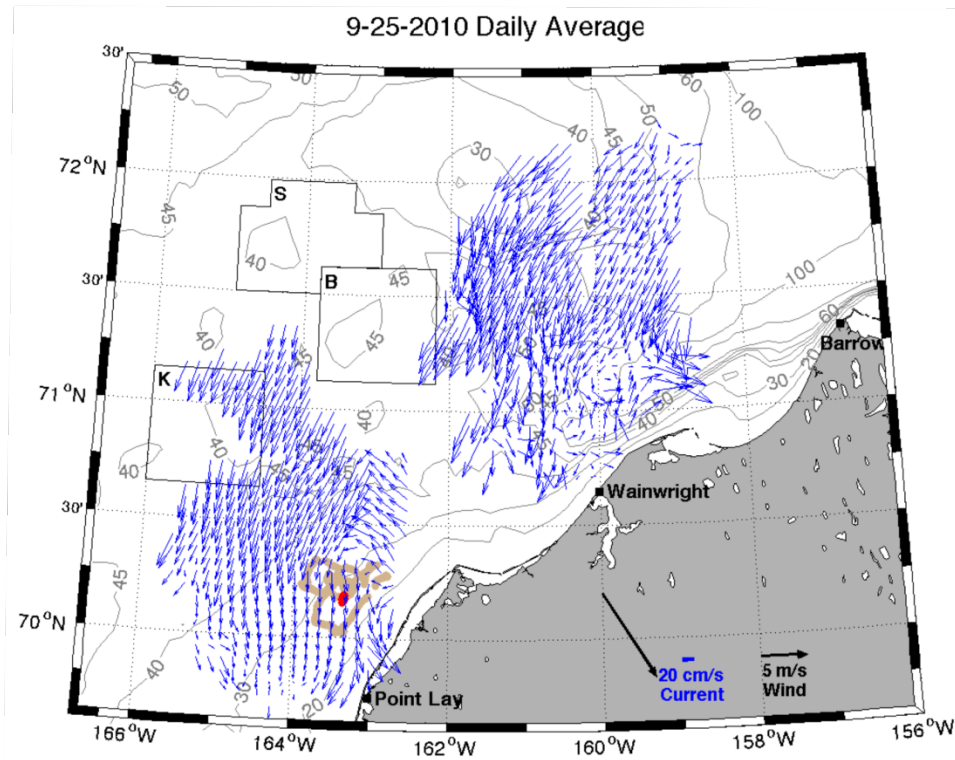
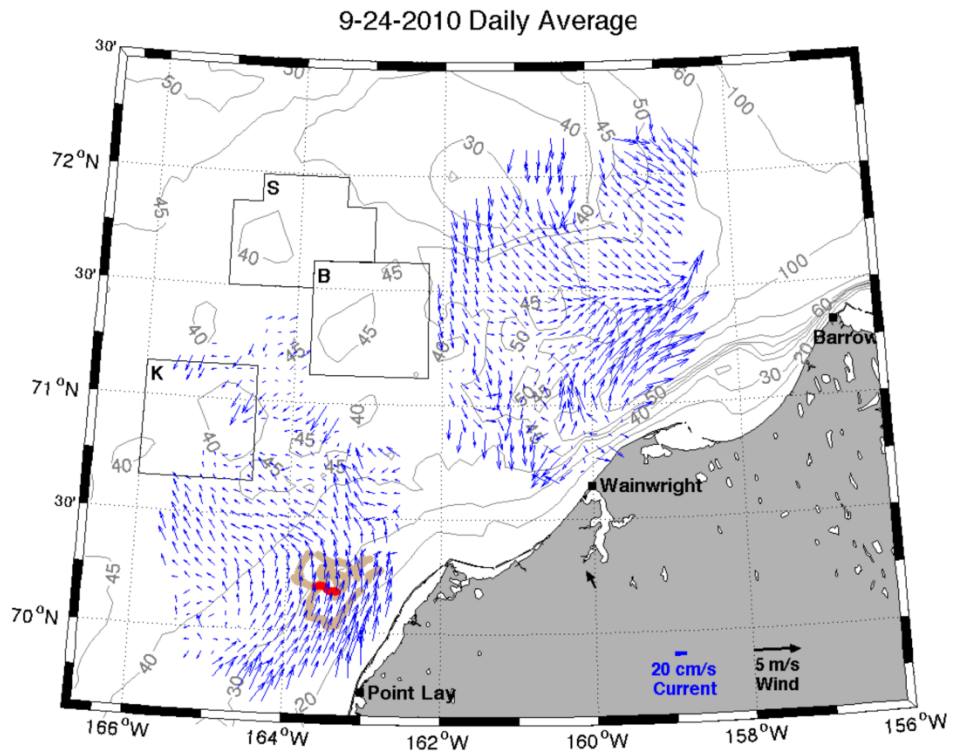


Figure 91. Mean surface currents on September 24 (top) and 25 (bottom), 2010. The glider track is red (denoting the track on the indicated day) and tan (denoting the entire glider track).

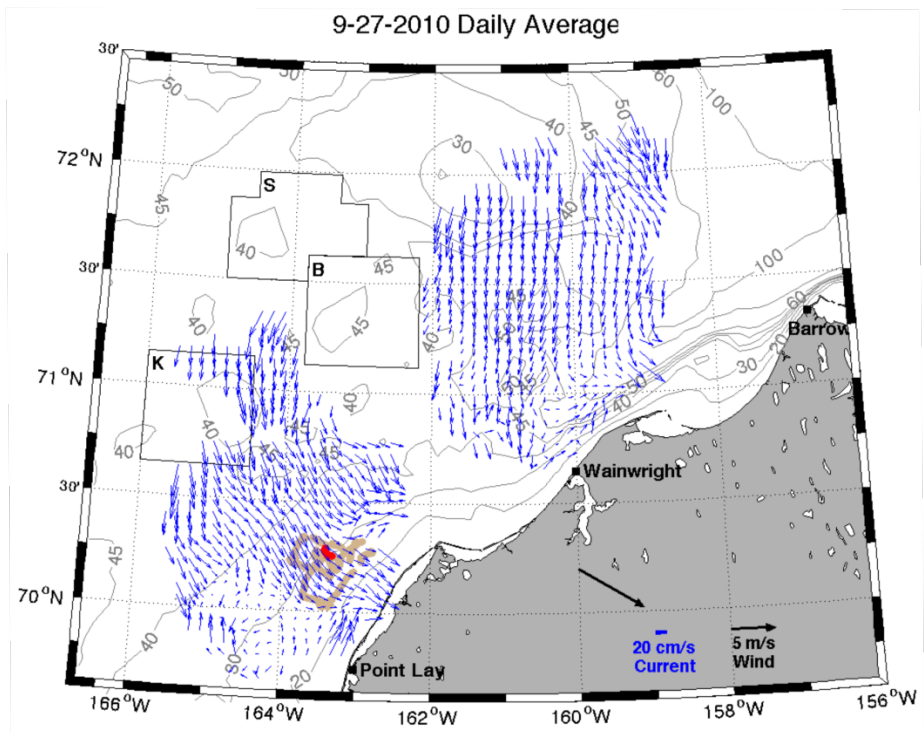
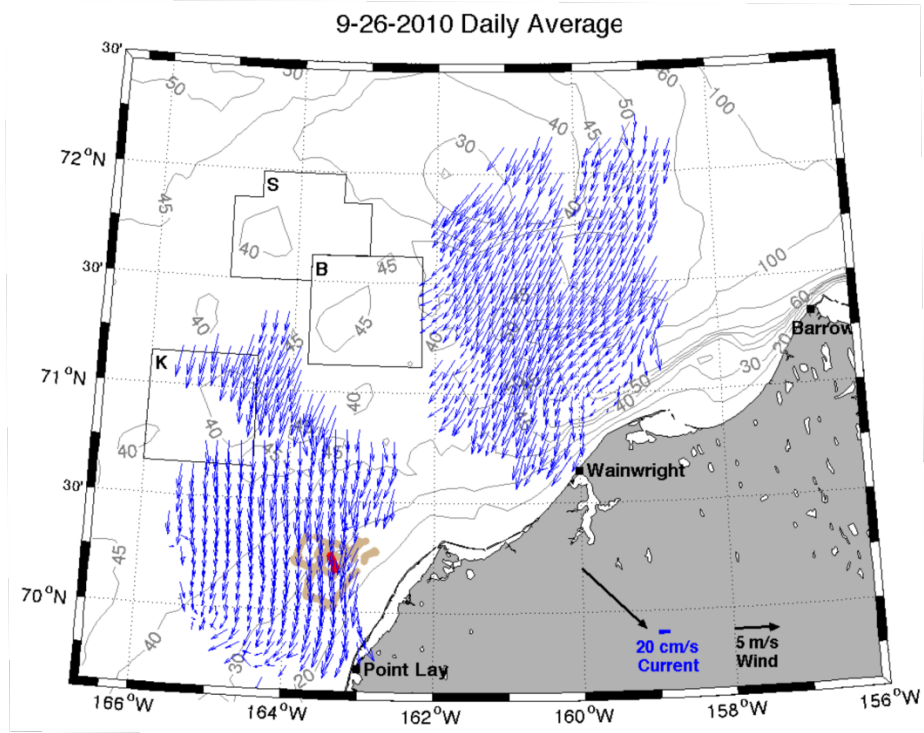


Figure 92. Mean surface currents on September 26 (top) and 27 (bottom), 2010. The glider track is red (denoting the track on the indicated day) and tan (denoting the entire glider track).

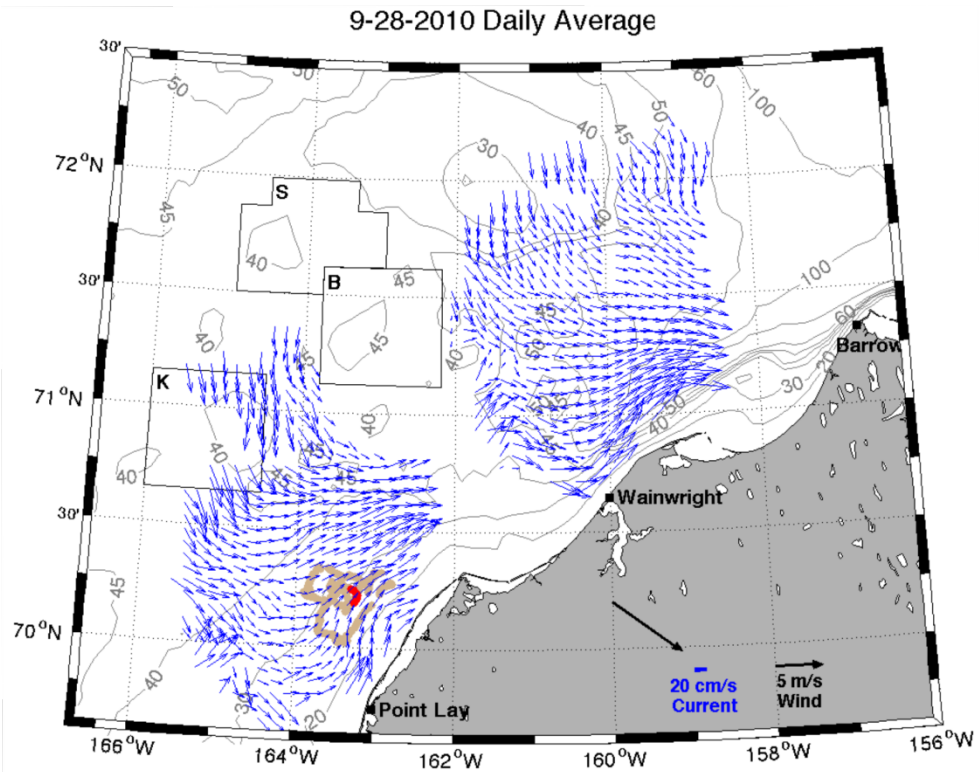


Figure 93. Mean surface currents on September 28 (top) and 29 (bottom), 2010. The glider track is red (denoting the track on the indicated day) and tan (denoting the entire glider track).

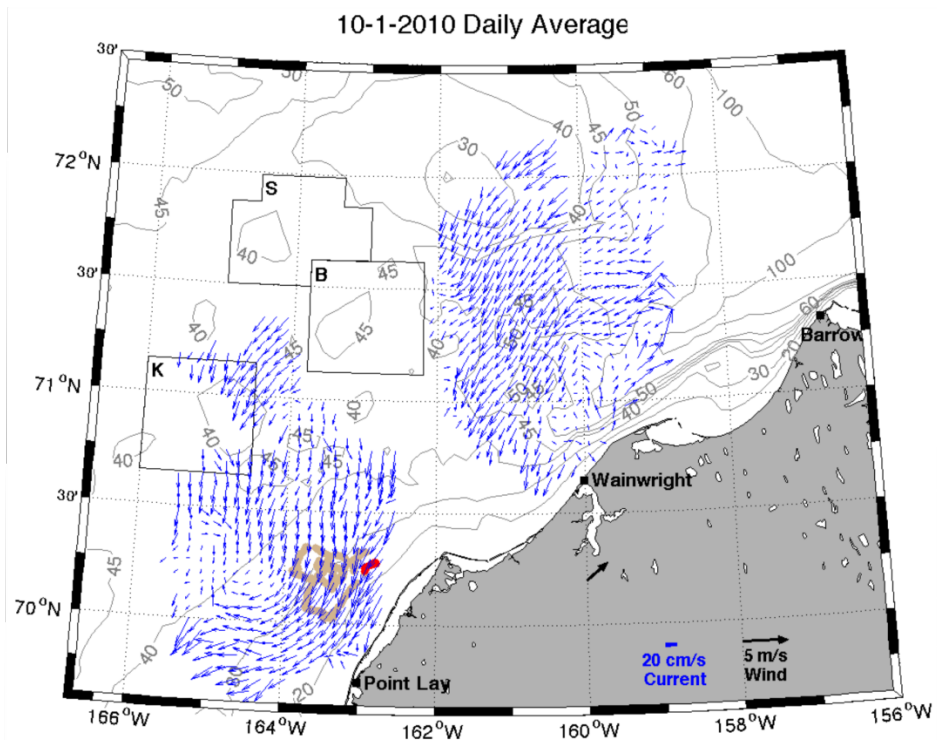
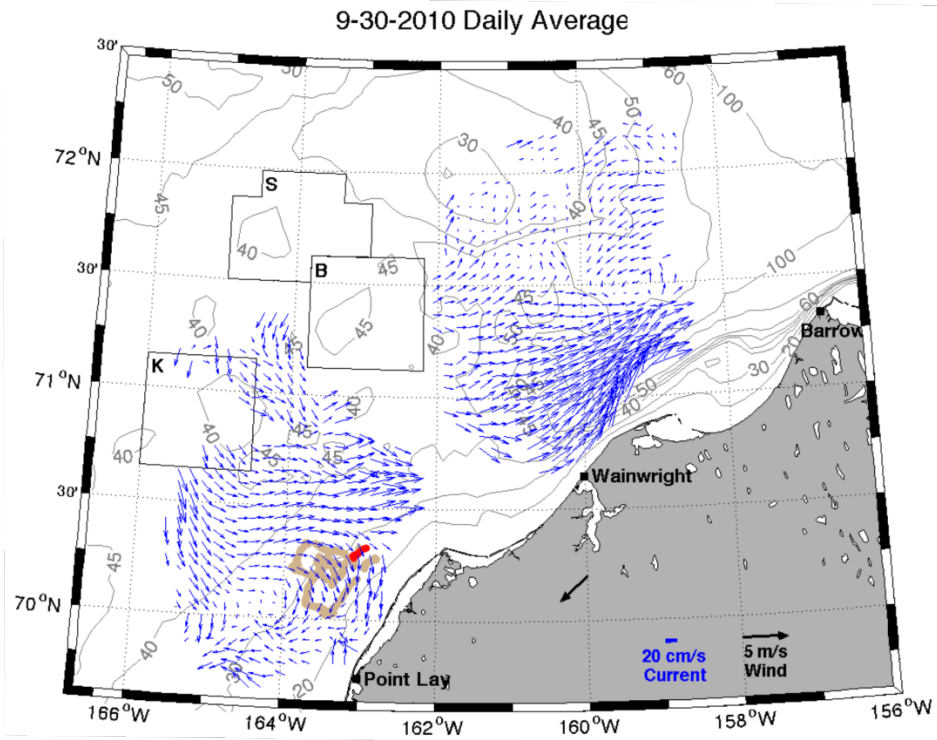


Figure 94. Mean surface currents on September 30 (top) and October 1 (bottom), 2010. The glider track is red (denoting the track on the indicated day) and tan (denoting the entire glider track).

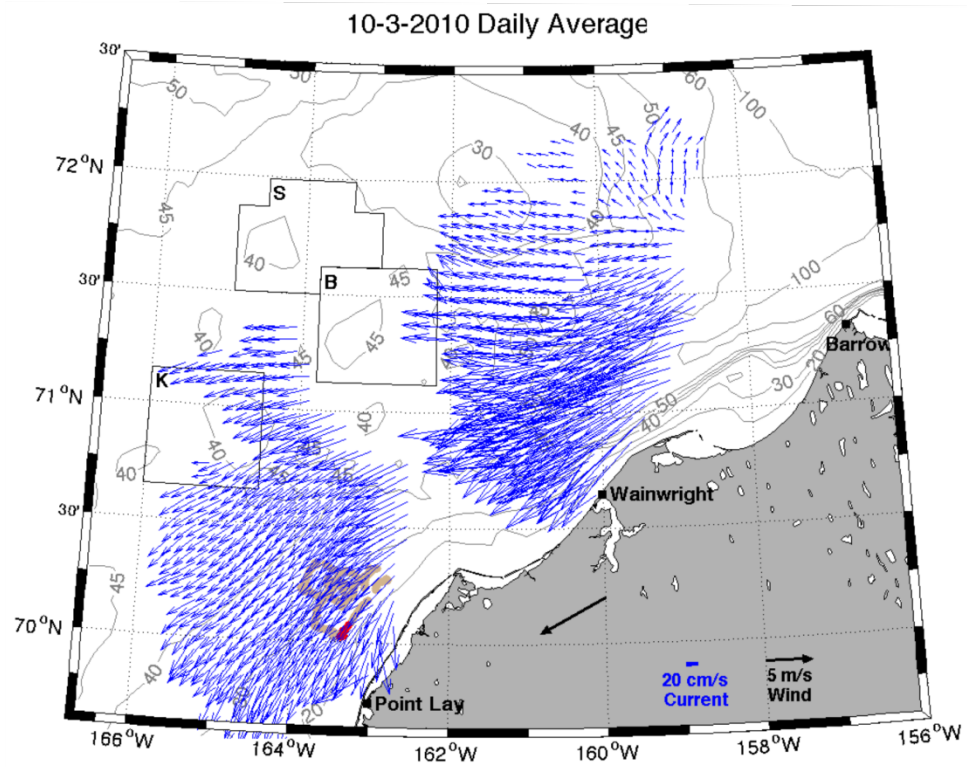
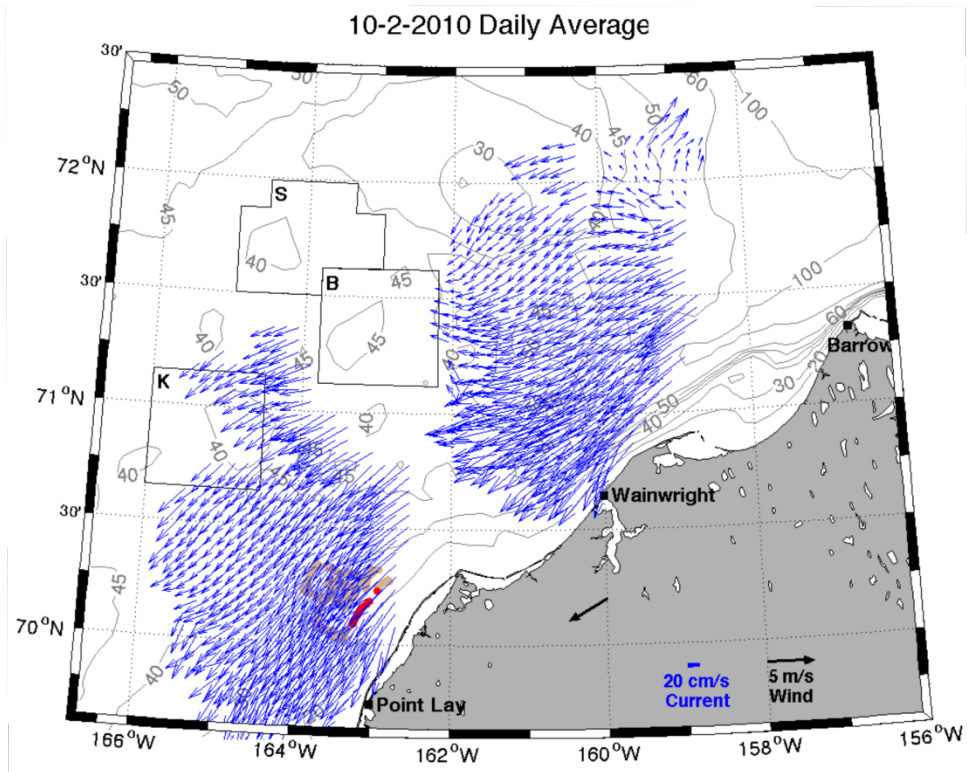


Figure 95. Mean surface currents on October 2 (top) and 3 (bottom), 2010. The glider track is red (denoting the track on the indicated day) and tan (denoting the entire glider track).

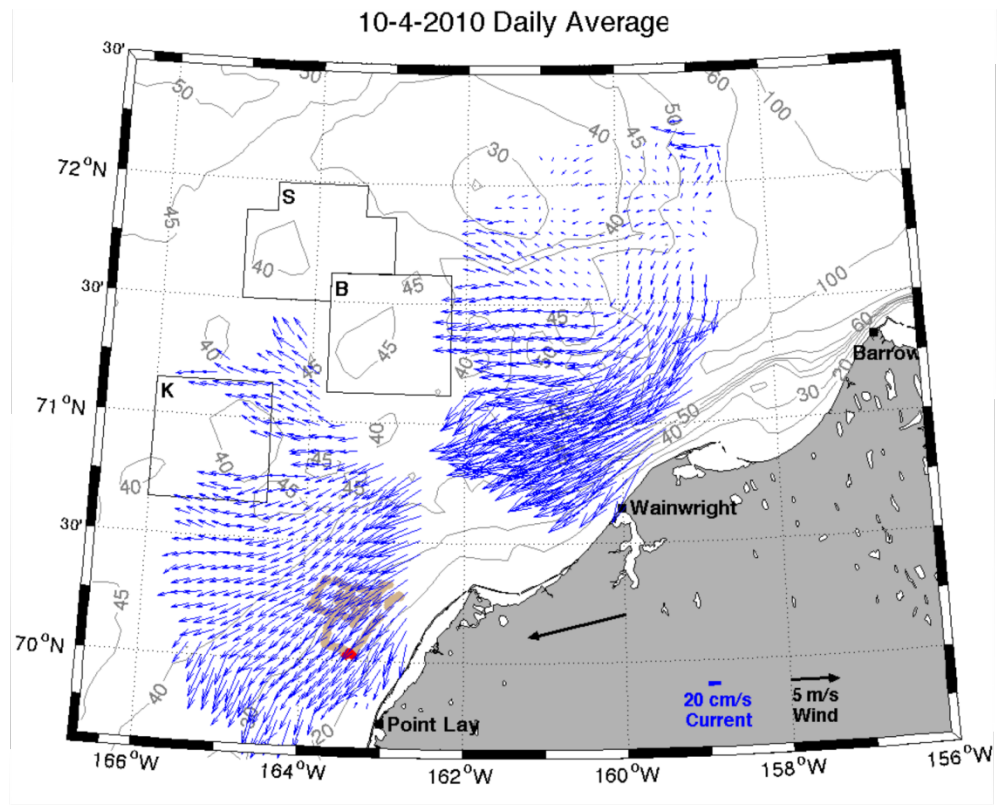


Figure 96. Mean surface currents on October 4 (top) and 5 (bottom), 2010. The glider track is red (denoting the track on the indicated day) and tan (denoting the entire glider track).

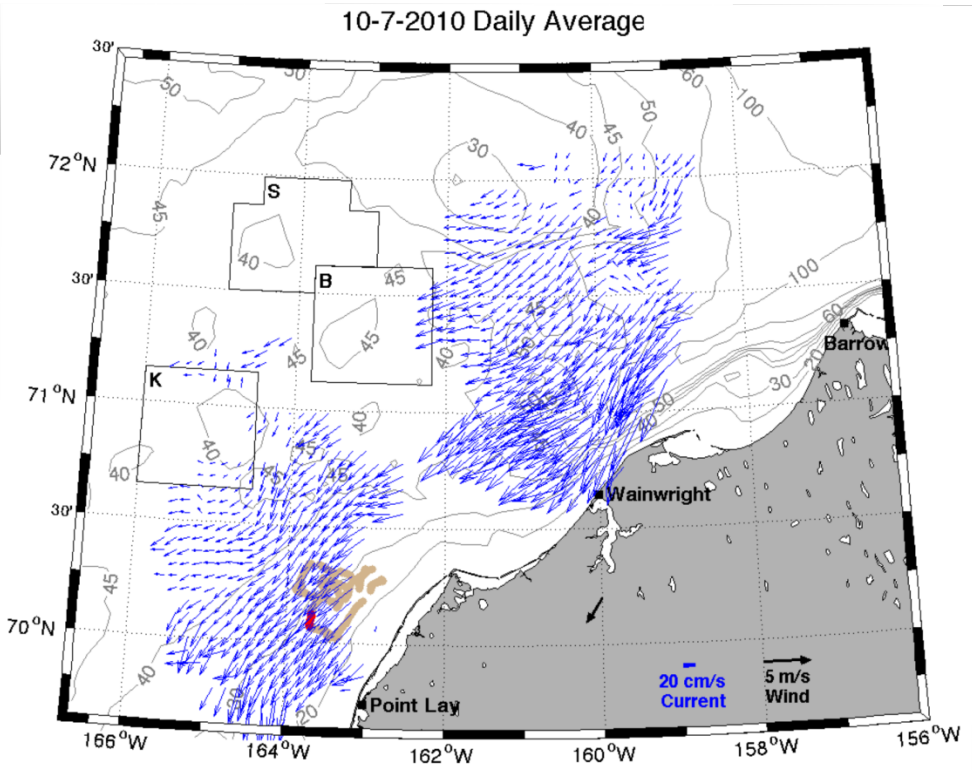
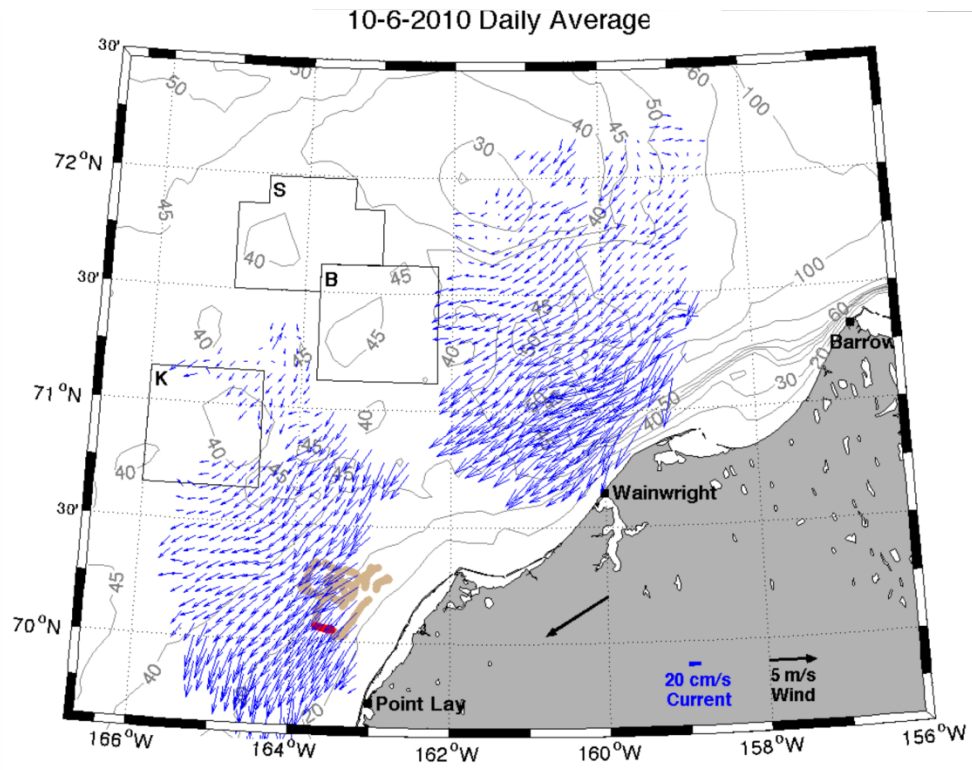


Figure 97. Mean surface currents on October 6 (top) and 7 (bottom), 2010. The glider track is red (denoting the track on the indicated day) and tan (denoting the entire glider track).

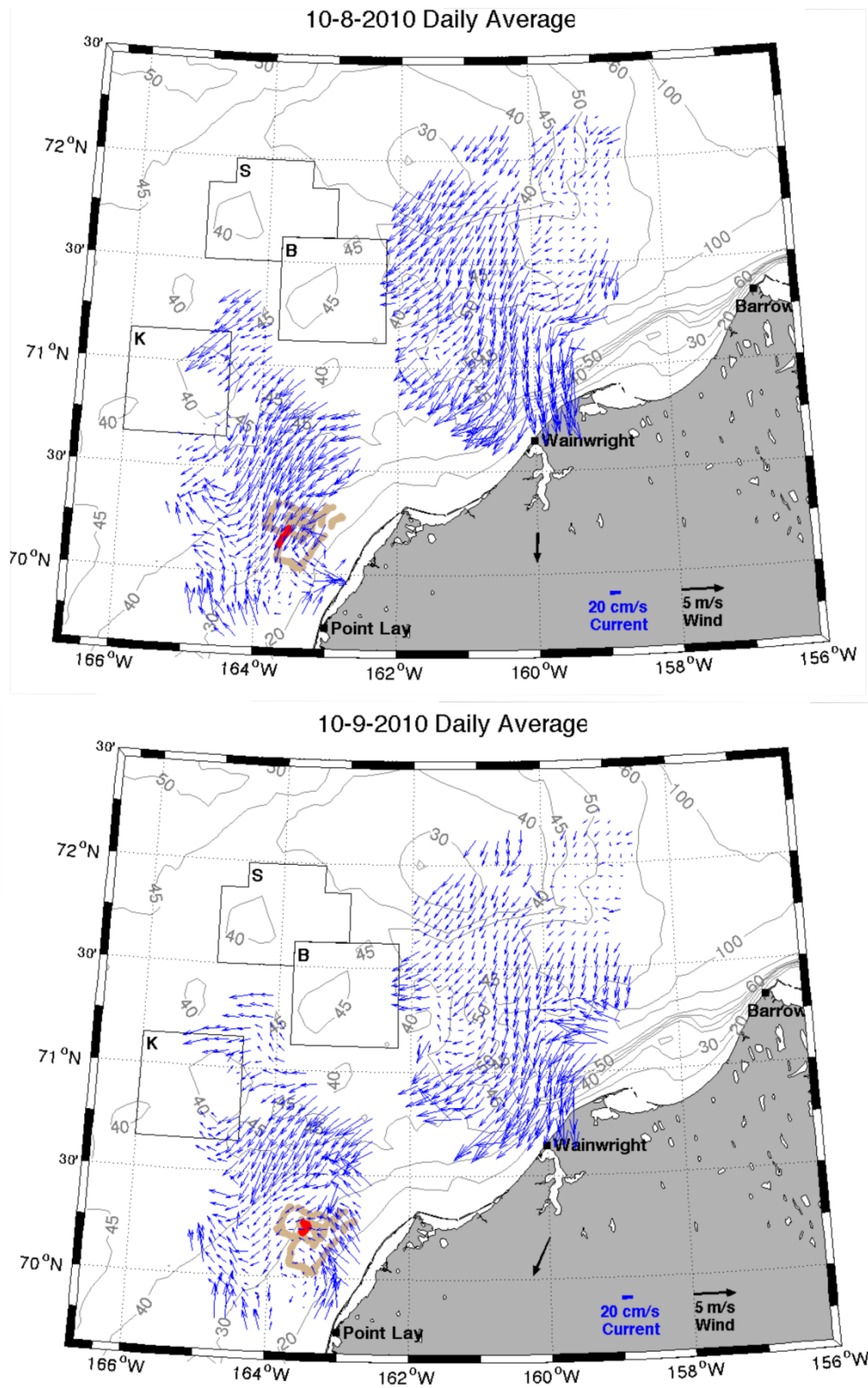


Figure 98. Mean surface currents on October 8 (top) and 9 (bottom), 2010. The glider track is red (denoting the track on the indicated day) and tan (denoting the entire glider track).

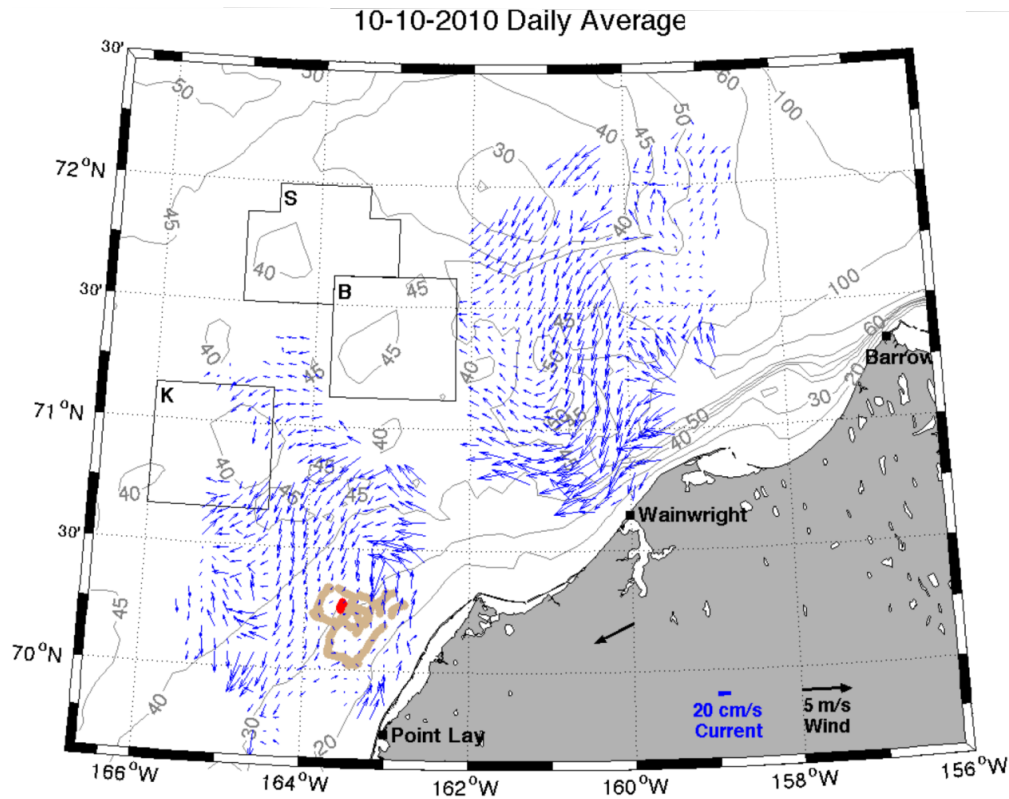


Figure 99. Mean surface currents on October 10, 2010. The glider track is red (denoting the track on the indicated day) and tan (denoting the entire glider track).

formation. Moreover, the mean flow in October 2010 was southwestward (Figure 64) implying that the cold water advected into the area in early October was not replaced by warmer water later in the month. For the next 15 days the mean daily heat loss to the atmosphere averaged $\sim 165 \text{ W m}^{-2}$, which was sufficient to decrease ocean temperatures to the freezing point whereupon ice formation could have begun. These results, along with *Weingartner et al's* [2013], further underscore the importance of advection in the shelf heat budget of the Chukchi Sea and imply that realistic predictions of ice formation will require accurate forecasting of wind-forced oceanic heat flux convergences.

4.5.3 Glider 167 Deployment: September 18 – September 30, 2010

Glider 167 was deployed offshore of Wainwright along latitude 70.5°N on September 18, 2010 and transited westward (outbound leg) across the shelf until September 24 at which time it turned eastward (inbound leg) toward the coast and was recovered on September 30. The inbound leg was about 30 km north of the outbound leg. Its sampling interval thus overlapped with the first half of Glider 159's mission, described in the previous section, and captured the cross-shore hydrographic structure. The surface current descriptions are thus identical to those for Glider 159 and, although shown in Figures 102 - 108, are not discussed. The hydrographic property

Glider 159 09/19/10 – 09/30/10

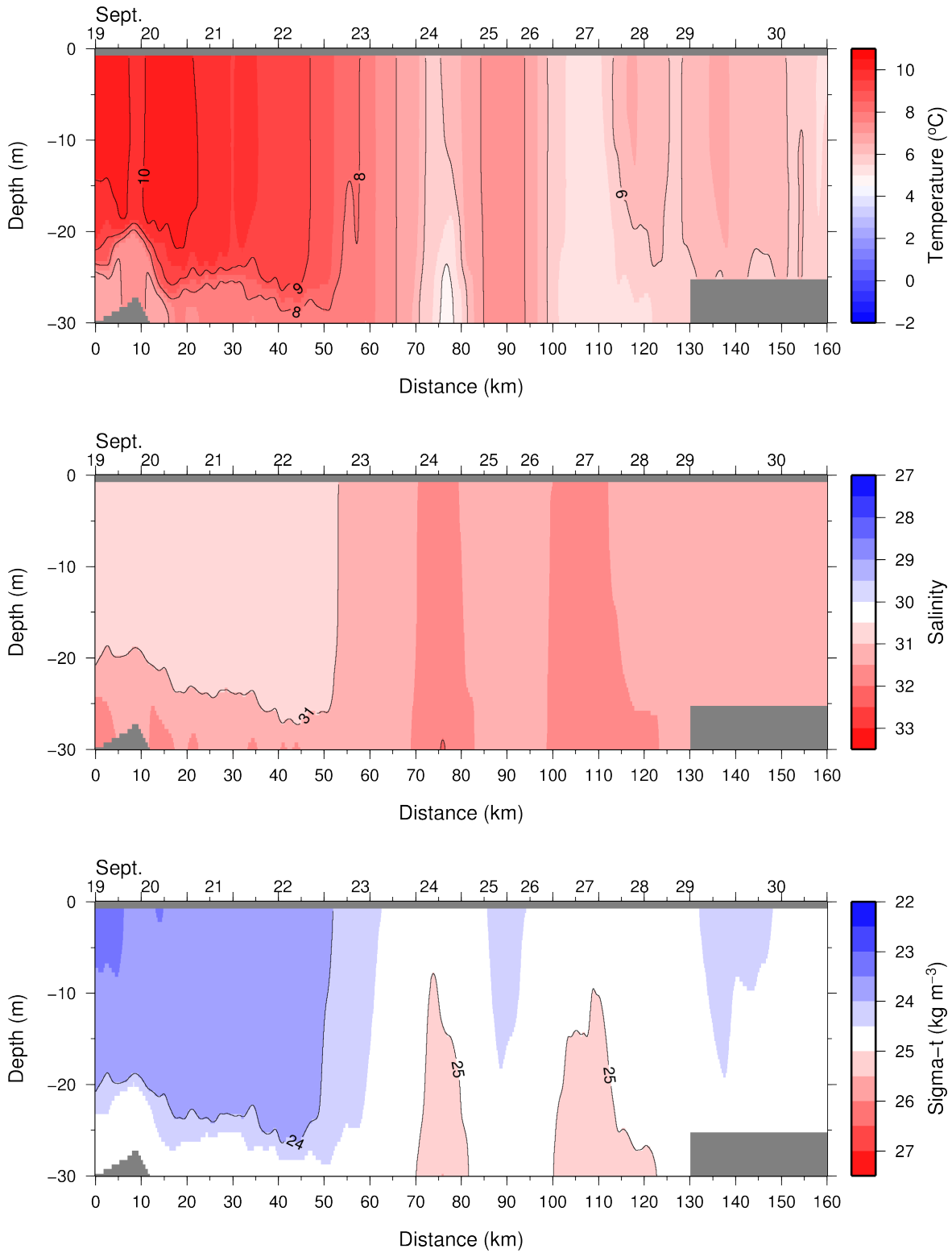


Figure 100. Section plots of temperature (top), salinity (middle), and density (sigma-t; bottom) from glider 159 September 19-30, 2010.

Glider 159 10/1/10 – 10/10/10

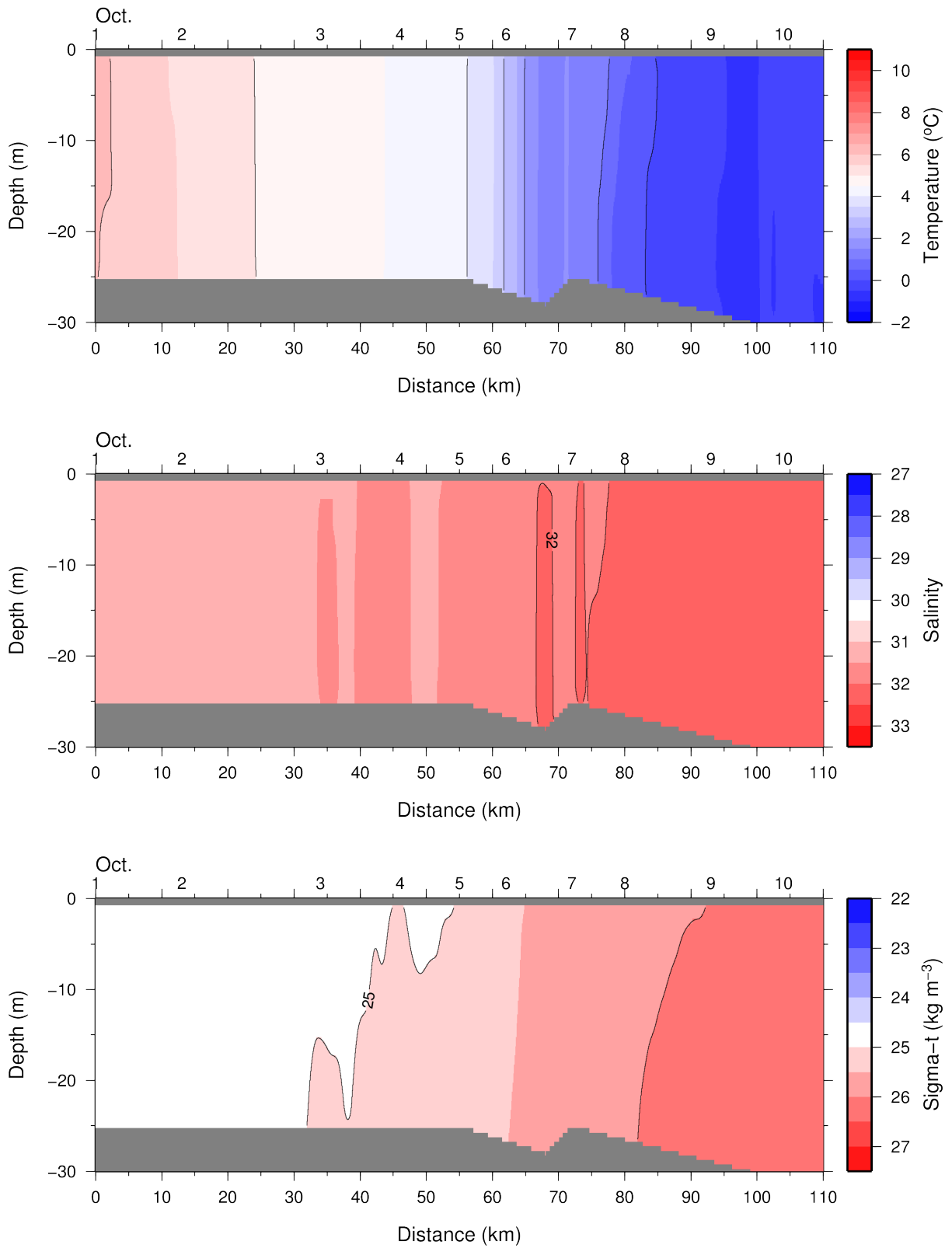


Figure 101. Section plots of temperature (top), salinity (middle), and density (sigma-t; bottom) from glider 159 October 1-10, 2010.

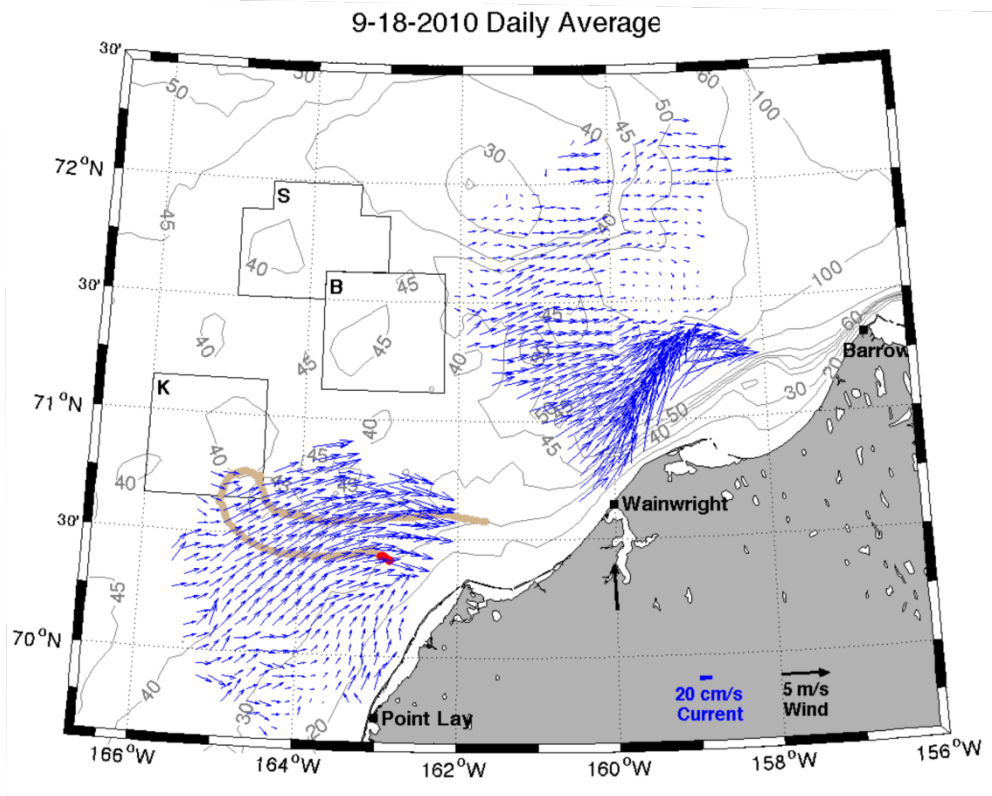
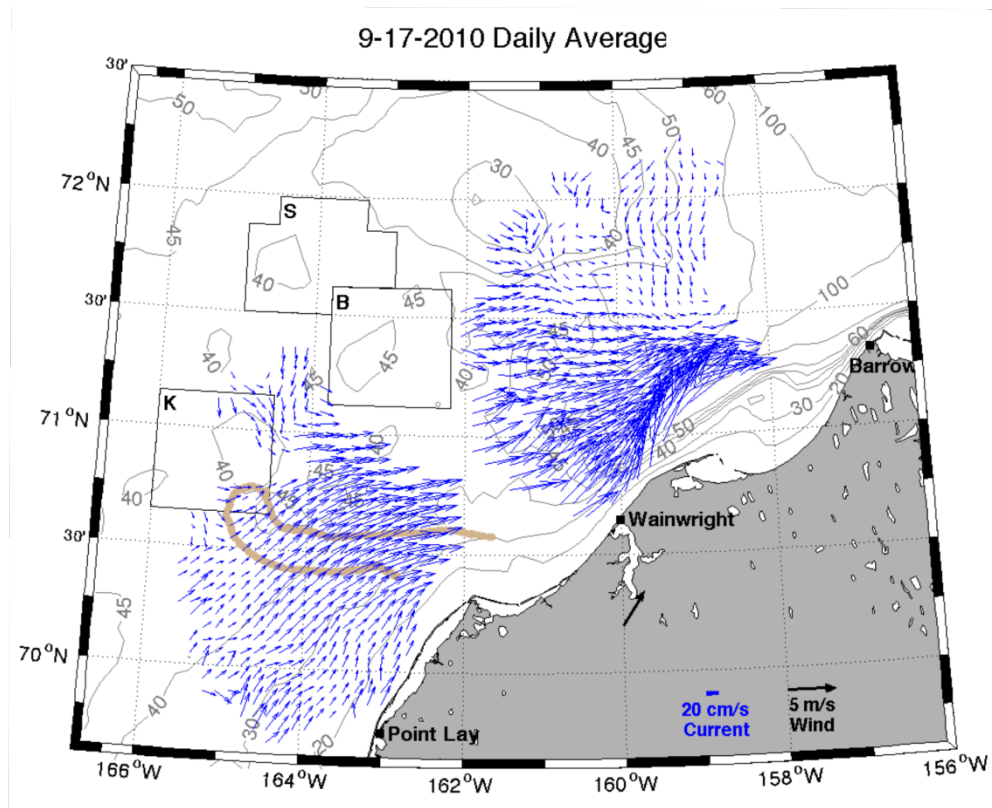


Figure 102. Mean surface currents on September 17 (top) and 18 (bottom), 2010. The glider track is red (denoting the track on the indicated day) and tan (denoting the entire glider track).

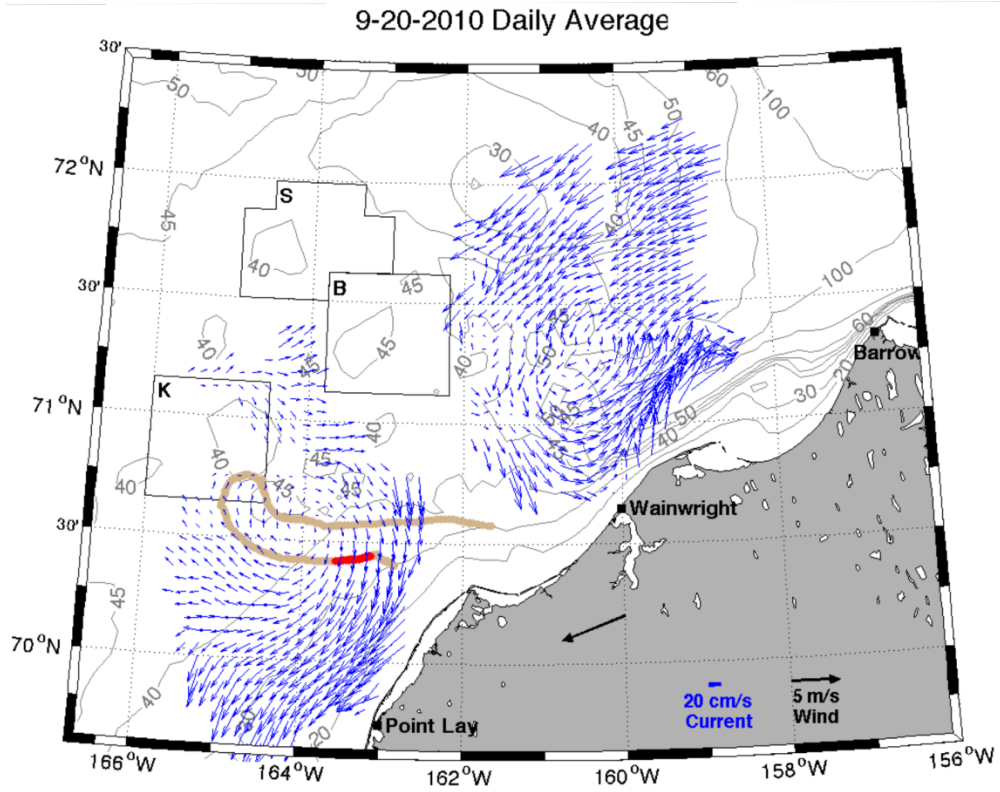
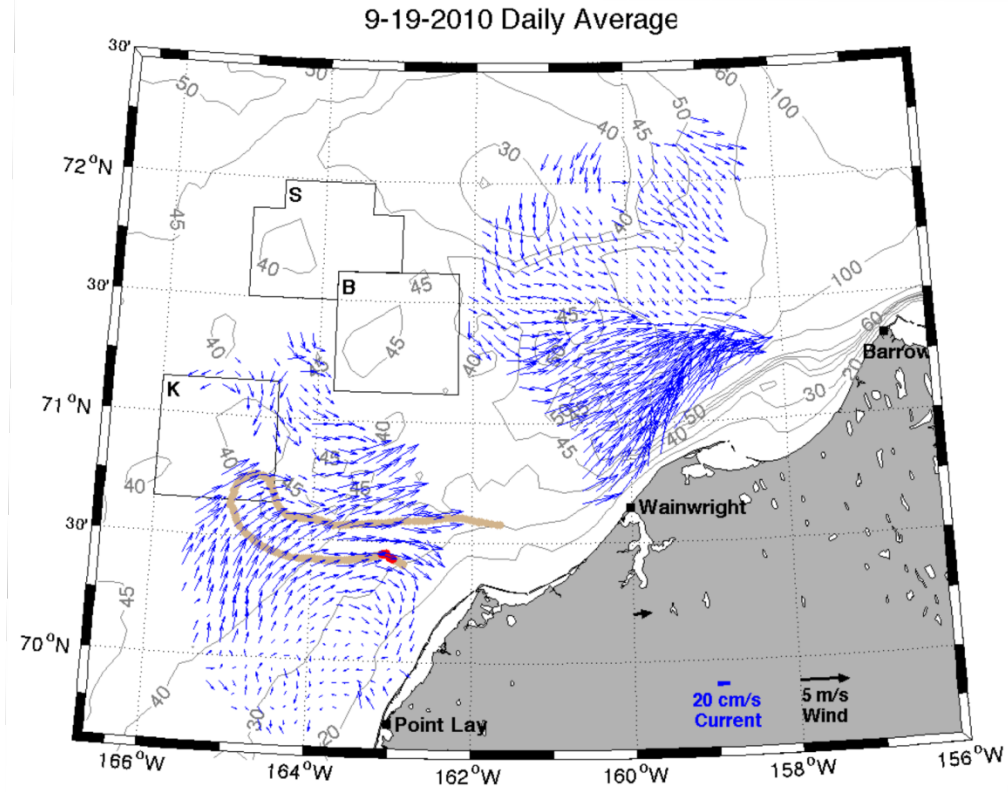


Figure 103. Mean surface currents on September 19 (top) and 20 (bottom), 2010. The glider track is red (denoting the track on the indicated day) and tan (denoting the entire glider track).

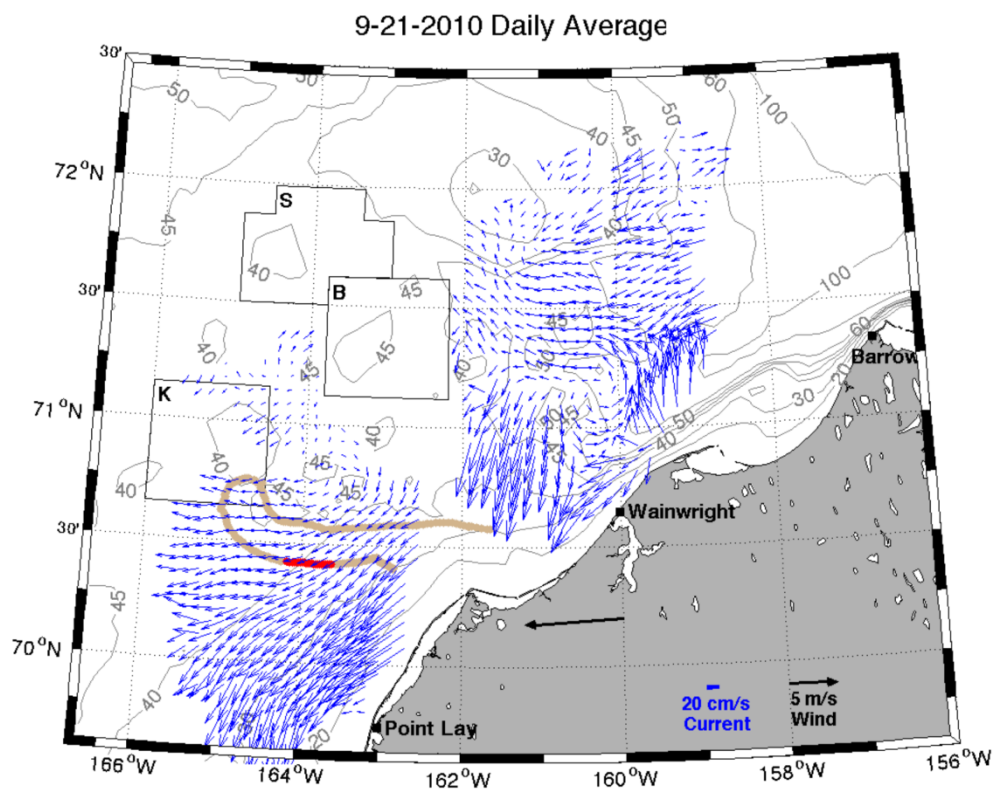
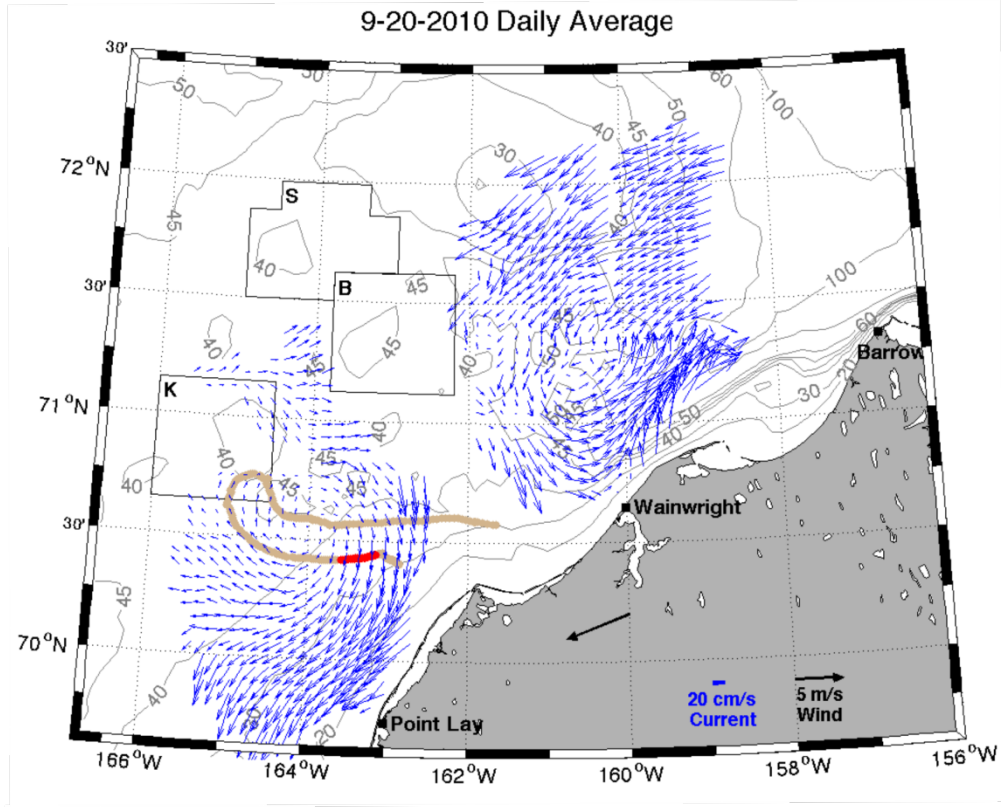


Figure 104. Mean surface currents on September 20 (top) and 21 (bottom), 2010. The glider track is red (denoting the track on the indicated day) and tan (denoting the entire glider track).

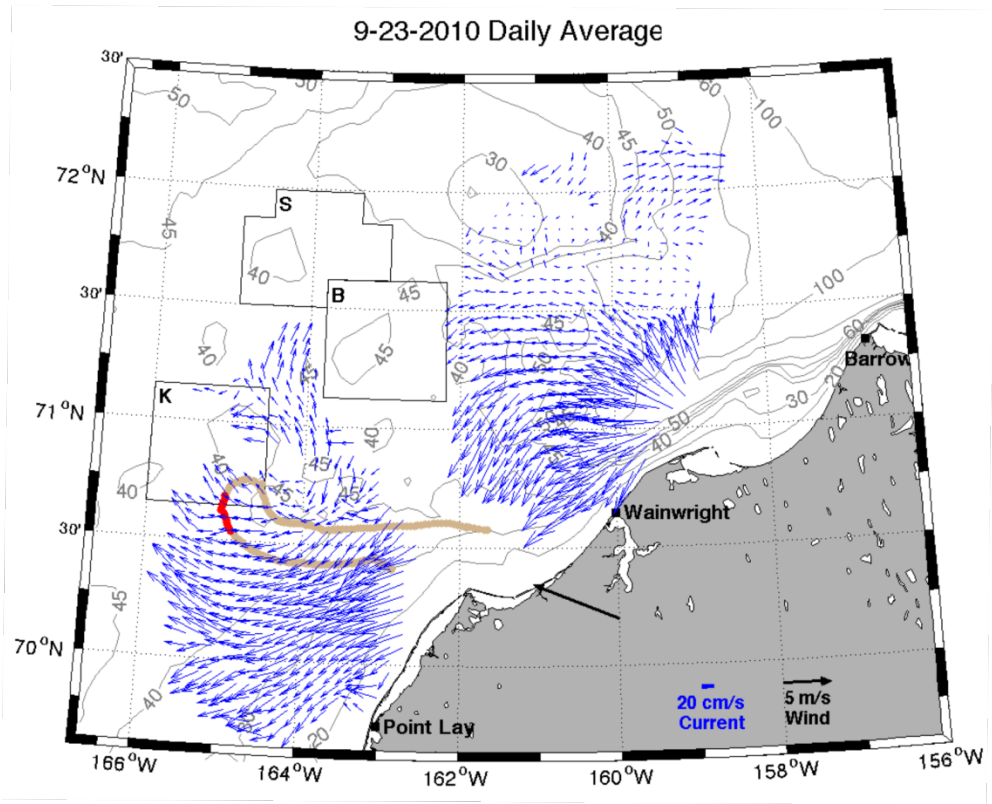
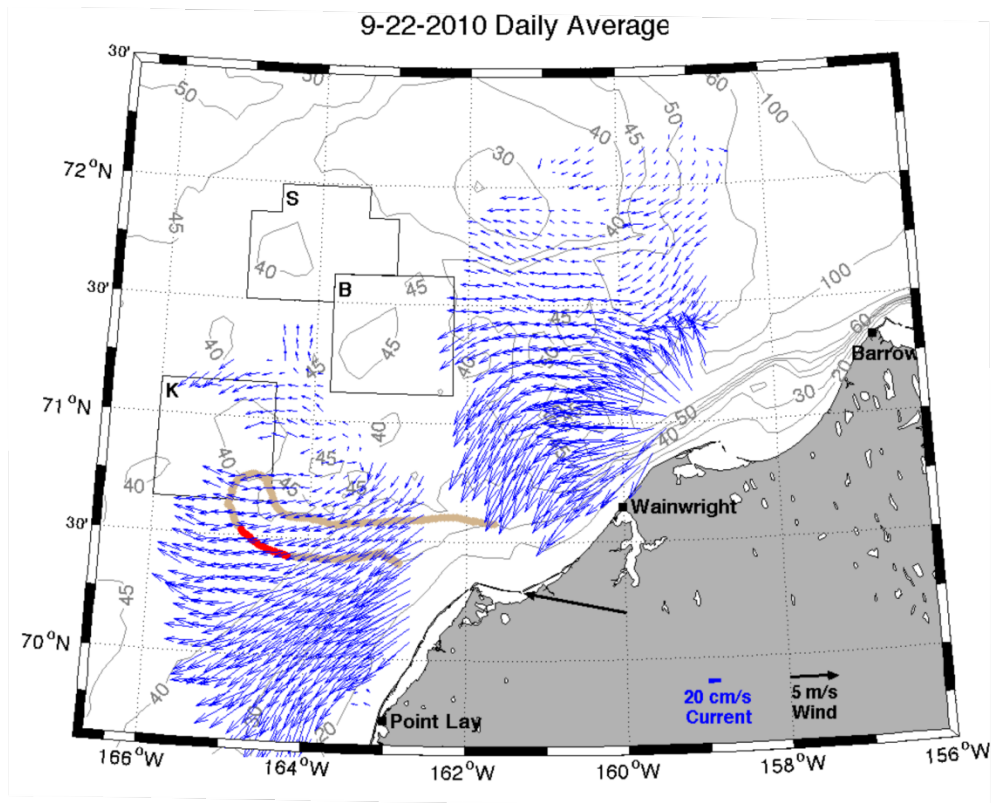


Figure 105. Mean surface currents on September 22 (top) and 23 (bottom), 2010. The glider track is red (denoting the track on the indicated day) and tan (denoting the entire glider track).

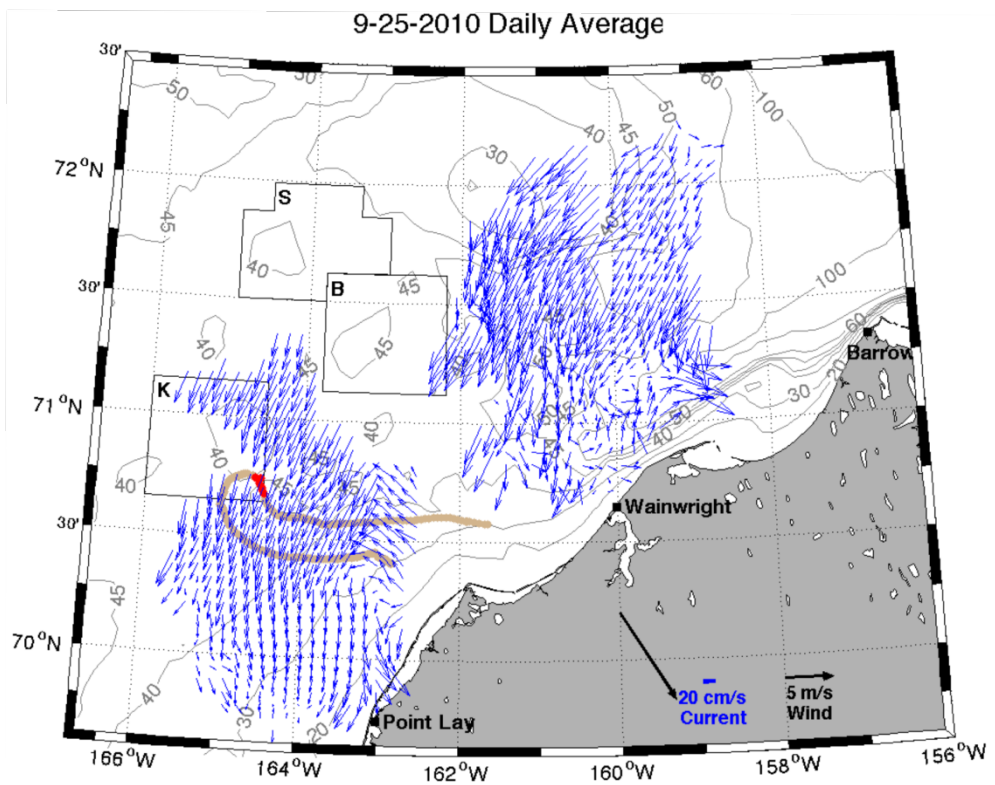
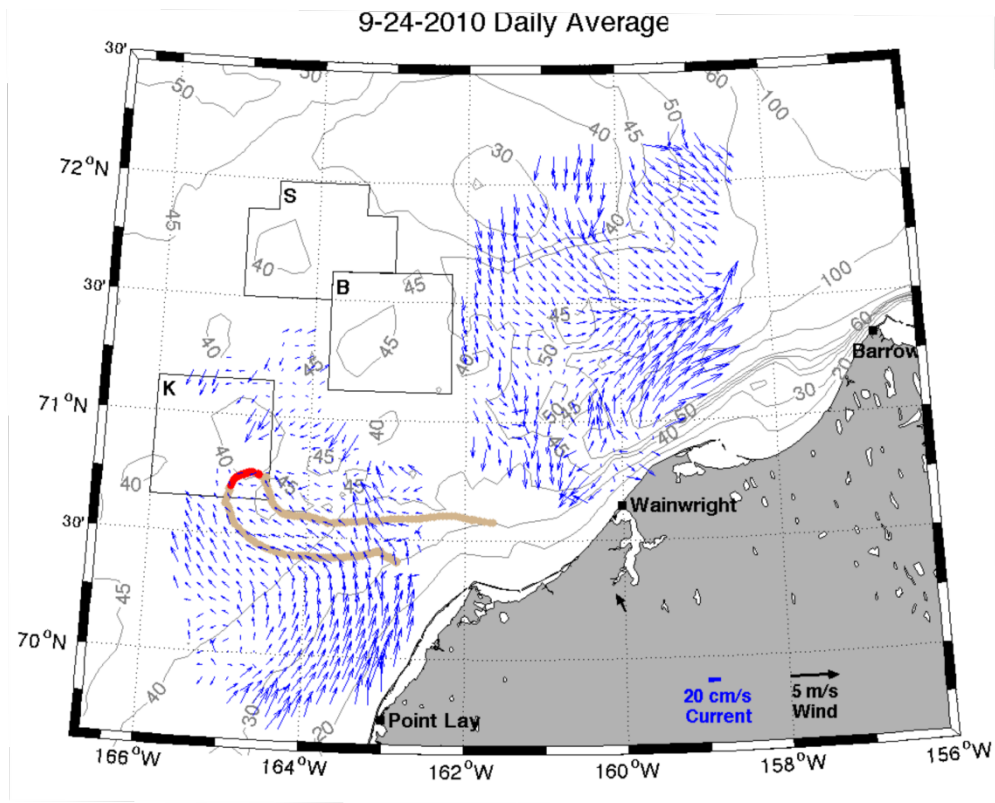


Figure 106. Mean surface currents on September 24 (top) and 25 (bottom), 2010. The glider track is red (denoting the track on the indicated day) and tan (denoting the entire glider track).

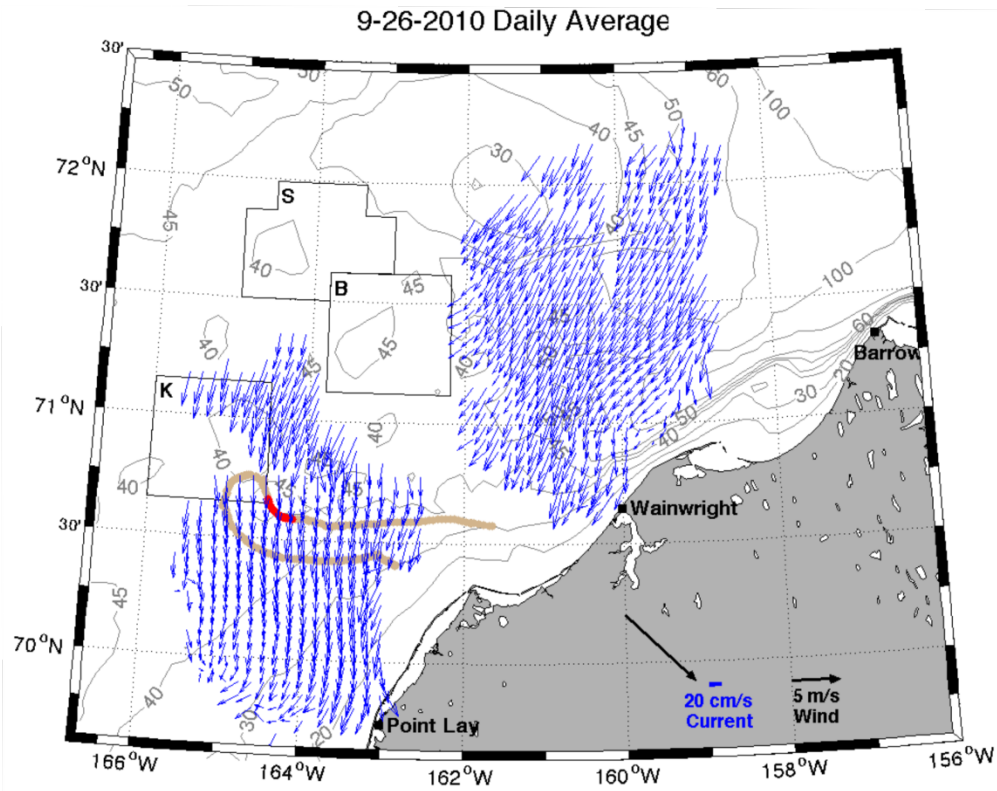


Figure 107. Mean surface currents on September 26 (top) and 27 (bottom), 2010. The glider track is red (denoting the track on the indicated day) and tan (denoting the entire glider track).

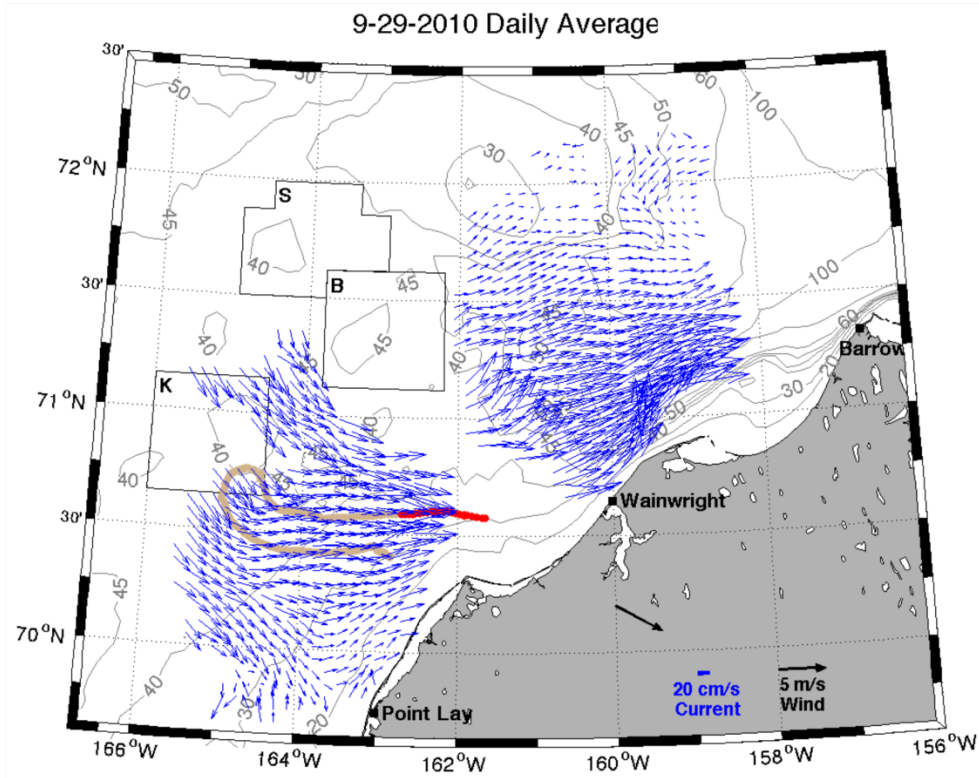
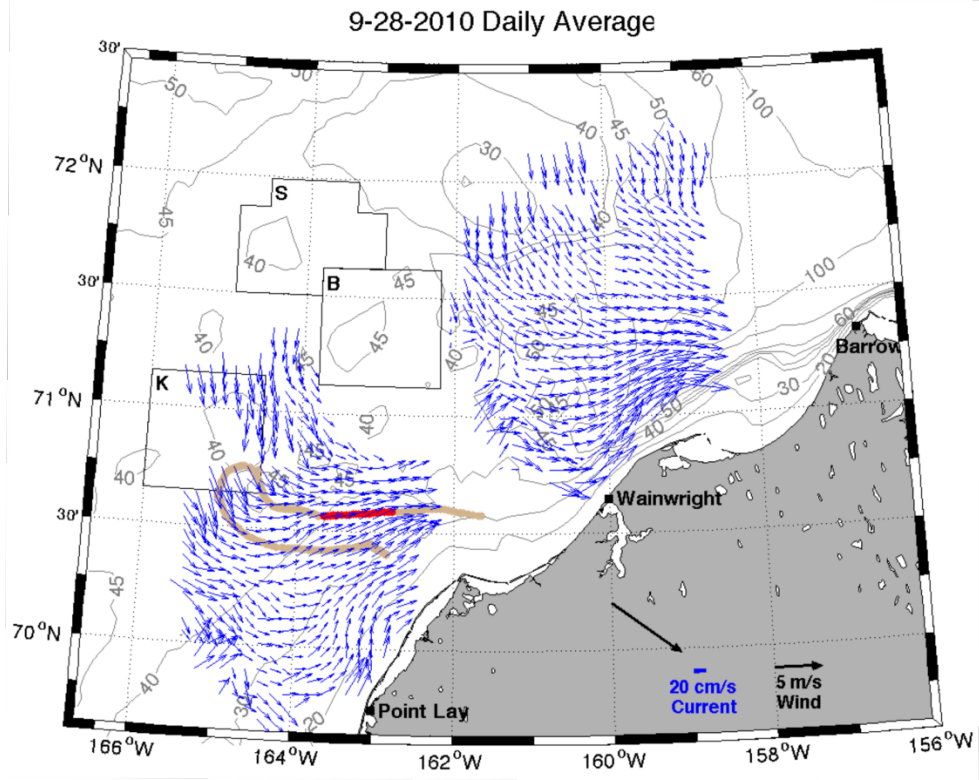


Figure 108. Mean surface currents on September 28 (top) and 29 (bottom), 2010. The glider track is red (denoting the track on the indicated day) and tan (denoting the entire glider track).

distributions along the inbound and outbound legs of glider 167 are shown in Figures 109 and 110, respectively.

These section profiles indicate a nearly homogeneous water column with temperatures decreasing and salinities increasing from inshore to offshore. Between the beginning and end of the mission inshore temperatures had decreased by about 5°C, and salinities had increased by ~0.5, primarily by advection as discussed above. The horizontal density gradients are also small indicating that the vertical shear in the geostrophic currents is negligible. Hence any vertical variation in the water column is associated with frictional shears induced by the wind at the surface and friction on the bottom. The surface current maps indicate that there are no large horizontal velocity gradients. This implies that the Rossby numbers of the flow field are $\ll 1$, hence the non-linear terms in the momentum balance are negligible. For this period the flow field largely consisted of a balance amongst local acceleration, surface wind stress, bottom friction, horizontal pressure gradients, and horizontal gradients in sea level. The latter is associated with wind-induced sea surface convergences and divergences.

4.5.4 Glider 191 Deployment: August 1 –14, 2011

We next examine the transect of glider 191 for the period of August 1 – 14, 2011, which occurred offshore of Wainwright (dark blue transect in Figure 85). From August 1 – 8, the glider moved from west to east, then it veered northeastward on August 9, and then northward on August 12 where it continued in this direction until August 14. (Note that the intended glider transect was to be offshore, but the glider was unable to overcome the swift currents encountered near the head of Barrow Canyon and thus moved northward.) Mean daily surface current maps (beginning July 31) were prepared for each day of this transit (Figures 111 – 117) along with the water property distributions along the glider track (Figures 118 - 119).

Throughout most of this period the winds were light ($\leq 5 \text{ m s}^{-1}$) and variable, although northeasterly winds of $\sim 10 \text{ m s}^{-1}$ developed from August 11 to 14. Consequently, the surface currents within 60 km of Wainwright were swift ($\sim 40 \text{ cm s}^{-1}$) and flowed onshore south of the head of Barrow Canyon and then veered northeastward into the canyon (consistent with the discussion in section 4.4.2). Note however, that on August 9 the winds were from the northeaster. These were not strong enough to reverse the flow in Barrow Canyon or offshore of Wainwright, but the currents offshore of Point Lay began veering offshore. Although the radar gap southwest of Wainwright does not allow us to delineate precisely where this veering begins, the August 9 current map suggests that it occurs along the southern portion of the glider transect. Beginning on August 12, the currents approaching the coast and entering the canyon slackened (but maintained the same general flow pattern), while currents offshore of Point Lay were uniformly northward.

As is evident from the current maps, the current veers almost 90° entering the canyon, with this turning amounting to $\sim 45^\circ$ over a $\sim 10 \text{ km}$ distance. This observation suggests that the centrifugal term may be a significant component in the dynamics of the veering. For current speeds as small $\sim 0.2 \text{ m s}^{-1}$, the ratio of the centrifugal term (U^2/R) to the Coriolis acceleration (fU) is ~ 0.15 .

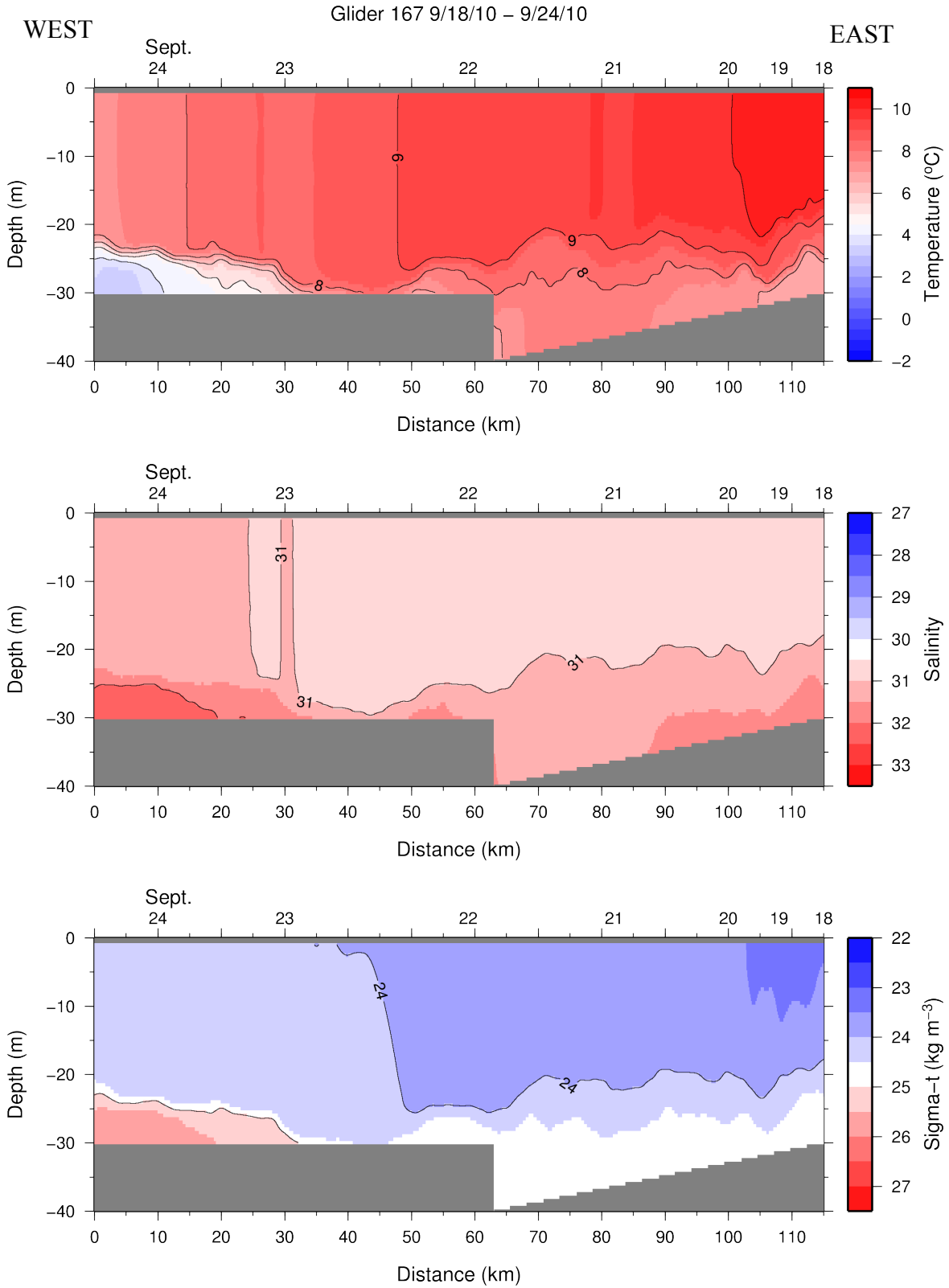


Figure 109. Section plots of temperature (top), salinity (middle), and density (sigma-t; bottom) from glider 159 September 18-24, 2010.

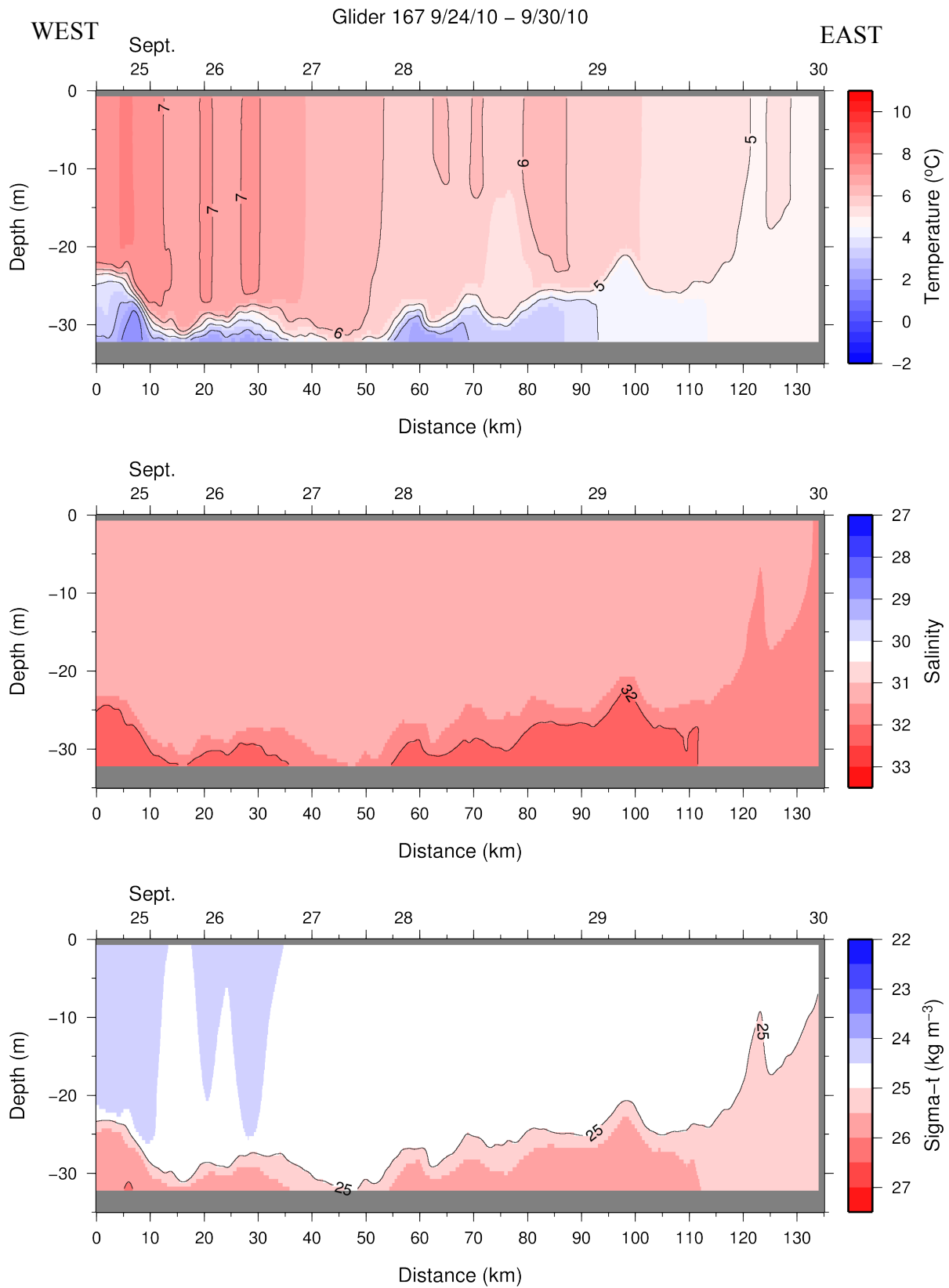


Figure 110. Section plots of temperature (top), salinity (middle), and density (sigma-t; bottom) from glider 159 September 24-30, 2010.

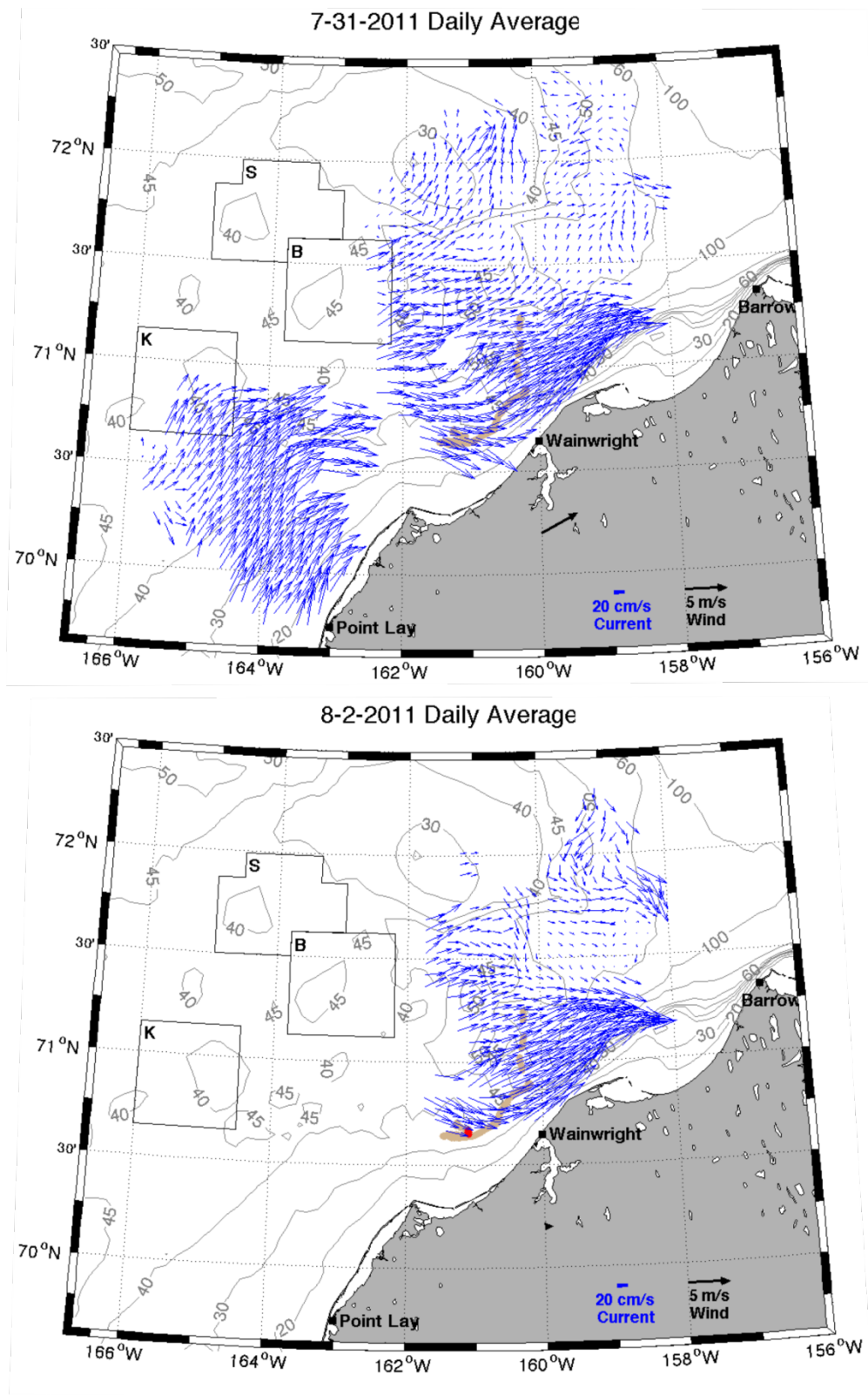


Figure 111. Mean surface currents on July 31 (top) and August 2 (bottom), 2011. The glider track is red (denoting the track on the indicated day) and tan (denoting the entire glider track).

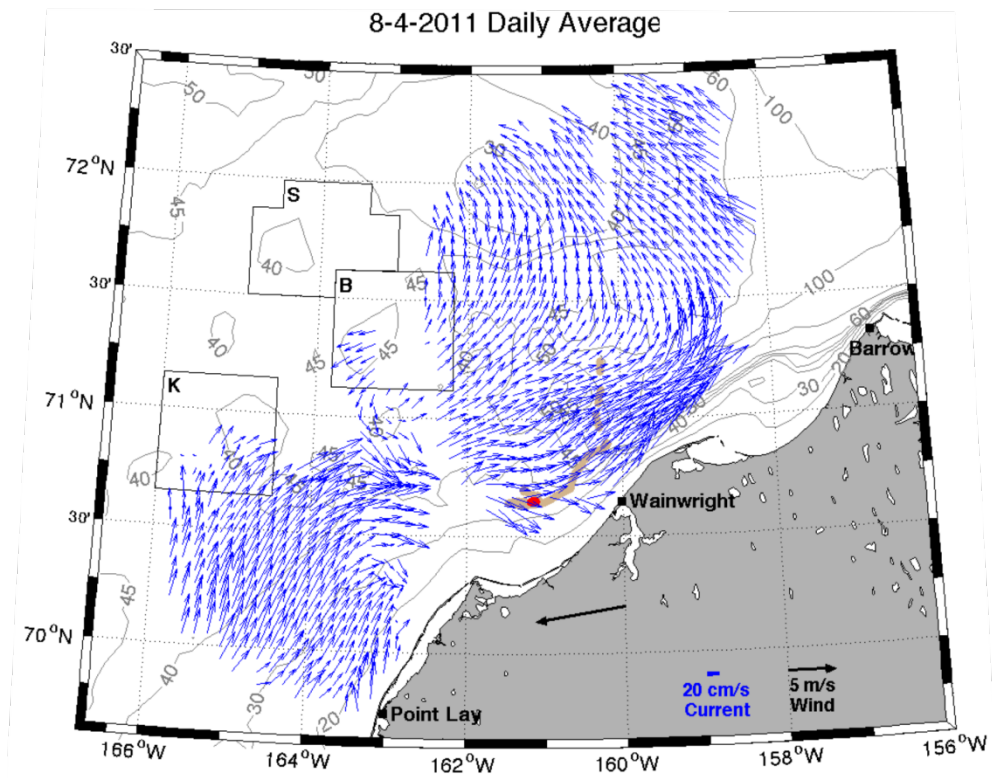
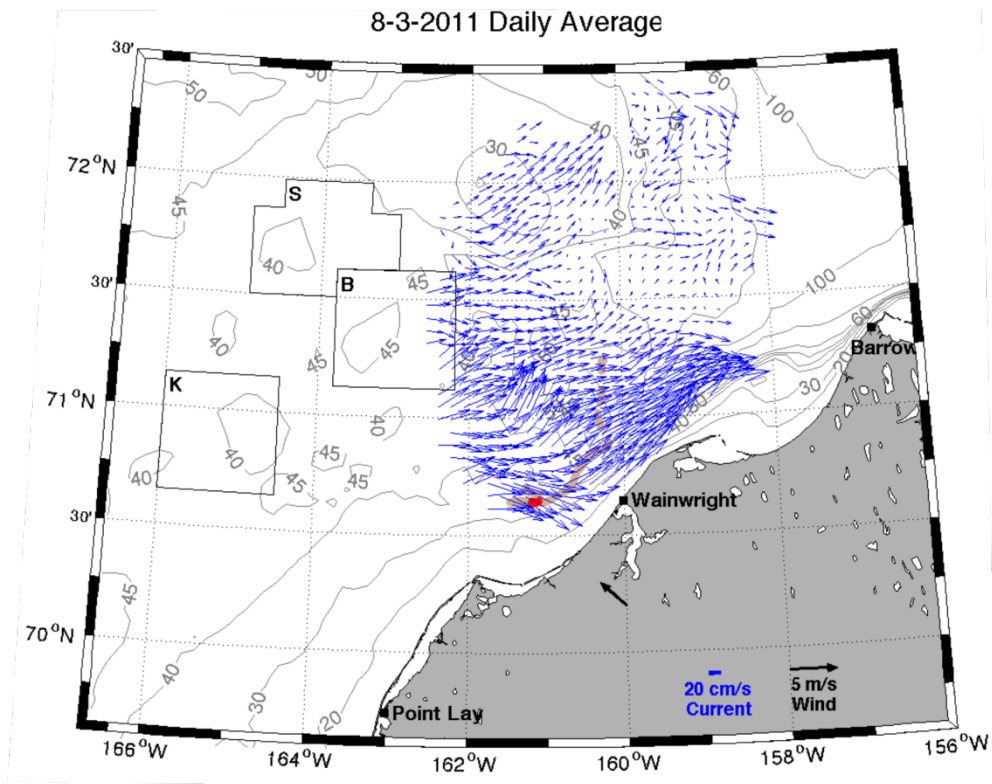


Figure 112. Mean surface currents on August 3 (top) and August 4 (bottom), 2011. The glider track is red (denoting the track on the indicated day) and tan (denoting the entire glider track).

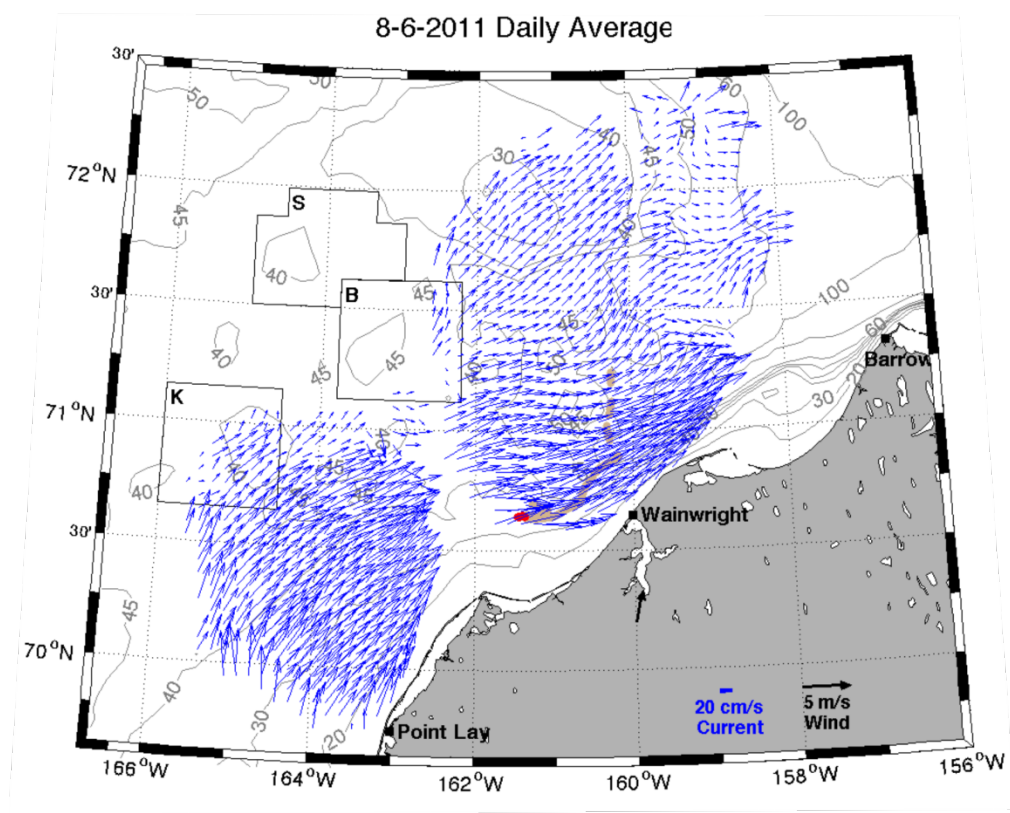
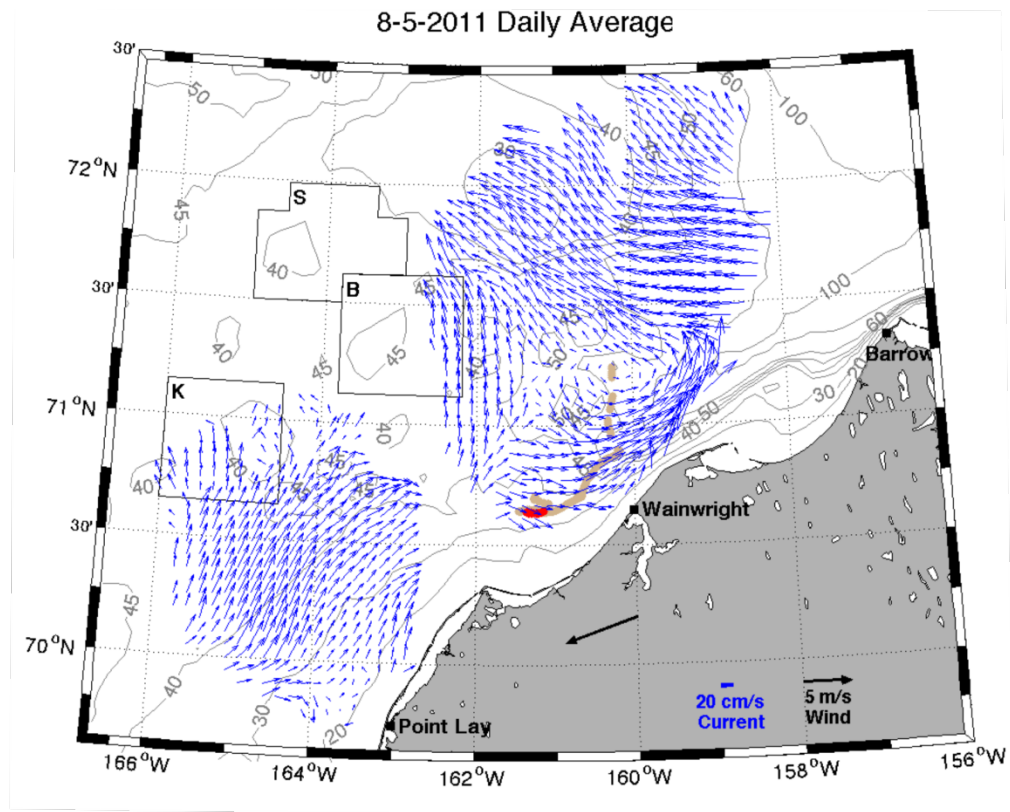


Figure 113. Mean surface currents on August 5 (top) and August 6 (bottom), 2011. The glider track is red (denoting the track on the indicated day) and tan (denoting the entire glider track).

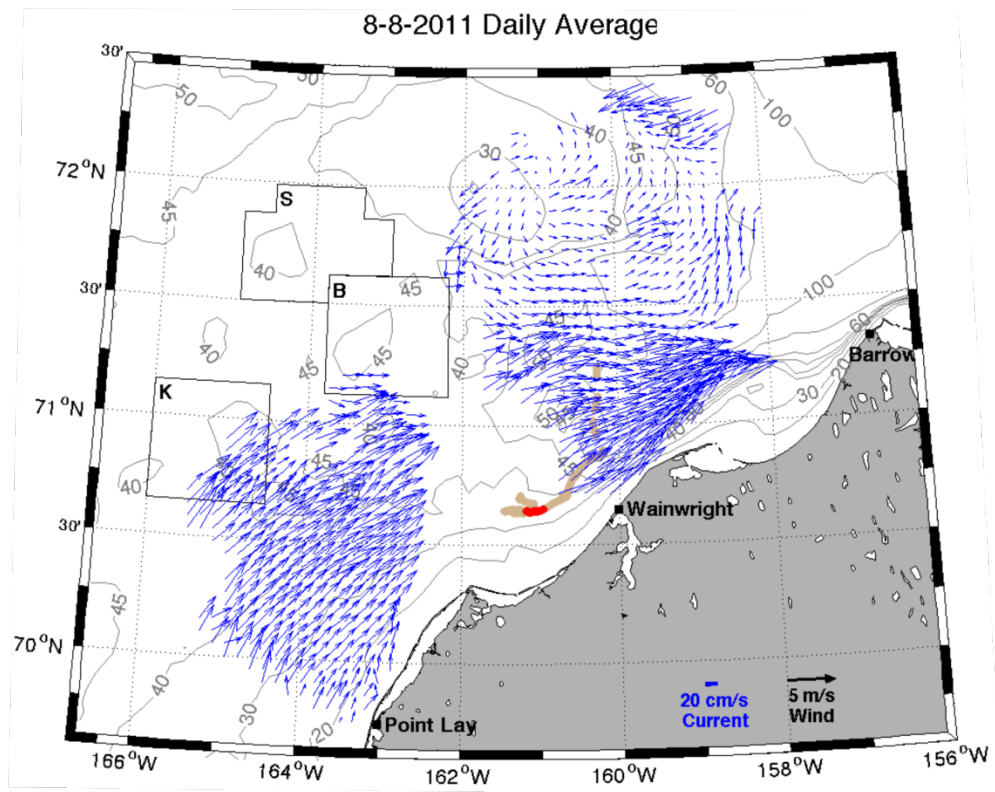
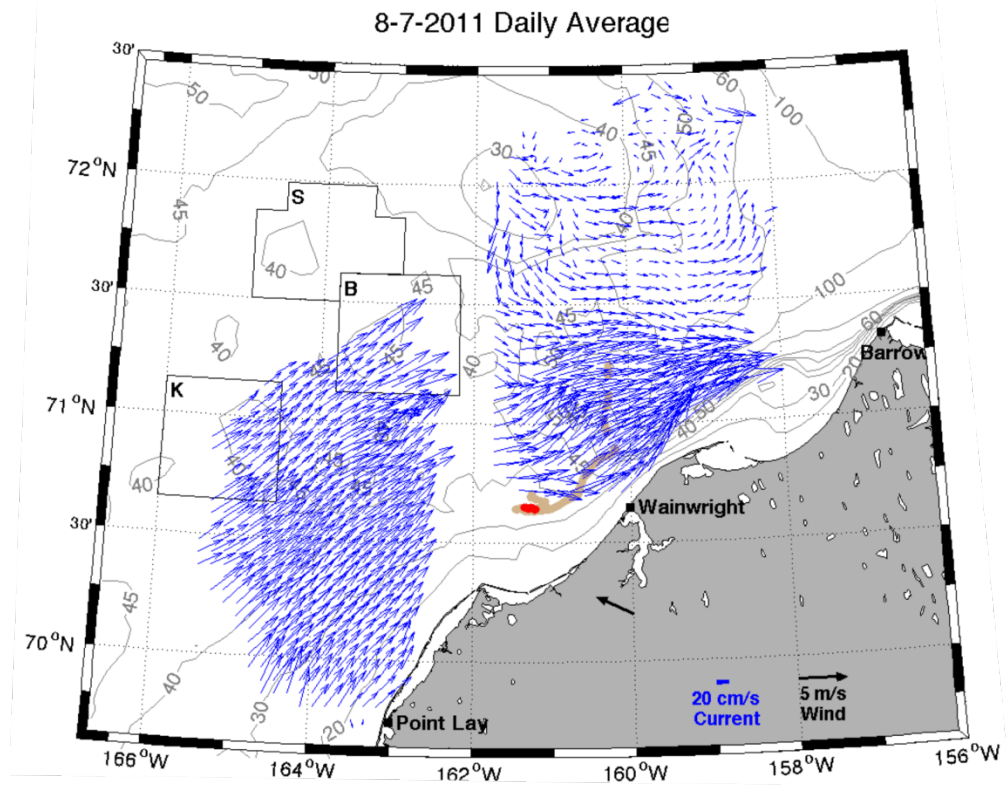


Figure 114. Mean surface currents on August 7 (top) and August 8 (bottom), 2011. The glider track is red (denoting the track on the indicated day) and tan (denoting the entire glider track).

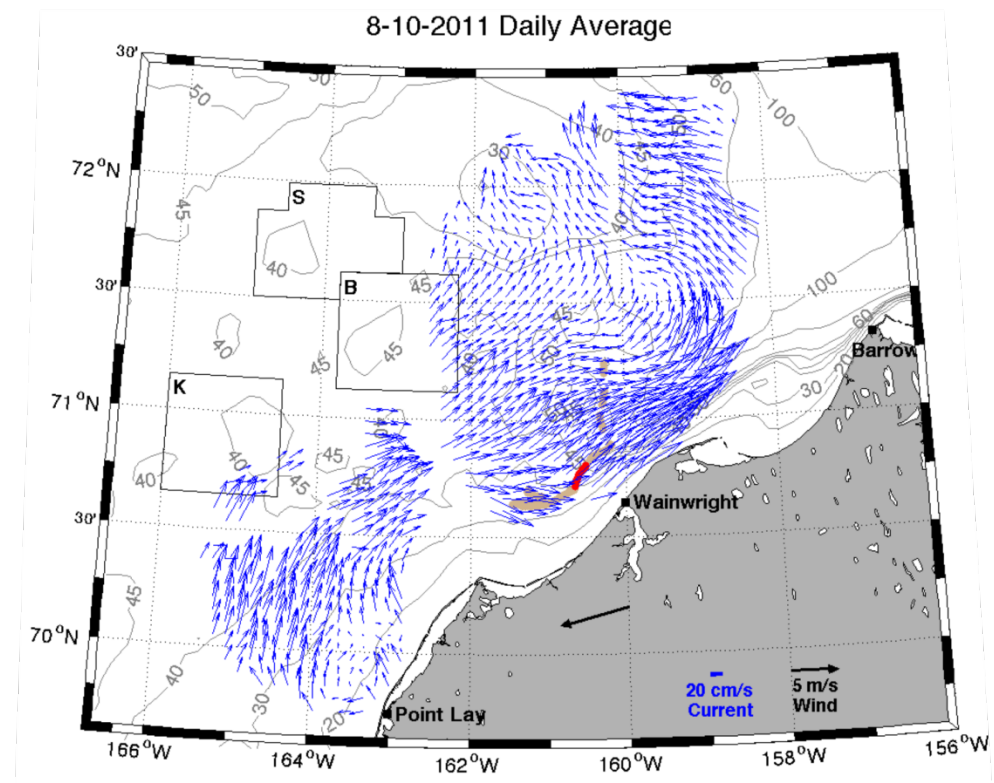
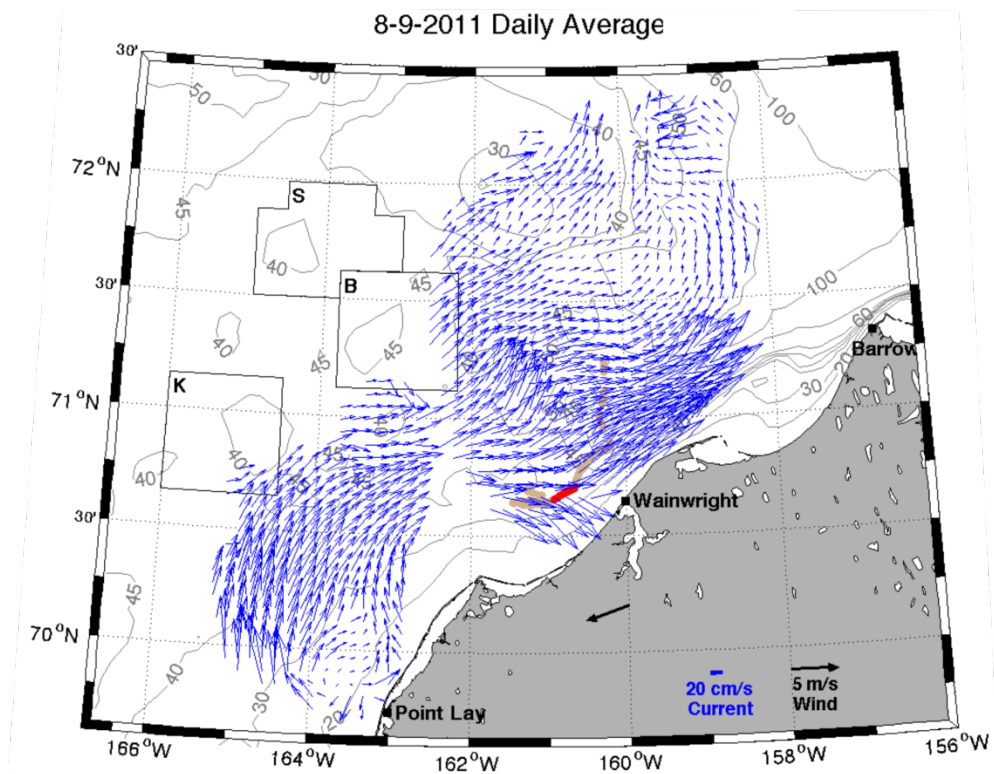


Figure 115. Mean surface currents on August 9 (top) and 10 (bottom), 2011. The glider track is red (denoting the track on the indicated day) and tan (denoting the entire glider track).

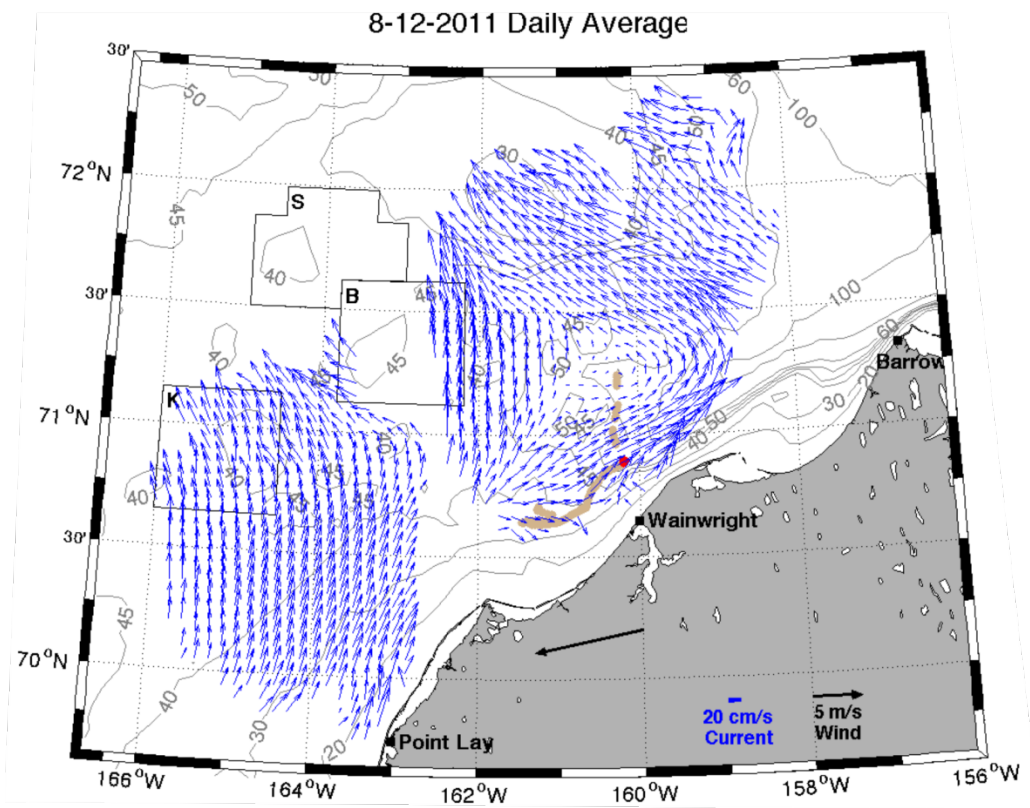
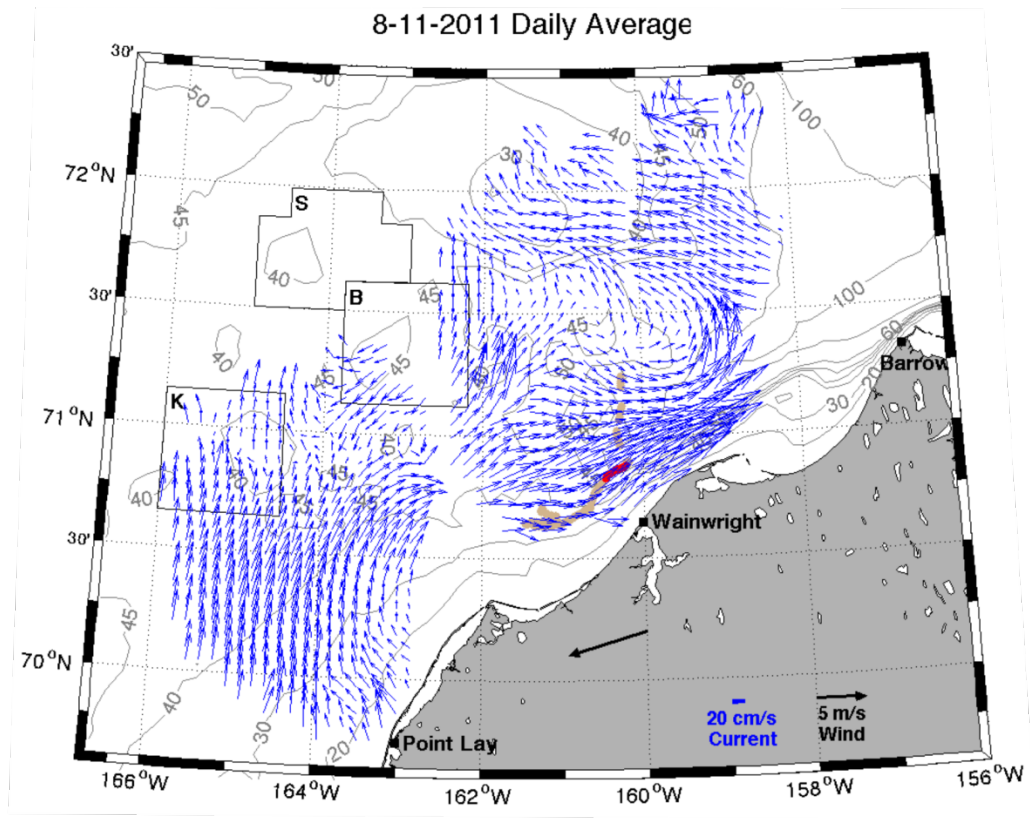


Figure 116. Mean surface currents on August 11 (top) and 12 (bottom), 2011. The glider track is red (denoting the track on the indicated day) and tan (denoting the entire glider track).

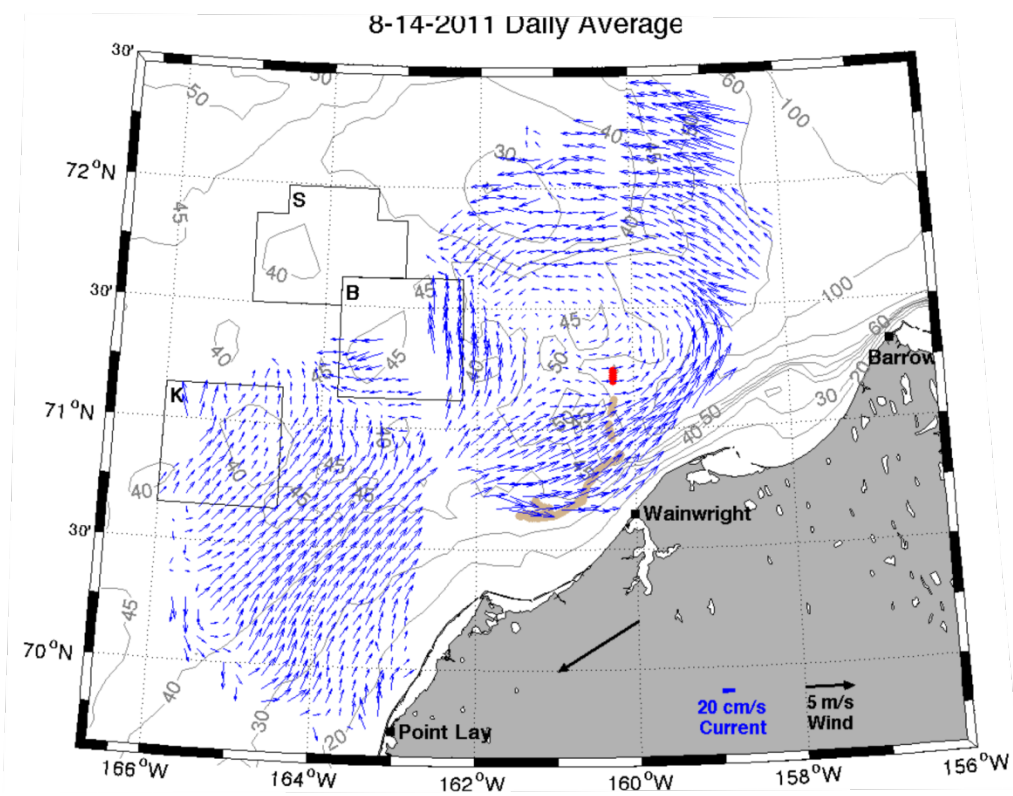
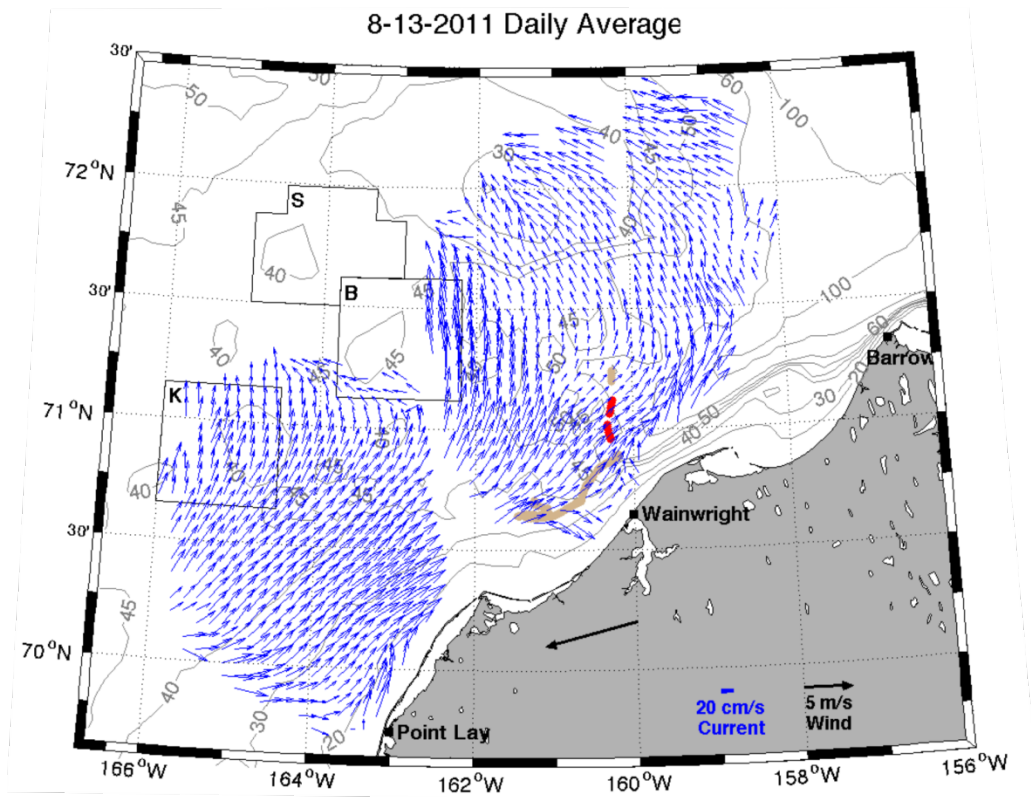


Figure 117. Mean surface currents on August 13 (top) and 14 (bottom), 2011. The glider track is red (denoting the track on the indicated day) and tan (denoting the entire glider track).

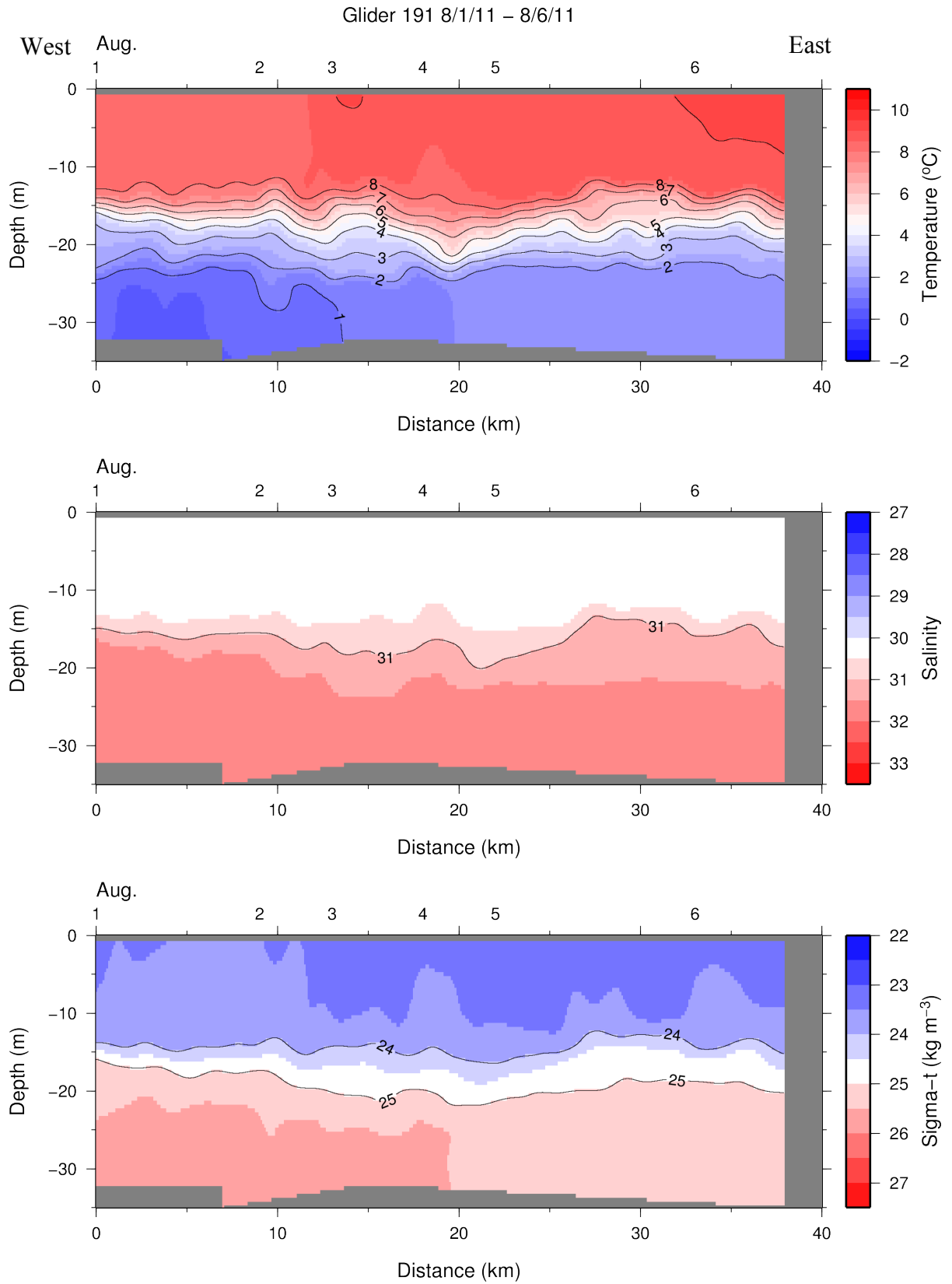


Figure 118. Section plots of temperature (top), salinity (middle), and density (sigma-t; bottom) from glider 191 August 1-6, 2011.

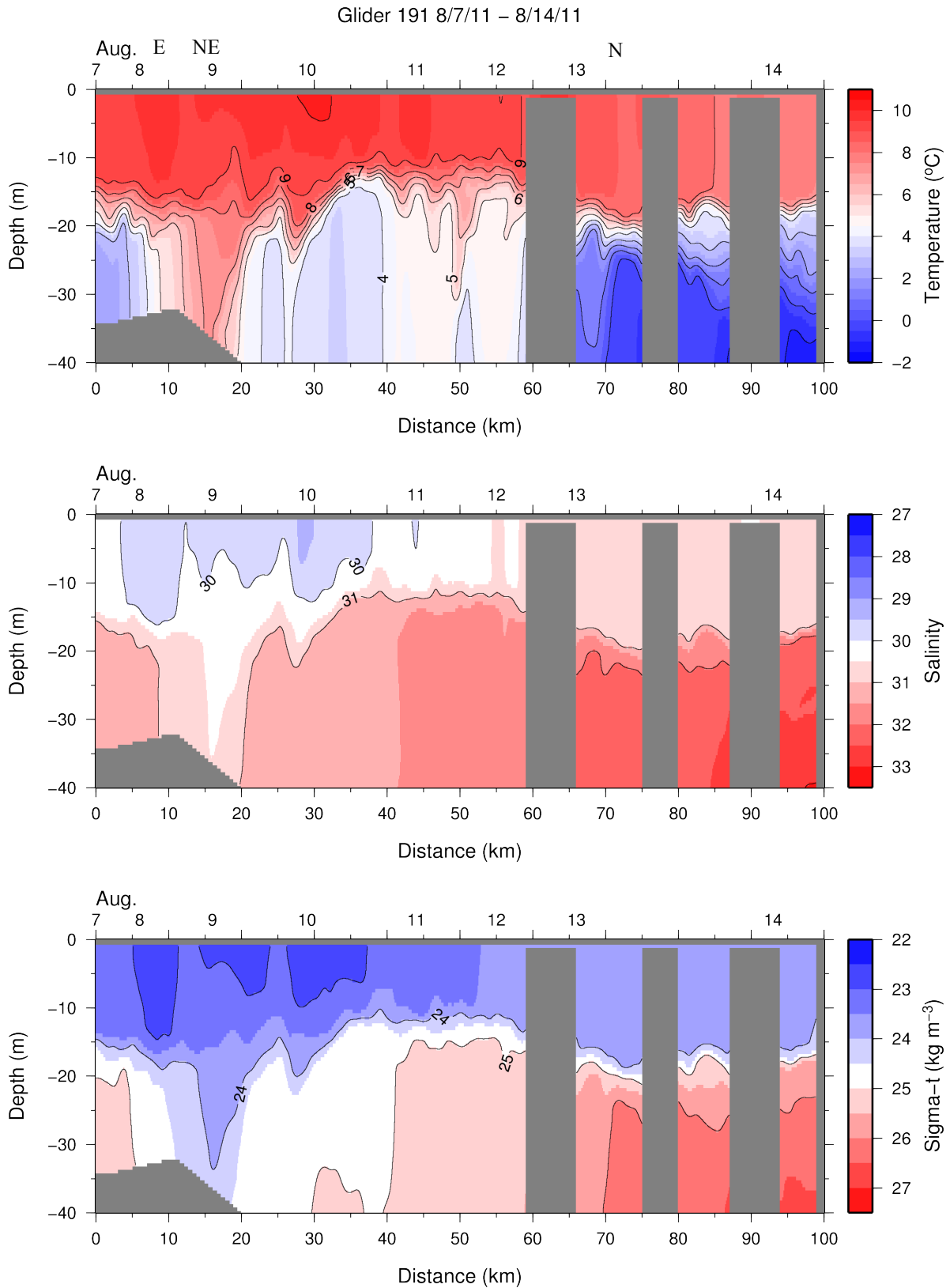


Figure 119. Section plots of temperature (top), salinity (middle), and density (sigma-t; bottom) from glider 191 August 7-14, 2011. Glider headings are given in uppermost panel.

Since current speeds are often of this magnitude entering or leaving the canyon, the result implies that gradient wind dynamics apply to the flow in this area.

From August 1- 7, the glider moved only a few km, hence it sampled water moving eastward and eventually into the canyon. The water properties in this period (Figure 118) indicate that the upper 15 m of the water column was uniformly warm ($\geq 8^{\circ}\text{C}$), moderately salty (30 - 30.5), and separated from deeper waters by a pycnocline at $\sim 15\text{-}20$ m depth. Below ~ 20 m, temperatures were $\sim 2^{\circ}\text{C}$ and salinities were > 31.5 . As the glider moved northeastward it encountered a more weakly-stratified water column (August 9) in which bottom temperatures increased to $\sim 7^{\circ}\text{C}$, and salinities decreased to < 30.5 . Farther northeastward, bottom temperatures decreased and salinities increased once again (Figure 119).

On crossing the head of the canyon on August 12 – 13, bottom water temperatures decreased to $\sim 0^{\circ}\text{C}$ and salinities increased to > 32 . These results imply that a variety of water masses, having variable stratification, were entering the canyon. The warmest and freshest bottom waters likely entered the east side of the canyon, while colder, more saline winter waters (confined to the lower half of the water column) entered the western side of the canyon. The subsurface waters along this transect included at least two fronts (encountered on August 9 and between August 12 and 13). The implied vertical shears in the geostrophic component of velocity were 0.01 s^{-1} (equivalent to a 10 cm s^{-1} velocity difference over 10 m). These shears are comparable to those observed over the upper 25 m in the along-canyon velocity component in the center of Barrow Canyon in August 2011 (Figure 34). However, because the fronts did not extend to the surface, these geostrophic shears are confined to the lower half of the water column.

4.5.5 Glider 191 Deployment: September 1 –12, 2011

Glider 191 was at 70.5°N , 165°W on September 1, 2011 and transited southward for 150 km along this longitude to $\sim 69.2^{\circ}\text{N}$ until September 7. It then turned northward and resampled the same transit until September 12 when it reached the same point as on September 1. Figures 120 - 126 contain the mean daily surface currents and winds (beginning on August 31), and Figures 127 and 128 show the hydrography along these glider tracks.

From August 31 to September 3 winds were weak ($< 5\text{ m s}^{-1}$) and varied from being initially northward and then to the southwest. The currents were initially northeastward over the region of the glider transect but weakened and became less organized through September 3. (Weak winds and small wavelengths probably contributed to the sparse radar coverage on September 2.). The northeast winds intensified from $< 5\text{ m s}^{-1}$ to $> 7\text{ m s}^{-1}$ on September 4, and the current pattern evolved into the divergent mode, which included a large anticyclonic recirculation offshore of Point Lay. From September 6 to 7, the winds were from the north, and the shelf circulation, including Barrow Canyon became southward. The southerly flow began relaxing on September 8, when the winds veered to be from the northwest at $< 5\text{ m s}^{-1}$. Beginning on September 9, the winds were from the south-southeast, and the circulation pattern began adjusting with weak northeastward flow beginning offshore of Point Lay, while southwestward flow continued in Barrow Canyon, albeit at reduced strength. Thereafter the winds were $> 7\text{ m s}^{-1}$ from the

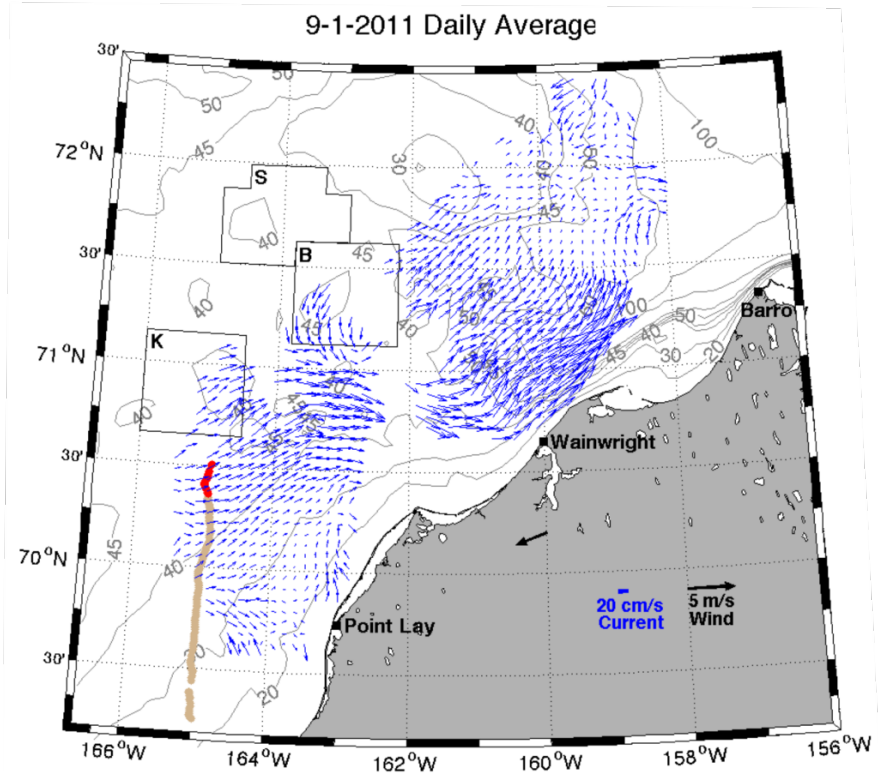
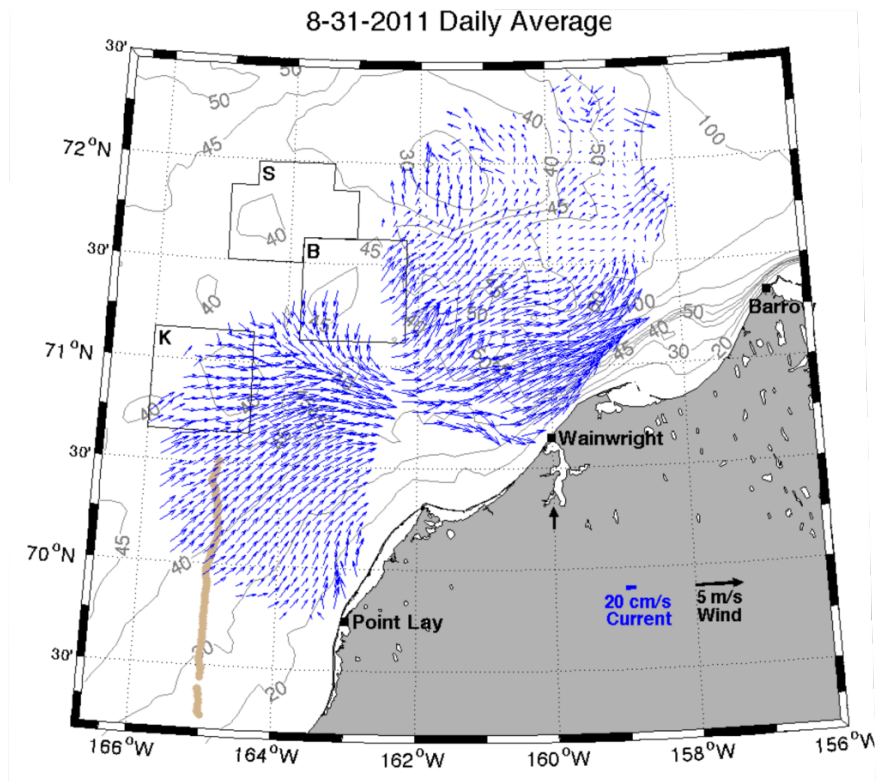


Figure 120. Mean surface currents on August 31 (top) and September 1 (bottom), 2011. The glider track is red (denoting the track on the indicated day) and tan (denoting the entire glider track).

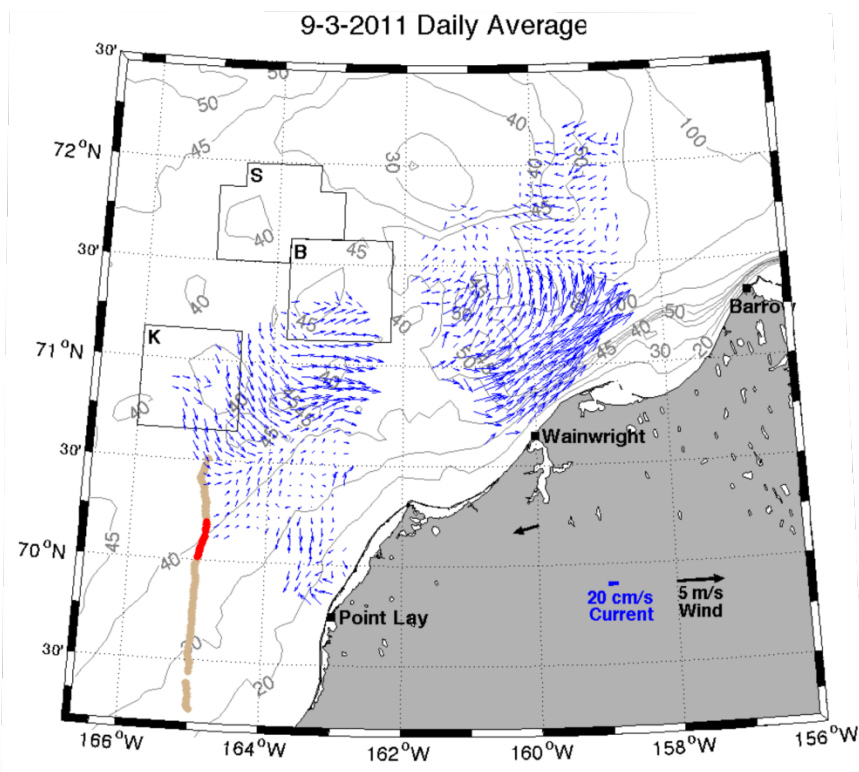
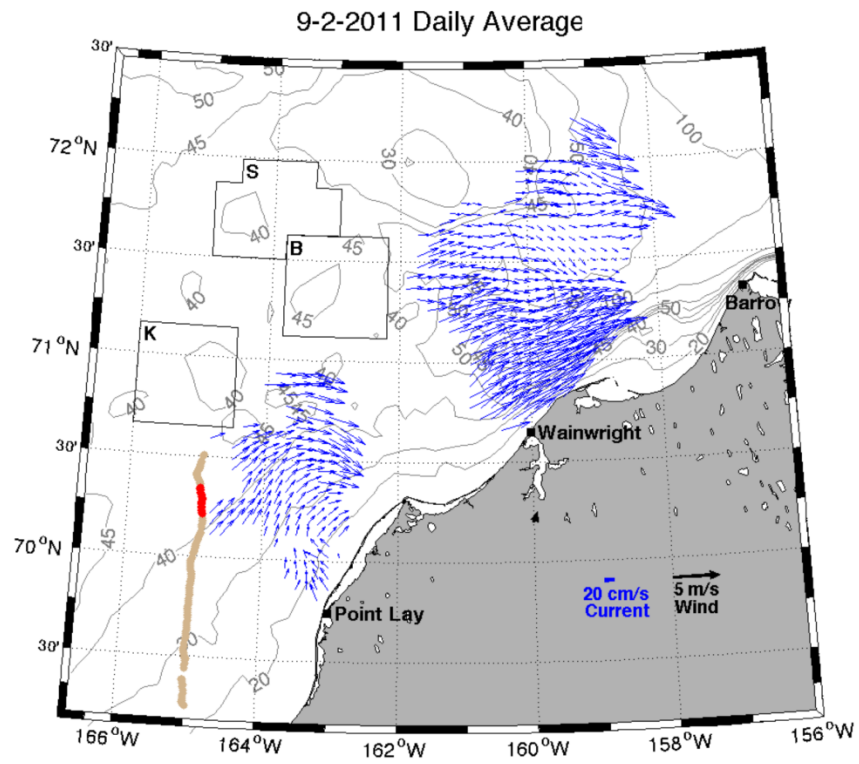


Figure 121. Mean surface currents on September 2 (top) and 3 (bottom), 2011. The glider track is red (denoting the track on the indicated day) and tan (denoting the entire glider track).

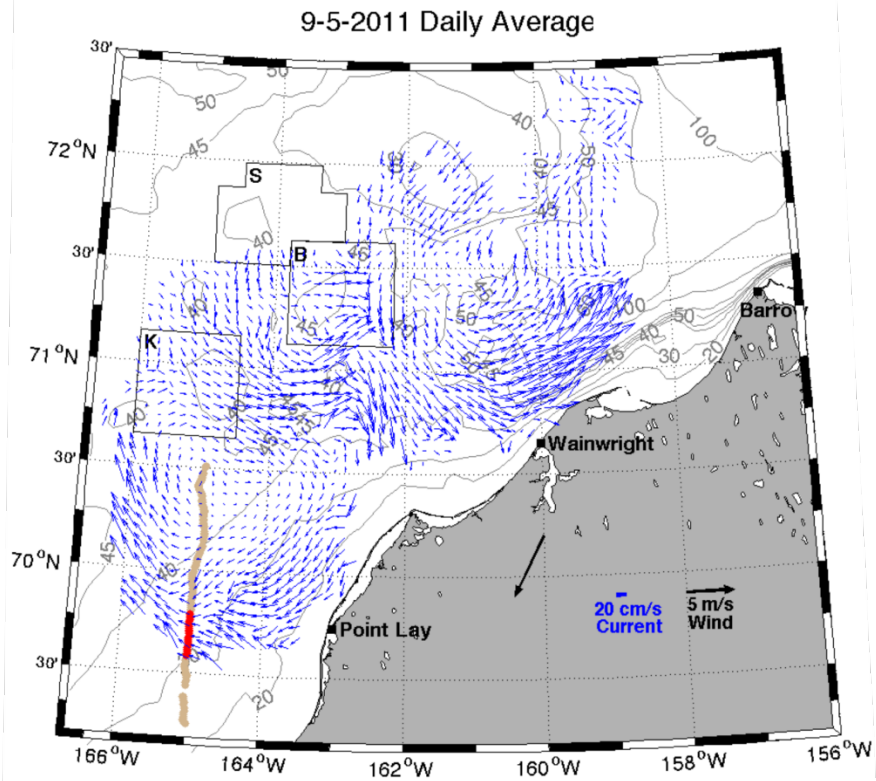
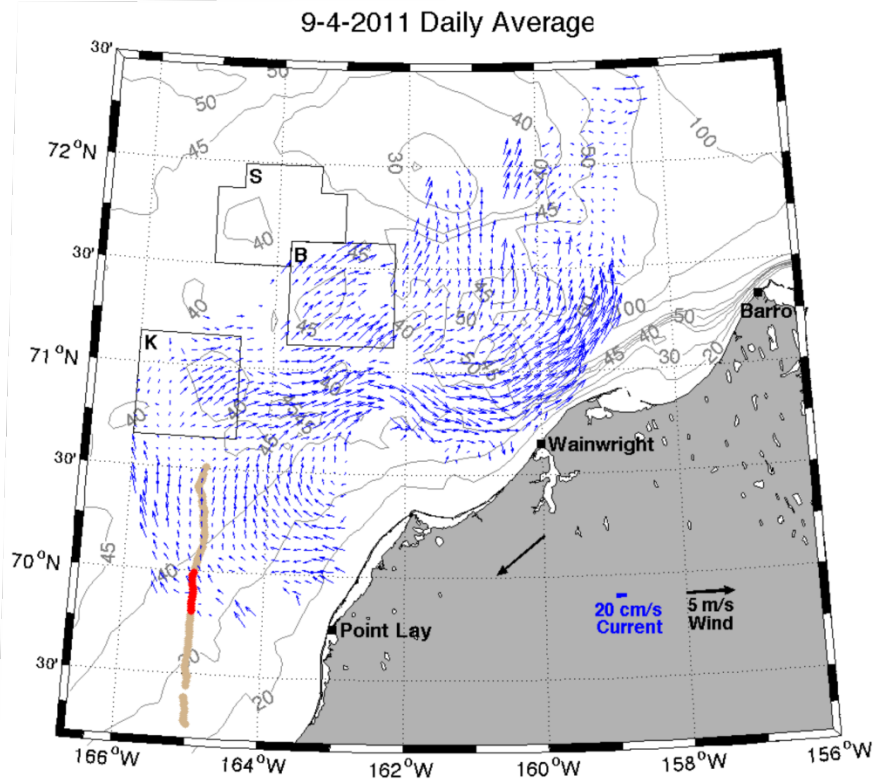


Figure 122. Mean surface currents on September 4 (top) and 5 (bottom), 2011. The glider track is red (denoting the track on the indicated day) and tan (denoting the entire glider track).

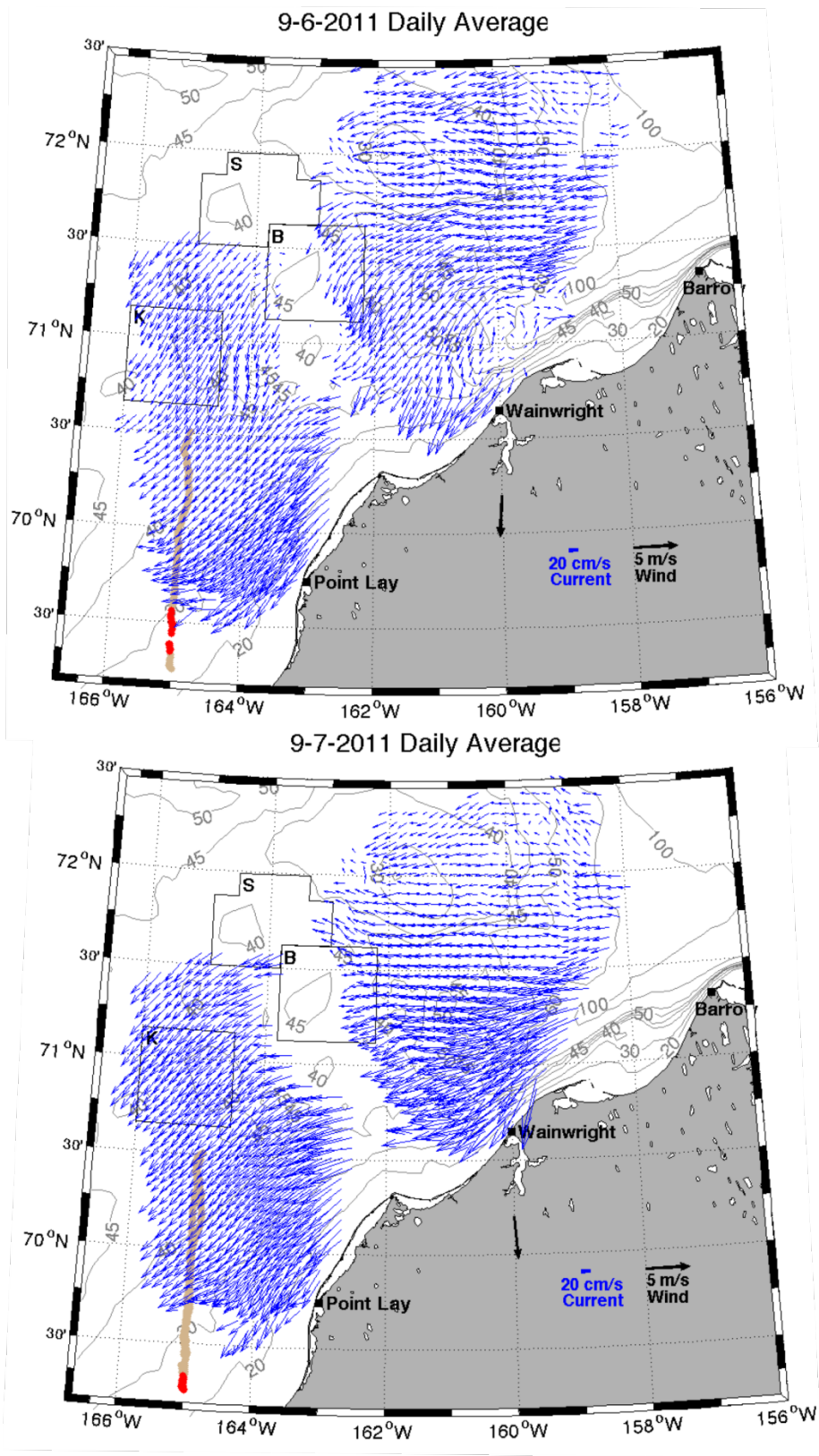


Figure 123. Mean surface currents on September 6 (top) and 7 (bottom), 2011. The glider track is red (denoting the track on the indicated day) and tan (denoting the entire glider track).

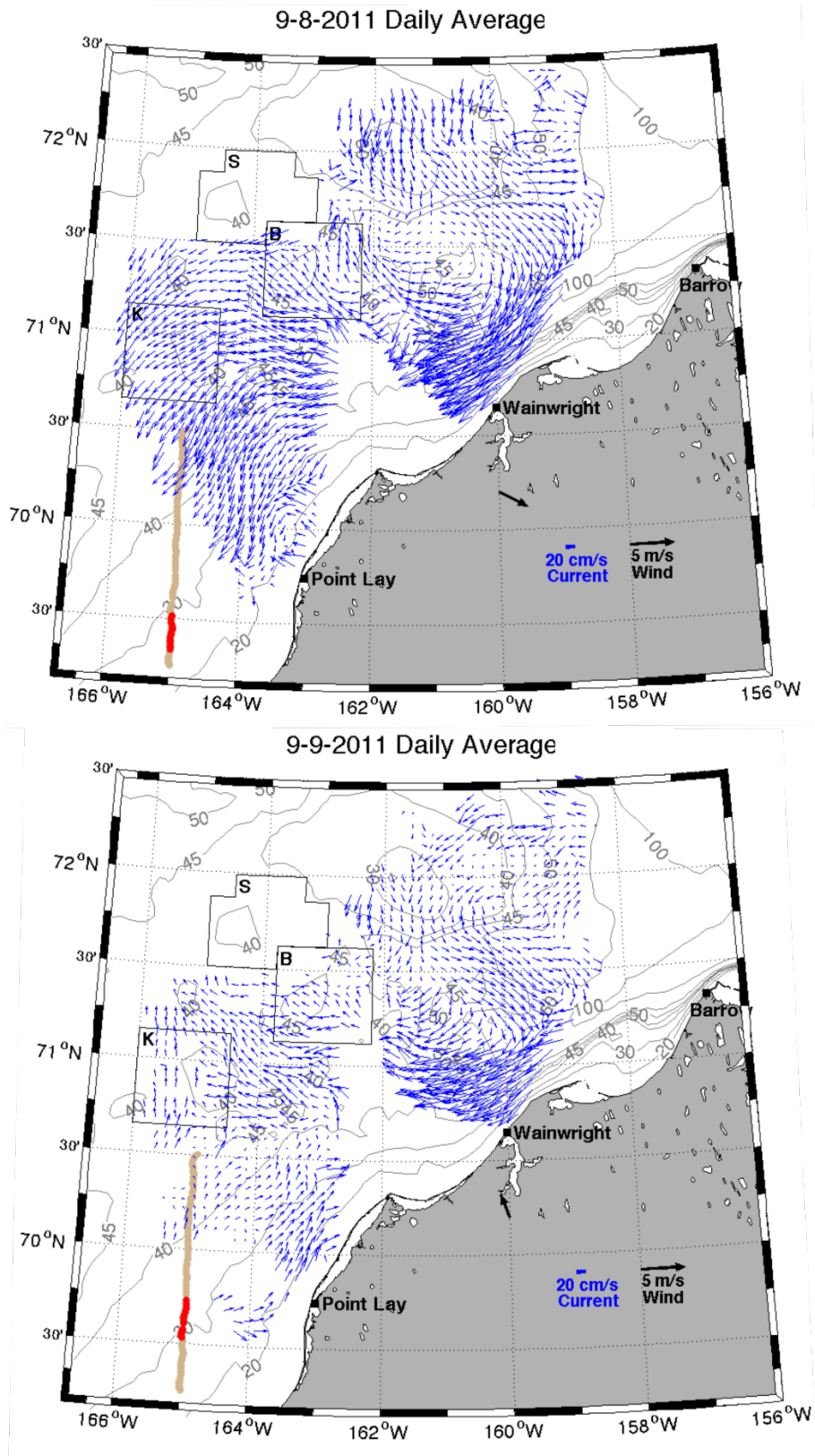


Figure 124. Mean surface currents on September 8 (top) and 9 (bottom), 2011. The glider track is red (denoting the track on the indicated day) and tan (denoting the entire glider track).

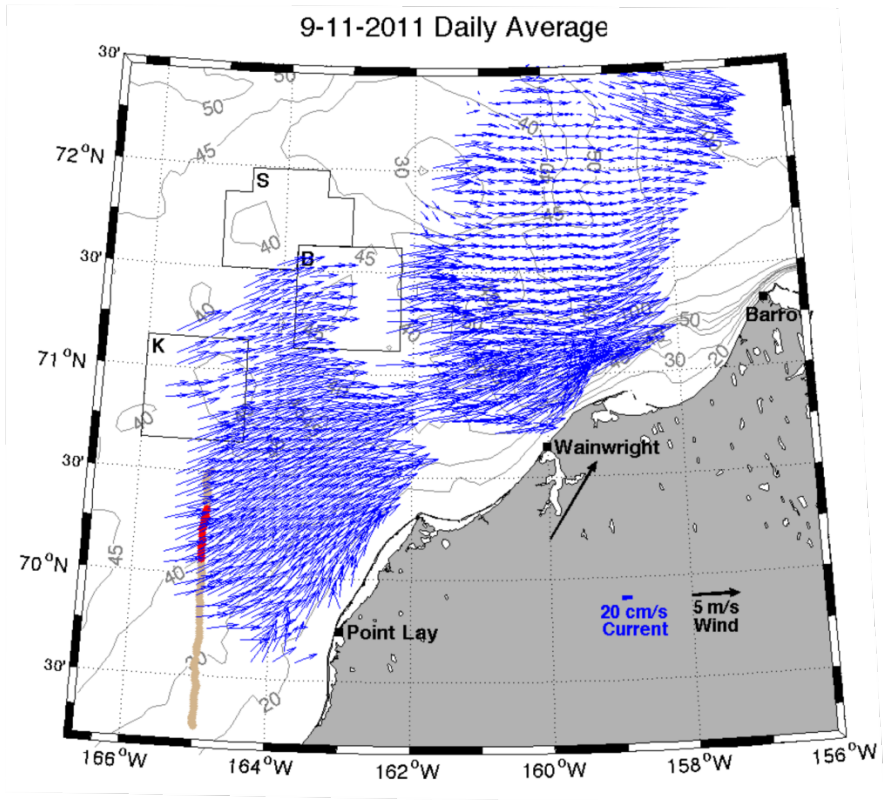
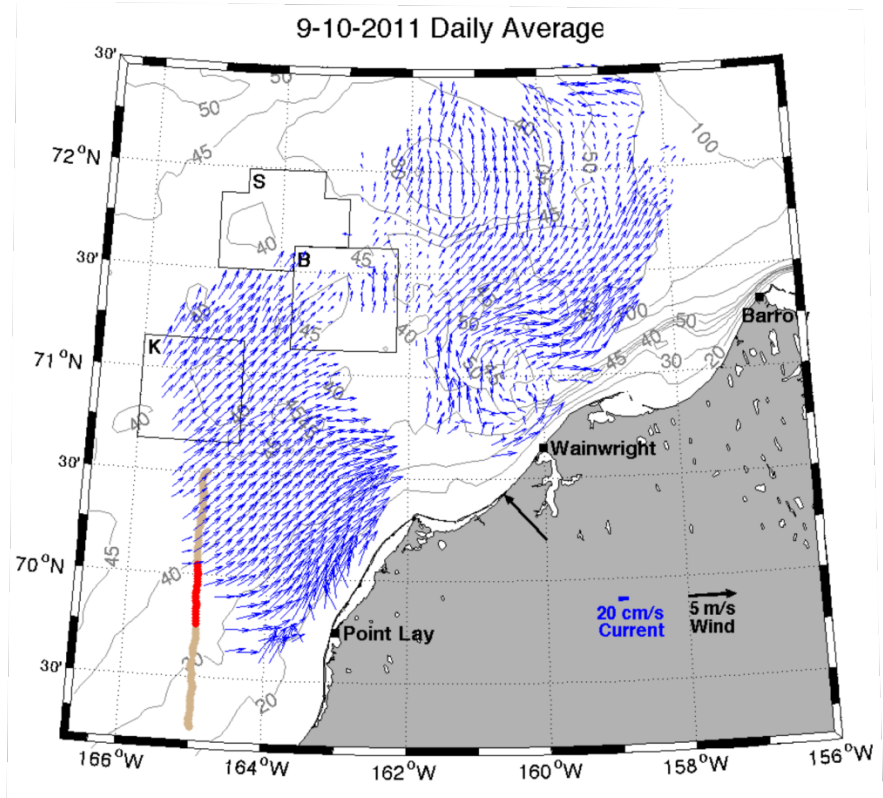


Figure 125. Mean surface currents on September 10 (top) and 11 (bottom), 2011. The glider track is red (denoting the track on the indicated day) and tan (denoting the entire glider track).

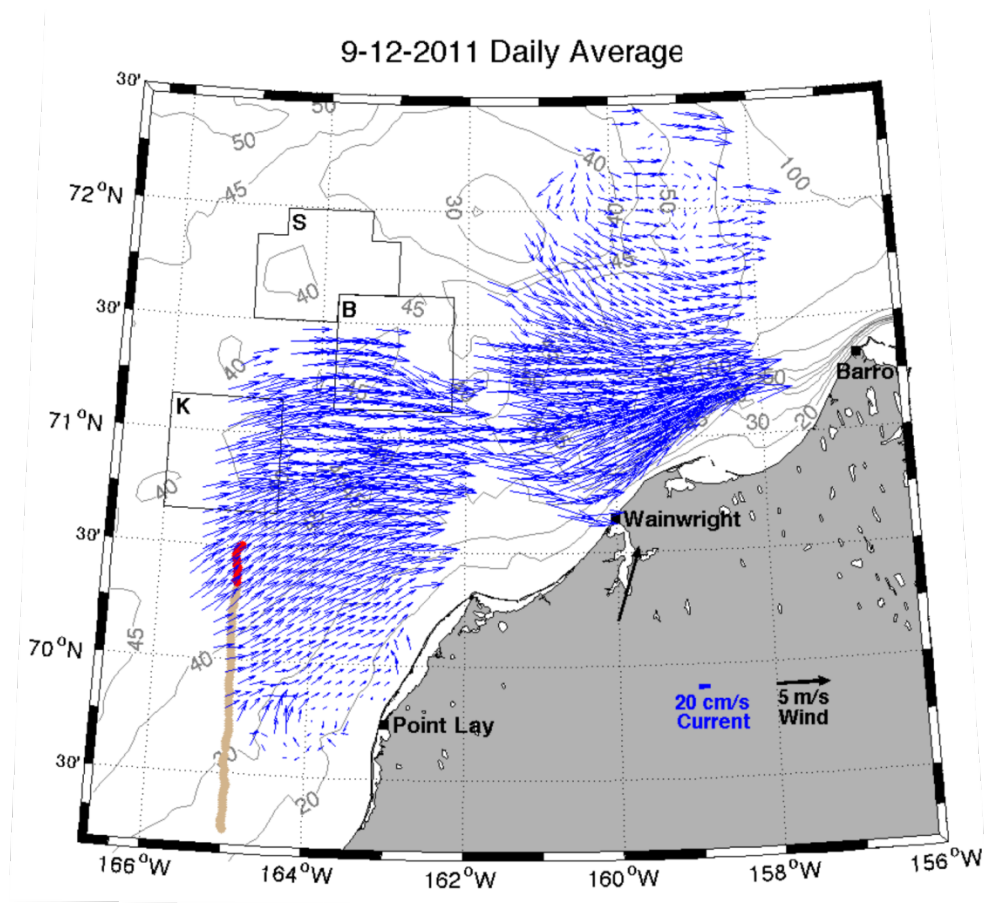


Figure 126. Mean surface currents on September 12 (top), 2011. The glider track is red (denoting the track on the indicated day) and tan (denoting the entire glider track).

southeast and impelled strong ($\sim 40 \text{ cm s}^{-1}$) northeastward currents offshore of Point Lay and in Barrow Canyon.

In spite of the large variations in both winds and currents over this period, the water properties along the glider transect were fairly uniform in time and space. There was a well-mixed upper layer which initially contained warm ($8 - 9^\circ\text{C}$), dilute (<30) waters, separated from cooler ($6 - 8^\circ\text{C}$), saltier (>30.5) bottom waters by a weak pycnocline at about 20 m depth. By the end of the survey the surface layer had cooled by $\sim 1^\circ\text{C}$, although there was virtually no change in subsurface water, nor the depth and strength of the pycnocline. These results suggest that most of the waters inshore, offshore and south of the glider transect contained similar properties. Moreover, no substantial fronts were encountered on either the south- or northbound glider transects, implying minimal vertical shear in the geostrophic velocity. As with the 2010 data sets, these results suggest that a simplified vertically integrated momentum balance can be estimated from these data sets.

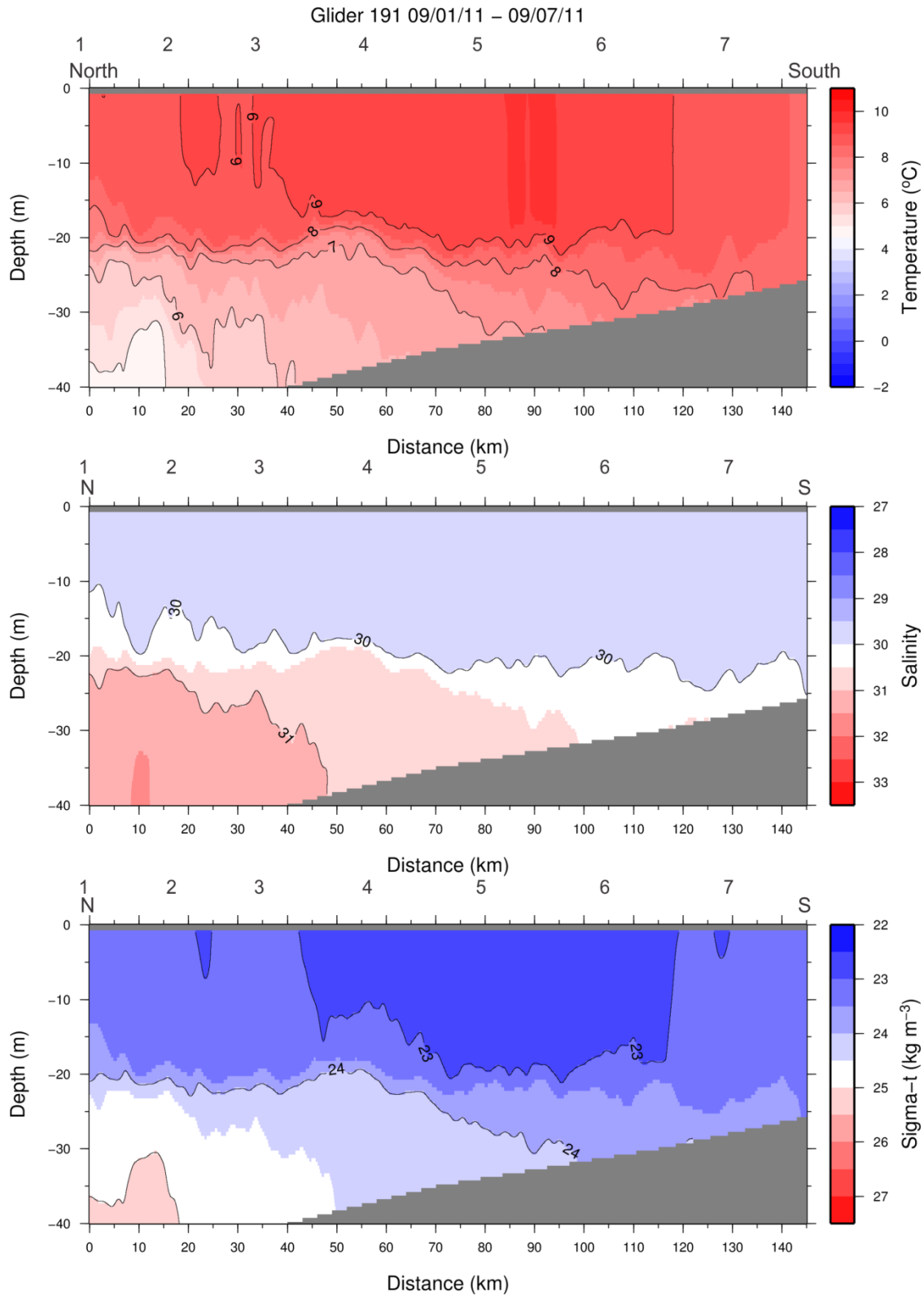


Figure 127. Section plots of temperature (top), salinity (middle), and density (sigma-t; bottom) from glider 191 September 1-7, 2011.

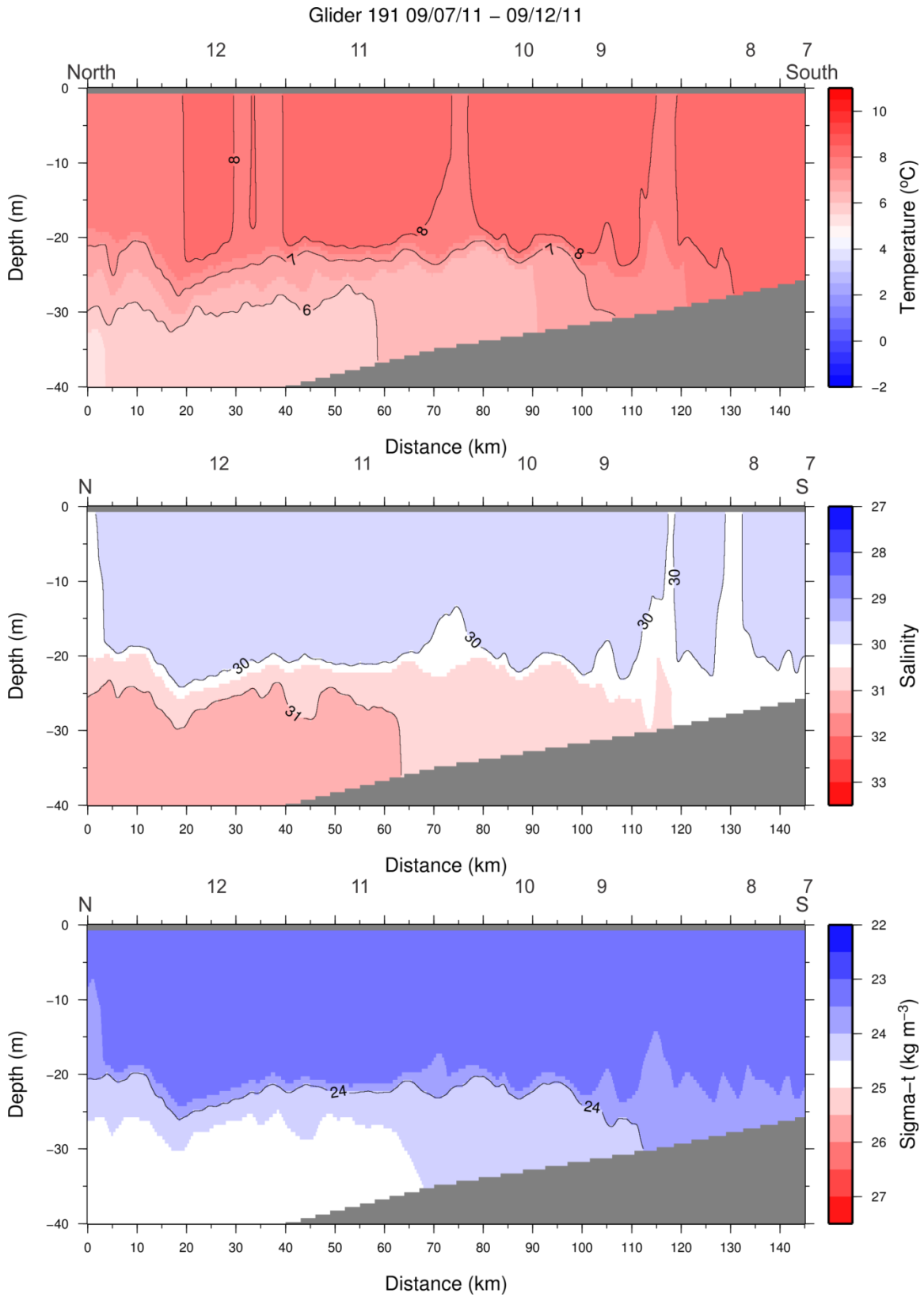


Figure 128. Section plots of temperature (top), salinity (middle), and density (sigma- t ; bottom) from glider 191 September 7-12, 2011.

4.5.6 Glider 191 Deployment: September 12 –16, 2011

After completing the north-south transect described above, Glider 191 continued northward into the Klondike area for another 100 km. Mean surface current maps and winds for this leg are shown in Figures 129 – 131, and the water property section map is shown in Figure 132. The glider's sensors were intermittently clogged during portions of the transect, and the data had to be discarded. Over most of this time period surface flow along the glider track was northward until the glider entered the Klondike area, whereupon it was mainly eastward. Winds were initially strong to the north-northeast but shifted to the west-southwest September 13 through 15. Temperature, salinity and density distributions were similar to those further south, although along the northernmost portions of this transect surface temperatures had decreased to $< 7^{\circ}\text{C}$ and salinities had increased to >31 , while bottom temperatures had decreased to $< 6^{\circ}\text{C}$ and salinities to >31.5 . Nevertheless, the pycnocline was weak and also centered at ~ 25 m depth. Again there were no prominent horizontal density gradients observed along the transect suggesting little vertical shear in the geostrophic currents throughout the water column. Indeed the stratification conditions observed along this transect in 2011, were not substantially different from those in 2009 when results from a moored current meter in Klondike showed no substantial vertical shear in the horizontal currents in Klondike [Weingartner *et al.*, 2013].

4.5.7 Interannual Hydrographic Variability

The annual repeat glider surveys allow us to compare oceanographic conditions from 2010 and 2011 in both Burger and Klondike. Starting with Burger, gliders 159 and 191 occupied the northeast corner of the Burger lease in mid-August 2010 (159) and 2011 (191). A T/S plot from this area and time period is shown in Figure 133. Hydrographic conditions were markedly different in several ways between the two years; the glider survey in 2010 (left panel in Figure 133) shows small temperature changes and consistently cold temperatures throughout the water column ($-1.6 - 2^{\circ}\text{C}$). Salinities show large variations, from very fresh surface waters due to ice melt with salinities slightly greater than 28 to salty bottom waters (>33) associated with winter waters. Conditions in 2011 (right panel in Figure 133) were remarkably different. Temperatures ranged from $\sim -1^{\circ}\text{C}$ at the bottom to very warm surface waters ($\sim 8^{\circ}\text{C}$) and generally a much warmer water column, with no surface melt water present. The salinity ranged from ~ 30 at the surface to 32.5 at the bottom. This comparison shows that hydrographic conditions in the Burger lease patch between consecutive years can be extreme and suggests that spatial and temporal variations in surface ice melt, winter water, and local heating due to solar radiation can account for most of these changes.

A similar comparison is possible for Klondike, where the glider surveyed the southeast corner in both 2010 and 2011 in the mid- to late-September time period (Figure 134). In 2010, CTD data from glider 167 showed an overall warm water column with temperatures ranging from $\sim 1.6^{\circ}$ to 8°C and salinities ranged from 30.5 to 33. The bottom waters show remnants of cold winter water that has been diluted by diapycnal mixing, and the upper water column is relatively fresh and very warm. In 2011 (right panel in Figure 134) conditions were markedly different, showing hydrographic data being tightly constrained in T-S space. Temperatures were between 4 and 8°C , and salinities were relatively fresh throughout the water column, being <31.3 everywhere.

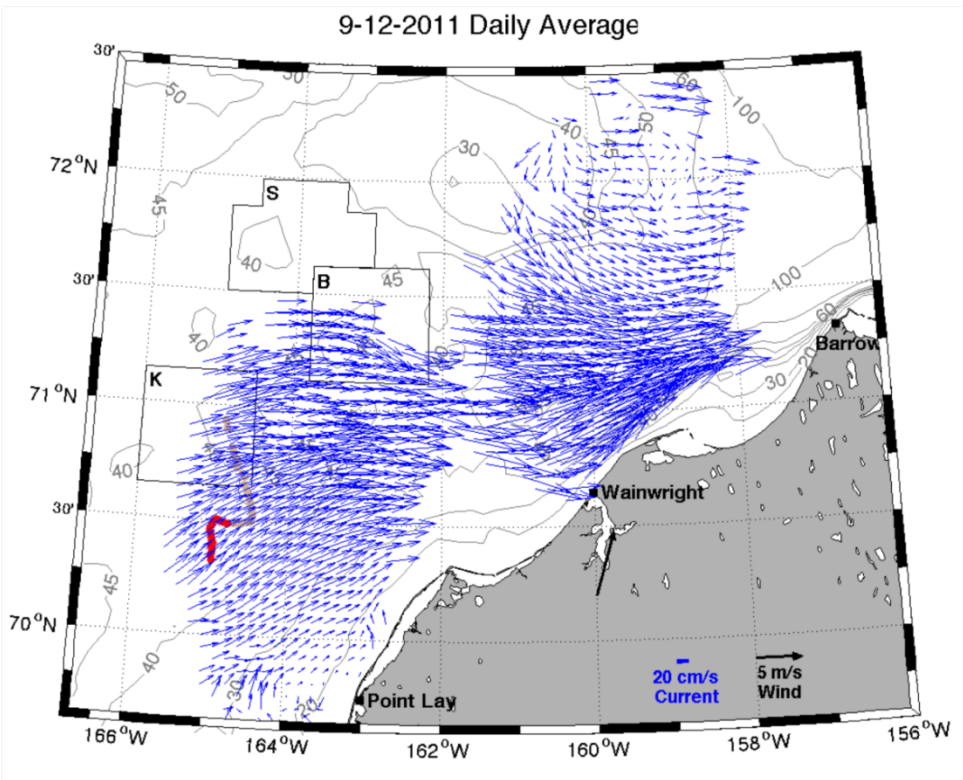
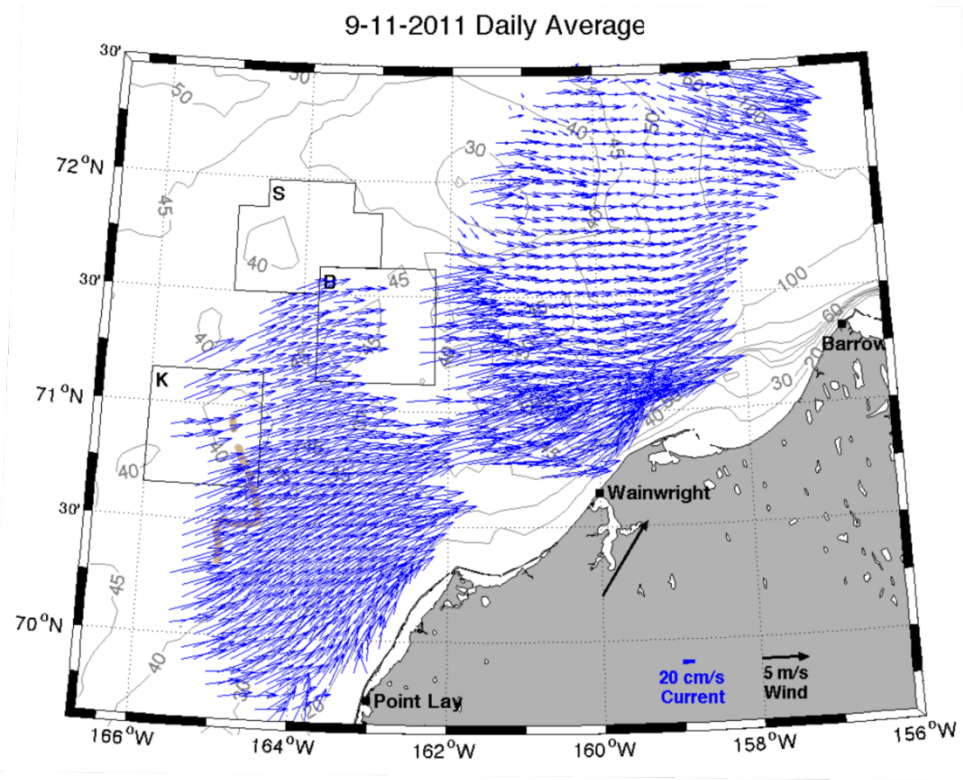


Figure 129. Mean surface currents on September 11 (top) and 12 (bottom), 2011. The glider track is red (denoting the track on the indicated day) and tan (denoting the entire glider track).

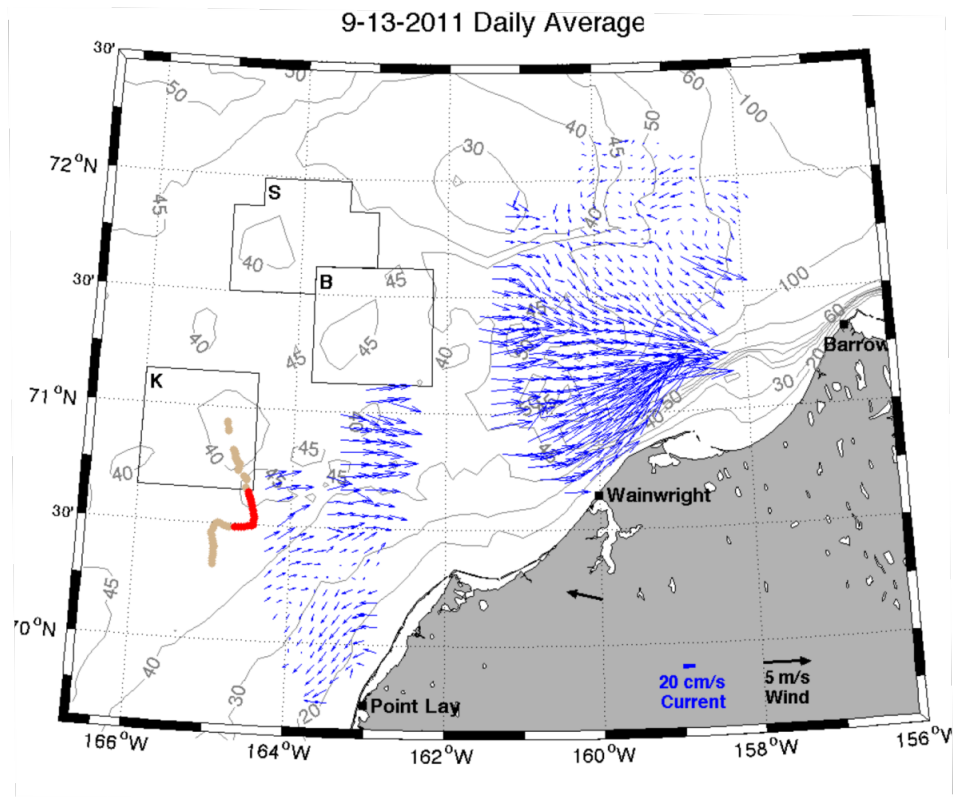


Figure 130. Mean surface currents on September 10 (top) and 11 (bottom), 2011. The glider track is red (denoting the track on the indicated day) and tan (denoting the entire glider track).

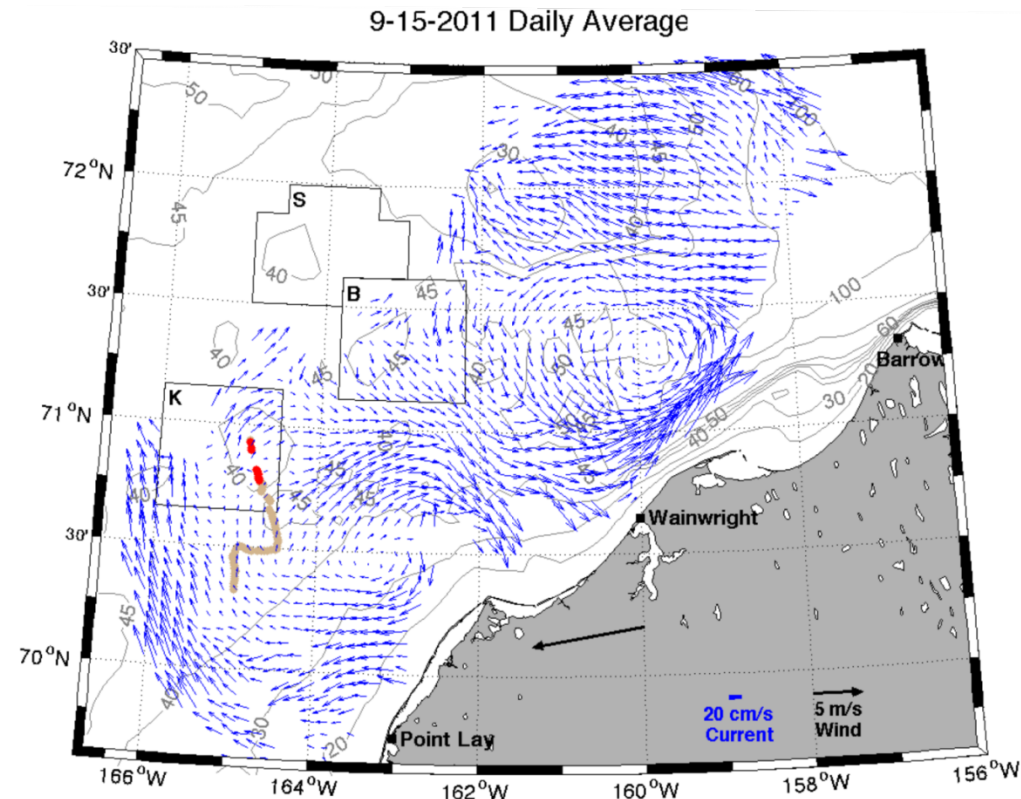


Figure 131. Mean surface currents on September 10 (top) and 11 (bottom), 2011. The glider track is red (denoting the track on the indicated day) and tan (denoting the entire glider track).

5. Discussion and Summary

The overall goal of this program was to improve our understanding of the circulation in the northeast Chukchi Sea in anticipation of potential offshore hydrocarbon development activities. We used a combination of measurement approaches, including moored oceanographic instruments, gliders, and HFR. The results have corroborated a number of features inferred from numerical models [Winsor and Chapman, 2004; Spall, 2007] and/or prior observations, quantified the variability of the transport into Barrow Canyon, and offered a variety of new insights on the circulation, its variability and dynamics, as well as spatial and temporal variability in the water masses of the northeast Chukchi Sea.

Our research approach was guided by a number of objectives. One principal objective was to determine if the surface (upper ~1 m) circulation reflected the sub-surface circulation as captured by historical current meter measurements and/or numerical models. We have partially addressed this issue. We find that, on average, the surface circulation flows eastward across the central Chukchi shelf (from the Central Channel and between at least 70.5°N and 71.5°N), under all wind conditions, except those winds blowing toward the 220° - 260°T sector at speeds $> \sim 6 \text{ m s}^{-1}$. This appears to be in general agreement with the findings of Weingartner *et al.* [2013], who analyzed summer and fall current meter records from Klondike and Burger. They found

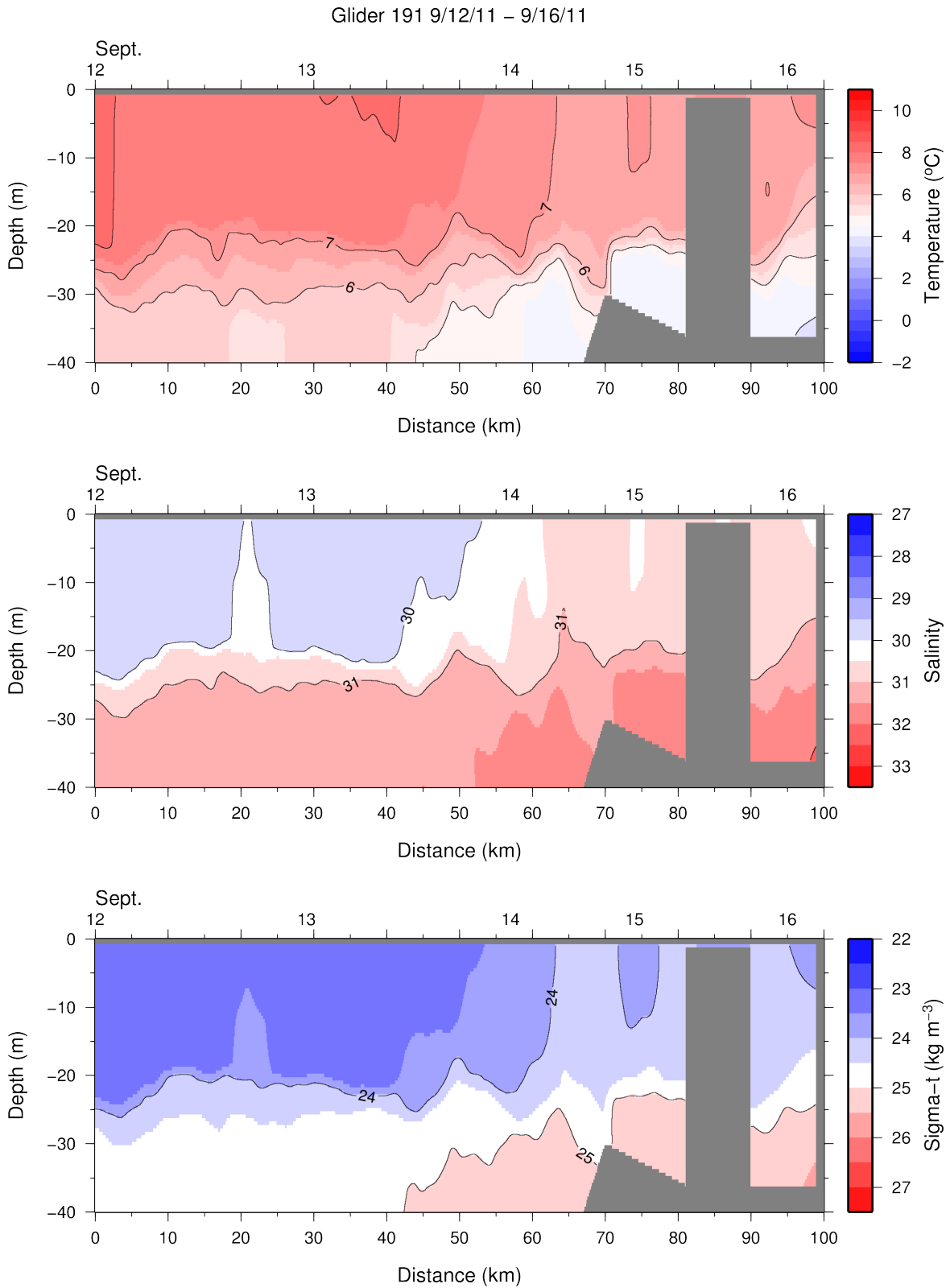


Figure 132. Section plots of temperature (top), salinity (middle), and density (sigma-t; bottom) from glider 191 September 12-16, 2011.

Northeast Corner of Burger Prospect, 2010 vs 2010

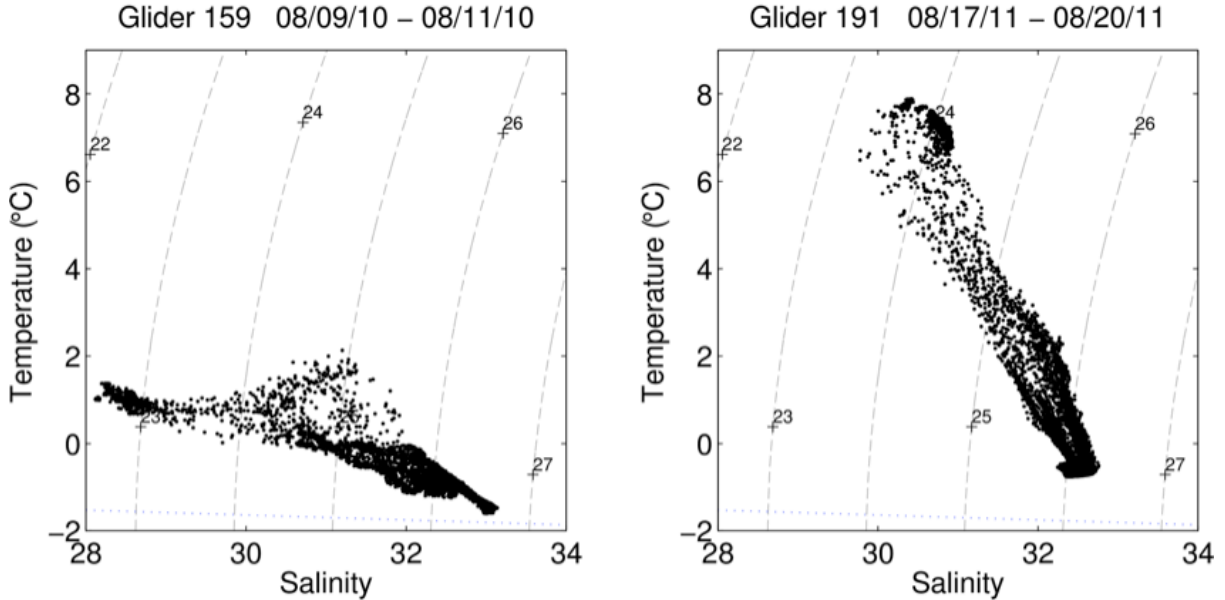


Figure 133. Temperature-Salinity plot of CTD data collected in the northeast corner of the Burger lease patch in 2010 and 2011. Left panel shows CTD data from August 9-11, 2010, and right panel data are from August 17-20, 2011.

Southeast Corner of Klondike Prospect, 2010 vs 2010

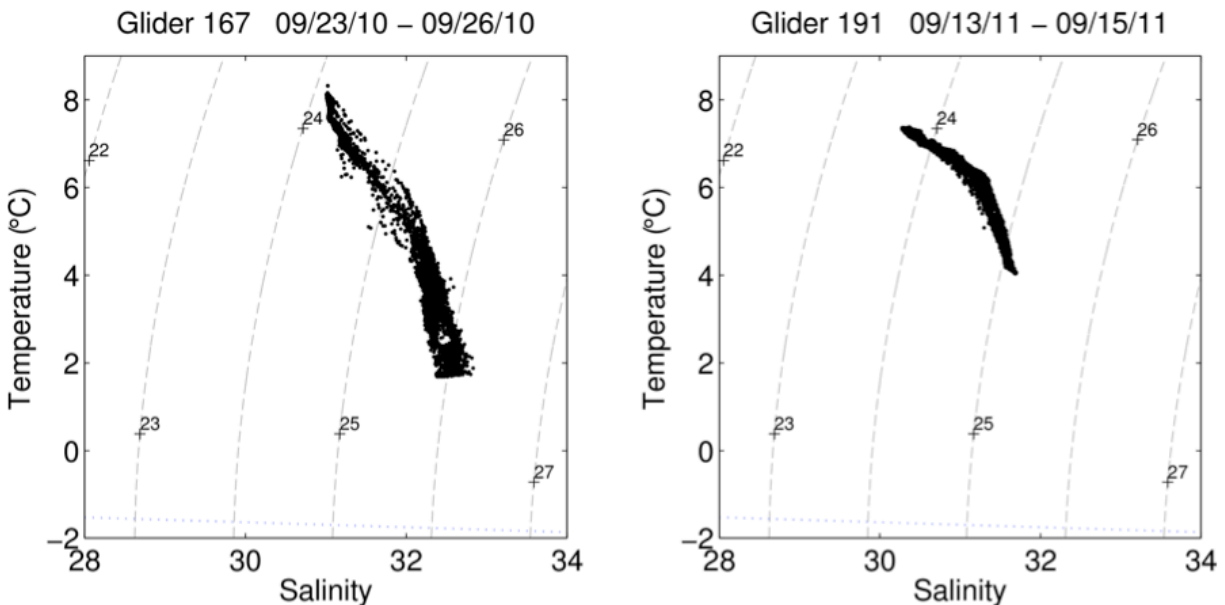


Figure 134. Temperature-Salinity plot of CTD data collected in the southeast corner of the Klondike lease patch in 2010 and 2011. Left panel shows CTD data from September 23-36, 2010, and right panel data are from September 13-15, 2011.

approximately eastward sub-surface flow, except when southwestward wind speeds exceeded this threshold. Similarly, results from satellite-tracked drifters deployed in August 2011 and August 2012 on the shelf south of Hanna Shoal also indicate eastward drift under mean westward winds $<6 \text{ m s}^{-1}$ [Weingartner *et al.*, in prep.]. The drifters approached the coast near Wainwright and then turned northeast and entered the ACC. Qualitatively, the drifter trajectories are similar to the HFR data in this regard.

Glider results suggest that by August the shelf south of about 71°N and west of 161°W contains weakly stratified or unstratified waters that have arrived throughout the course of the summer from the Bering Sea. North of this latitude and within the northern half of Burger and east of Hanna Shoal, the shelf is strongly stratified. These results corroborate those reported by Weingartner *et al.*, [2013], based on shipboard measurements made in the Klondike, Burger, and Statoil regions. Moreover, they report that based on summer and fall current meter measurements, the flow across Klondike is vertically uniform, while within the stratified regions of Burger, the flow is vertically sheared. The flow in Burger beneath the pycnocline was eastward on average, while the flow above the pycnocline can be downwind. Thus the HFR surface velocity data likely reflects the flow throughout the water column in unstratified areas, while in heavily stratified regions, the HFR velocities are likely a good proxy for flow in the upper 10 – 20 m of the water column. Within these regions the uppermost 10 – 20 m consists of cool, fresh meltwater products, while the lower portion of the water column consists of near-freezing, salty water formed the previous winter on the shelves of the Chukchi and/or Bering seas as a consequence of ice production. However, the glider hydrographic data indicates that horizontal density gradients (fronts) are weak over most of the shelf and therefore make a negligible contribution to any current shears. Hence, the vertical shears are most likely associated with those established by the winds, largest in the heavily stratified portions of the shelf. The only location where we observed substantial horizontal density gradients was at the entrance to Barrow Canyon. Here, the HFR data indicates that eastward-flowing Bering Sea summer waters enter the head of the canyon from the south, while the meltwater and winter waters enter from the west. At this juncture, large horizontal density gradients are established that are capable of supporting large, sub-surface geostrophic shears. The magnitude of the shears determined from the glider transects are comparable to those measured by the Barrow Canyon moorings. In the near future, additional current meter data will be available within the radar mask, and outside of the ACC, to allow more detailed examination of the vertical structure of the flow field over other regions of the Chukchi shelf.

Our results, along with those from Weingartner *et al.* [2013], suggest that from May through August the strongly stratified waters (established as sea ice melts above dense winter water) gradually retreat northward and eastward across the Chukchi shelf, as Bering Sea summer waters flow northward from Bering Strait. By September most of the shelf south of Hanna Shoal consists of these summer waters. However, portions of Burger and the area to the east of Hanna Shoal may remain highly stratified until late fall.

The fate of the water moving eastward across the shelf remains somewhat uncertain. We find that approximately 15% of the open water period this eastward onshore flow diverges, with some entering Barrow Canyon and some apparently moving southwestward toward Icy Cape and at least as far south as Point Lay. The mechanism by which this develops is, at present, unclear.

Perhaps the simplest explanation for the divergent mode is that the along-shore pressure gradient, which on average propels nearshore waters to the northeast, is weaker between Wainwright and the coast to the south than it is between Wainwright and Barrow. In the mean, the along-shore sea level should decrease from south to north, consistent with the large-scale pressure gradient between the Bering Sea and Arctic Ocean. It is this mean pressure gradient that forces Chukchi shelf water into Barrow Canyon and the Arctic Ocean. If we surmise that the alongshore pressure (sea-level) gradient south of Wainwright is weaker than the along-shore pressure gradient north of Wainwright and along Barrow Canyon, then the currents may be able to overcome the along-shore pressure gradient south of Wainwright, even when the winds are not sufficiently strong to reverse the along-canyon pressure gradient or the eastward flow carrying water from the central shelf toward the head of Barrow Canyon. At high wind speeds from the northeast, $>6 \text{ m s}^{-1}$, the entire coastal circulation within and to the south of Barrow Canyon flows west/southwestward.

Alternatively, the onshore flow that approaches the coast may interact with the coastline in a non-linear manner as described by *Whitehead* [1985]. In that case the approaching flow may split, although the details of the splitting jet depend upon the potential vorticity of the approaching flow and the coastal wall. The glider and HFR data suggest that the eastward flow from the central shelf has constant potential vorticity (potential vorticity= f/h , where f = Coriolis parameter and h is the bottom depth). On approaching the coast, the fluid should follow isobaths (and thus turn into the canyon). However, any cross-isobath flow component will bring the flow into shallower water and induce development of anticyclonic relative vorticity (e.g., clockwise turning of the flow). These are issues deserving of future investigation.

Conceivably, the divergence results in shallow upwelling between Wainwright and Icy Cape, which may enhance biological production in this region. The flow in the branch moving southwestward can be highly variable inshore of the 30 m isobath, and occasionally includes an anticyclonic circulation that fosters exchange between nearshore and offshore waters. These results further suggest that prior notions regarding the pathway of the ACC south of Wainwright must be reconsidered. The impression gleaned, perhaps incorrectly, from the literature dating back to *Coachman et al.* [1975] is that, in summer, the ACC flows northward as a coastal-trapped, buoyant current, hugging the coast en route to Barrow Canyon. This flow does materialize occasionally in the HFR data, but in general the flow is much more organized (and northward) offshore of the 30 m isobaths, while the region inshore and south of Icy Cape (and perhaps as far south as Cape Lisburne) may be engaged in recirculation.

A more unified circulation develops when winds are west-southwestward and $>\sim 6 \text{ m s}^{-1}$. Under such conditions the surface currents have a west to southwestward component over the entire area captured by the radars, and there is generally along-shore continuity in the nearshore flow field from Wainwright to the south. However there is westward spreading of waters flowing up Barrow Canyon due to the change in orientation of the isobaths. The isobaths are parallel to the coast within, and at the head of, the canyon and then veer offshore south of Wainwright. As a consequence, waters upwelled into Barrow Canyon can be carried toward the central shelf. This can easily happen during prolonged canyon-upwelling events.

We cannot conclusively state that the surface waters over the shelf between Barrow Canyon and east and north of Hanna Shoal flow clockwise around the Shoal as suggested by numerical

models, i.e., *Winsor and Chapman, 2004; Spall, 2007*. On some occasions, this does appear to be the case; however, the circulation in this region is typically weaker and more variable in direction than the flow south of 71.5°N, except under comparatively strong westward winds ($>6 \text{ m s}^{-1}$). HFR results suggest that there may be a front along 71.5°N, possibly separating summer Bering Sea waters from winter waters that have not been entirely flushed from the region. Alternatively, these winter waters may be resupplied below the surface by a clockwise flow around Hanna Shoal. Mooring, drifter, glider, and HFR measurements (under BOEM funding) that commenced in 2012 and will continue through 2014 should resolve this issue.

We did not observe a vigorous cross-shelf flux of dense water as predicted by the *Gawarkiewicz and Chapman [1995]* model and as hypothesized to have occurred over the Chukchi Sea shelf in the past by *Weingartner et al. [1998; 2005]*. Instead we found that the hyper-saline waters formed in polynyas during winter 2010 – 2011 were largely confined to the nearshore region, evident in moorings BC1 – BC3. However, the present set of observations do not provide sufficient evidence to refute the model for two reasons. First, the polynyas that formed in winter 2011, appear to have been narrow ($\sim 30 \text{ km}$), so that initially much of the dense water may have been confined close to the coast. Second, most of our array was located in the heart of the ACC. Therefore the dense water may have flushed rapidly into the canyon before instabilities in the dense water plume could grow appreciably in accordance with *Chapman and Gawarkiewicz [1995]*. Our data do suggest another mechanism to account for the dense water observations measured far offshore by *Weingartner et al. [1998; 2005]*. When present, polynyas along the Chukchi coast extend from Barrow to Cape Lisburne. Dense waters formed to the southwest of Wainwright may be carried offshore as part of the recirculating flow offshore of Point Lay that accompanies the divergent transport mode. Moreover, when the coastal flow is upcanyon, the nearshore flow is directed to the southwest and offshore and can easily advect polynya waters with it. Most of the dense, cold and salty winter waters, as observed by the gliders, were located south and southwest of Hanna Shoal, substantially farther offshore than traditional polynya regions.

The mooring data have provided the first highly-resolved estimates of the transport through Barrow Canyon. On annual average it amounts to $\sim 0.3 (\pm 0.15) \text{ Sv}$ or nearly 40% of the estimated annual transport through Bering Strait. The HFR data suggest that additional waters may enter the canyon north of the mooring transect, such that the mean transport in the canyon may be substantially greater downstream of the array. We did not observe a distinct annual cycle in Barrow Canyon transport, although it appears steadier in summer and early fall compared to winter.

Up canyon transport often, but not consistently, includes waters drawn from depths of $\sim 200 \text{ m}$ along the continental slope ($\sim 200 \text{ km}$ northeast of our mooring array). Up canyon velocities are typically $\sim 50 \text{ cm s}^{-1}$; therefore it would take an up canyon flow event of at least 5 days in duration to bring slope water to the location of the mooring array. Since several of the observed up canyon events were more than 10 days in length, it seems likely that slope waters can spread over a large area of the northeast Chukchi shelf before draining back down the canyon.

Variations in the canyon transport are coherent with the local winds, although the correlation varies through time, being weaker in summer and stronger in winter. Several reasons may

explain the time-varying strength of the correlation. For one, there may be differences in the regional ice distribution (concentration and thickness) and mobility that lead to along-shore differences in the ice-water stress, thus modulating the ocean's response to the same wind-forcing. Second, we find suggestions that the transport may respond to wind-forcing over the southern Chukchi/northern Bering Sea. This response may propagate northward along the coast as topographic vorticity waves, generated either by the wind or a fluctuating transport in Bering Strait. There may also be fluctuations in the shelfbreak flow field [Pickart *et al.*, 2011] that give rise to transport variability in the canyon. Finally, circulation dynamics within the canyon do not appear to be linear. On occasion we find that the Rossby number is >0.1 in the along-shore momentum balance, implying that non-linear advection of momentum can be important. The non-linear processes included the cross-shore advection of along-shore momentum, as well as along-shore advection of this momentum. The latter appears to be associated with the divergent flow mode offshore of Wainwright.

We succeeded in attaining several additional project objectives. We obtained a better assessment of the wave climate of the northeast Chukchi Sea. Our results indicate that the wind-wave field consists largely of waves at 4 – 8 s periods with a significant wave height of $\sim 1 - 2$ m. The wind waves mainly propagate from the northeast, north, and northwest. The largest waves observed were from the northwest with significant wave heights of ~ 4 m. Swells appeared primarily to originate from the southwest. These results should be regarded with caution, however. The waves from the northeast and east were may be fetch-limited and so the wave heights recorded at BC1 may not be representative of conditions farther offshore. Moreover, our sample size is small, and although we have measured waves throughout the entire open water season, it is doubtful that we have captured the extremes in wave height needed to reliably estimate the wave climate. Our limited comparison with the NOAA Wavewatch model suggests that the model does quite well in capturing the regional wave climate; however, important discrepancies did occur between the modeled and observed wave field. Wavewatch model significant wave heights were substantially smaller (by 1 – 2 m) than observed wave heights. We speculate that these differences may be due to under-estimating the fetch. Most likely the fetch used in the model depends upon the position of the ice edge. Our limited results suggest that the Wavewatch model overestimates the southward location of the ice-edge.

This project successfully developed the techniques needed to deploy and operate HFR systems in remote Alaska. Except for power outages in the village power grids that our HFR systems utilized, we encountered few problems. This is encouraging because it suggests that HFRs can be economically operated and maintained for long deployments in regions that are not accessible by road. The one constraint we experienced was associated with the need to locate our HFR sites in the villages. Although this choice was dictated by operational requirements, the HFR sites were far from optimal from a sampling perspective. Indeed, an unexpected result of this study was the divergence of the along-shore flow field between Wainwright and Point Lay. However, we do not understand the structure of this divergence because of data gaps due either to distance and/or land interference with the radar wave propagation. This difficulty can be overcome, however, due to recent developments. *Statscewich et al.* [2011] developed an autonomous remote power module (RPM) to support HFR operations along remote coastlines (where grid power is unavailable) that relies on renewable energy. These modules are portable, resilient, and include a satellite-communications package that delivers both the HFR data and information on the status

of the power generating systems. The device has been tested successfully for 7 months in Barrow, Alaska. HFR-RPM systems deployed at Icy Cape and Point Franklin would alleviate much of the land-masking encountered in this project. When combined with extended long-range radars, the distance gaps could also be limited.

We also successfully deployed, operated and recovered gliders over large distances and time periods in the northeast Chukchi Sea. This work resulted in the collection of a vast amount of unique, high-resolution hydrographic data which helped us put the HFR and mooring data into a three dimensional context and to understand water mass variations through time. The observations of bottom-bound cold pools and their lateral extent has implications for both physics and biology. The dynamics of the surface mixed layer and its horizontal density structure, including small-scale (sub-mesoscale) fronts were observed in detail. The observed sub-mesoscale fronts play a role in setting surface-layer properties because they restratify the mixed layer and may oppose one-dimensional processes (e.g. buoyancy fluxes and winds) that vertically mix the surface ocean [*Timmermans and Winsor, 2012*].

Finally, we have acquired a wealth of data on the structure and variability of the circulation field and the regional hydrography. The program has produced the first-ever reliable estimates of transports at the head of Barrow Canyon, the mesoscale variability in the surface circulation, and high-resolution hydrographic data. All of these data sets can be used to evaluate and guide the development of oil spill trajectory models.

6. Future Directions

Our presentation has purposefully focused on broader aspects of this rich data set. In the future, we will attempt to improve the spatial coverage of the HFR data, especially in those regions where landforms limit signal propagation. We are at present comparing the optimal interpolation procedure [*Kim et al., 2008*] and the variational approach suggested by *Yaremchuk and Sentchev* [2011] to fill gaps in data coverage. Once we have settled on an interpolation procedure we will remap the HFR data sets and classify these using the self-organized mapping (SOM) methodology [*Liu and Wesiberg, 2005*]. SOM finds similar flow patterns that are then mapped onto the region with an estimate of their frequency of occurrence. When combined with winds, these could be useful in an operational setting by helping to understanding the probability of a circulation pattern under particular wind conditions. The SOM approach should also be useful in guiding a dynamical understanding of some of the kinematic transitions observed in the flow fields.

Finally the HFR and glider surveys suggest that we may be able to perform some dynamical estimates based on barotropic dynamics, especially over the unstratified portions of the shelf. These estimates will be based on the vertically-integrated momentum balance, which if successful should provide us with estimates of the barotropic pressure gradients (sea-level slopes) and how these vary with the winds. These efforts will be enhanced by additional moored current meter data sets from this shelf.

7. Acknowledgments

This research was funded by a consortium including BOEM, US Dept of Interior, ConocoPhillips Alaska Company, Anchorage, AK, and Shell Exploration and Production Company, Anchorage, AK. Additional support for batteries, sensors, and a glider was provided by the Alaska Ocean Observing System (AOOS) and the University of Alaska. The Coastal Impact Assistance Program (CIAP) provided the funding for mooring BC1. We are grateful to the many people who assisted in various phases of the project, especially Caryn Rea and John Colloggi (ConocoPhillips), Michael Macrander, Robert Raye, and Allan Reece, retired (all with Shell) and Molly McCammon (AOOS). Sheyna Wisdom, Dave Aldrich, Jeff Hastings, and the officers and crews of the R/V *Westward Wind* and the R/V *Norseman II* assisted with the logistics associated with the mooring work. David Leech (UAF) fabricated, deployed, and recovered the moorings. Robert Shears and crew of the *Tukpuk*, Olgoonik Oilfield Services, assisted in the glider operations conducted from Wainwright. We thank the residents and councils of Point Lay, Wainwright, and Barrow for permission to conduct HFR operations in their villages, and Ukpeaġvik Iñupiat Corporation in Barrow, Olgoonik Corporation in Wainwright, and Cully Corporation in Point Lay for allowing us to use their lands. We also thank the Barrow Arctic Science Consortium for assistance with the HFR effort. Finally, we are grateful to the support provided by Warren Horowitz (BOEM), whose vision made this unique effort possible.

8. Publications and Presentations

Project Publications:

Timmermans, M.-L. and P. Winsor, 2012. Scales of horizontal density structure in the Chukchi Sea surface layer. *Cont. Shelf. Res.*, 52, 39-45, doi:10.1016/j.csr.2012.10.015.

Weingartner, T., E. Dobbins, S. Danielson, P. Winsor, R. Potter, and H. Statscewich (2013) Hydrographic variability over the northeastern Chukchi Sea shelf in summer-fall 2008–2010. *Cont. Shelf. Res.*, Accepted, doi:10.1016/j.csr.2013.03.012.

Project Presentations:

2009: Potter, R. Mapping Ocean Surface Currents in the Chukchi Sea, August 2009, Wainwright City Council, Oral Presentation

2010: Potter, R., S. Danielson, H. Statscewich, T. Weingartner, and P. Winsor, Physical Oceanography of the Northeast Chukchi Sea, January 2010, AMSS, Anchorage, AK, Oral Presentation.

2010: Potter, R. Studying Ocean Surface Currents in the Chukchi Sea, August 2010, Native Village of Point Lay, Oral Presentation.

2011: Potter, R., T. Weingartner, H. Statscewich, and P. Winsor, Surface Current Measurements in the Northeast Chukchi Sea Using Shore-Based High-Frequency Radar, January 2011, AMSS, Anchorage, AK, Oral Presentation.

2011: Winsor, P., T. Weingartner, H. Statscewich and R. Potter, AUV glider missions in the northeast Chukchi Sea, January 2011, AMSS, Anchorage, AK, Oral Presentation.

2012: Potter R., T. Weingartner, H. Statscewich, P. Winsor, Surface Currents in the Northeast Chukchi Sea, January 2012, AMSS, Anchorage, AK, Poster Presentation.

2012: Potter R., T. Weingartner, H. Statscewich, P. Winsor, Surface Currents in the Northeast Chukchi Sea, February 2012, Ocean Sciences Meeting, Salt Lake City, UT, Poster Presentation.

2012: Winsor, P., T. Weingartner, H. Statscewich, R. Potter, and M. Merck, AUV Glider and HF Radar observations of circulation and stratification features in the Chukchi Sea, January 2012, AMSS, Anchorage, AK, Poster Presentation.

2012: Winsor, P., T. Weingartner, H. Statscewich, R. Potter, and M. Merck, AUV Glider and HF Radar observations of circulation and stratification features in the Chukchi Sea, February 2012, Ocean Sciences Meeting, Salt Lake City, UT, Oral Presentation.

2012: Weingartner, T., R. Potter, H. Statscewich, P. Winsor, and S. Danielson: Circulation in the Northeast Chukchi Sea Depicted by Oceanographic Moorings, Drifters, and HF Radar, January 2012, AMSS, Anchorage, AK, Oral Presentation.

9. References

- Aagaard, K., T. J. Weingartner, S. L. Danielson, R. A. Woodgate, G. C. Johnson, T. E. Whitledge, 2006. Some controls on flow and salinity in Bering Strait. *Geophys. Res. Lett.*, 33, L19602, doi:10.1029/2006GL026612.
- Aagaard, K. and A. T. Roach, 1990. Arctic ocean-shelf exchange: Measurements in Barrow Canyon. *J. Geophys. Res.*, 95: 18163-18175.
- Aagaard, K., 1988. Current, CTD, and pressure measurements in possible dispersal regions of the Chukchi Sea, Outer Continental Shelf Environmental Research Program, Final Rep., Princ. Invest. 57, pp. 255-333. Dept. of Commerce/Dept. of Interior, Anchorage, AK.
- Aagaard, K., J. H. Swift, and E. C. Carmack, 1985. Thermohaline circulation in the Arctic Mediterranean seas. *J. Geophys. Res.*, 90, 4833-4846, 1985.
- Barrick, D. E., B. J. Lipa, and R. D. Crissman, 1985. Mapping Surface Currents with CODAR. *Sea Technology*, 26:43-48.
- Barrick, D. E. and B. J. Lipa, 1986. Correcting for Distorted Antenna Patterns in CODAR Ocean Surface Measurements. *IEEE J. of Oceanic Engr.*, OE-11(2):304-309.
- Barrick, D. E., 2002. Geometrical Dilution of Statistical Accuracy (GDOSA) in Multi-Static HF Radar Networks. White Paper.
http://www.codar.com/Manuals/SeaSonde/Docs/Informative/GDOSA_Definition.pdf
- Barrick, D. E. and R. Long, 2006. How Salinity Affects Radar Performance: A Case Study of 24 MHz HF Radar Performance in San Francisco Bay During the 2006 New Year Storm Floor. White Paper.
- Chapman, D. C. and G. Gawarkiewicz, 1995. Offshore transport of dense shelf water in the presence of a submarine canyon. *J. Geophys. Res.*, 100, 13373-13387.
- Coachman, L. K., K. Aagaard, and R. B. Tripp, 1975. *Bering Strait: The Regional Physical Oceanography*, 172 pp., University of Washington Press, Seattle, Washington.
- Garau, B., S. Ruiz, W. G. Zhang, A. Pascual, E. Heslop, J. Kerfoot, and J. Tintore, 2011. Thermal Lab Correction on Slocum CTD Glider Data. *J. Atmos. Oceanic Technol.*, 28, 1065-1071, doi:10.1175/jtech-d-10-05030.1.
- Gawarkiewicz, G. and D. C. Chapman, 1995. A numerical study of dense water formation and transport on a shallow, sloping continental shelf. *J. Geophys. Res.*, 100, 4489-4507.
- Gong, D. and R. S. Pickart, 2011. Transformation of Pacific water masses north of Bering Strait. Proceedings of the 11th Conference on Polar Meteorology and Oceanography, American Meteorology Society. <http://www.ametsoc.org/MEET/fainst/201111polar.html>
- Grebmeier, J. M. and C. P. McRoy, 1989. Pelagic-benthic coupling on the shelf of the northern Bering and Chukchi Seas. III. Benthic food supply and carbon cycling. *Mar. Ecol. Prog. Ser.*, 53, 79-91.
- Gurgel, K. W., 1997. Experience with shipborne measurements of surface currents fields by HF Radar. *Oceanography*, 10(2):82-84.
- Hansell, D., T. E. Whitledge, and J. J. Georing, 1993. Patterns of nitrate utilization and new production over the Bering-Chukchi shelf. *Cont. Shelf Res.*, 13, 601 – 627.

- Johnson, W. R., 1989. Current response to wind in the Chukchi Sea: a regional coastal upwelling event. *J. Geophys. Res.*, 94, 2057 – 2064.
- Kim, S-Y., E. J. Terrill, and B. D. Cornuelle, 2008. Mapping surface currents from HF radar radial velocity measurements using optimal interpolation. *J. Geophys. Res.*, 113, C10023, doi:10.1029/2007JC004244.
- Kohut, J. T. and S. Glenn, 2003. Improving HF radar surface current measurements with measured antenna beam patterns. *J. Atmos. and Ocean. Tech.*, 20, 2303 – 1316.
- Kundu, P. K., 1976. Ekman Veering Observed near the Ocean Bottom. *J. Physical Oceanography*, 6, 238 – 242.
- Liu, Y. and R. H. Weisberg, 2005. Patterns of ocean current variability on the West Florida Shelf using the self-organizing map. *J. Geophys. Res.*, 110, C06003, doi:10.1029/2004JC002786.
- Mathis, J. T., R. S. Pickart, D. A. Hansell, D. Kadko, and N. R. Bates, 2007. Eddy transport of organic carbon and nutrients from the Chukchi shelf into the deep Arctic basin. *J. Geophys. Res.*, 112, c05011, doi:10.1029/2006JC003899.
- Mountain, D. G., L. K. Coachman, and K. Aagaard, 1976. On the flow through Barrow Canyon. *J. Phys. Oceanogr.* 6, 461 – 470.
- Münchow, A. and E. C. Carmack, 1997. Synoptic flow and density observations near an Arctic shelfbreak. *J. Phys. Oceanogr.*, 6, 461 - 470.
- Münchow, A., E. C. Carmack, and D. A. Huntley, 2000. Synoptic density and velocity observations of slope waters in the Chukchi and East Siberian Seas. *J. Geophys. Res.*, 105: 14103-14119.
- Nikolopoulos, A., R. S. Pickart, P. S. Fratantoni, K. Shimada, D. J. Torres, and E. P. Jones, 2009. The western Arctic boundary current at 152°W: Structure, variability, and transport. *Deep-Sea Res. II*, 56, 1164-1181.
- Paquette, R. G. and R. H. Bourke, 1974. Observations on the Coastal Current of Arctic Alaska. *J. Mar. Res.*, 32, 195-207.
- Paquette, R. G. and R. H. Bourke, 1981. Ocean circulation and fronts as related to ice melt-back in the Chukchi Sea. *J. Geophys. Res.*, 86, 4215-4230.
- Pickart, R. S., L. J. Pratt, D. J. Torres, T. E. Whitledge, A. Y. Proshutinsky, K. Aagaard, T. A. Agnew, G. W. K. Moore, and H. J. Dail, 2010. Evolution and dynamics of the flow through Herald Canyon in the Western Chukchi Sea. *Deep-Sea Res. II*, 57, 5-26, doi:10.1016/j.dsr2.2009.08.002.
- Pickart, R. S., M. A. Spall, G. W. K. Moore, T. J. Weingartner, R. A. Woodgate, K. Aagaard, and K. Shimada, 2011. Upwelling in the Alaskan Beaufort Sea: Atmospheric Forcing and local versus non-local response. *Prog. Oceanogr.*, 88, 78-100, doi:10.1016/j.pocean.2010.11.005
- Pickart, R. S., T. Weingartner, L. J. Pratt, S. Zimmermann, and D. J. Torres, 2005. Flow of winter-transformed Pacific water into the western Arctic. *Deep-Sea Res. II*, 52: 3175 - 3198.
- Potter, R. A and T. J. Weingartner, 2009. Surface Circulation Radar Mapping in Alaskan Coastal Waters: Beaufort Sea and Cook Inlet. MMS OCS Study 2009-049. Final Report. 164 pp.

- Shimada, K., T. Kamoshida, M. Itoh, S. Nishino, E. Carmack, F. McLaughlin, S. Zimmermann, and A. Proshutinsky, 2006. Pacific Ocean inflow: Influence on catastrophic reduction of sea ice cover in the Arctic Ocean, *Geophys. Res. Lett.*, 33(8), doi:10.1029/2005GL025624L08605.
- Shroyer, E. L. and A. J. Plueddemann, 2012. Wind-driven modification of the Alaskan coastal current. *J. Geophys. Res.*, Accepted, doi:10.1029/2011JC007650.
- Spall, M. A., 2007. Circulation and water mass transformation in a model of the Chukchi Sea. *J. Geophys. Res.*, 112, C05025, doi:10.1029/2005JC002264.
- Springer, A. M. and C. P. McRoy, 1993. The paradox of pelagic food webs in the northern Bering Sea-III, Patterns of primary production. *Cont. Shelf. Res.*, 13, 575-599.
- Statscewich, H., T. Weingartner, S. Danielsen, B. Grunau, G. Egan, and J. Timm, 2011. A High-Latitude Modular Autonomous Power, Control, and Communication System for Application to High-Frequency Surface Current Mapping Radars. *Marine Technology Society*, 45(3): 59 – 68.
- Teague, C., 2001. Ionospheric Effects on Coastal Radar Systems. Radiowave Oceanography the First International Workshop, H.C. Graber and J. D. Paduan (ed.), p. 56-61.
- Timmermans, M.-L. and P. Winsor, 2012. Scales of horizontal density structure in the Chukchi Sea surface layer. *Cont. Shelf. Res.*, 52, 39-45, doi:10.1016/j.csr.2012.10.015.
- United States Army Corps of Engineers, Shore Protection Manual, 1984, Dept. of the Army, Waterways Experiment Station, Corps of Engineers, Coastal Engineering Research Center, PC Box 631 Vicksburg, Mississippi 39180, 4th ed. 652 p.
- Von Appen, W.-J., and R. S. Pickart, 2012. Two configurations of the Western Arctic shelfbreak current in summer. *J. Phys. Oceanogr.*, 42, 329-351, doi:10.1175/JPO-D-11-026.1.
- Walsh, J. J., C. P. McRoy, L. K. Coachman, J. J. Goering, J. J. Nihoul, T. E. Whitley, T. H. Blackburn, P. L. Parker, C. D. Wirick, P. G. Shuert, J. M. Grebmeier, A. M. Springer, R. D. Tripp, D. A. Hansell, S. Djenedi, E. Deleersnijder, K. Henriksen, B. A. Lund, P. Andersen, F. E. Müller-Karger, and K. Dean, 1989. Carbon and nitrogen cycling within the Bering/Chukchi seas: Source regions for organic matter affecting AOU demands of the Arctic Ocean. *Prog. Oceanogr.*, 22, 277-359.
- Weingartner, T., E. Dobbins, S. Danielson, P. Winsor, R. Potter, and H. Statscewich, 2013. Hydrographic variability over the northeastern Chukchi Sea shelf in summer-fall 2008–2010. *Cont. Shelf. Res.*, Accepted, doi:10.1016/j.csr.2013.03.012.
- Weingartner, T., K. Aagaard, R. Woodgate, S. Danielson, Y. Sasaki, and D. Cavalieri, 2005. Circulation on the North Central Chukchi Sea Shelf. *Deep-Sea Res. II*, 52: 3150-3174, doi:10.1016/j.dsr2.2005.10.015.
- Weingartner, T. J., D. J. Cavalieri, K. Aagaard, and Y. Sasaki, 1998. Circulation, dense water formation, and outflow on the northeast Chukchi shelf. *J. Geophys. Res.*, 103: 7647 – 7661.
- Whitehead, J. A., 1985. The deflection of a baroclinic jet by a wall in a rotating fluid. *J. Fluid Mech.*, 157, 79 – 93.

- Winsor, P. and D. C. Chapman, 2004. Pathways of Pacific Water across the Chukchi Sea: A numerical model study. *J. Geophys. Res.*, 109, C03002, doi:10.1029/2003JC001962.
- Woodgate, R. A., K. Aagaard, T. J. Weingartner, 2006. Interannual changes in the Bering Strait fluxes of volume, heat and freshwater between 1991 and 2004. *Geophys. Lett.*, 33, L15609, doi:10.1029/2006GL026931.
- Woodgate, R. A., K. Aagaard, and T. Weingartner, 2005. A Year in the Physical Oceanography of the Chukchi Sea: moored measurements from autumn 1990-91. *Deep-Sea Res. II*, 52, 3116-3149.
- Yaremchuk, M. and A. Sentchev, 2011. A combined EOF/variational approach for mapping radar-derived sea surface currents. *Cont. Shelf Res.*, 31: 758 – 768.